

Quantitative Fluorescence Microscopy of Protein Dynamics in Living Cells

Shehu Mustapha Ibrahim

The work described in this thesis was performed at the Department of Pathology of the Josephine Nefkens Institute, Erasmus MC, Rotterdam and Department of Biophysics and Cell Biology, University of Debrecen, Medical and Health Science Centre, Hungary.

Quantitative Fluorescence Microscopy of Protein Dynamics in Living Cells

Kwantitatieve Fluorescentiemicroscopie van Eiwitdynamiek

in Levende Cellen

Proefschrift

**ter verkrijging van de graad van doctor
aan de Erasmus Universiteit Rotterdam
op gezag van de rector magnificus**

Prof. dr. S.W.J. Lamberts

en volgens besluit van het College voor Promoties.

**De openbare verdediging zal plaatsvinden op
donderdag 21 december 2006 om 09:00 uur**

door

Shehu Mustapha Ibrahim
Geboren te Ilorin, Nigeria

Promotiecommissie

Promotor: Prof.dr. J.H.J. Hoeijmakers

Overige leden: Prof.dr.ir. J. Trapman
Prof.dr. J. Szöllösi
Dr. R. Krams

Copromotores: Dr. A.B. Houtsmuller
Dr. G. Vereb

Contents

Abbreviations		7
Chapter 1	General Introduction	9
Chapter 2	Light Driven Dynamics of GFP Fluorescence Emission in Living Cells	49
Chapter 3	Dynamics of Nuclear Proteins: Complementarities of Fluorescence Correlation Microscopy and Photobleaching in Intra-Cellular Mobility Measurements	73
Chapter 4	In the Absence of DNA Damage the Nuclear Mobility of Most Nucleotide Excision Factors is Mainly Determined by their Molecular Size	109
Chapter 5	Recruitment of the Nucleotide Excision Endonuclease XPG to sites of UV-induced Damage Depends on Functional TFIIH	131
Chapter 6	Translational Mobility of EGF Receptor Fusion Proteins over Short and Long Distances – Complementarity of Fluorescence Correlation Microscopy and FRAP in Cellular Diffusion Measurements	169
Chapter 7	Cholesterol-dependent Clustering of IL-2Rα and its Colocalization with HLA and CD48 on T Lymphoma Cells suggests their Functional Association with Lipid	223
Summary		249
Samenvating		253
Acknowledgements		257
List of publications		259
Curriculum Vitae		261

Abbreviations

AOM	Acousto-optical modulator
AR	Androgen receptor
ARE	Androgen response element
BCIP	Bromo-4-chloro-3-indolyl phosphate
CAF I	Chromatin assembly factor I
CHO	Chinese hamster ovary
CLSM	Confocal laser scanning microscopes
CPD	Cyclobutane pyrimidine dimers
CS	Cockayne syndrome
DBD	DNA binding domain
DBD	DNA-binding domain
DM	Dichroic mirror
EBFP	Enhanced blue fluorescent protein
ECFP	Enhanced cyan fluorescent protein
EGF	Epidermal growth factor
EGFP	Enhanced green fluorescent protein
EGFR	Epidermal growth factor receptor
ERCC	Excision repair cross complementing protein
ESPT	Excited state proton transfer
EYFP	Enhanced yellow fluorescent protein
FCM	Fluorescence correlation microscopy
FCS	Fluorescence correlation spectroscopy
FP	Fusion protein
FRAP	Fluorescence recovery after photobleaching
FRET	Fluorescence resonance energy transfer
FWHM	Full width half-maximum
GFP	Green fluorescence protein
GG-NER	Global genome NER
IC	Internal conversion
IL-2	Interleukin-2
IL-2R	Interleukin-2 receptor
ISC	Intersystem crossing
LBD	ligand-binding domain

NA	Numerical aperture
NBT	Nitro blue tetrazolium
NER	Nucleotide excision repair
NLS	Nuclear localisation signal
NTD	N-terminal transactivation domain
PBS	Phosphate-buffered saline
PMT	Photomultiplier tube
RCFPs	Reef coral fluorescent proteins
ROI	Region of interest
RPA	Replication Protein A
RT	Room temperature
S ₀	Electronic ground state
S ₁ , S ₂ and so on	Singlet excited energy states
SNOM	Scanning near-field optical microscopy
SR	Steroid receptor
T ₁	Excited triplet state
TC-NER	Transcription-coupled NER
TIR	Total internal reflection
TrfR	Transferrin receptor
TTD	Trichothiodystrophy
UV	Ultraviolet
wt-GFP	Wild-type green fluorescent protein
XP	Xeroderma pigmentosum
XPA	Xeroderma pigmentosum A
XPB	Xeroderma pigmentosum B
XPC	Xeroderma pigmentosum C
XPD	Xeroderma pigmentosum D
XPE	Xeroderma pigmentosum E
XPF	Xeroderma pigmentosum F
XPG	Xeroderma pigmentosum G
XPV	Xeroderma pigmentosum V

Chapter

1

General Introduction

In fluorescence microscopy, the ability of fluorescent molecules to emit light of specific wavelengths following the absorption of light of shorter wavelengths is utilized to observe the molecules directly or to indicate the position of fluorescently tagged target molecules in a cell. Recent advances in laser and computer technologies have led to the availability of commercial confocal laser scanning microscopes (CLSM) thereby making fluorescence microscopy widely accessible. Furthermore, the development of genetically encoded fluorescent proteins have led to advances in the analytical techniques used for the evaluation of protein localization, dynamics and interactions in the cellular environment.

A perfect fluorescence assay is one, which could monitor every protein directly and map its behaviour in time. However, at present no single imaging modality can assess all aspects of the complicated processes a protein undergoes in carrying out its functions in the living cell. Proteins are mostly observed indirectly with the use of fluorescent tags, which are assumed not to interfere with the behaviour of the target protein being studied. High-resolution digital imaging of fusion proteins (FP) enables protein localization and colocalization to be monitored in time. More sophisticated quantitative techniques, such as fluorescence recovery after photobleaching (FRAP) and fluorescence correlation spectroscopy (FCS) are used to study protein dynamics and protein-protein interactions. Although FRAP is a bulk assay method and FCS is more effective when only a few molecules are monitored at a time, the complementary use of both methods provides a more accurate insight into the movement of proteins and their interactions with cellular components in living cells.

Most fluorescence assay methods rely on fluorescence changes to quantify the dynamics leading to these changes. Therefore an accurate understanding of protein behaviour does not only require the use of more than one assay technique where

necessary but also a knowledge of the photodynamic properties of the fluorescent tag being used, for a proper interpretation of the fluorescence data generated by these techniques.

In this thesis, the efficacies of various fluorescence microscopy techniques in the analysis of protein localizations and dynamics in living cells are examined. In particular the complementarities of these methods have been investigated and the fluorescence behaviour of the enhanced green fluorescent protein (EGFP) considered in the interpretation of the fluorescence data. In the following paragraphs the basic principles of fluorescence microscopy will be discussed after a short history of the optical microscope. The green fluorescence proteins (GFPs) and their properties that make them convenient fluorescent probes for in vivo and in-situ analysis of proteins will be presented followed by a description of various fluorescence assay methods. Finally, a description of the proteins studied in this thesis will be given, followed by an outline of the thesis.

1.1 Short history of the optical microscope

The magnifying and light focussing abilities of lenses have been observed as early as the first century when rudimentary lenses formed from transparent crystals were used to focus sunlight on dry materials to make fire. It was, however, not until the Renaissance when the first simple microscope was constructed. The humble 10x magnification achieved by the assembly, consisting of a magnifying lens and a plate situated at either ends of a tube, was then unprecedented as it made visible the fascinating details of objects. This inspired the Dutch spectacle maker Zacharias Janssen and his son Hans in 1590 to experiment with several lenses in a tube to enhance the achievable magnification thereby constructing the forerunner of the compound microscope and of the telescope. Galileo in 1609 worked out the principles of lenses and made an improved instrument

equipped with a focussing device. Later, Antonie van Leeuwenhoek (1632-1723), credited with founding the field of microscopy, built microscopes using tiny lenses of very high magnifications to make his pioneering studies on bacteria, yeast, plants and the circulation of blood corpuscles in capillaries.

Ingenious improvements to the light microscope continued through the nineteenth century. High quality lenses were being used in the optical elements and illumination systems were introduced. However, with the introduction of oil-immersion objectives at the end of the nineteenth century, the optical microscope reached its limits of resolution imposed by the diffraction of light. As discovered by Ernest Abbe in 1878, the best resolution attainable with the use of white light of average wavelength of $0.55 \mu\text{m}$ is $0.275 \mu\text{m}$. It was thus realised that better resolutions could only be achieved by the use of a source of illumination with a much shorter wavelength. (The shortest wavelength of visible light, $0.4 \mu\text{m}$ could yield a resolution of $0.2\mu\text{m}$.)

In 1904, Köhler and Moritz von Rohr designed the ultraviolet microscope which was illuminated by ultraviolet radiation generated through a cadmium arc and used lenses fabricated from fused quartz. Operating in the shortest wavelength range of visible light, the microscope enabled images of high resolutions to be made. Inevitably, fluorescence was observed, thus establishing the foundation for ultraviolet and fluorescence microscopy. In 1934 Frits Zernike introduced the phase-contrast technique, which enabled the study of live organisms under the microscope. The confocal imaging technique, first proposed by Marvin Minsky in 1953, introduced a confocal "pinhole" in front of the image plane so that out-of-focus light from above and below the plane of focus in the object are filtered out of the image. Recent (1980s) advances in laser technology and the availability of high speed and large storage capacity microcomputers

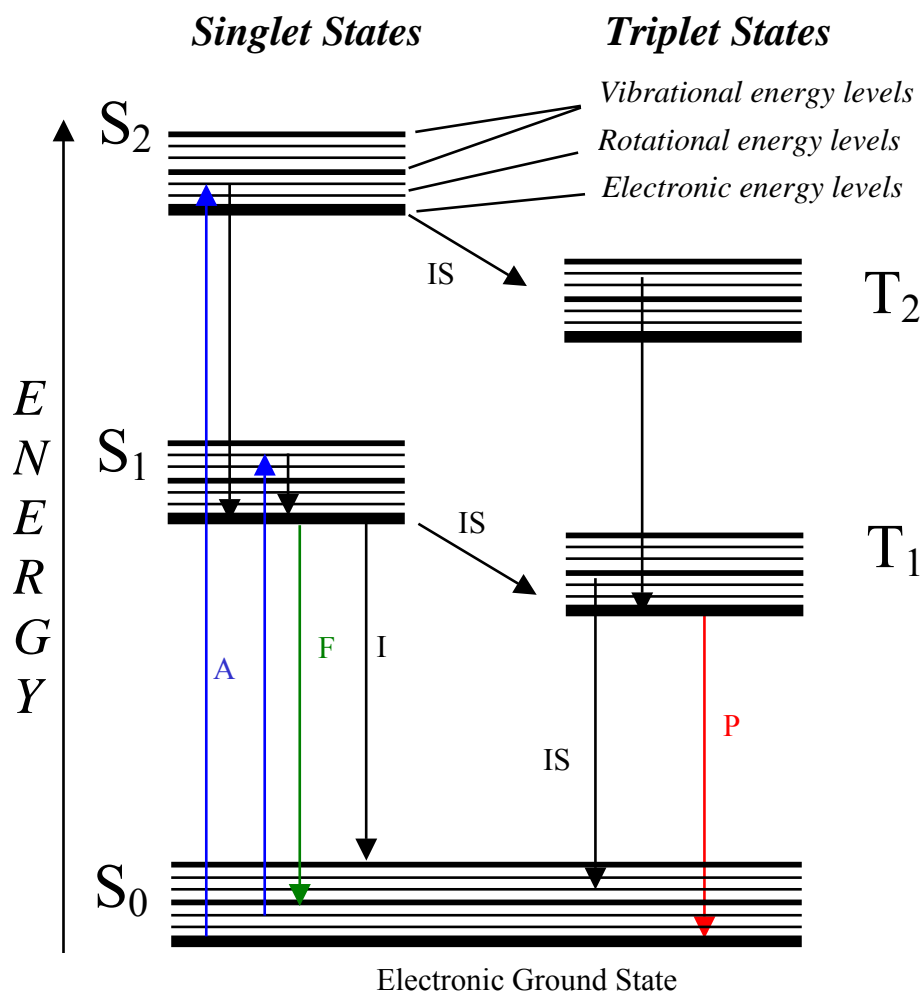
have made confocal microscopy a very valuable tool in the field of biology and biomedical research.

1.2 Fluorescent Probes – Visible Fluorescent proteins

1.2.1 Fluorescence

Fluorescence is a form of luminescence in which susceptible molecules referred to as fluorophores emit light of specific wavelength following their absorption of light of shorter wavelength (higher energy). Fluorescence emission occurs when the excited electron of a fluorochrome relaxes from the excited singlet state to the ground state. The process can be represented schematically by the Jablonski energy level diagram (Fig. 1.1). Upon the absorption of photons of specific wavelength, a fluorochrome is excited from the ground state (S_0) to any of the vibrational levels of the singlet excited energy states (S_1 , S_2 and so on) depending on the photon energy and the absorption probability. Photon absorption takes place very rapidly (10^{-15} s) followed by the relaxation of excited molecules to the lowest vibrational level of the first excited state in about 10^{-13} - 10^{-11} s through internal conversion. The molecules remain at this level for 10^{-9} - 10^{-7} s, before further relaxation to any of the vibrational levels of the ground state (S_0). Relaxation may be achieved by the emission of fluorescence photons of a lower energy than the excitation energy. The emitted fluorescence photons are therefore of longer wavelengths than the excitation wavelength and form a spectrum peaking at a unique characteristic wavelength for the fluorochrome (Fig. 1.2C). The difference in wavelength between a fluorochrome's excitation and emission is termed its Stokes shift.

Other possible relaxation processes include internal conversion where excess energy is lost by heat dissipation. Alternatively, radiationless excited state depopulation



$S_{0,1,2}$ - Singlet Electronic Energy Levels
 $T_{1,2}$ - Corresponding Triplet States
 ISC - Intersystem Crossing
 IC - Nonradiative Internal Conversion
 A - Photon absorption
 F - Fluorescence emission
 P - Phosphorescence

Fig. 1.1 Jablonski energy level diagram illustrating the processes involved in the excitation and relaxation of a chromophore. Photon absorptions (A) are depicted by blue lines with arrows pointing upward while lines with arrows pointing downward depict relaxation processes. Non-radiative relaxation processes, internal conversion (IC) and intersystem crossing (ISC) are depicted by black lines while the fluorescence emission process (F) is depicted by green line and phosphorescence (P) depicted by red line. See the main text for all full description of the processes.

in their environment. Interactions with quenchers such as oxygen may lead to may also occur as a result of the excited fluorochromes interacting with other molecules bleaching, an irreversible modification resulting in the fluorochrome losing its fluorescence (see section 1.2.5). Interactions with suitable molecules (acceptor) in close proximity may lead to fluorescence resonance energy transfer (FRET). This is a radiationless relaxation process of the excited fluorophore (donor), where the acceptor may itself be a fluorophore. The application of FRET in fluorescence microscopy is discussed in section 1.3.4.

An excited fluorochrome may also undergo intersystem crossing (ISC) to the excited triplet state (T_1) from which a return to the ground state is spin-forbidden making the triplet-state lifetime extremely long. Though the process is forbidden, it sometimes occurs with the emission of phosphorescence photons. Phosphorescence lifetimes (up to seconds) are much longer than fluorescence lifetimes. The process is not usually observed in liquids at room temperature, instead the fluorochrome relaxes from the triplet state through radiationless processes such as internal conversion and quenching. The fluorochrome may also revert back to the singlet-excited state from which it may give off delayed fluorescence.

1.2.2 Fluorescent Probes

Fluorescence typically occurs from synthesized organic aromatic molecules such as fluorescein, rhodamine-6G and alexa-488. Many of the conventional fluorescent dyes are used to tag antibodies that bind to target cellular proteins to form fluorescent probes, which are observable under the microscope. A specimen stained with this probe is illuminated with light of suitable wavelength and then viewed through an emission filter that allows only photons having the wavelength of the emitted light to pass through.

Structures tagged with the fluorescent probe will appear to light up against a black background in the microscope.

Fluorescence has also been found to occur in natural proteins such as the green fluorescent protein and its variants (GFPs). The GFP was first discovered in the pacific jellyfish (*aequorea victoria*) in which it absorbs the energy that would lead to blue bioluminescence of aequorin if no GFP was close and emits green fluorescence [1,2]. Upon purification after isolation from the jellyfish, GFP by itself was found to fluoresce requiring no specialised cellular machinery [3]. It is thus possible to fuse the gene encoding a GFP to that encoding virtually any protein of interest to form a fusion protein chimera which when expressed in a cell or organism can be monitored non-invasively by fluorescence microscopy. A successful GFP fusion protein is one that retains the intrinsic fluorescence properties of the GFP as well as the normal biological functions of the target protein.

1.2.3 The green fluorescent protein (GFP) and its variants

The wild-type GFP (wt-GFP) fluorescence emitted by the pacific jellyfish originates from a chromophore that consists of an amino-acid triplet (Ser-Tyr-Gly) at positions 65-67 (Fig. 1.2A) which automatically undergoes a chemical rearrangement (autocatalytic posttranslational cyclization and oxidation) after synthesis to become 4-(phydroxybenzylidene)-imidazolidin-5-one making the protein fluorescent [4,5]. Most of the 238 amino acids making up the 27-kDa protein are used in forming a rigid cylindrical β -barrel scaffold structure of 11 strands sometimes referred to as the β -can. (Fig. 1.2B) [6,7]. The β -strands are threaded by an α -helix running up the axis of the cylinder and the chromophore is attached to the α -helix at the centre of the cylinder where it is well isolated from its environment [6,8].

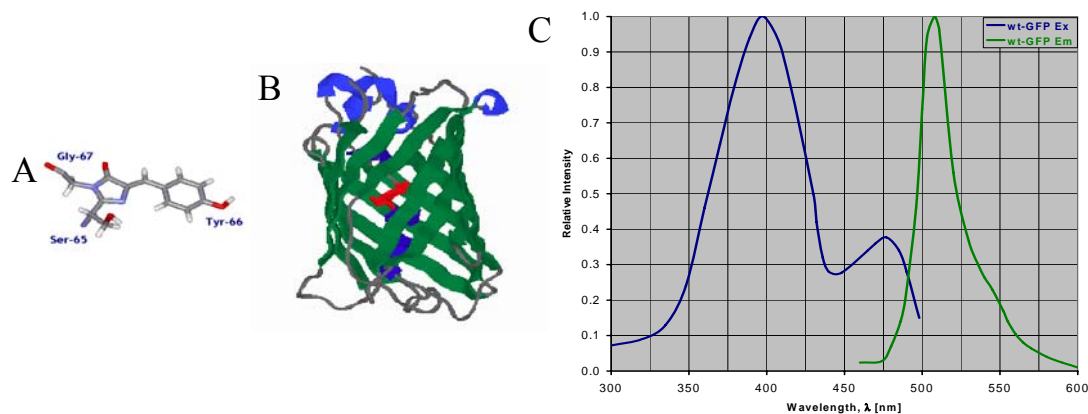


Fig. 1.2 The chromophore and spectra of the wild type GFP. (A) The wild type GFP chromophore, consisting of a cyclized amino-acid tripeptide Ser⁶⁵-Tyr⁶⁶-Gly⁶⁷. (B) A 3-D perspective of the GFP showing the location of the chromophore within an α -helix inside the rigid cylindrical scaffold structure of 11 β -strands (β -barrel) which contains most of the 238 amino-acids making up the protein [6,8]. [9] GFP's major and minor absorbance peaks (blue) and single fluorescence emission peak (green). Absorption of the blue light spectrum of 360 – 530 nm raises the fluorochrome from the ground state to various vibrational levels of the excited states. The excited fluorochrome emits green fluorescence with an emission maximum at 508 nm as the fluorochromes relax to various vibrational levels of the ground state.

Wt-GFP emits green light ($\lambda_{\text{max}} = 508 \text{ nm}$) when excited with ultraviolet (UV) or blue light ($\lambda_{\text{max}} = 395 \text{ nm}$, minor peak at 473 nm) (Fig. 1.2C) [10]. The fluorescence is stable and insensitive to pH variation. Properly folded and mature GFP is also insensitive to temperature variations up to 65°C [11]. However wt-GFP tends to misfold producing mostly nonfluorescent aggregates at 37°C [11]. Mutagenesis of GFP directed at solving this and other problems has yielded GFP variants with improved folding and various expression properties. GFP mutants retain the cylindrical β -can shielding the chromophore from the environment thereby protecting the environment from toxic photo-products while at the same time minimizing the access of quenchers to the chromophore.

Modifications of the wt-GFP protein codon to optimise codon usage by host organisms were found to improve protein expressions [11,12] in the enhanced variants used in most live cell studies. These variants include the enhanced green fluorescent protein (EGFP), the blue (EBFP) and cyan (ECFP) short-wavelength-shifted variants, and the red shifted variant, the enhanced yellow fluorescent protein (EYFP).

The enhanced green fluorescent protein (EGFP) is the most widely used GFP for mammalian live cell studies. The protein is structurally similar to the GFP originally found in jellyfish, except that it contains two amino acid substitutions F64L and S65T. The S65T substitution quickens the rate of chromophore formation (from 2hrs to 0.45 hr) and eliminates the wild-type double excitation peaks replacing them with a six-times higher amplitude single excitation peak at 489 nm [13]. This combined with the F64L substitution that improves protein-folding efficiency makes the EGFP chromophore 35-times brighter than the wild type when excited at 488 nm [14,15]. Mutations that increase the efficiency of protein folding and chromophore formation also suppress the thermosensitivity of chromophore formation [12,14]. All enhanced GFP variants show little difference in fluorescence when expressed at either 25°C or 37°C.

EGFP is very stable with a half-life in excess of 24 hr [16]. The protein is predominantly monomeric at the low concentrations usually studied in living cells but it is fluorescent either as a monomer or as a dimer. It is relatively resistant to detergents, chaotropic salts, and organic solvents [17]. Fixations with glutaraldehyde and formaldehyde have also been shown to have no significant adverse effect on the protein [3].

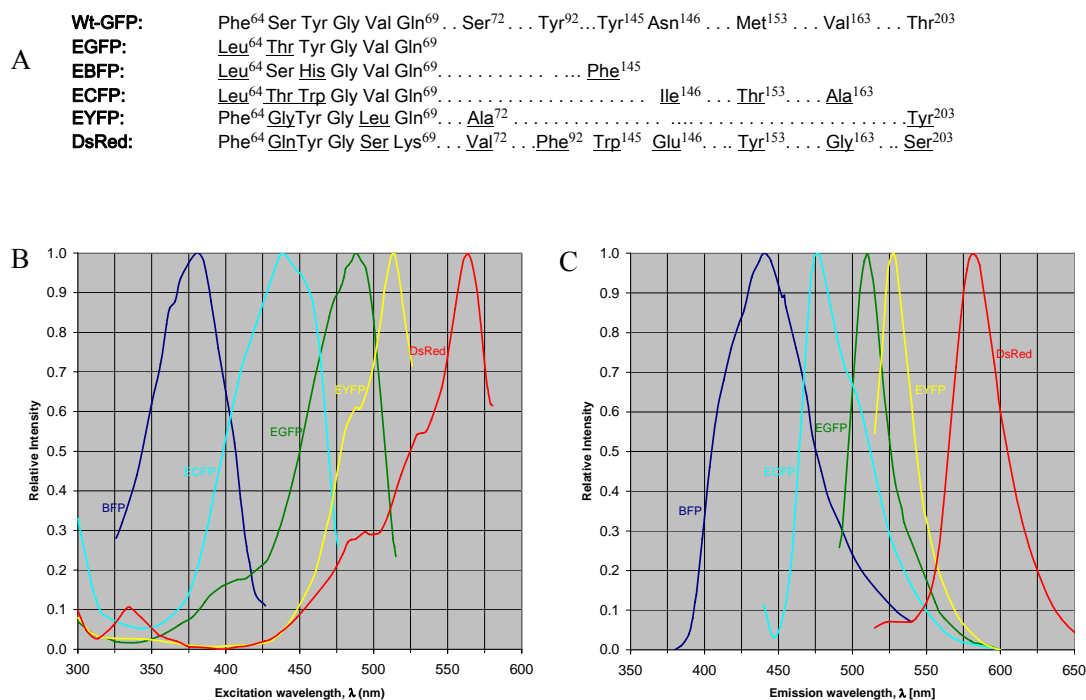


Fig. 1.3 The effect of mutagenesis on GFP spectra. (A) Amino acid sequence differences between wt-GFP and some other fluorescent protein variants. Variations in the 65, 66, 67 amino acids forming the fluorescent ring not only influence the rate of chromophore formation but also have a large effect on absorption and excitation spectra. (B) The absorption and [9] emission spectra of some variants of GFP and DsRed as indicated.

TABLE I. Spectral properties of some fluorescent proteins

Protein	Excitation Maxima (nm)	Emission Maxima (nm)	Em (cm ⁻¹ M ⁻¹)	Quantum Yield (%)	Brightness
wt GFP	395 (470)	509 (540)	9,500	80	1
EGFP	488	507	56,000	60	33.6
EBFP	380	440	29,000	31	9.0
ECFP	433 (453)	475 (501)	32,500	40	13.0
EYFP	513	527	83,400	61	50.9
DsRed	558	579	31,000	42	13.0
HcRed	588	618	-	-	-

However, EGFP fluorescence exhibits a limited resistance to pH variation [3,12]. The fluorescence is stable between pH 7.0 and pH 11.5, drops sharply above pH 11.5, and decreases between pH 7.0 and pH 4.5, retaining about 50% of fluorescence at pH 6.0 [18]. The pH sensitivity of the protein is put to use in live cell pH determination [19].

In addition to improving the efficiency and stability of wt-GFP mutagenesis has also been used in the formation of colour variants. Substituting Y66 of the wild type with tryptophan (Y66W), histidine (Y66H) or with phenylalanine (Y66F) results in short wavelength shifts in fluorescence emission. In the enhanced blue fluorescent protein (EBFP) the minor absorption peak of the wt-GFP is suppressed and the major one shifted to 384 nm yielding an emission spectrum peaking in the blue region at 448 nm (Fig. 1.3B&C) [20]. The enhanced cyan fluorescent protein (ECFP) variant contains seven amino acid substitutions (Fig. 1.3A). The Tyr-66 to Trp substitution shifts the chromophore's excitation maxima to 433 nm (major peak) and 453 nm (minor peak), and the emission maximum to 475 nm with a small shoulder at 501 nm (Table I; Fig. 1.3B&C). EBFP and EGFP are often used as partners in multicolour fluorescence techniques [21,22] while ECFP is used together with the red-shifted yellow fluorescent protein (EYFP) [22]. EYFP is efficiently excited with the 514 nm line of an argon laser producing a yellow-green emission at 527 nm [8] (Table I; Fig. 1.3B&C).

To broaden the spectrum of fluorescent proteins for multispectral imaging, genetic fluorescent labelling technology has been expanded to fluorescent proteins from non-jelly fish marine organisms [23]. A wide range of reef coral fluorescent proteins (RCFPs), derived from *Anemonia majano*, *Zoanthus* sp., *A. sulcata* and *Discosoma* sp. designated AmCyan, ZsGreen, ZsYellow, AsRed, and DsRed respectively, have unique excitation and emission patterns within the visible spectrum [24-27]. Furthermore, a range of improved monomeric red, orange and yellow fluorescent proteins (mHoneydew, mBanana, mOrange, tdTomato, mTangerine, mStrawberry, and mCherry) have been produced from DsRed through directed evolution further broadening the spectrum of fluorescent markers [28-30]. Thus, a wide range of fluorescent proteins of emission spectra between 489 nm and 618 nm are now available commercially.

1.2.4 Blinking of GFP molecules

The GFP chromophore is connected to the rest of the protein by an intricate hydrogen-bond network, which determines the protonation state of the tyrosyl group. In the wild type, the double absorption maxima of the absorption spectrum are associated with the possibility of the chromophore existing in the neutral (protonated) A-form and the anionic (deprotonated) B-form. The major absorption peak at 395 nm is attributed to the neutral form and the minor peak at 473 nm attributed to the anionic form. Studies on the GFPs have shown that only a deprotonated form of the chromophore can fluoresce [31-36]. Excitation of the anionic form results in an emission centred at 503 nm while emission from the neutral form only occurs after a fast excited state proton transfer (ESPT) from the tyrosyl group to the hydrogen bond network leading to a deprotonated intermediate I-form which gives off the emission centred at 508 nm [31,32]. Although the I-form is quickly reprotonated to the neutral form of the chromophore after fluorescence emission, the intermediate state has been detected at cryogenic temperatures by optical spectroscopy and by time-resolved spectroscopy at room temperatures [33-36]. The multiplicity of possible conformations of the chromophore is utilized in GFP technology to produce fluorescent probes of desired excitation and emission characteristics. Site-specific mutagenesis in the surrounding protein scaffold is used to stabilize a desired conformation or modify the photodynamics of the chromophore [11,37,38].

Due to the interconvertibility of the various possible states of the GFP chromophore [39,40] the excited-state molecular dynamics are very complex [11,31,32,41-43]. Fluorescence fluctuations attributed to the interconvertibility of states have been observed in GFPs in addition to the triplet state induced fluctuations in fluorescence. Conformational change related fluctuations in the order of milliseconds

have been observed [42-49]. A seconds-time-scale fluctuation in the fluorescence of GFPs is the subject of investigation in chapter 2.

1.2.5 Photobleaching

Photobleaching is the loss of fluorescence by a fluorophore due to photon-induced chemical alteration of the fluorochrome. Irreversible photobleaching occurs when an excited chromophore reacts with free radicals to irreversibly form a nonfluorescent product. The number of excitation and emission cycles which a particular fluorophore can undergo before it is irreversibly bleached depends on its molecular structure and the local environment. Some fluorophores bleach quickly after emitting only a few photons, while more robust fluorophores can undergo thousands of cycles before bleaching. However, the maximum number of photons emittable by a single fluorochrome under continuous irradiation is usually less than a million [50].

GFPs are strongly resistant to photobleaching thus allowing prolonged visualizations under low-intensity imaging conditions in confocal microscopy. In addition, when they bleach under high intensity illuminations, GFPs bleach irreversibly without detectably damaging intracellular structures [18]. This is because the compact cylindrical barrel inside which the fluorochrome is buried does not only protect the chromophore from its cellular environment but also shelters the cell from reactive intermediates generated by photobleaching [51]. Photobleaching can be utilized to probe the in-vivo behaviour of proteins in a living cell. EGFP, efficiently excited with 488 nm argon-ion laser, is particularly suitable for photobleaching studies in living cells to determine protein dynamics.

1.3 Qualitative and Quantitative Fluorescence Microscopy

In fluorescence microscopy, proteins or cellular organelles to be studied are tagged to fluorescent probes and then imaged using a fluorescence microscope. In its simplest form, a fluorescence microscope basically illuminates the fluorescent specimen with filtered light of suitable wavelength and then collects the emitted light of longer wavelength from the specimen excluding the much brighter excitation light to form the image of the specimen. Modern fluorescence microscopes are based on the epi-illumination design (Fig. 1.4A) in which light from an illumination source is directed to the specimen through an objective lens that also collects emitted light from the sample

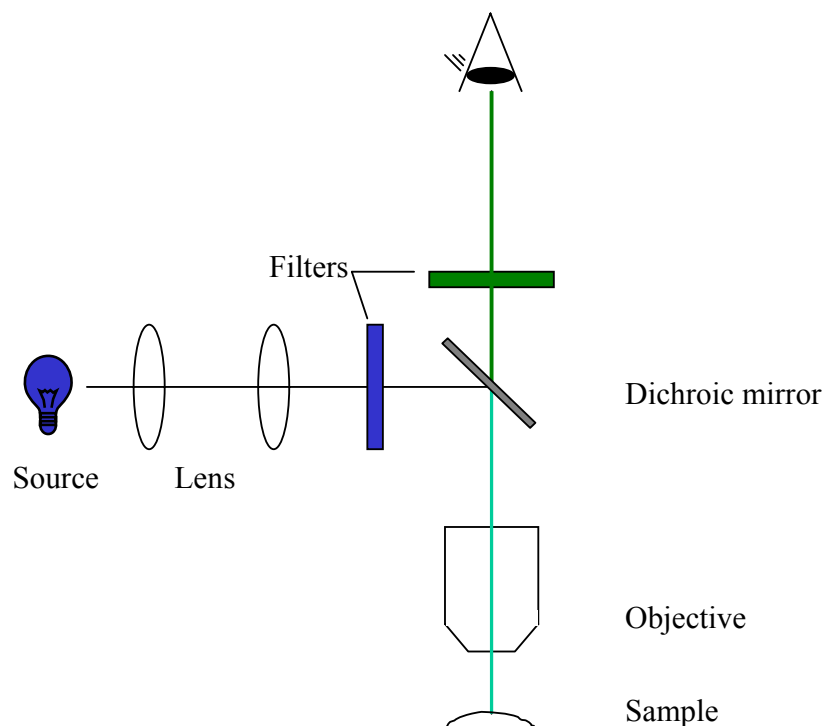


Fig. 1.4 Basic setup of an epi-fluorescence microscope. (A) Light from the source is reflected off a dichroic mirror towards the specimen. Fluorescence photons of longer wavelength from the specimen are allowed to pass through the dichroic mirror to the eyepiece. The excitation filter (blue) stops photons of undesirable wavelengths in the source beam from getting to the specimen while the emission filter blocks the excitation light and selectively allows only photons of interesting wavelength range in the fluorescence spectrum to get to the ocular.

providing an efficient illumination and detection system. Usually, objective lenses with high numerical apertures (NA) are used to provide good resolution in x-, y- and z-direction. Nonetheless, a thick specimen imaged in a conventional wide-field microscope (Fig. 1.4A) produces an image that represents an overlay of sharp image details from the in-focus region superimposed on blurred images from all out of focus regions resulting in poor contrast.

To produce better images of details within thick specimens, modern fluorescence microscopes use optical sectioning to discriminate against light originating from out-of-focus planes. The techniques involved include multiphoton excitation, image deconvolution and confocal microscopy. Multiphoton approach to excitation enables the use of longer wavelength photons that penetrate deeper into a specimen and produce less bleaching. In deconvolution technique, images obtained by normal wide-field fluorescence microscope are reconstructed mathematically by reassigning out-of-focus light to their points of source by deconvolution [52]. This method is particularly advantageous in imaging very weakly fluorescent structures [53].

1.3.1 Confocal laser scanning microscopy

The confocal technique achieves optical sectioning through a point-by-point illumination of the specimen and the rejection of out-of-focus light with a pinhole situated at the conjugate focal (confocal) plane of the objective (Fig. 1.5A). Confocal laser scanning microscopy (CLSM), widely available in commercial instruments has proved to be a popular technique for live cell imaging. By scanning one pixel (voxel) of the in-focus plane at a time in a confocal microscope, an optical section containing information from only the focal plane (x-y plane) of limited thickness (typically 1 μ m) of a 3-dimensional (3-D) specimen is produced. A 3-D image of the specimen can be obtained from a series of optical sections formed by moving the focal plane of the

instrument step-by-step through the depth (z-direction) of the specimen. The in-focus light usually constitutes a small portion of the total emission from the specimen making the amount of light forming a confocal image a very small fraction of that of a normal fluorescence microscope, thus making the application of the technique to weakly fluorescent structures very challenging in its early days (1950s). This problem was compounded by the difficulties associated with recording the large amount of information generated by confocal imaging to prevent a wider application of the technique. Not until the advances in laser technology, availability of highly sensitive photo-detectors and improvements in the speed and storage capabilities of microcomputers (in the 1980s) did confocal microscopy receive the prominence it now enjoys.

Modern confocal microscopes (Fig.1.5B) use the beam of a laser to illuminate the specimen and the reduced signal from the confocal pinhole is collected with highly sensitive photomultiplier tubes (PMTs), which are connected to large data storage facilities provided by microcomputers. To image the specimen point by point, collimated light of suitable wavelength from a laser module is reflected by the dichroic mirror to the scanning unit (two scanning mirrors) before being focussed onto the specimen by the objective lens. The scanning mirrors deflect the beam in the x- and y-direction over a specified region of interest in the focal plane. The emitted, longer-wavelength fluorescent light collected by the objective lens passes through the dichroic mirror (transparent for the longer wavelength) and is focused into the pinhole by a lens. Only the light emanating from the point of focus of the objective in the specimen passes through the pinhole to be registered on the photomultiplier tube positioned behind the confocal aperture. The analogue output signal of the detector is digitised and fed into the computer which builds up the image for instant display on the monitor. The computer also controls the scanning mirrors, the motorized focussing mechanism and stores the data for analysis. The stored

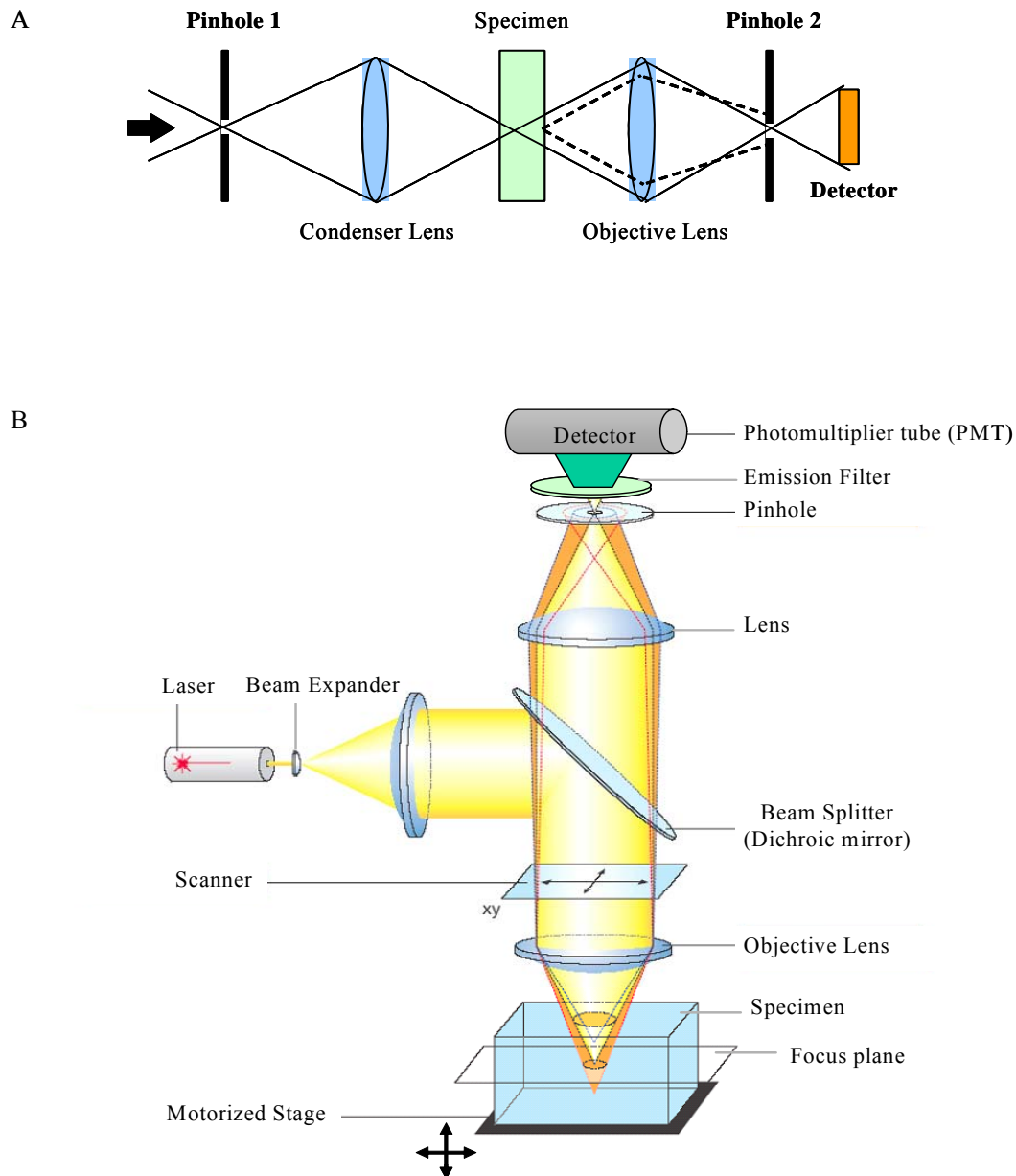


Fig. 1.5 The confocal laser scanning microscope. (A) Formation of a confocal image. A diaphragm with a pinhole (Pinhole 2) is situated on a plane conjugate to the focal plane of the objective so that light from the focal point reaching the pinhole is allowed through while light originating outside the focal point is rejected. (B) The beam path in a confocal laser scanning microscope (CLSM). The intense beam of a laser source is directed to the specimen through a scanning system and an objective lens. The fluorescence signal from the specimen is projected by the same lens onto the confocal pinhole and collected with highly sensitive photomultiplier tubes (PMTs), which are connected to a computer (not shown). Scanning of the specimen is achieved by piezo-controlled scanning mirrors, controlled by the computer, to deflect the excitation beam in the x- and y-direction over a specified region of interest. (Adopted from Zeiss market promotion material)

data of the serial optical sections (Z-stack) through the specimen can be used to generate a computer graphics projection image or a volume-rendered 3-D representation of the specimen.

The main advantage of the confocal laser scanning microscope (CLSM) over a conventional microscope is its ability to produce high-resolution images of structures within the interior of intact cells thereby enabling a look inside them. Further more, although axial (z-) resolution is still lower than lateral (xy-) resolution, z-stack data collected from several focal planes can be processed and analysed to solve 3-D biological problems of thick samples. 3-D sequential time-lapse imaging is also possible on a CLSM producing a four-dimensional (4-D) data series with time being the fourth dimension. This is useful in monitoring dynamic processes in living cells or tissues that are better understood when studied in real time. The 4-D data sets generated can be analysed using a 4-D viewer program that allows three-dimensional reconstruction for each time point and processing for display as a movie.

In addition to localization of single proteins and observation of cellular organelles within intact cells fluorescence confocal microscopy also permits colocalization studies. In a colocalization study, the specimen is multiply labelled for the different molecules or structures of interest. The fluorescent labels used should be sufficiently different in their excitation and emission properties to enable separate collection of fluorescent signals to different channels. The fluorescence signals are combined to make colour images, which along with the three-dimensional information obtained by confocal sectioning can precisely show colocalizations as overlaps of the signals.

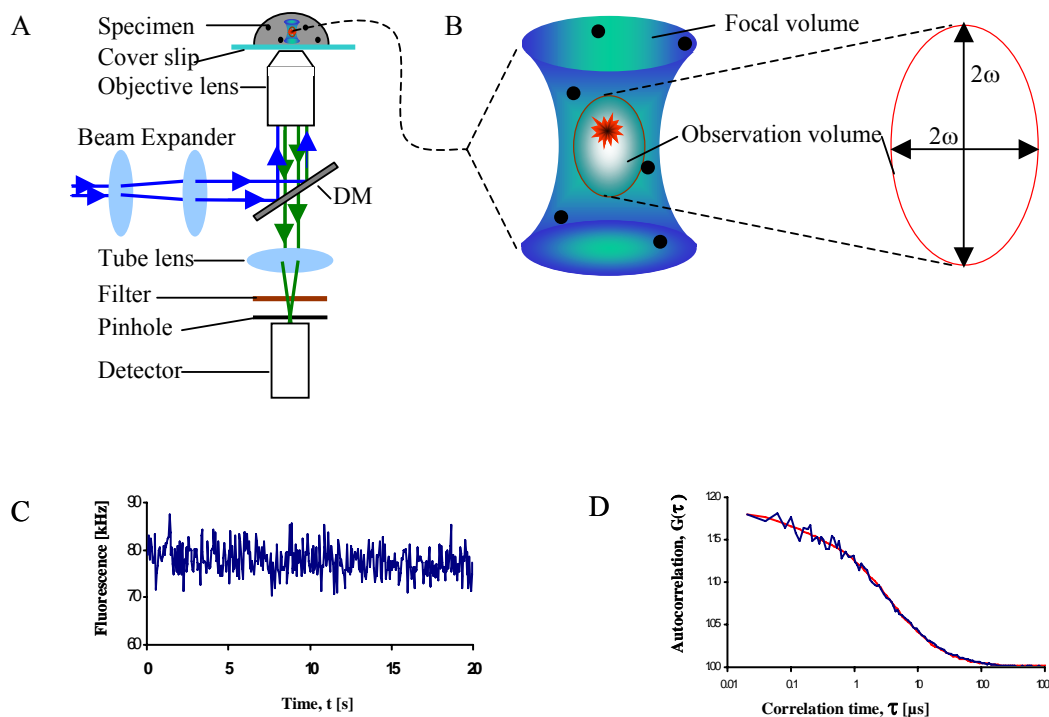


Fig. 1.6 Experimental set-up for fluorescence correlation spectroscopy. (A) A laser beam is first lead through a beam expander and then focused by a high-NA objective lens on a fluorescent specimen. Fluorescence from the specimen is collected by the same objective, reflected by a dichroic mirror (DM), focused by a tube lens and then passed through an emission filter and a confocal pinhole onto the detector. (B) Schematic drawing of the focal volume (green) within which the specimen particles (black circles) are illuminated. The observation volume, contained within the focal volume, is determined by the detector pinhole of the confocal volume. The dimensions ω_x and ω_z are obtained from a calibration using a dye (such as Rh 6G) of known diffusion coefficient as explained in the main text. [9] A fluorescence signal trace measured for Rh 6G with a 488 nm laser beam (D) The autocorrelation function $G(\tau)$ of the measured fluorescence intensities. Assuming a Gaussian observation volume, $G(\tau)$ can be fitted (for instance by ordinary least squares) to various analytical functions to extract information about molecular concentration, brightness, diffusion, and chemical kinetics, for one or more diffusing fluorescent species.

1.3.2 Fluorescence correlation spectroscopy (FCS)

Fluorescence correlation spectroscopy (FCS) is a fluorescence fluctuation technique developed in the early nineteen seventies to study diffusion and reaction dynamics of fluorophores at thermodynamic equilibrium [54-56]. In FCS, minute

fluctuations in the fluorescence intensity of a low concentration of fluorescent molecules excited within a microscopic volume are utilized to evaluate the physical parameters contributing to these fluctuations. Using FCS, such physical parameters as local concentration, diffusion coefficients, chemical reaction rate constants as well as photophysical properties of fluorophores can be determined [57]. The technique is characterized by high sensitivity to mobility, ability to distinguish between different diffusing species and high sampling rate.

Modern FCS instruments possess single molecule sensitivity made feasible by the advances in confocal microscopy [58]. Using confocal principles, sub-femtolitre observation volumes of FCS systems have been attained while the use of avalanche photodiode detectors has facilitated the detection of photons from the few molecules observed at any given time. In an FCS experiment, a focused laser beam continuously illuminates the specimen containing a dilute concentration fluorescently tagged target molecules (Fig. 1.6). Excitation of a fluorescent molecules moving through the sensitive volume of the system results in a burst of fluorescence photons. The duration of a burst reflects the dwell time of the molecule within the observation volume and the intensity of the burst depends on the number molecules traversing the volume at any given time and the molecular brightness. The intensity time trace of the fluorescence signal is analysed [59] to obtain an autocorrelation curve which is displayed together with the intensity time trace during the experiment for easy adjustments when necessary.

The autocorrelation curves can be analysed to determine the average number of molecules in the observation volume and the diffusion times which can be converted to diffusion coefficients. The analysis of autocorrelation curves are usually carried out by Levenberg-Marquardt non-linear least-squares method to fit the data to model single- or multi-component diffusion equations which correct for triplet state induced fluctuations in intensity as well as blinking and possible anomalous diffusion of the particles [60-63].

A key advantage of FCS is its single molecule studies capability. However, limitations to the application of FCS in cellular protein dynamics arise when a fraction of the molecules under study are immobile. Immobile fluorescent molecules in the detection volume of an FCS system are susceptible to bleaching resulting in high apparent number of molecules and faster than normal diffusion coefficients [64].

1.3.3 Photobleaching methods

Photobleaching, a seemingly undesirable consequence of high intensity illumination of fluorescent molecules has found extensive use in studying the mobility of cellular proteins. Fluorescence recovery after photobleaching (FRAP), developed in the 1970s, was first applied in cell biology to study membrane diffusion of fluorescently labelled lipids and proteins [65-67]. But the accuracy of selective illumination of regions of interest made possible by laser scanning microscopy and the advances in GFP-technology have boosted the application of FRAP in the investigation of protein dynamics in the interior of living cells [68-71].

FRAP is a procedure in which a defined area of the cell is swiftly irradiated with a high-intensity laser beam resulting in the irreversible photobleaching of most of the fluorophores present in the illuminated area (Fig. 1.7). As fluorophores move in and out of the bleached region, bleached molecules are replaced by fluorescent ones resulting in a gradual recovery of fluorescence until equilibrium is reached. The recovery can be moni-

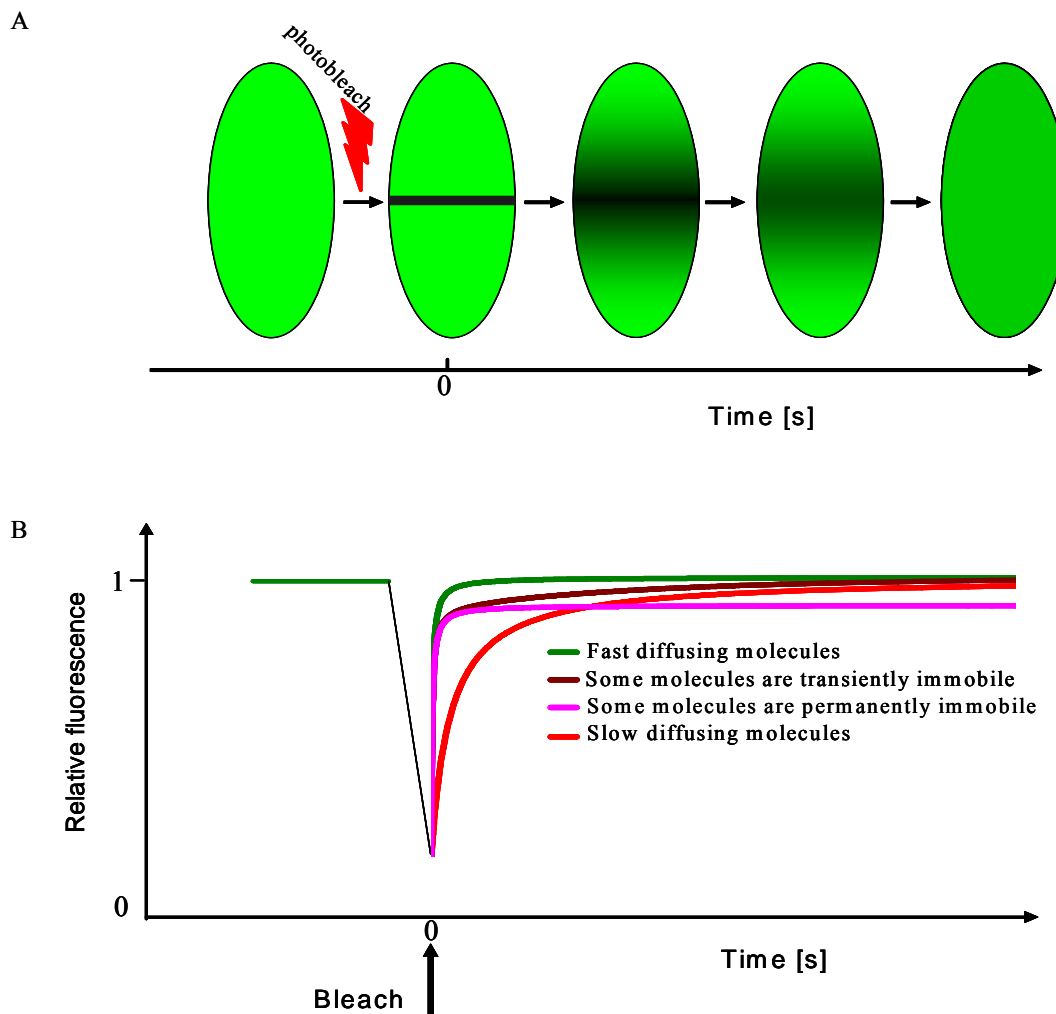


Fig. 1.7 Quantitative fluorescence recovery after photobleaching (FRAP). (A) A schematic representation of a FRAP experiment. The level of fluorescence in a user-defined region of a fluorescently tagged sub-cellular structure (a cell nucleus in this case) is measured with a low laser power and then rapidly bleached at high laser intensity. The recovery of the fluorescence signal in the bleached region due to the influx of mobile unbleached molecules is measured as a function of time at low laser power. (B) Plots of fluorescence intensity in a region of interest (ROI) normalized to the pre-bleach intensity versus time (recovery kinetics) for different types of recovery as indicated. Recovery kinetics contains information about the apparent mobility of the labeled molecules. The kinetics can be modeled by suitable mathematical algorithms to extract dynamic properties, such as diffusion coefficients, immobile fractions, and average residence times at binding sites of the labelled molecules [51,71-74] from the curves. In addition, computer simulation of the FRAP process can be applied to generate curves with varying diffusion coefficients and kinetic parameters [73,75]. Subsequently, the experimental curve can be fitted to the generated curve set.

tored in time with a low intensity beam [71]. Fast moving molecules lead to a steep recovery curve with a short time of recovery while slow moving molecules produce a curve with a longer recovery time. The recovery curve can be used to estimate the dynamic properties, such as diffusion coefficients, immobile fractions, and average residence times at binding sites of the labelled molecules [51,71-74].

The interpretation of FRAP data is often complicated by the finite duration of measurements, possible restricted diffusion and sometimes multicomponent diffusion of the protein of interest in the nucleus. Slower than expected diffusion coefficients are often observed and attributed to transient binding events and multicomponent diffusion [73,75]. In such cases, binding parameters such as bound fraction and residence time reflecting the on and off (k_{on} and k_{off} respectively) rates of the studied molecules binding to and release from immobile structures are often extracted from the FRAP data based on the difference between the expected diffusion coefficient of the protein under investigation and the measured effective diffusion coefficient [73,74].

1.3.4 Fluorescence resonance energy transfer (FRET)

Fluorescence resonance energy transfer (FRET) is the transfer of excited-state energy from an excited donor (D) molecule to an acceptor (A) molecule in each other's close proximity (< 10 nm). FRET occurs only if the emission spectrum of the donor overlaps with the absorption spectrum of the acceptor. Energy transfer is a result of dipole-dipole interaction between the donor and the acceptor and takes place without the emission of a photon by the donor. FRET therefore constitutes a radiationless relaxation process of a donor molecule in the presence of an acceptor. The fraction of excitation quanta transferred to the acceptor, described as the energy transfer efficiency, is highly dependent on the distance between the fluorophore pair. Energy transfer efficiency E is given by the equation [76].

$$E = 1/[1 + (R/R_0)^6] \quad (1.1)$$

where R is the donor-to-acceptor distance, and R_0 the distance at which $E = 50\%$, is called the Förster distance. R_0 is typically in the range 20-60 Å which is comparable with the dimensions of biological macromolecules. The steep dependence of FRET on distance coupled with the associated high efficiency of the phenomenon at macromolecular dimensions makes FRET suitable for the measurement of (changes in) distances between two sites on a macromolecule and for protein-protein separations. FRET is particularly useful for the study of protein interactions.

With the advances in GFP technology there are several fluorescent probes suitable for the use of FRET in measurement of protein-protein interactions in living cells. FRET assay in living cells reviewed in [77] involves the labelling of target protein with suitable donor and acceptor fluorophores and subsequent imaging under the microscope. Energy transfer can, among other methods, be measured through the increased (sensitised) acceptor emission. This involves the acquisition of fluorescence images of the specimen with three distinct filter sets: one contains the donor excitation filter and acceptor emission filter to detect sensitised emission, one set is specific for the donor excitation and emission alone, and one is specific for the acceptor alone. The acceptor fluorescence intensity upon donor-wavelength excitation is corrected at every point of the image for the leak-through of the donor emission and for direct excitation of the acceptor to calculate the energy transfer efficiency [78].

1.4 Applications of quantitative fluorescence microscopy in live cell studies

Cellular functions are often performed through the transport of active proteins to sites of action followed by binding interactions. Free movement of the proteins allows a

dynamic interplay between different processes. An example of such interplay takes place between the nucleotide excision repair (NER), RNA Polymerase I transcription (POL I transcription) and RNA Polymerase II transcription. (POL II transcription) in the cell nucleus (Fig. 1.8). *In vivo* studies of proteins involved in such complex processes have been facilitated by the advances in GFP fusion technology and fluorescence microscopy techniques. To demonstrate the complementarities of fluorescence microscopy techniques we studied some model proteins involved in diverse cellular processes in the nucleus, cytoplasm and membrane: DNA-repair, transcription, and the immune defense system.

1.4.1 The Nucleotide excision repair (NER) proteins

Nucleotide excision repair (NER) is a continuous repair process eliminating a wide variety of helix-distorting DNA damage to safeguard the integrity of mammalian genome. Genetic studies have identified eight gene products (XPA through XPG and XPV) associated with NER in humans [79-82]. Seven of these (XPA-XPG) are involved in damage recognition, unwinding of the double helix around the damage, and the excision of the injury as a 24–32 oligonucleotide piece of DNA from the affected strand (Fig. 1.8). The last repair factor, XPV is involved in the replication of the damaged DNA. Several of the gene products occur in heterodimeric complexes with proteins that are essential for their stability and function. The XPA is a 273 aminoacid protein that participates in damage recognition and DNA binding [83,84]. XPC found in complex with HHR23B is the damage recognition initiator in nontranscribed regions of the genome [85,86], while the 48 kDa XPE protein (DDB2) also thought to be involved in DNA damage recognition is complexed with a larger 127 kDa subunit (DDB1). XPB and XPD helicases exist as components of TFIIH complex, which unwinds the DNA at the damaged site and serves as a basal transcription initiation factor [87]. The XPF is complexed with the excision repair cross complementing protein (ERCC) which makes

the 5' DNA incision to the damaged site [88,89] while the 1186 amino acid nuclease, XPG is involved in the 3' incisions [90,91].

1.4.2 Androgen receptors

The androgen receptor (AR) is a ligand-dependent transcription factor of the steroid receptor (SR) subfamily of nuclear receptors. ARs regulate the expression of genes involved in the development and maintenance of male phenotype and play a role in the growth of prostate cancer. Like all SRs, AR is composed of a central DNA-binding domain (DBD), a C-terminal ligand-binding domain (LBD), and an N-terminal transacti-

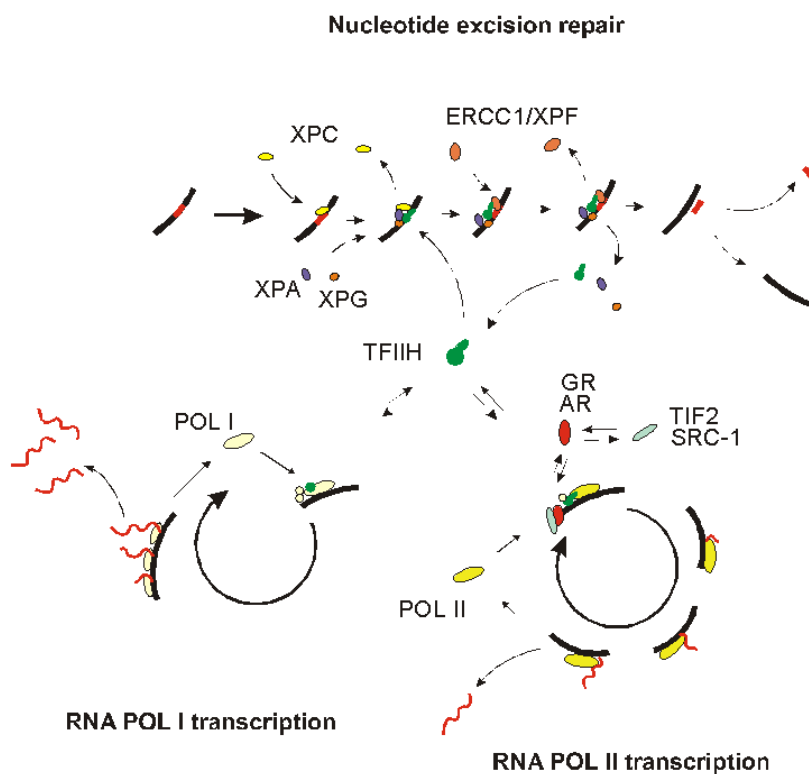


Fig. 1.8 Dynamic interplay between different DNA-interacting processes. The dynamic interplay amongs the three DNA-interacting processes: nucleotide excision repair (NER), RNA Polymerase I transcription (POL I transcription) and RNA Polymerase II transcription (POL II transcription) is an example of the complex dynamics and interactions that take place in the cell nucleus. Most of the factors involved move freely through the nucleus, as monomers, dimers or in small subunits and assemble 'on the spot' to either DNA damage or gene promoters, where they transiently form repair or transcription complexes.

vation domain (NTD). In the absence of androgens, ARs are mainly located in the cytoplasm. Upon ligand-binding ARs rapidly translocate to the nucleus, where they bind to androgen response elements (AREs) in the promoters/enhancers of target genes and recruit transcriptional coregulators. Confocal microscopy of GFP-tagged proteins, as well as quantitative assays such as FRAP and FRET have been instrumental in the investigation of the behaviour of SRs in living cells. Like many other nuclear factors interacting with DNA, SRs, including the AR, were shown to be highly mobile in the living cell nucleus and dynamically interact with specific binding sites. FRAP-analysis based on computer modelling have been used to show that agonist-bound wild type ARs are largely freely mobile in the nucleus and only transiently bind to immobile elements in the nucleus. Non-DNA binding mutants were found to be freely mobile showing no detectable immobile fraction suggesting that the transient immobilization of ARs is dependent on DNA-binding.

1.4.3 IL-R2

Understanding how the human body combats diseases is essential both in preventive medicine and drug design. It is known that lymph cells secrete cytokines in order to mediate and regulate immunity, inflammation, and haematopoiesis. Cytokines are small proteins of short half-lives, often acting over short distances and are produced *de novo* in low concentrations in response to immune stimuli. Interleukines regulate immune responses by binding to specific membrane receptors. Interleukin-2 (IL-2) secreted by T lymphocytes when stimulated with antigen or mitogens is essential for T cell growth [92,93]. The specific receptor for IL-2 is the monomeric subunit, IL-2R α that has also been found in the fully functional receptor assembly, the IL-2R $\alpha\beta\gamma$ heterotrimer [94], which has a higher affinity for the cytokine and is capable of transmitting signals intracellularly. The process by which IL-2R α is assembled with the less abundant β and γ

chains to form IL-2R $\alpha\beta\gamma$ can be investigated by fluorescence imaging techniques. Surprisingly, it was found using FRET that on various lymphoid cells the trimeric IL-2R is pre-assembled even in the absence of the ligand, however the addition of TL-2 enhanced the association of the 3 subunits [95].

In apparent contradiction of the fluid mosaic membrane model, studies on non-excitable cells have revealed a prevalence of assemblies of cell surface antigens and receptors forming clusters of several hundred nanometres in size [96,97]. This presumably enhances the efficiency of transmembrane signalling [98,99] by using the focussing effect of the clustering. The clustering of the receptor subunit and its colocalization can be assessed with high-resolution confocal microscopy and digital image processing while FRET can be used to evaluate average molecular proximities.

1.5 Thesis outline

In demonstrating the efficacies of fluorescence microscopy techniques in the study of protein localization and dynamics in living cells, the focus of this thesis shifts from a discussion of the techniques to the characterization of the fluorescence properties of the GFP used in making the proteins observable, through proper interpretation of data generated in fluorescence microscopy and finally to the application of the methods in the study of model biological systems.

In chapter 2, the long-lived dark state of the EGFP, the most common fluorescence protein used in protein dynamic studies, is investigated and the consequence of this so-called “blinking” on FRAP data is discussed. Chapter 3 presents a quantitative comparison between two different methods: FCS and FRAP in the study of protein mobility, first when biologically inert systems are the subjects of investigation and then in the interpretation of measured data when biologically active proteins are investigated. In chapters 4 to 7 the importance of complementary use of various techniques in the study

of protein localization and dynamics is demonstrated. Chapter 4 demonstrates the complementary use of both FRAP and FCS to show that the mobility of NER proteins is mostly determined by their respective molecular size and shape. Chapter 5 shows how the ability of the photobleaching techniques to characterize long-range diffusion was used to prove that the recruitment of the NER endonuclease XPG to sites of uv-induced DNA damage depends on the presence of functional TFIIH. Chapter 6 presents a minimal invasive assessment of the effects of stimulation on the localization and mobility of EGF receptor studied in the form of EGFP fusion protein. In chapter 7, the result of the investigation of IL2-receptor localization and organization in the cell membrane of lymphoid cells was investigated with respect to lipid rafts and MHC glycoproteins.

References

1. Shimomura O, Johnson FH, Saiga Y. (1962) Extraction, purification and properties of aequorin, a bioluminescent protein from the luminous hydromedusan, *Aequorea*. *J Cell Comp Physiol*; 59:223-39.
2. Morin JG, Hastings JW. (1971) Energy transfer in a bioluminescent system. *J Cell Physiol*; 77:313-318.
3. Chalfie M, Tu Y, Euskirchen G, Ward WW, Prasher DC. (1994) Green fluorescent protein as a marker for gene expression. *Science*; 263:802-805.
4. Prasher DC, Eckenrode VK, Ward WW, Prendergast FG, Cormier MJ. (1992) Primary structure of the *Aequorea victoria* green-fluorescent protein. *Gene*; 111:229-233.
5. Cody CW, Prasher, D.C., Westler, W.M., Prendergast, F.G., and Ward, W.W.,. (1993) Chemical structure of the hexapeptide chromophore of the *Aequorea* green-fluorescent protein. *Biochemistry*; 32:1212 - 1218.
6. Yang F, Moss LG, Phillips JGN. (1996) The molecular structure of green fluorescent protein. *Nature Biotechnol.*; 14:1246-1251.

7. Phillips GN, Jr. (1997) Structure and dynamics of green fluorescent protein. *Curr Opin Struct Biol*; 7:821-827.
8. Ormo M, Cubitt AB, Kallio K, Gross LA, Tsien RY, Remington SJ. (1996) Crystal structure of the *Aequorea victoria* green fluorescent protein. *Science*; 273:1392-1395.
9. Bini L, Pacini S, Liberatori S, Valensin S, Pellegrini M, Raggiaschi R, Pallini V, C TB. (2003) Extensive temporally regulated reorganization of the lipid raft proteome following T-cell antigen receptor triggering. *Biochem J*; 369:301-309.
10. Cubitt AB, Heim R, Adams SR, Boyd AE, Gross LA, Tsien RY. (1995) Understanding, improving and using green fluorescent proteins. *Trends in Biochemical Sciences*; 20:448-455.
11. Tsien RY. (1998) The green fluorescent protein. *Ann. Rev. Biochem.*; 67:509-544.
12. Cramer A, Whitehorn EA, Tate E, Stemmer WPC. (1996) Improved green fluorescent protein by molecular evolution using DNA shuffling. *Nat. Biotechnol.*; 14:315-319.
13. Heim R, Cubitt AB, Tsien RY. (1995) Improved green fluorescence. *Nature*; 373:663-664.
14. Cormack BP, Valdivia RH, Falkow S. (1996) FACS-optimized mutants of the green fluorescent protein (GFP). *Gene*; 173:33-38.
15. Yang TT, Cheng L, Kain SR. (1996) Optimized codon usage and chromophore mutations provide enhanced sensitivity with the green fluorescent protein. *Nucleic Acids Res*; 24:4592-4593.
16. Li X, Zhao X, Fang Y, Jiang X, Duong T, Fan C, Huang CC, Kain SR. (1998) Generation of destabilized green fluorescent protein as a transcription reporter. *J Biol Chem*; 273:34970-34975.
17. Bokman SH, Ward WW. (1981) Renaturation of *Aequorea* green fluorescent protein. *Biochem. Biophys. Res. Commun*; 101:1372-1380.

18. Patterson G, Knobel S, Sharif W, Kain S, Piston D. (1997) Use of the green fluorescent protein and its mutants in quantitative fluorescence microscopy. *Biophys. J.*; 73:2782-2790.
19. Kneen M, Farinas J, Li Y, Verkman AS. (1998) Green fluorescent protein as a noninvasive intracellular pH indicator. *Biophys J*; 74:1591-1599.
20. Heim R, Prasher DC, Tsien RY. (1994) Wavelength mutations and posttranslational autoxidation of green fluorescent protein. *Proc. Natl. Acad. Sci. USA*; 91:12501-12504.
21. Rizzuto R, Brini M, De Giorgi F, Rossi R, Heim R, Tsien RY, Pozzan T. (1996) Double labelling of subcellular structures with organelle-targeted GFP mutants in vivo. *Curr Biol*; 6:183-188.
22. Heim R, Tsien RY. (1996) Engineering green fluorescent protein for improved brightness, longer wavelengths and fluorescence resonance energy transfer. *Curr Biol*; 6:178-182.
23. Bourett TM, Sweigard JA, Czymmek KJ, Carroll A, Howard RJ. (2002) Reef coral fluorescent proteins for visualizing fungal pathogens. *Fungal Genetics and Biology*; 37:211-220.
24. Lukyanov KA, Fradkov AF, Gurskaya NG, Matz MV, Labas YA, Savitsky AP, Markelov ML, Zaraisky AG, Zhao X, Fang Y and others. (2000) Natural Animal Coloration Can Be Determined by a Nonfluorescent Green Fluorescent Protein Homolog. *J. Biol. Chem.*; 275:25879-25882.
25. Matz MV, Fradkov AF, Labas YA, Savitsky AP, Zaraisky AG, Markelov ML, Lukyanov SA. (1999) Fluorescent proteins from nonbioluminescent Anthozoa species. *17*: 969-973.
26. Bevis BJ, Glick BS. (2002) Rapidly maturing variants of the *Discosoma* red fluorescent protein (DsRed). *Nat. Biotechnol.*; 20:83-87.
27. Campbell RE, Tour O, Palmer AE, Steinbach PA, Baird GS, Zacharias DA, Tsien RY. (2002) A monomeric red fluorescent protein. *Proc Natl Acad Sci U S A*; 99:7877-7882.
28. Shaner NC. (2004) Improved monomeric red, orange and yellow fluorescent proteins derived from *Discosoma* sp. red fluorescent protein. *22*:1567-1572.

29. Nguyen AW, Daugherty PS. (2005) Evolutionary optimization of fluorescent proteins for intracellular FRET. *23*:355-360.
30. Patterson GH. (2004) A new harvest of fluorescent proteins. *22*:1524-1525.
31. Chattoraj M, King BA, Bublitz GU, Boxer SG. (1996) Ultra-fast excited state dynamics in green fluorescent protein: Multiple states and proton transfer. *Proc Natl Acad Sci U S A*; *93*:8362-8367.
32. Lossau H, Kummer A, Heinecke R, PollingerDammer F, Kompa C, Bieser G, Jonsson T, Silva CM, Yang MM, Youvan DC and others. (1996) Time-resolved spectroscopy of wild-type and mutant Green Fluorescent Proteins reveals excited state deprotonation consistent with fluorophore-protein interactions. *Chemical Physics*; *213*:1-216.
33. Creemers TM, Lock AJ, Subramaniam V, Jovin TM, Volker S. (1999) Three photoconvertible forms of green fluorescent protein identified by spectral hole-burning. *Nat Struct Biol*; *6*:557-560.
34. Seebacher C, Deeg FW, Brauchle C, Wiehler J, Steipe B. (1999) Stable Low-Temperature Photoproducts and Hole Burning of Green Fluorescent Protein (GFP). *J. Phys. Chem. B*; *103*:7728-7732.
35. Striker G, Subramaniam V, Seidel CAM, Volkmer A. (1999) Photochromicity and Fluorescence Lifetimes of Green Fluorescent Protein. *J. Phys. Chem. B*; *103*:8612-8617.
36. Cotlet M, Hofkens J, Habuchi S, Dirix G, Van Guyse M, Michiels J, Vanderleyden J, De Schryver FC. (2001) Identification of different emitting species in the red fluorescent protein DsRed by means of ensemble and single-molecule spectroscopy. *Proc Natl Acad Sci U S A*; *98*:14398-14403.
37. Zumbusch A, Jung G. (2000) Single Molecule Spectroscopy of the Green Fluorescent Protein: A Critical Assessment. *Single Molecules*; *1*:261-270.
38. Wiehler J, Jung G, Seebacher C, Zumbusch A, Steipe B. (2003) Mutagenic Stabilization of the Photocycle Intermediate of Green Fluorescent Protein (GFP). *ChemBioChem*; *4*:1164-1171.

39. Brejc K. (1997) Structural basis for dual excitation and photoisomerization of the *Aequorea victoria* green fluorescent protein. *Proc. Natl. Acad. USA*; 94:2306-2322.
40. Palm GJ, Zdanov A, Gaitanaris GA, Stauber R, Pavlakis GN, Wlodawer A. (1997) The structural basis for spectral variations in green fluorescent protein. *J Biol Chem*; 272:361-365.
41. Chalfie M, Kain S. *Green fluorescent protein : properties, applications, and protocols*. New York: Wiley-Liss; 1998. xiii, 385 p. p.
42. Heikal AA, Hess ST, Baird GS, Tsien RY, Webb WW. (2000) Molecular spectroscopy and dynamics of intrinsically fluorescent proteins: Coral red (dsRed) and yellow (Citrine). *Proc Natl Acad Sci U S A*; 97:11996-12001.
43. Heikal AA, S. T. Hess, and W. W. Webb. (2001) Multiphoton molecular spectroscopy and excited state dynamics of enhanced green fluorescent protein (EGFP): acid-base specificity. *Chem. Phys.*; 274:37-55.
44. Hess ST, Sheets ED, Wagenknecht-Wiesner A, Heikal AA. (2003) Quantitative Analysis of the Fluorescence Properties of Intrinsically Fluorescent Proteins in Living Cells. *Biophys. J.*; 85:2566-2580.
45. Haupts U, Maiti S, Schwille P, Webb WW. (1998) Dynamics of fluorescence fluctuations in green fluorescent protein observed by fluorescence correlation spectroscopy. *PNAS*; 95:13573-13578.
46. Widengren J, B. Terry, and R. Rigler. (1999) Protonation kinetics of GFP and FITC investigated by FCS: aspects of the use of fluorescent indicators for measuring pH. *Chem. Phys.*; 249:259-271.
47. Schwille P, Kummer S, Heikal AA, Moerner WE, Webb WW. (2000) Fluorescence correlation spectroscopy reveals fast optical excitation-driven intramolecular dynamics of yellow fluorescent proteins. *Proc Natl Acad Sci U S A*; 97:151-156.
48. Heikal AA, S. T. Hess, E. D. Sheets, and W. W. Webb, editor. *Mutation-photophysics relationships in intrinsically fluorescent proteins*. Singapore: World Scientific; 2002. 774–781.

49. Malvezzi-Campeggi F, Jahnz M, Heinze KG, Dittrich P, Schwille P. (2001) Light-Induced Flickering of DsRed Provides Evidence for Distinct and Interconvertible Fluorescent States. *Biophys. J.*; 81:1776-1785.
50. Kubitscheck U, Kuckmann O, Kues T, Peters R. (2000) Imaging and Tracking of Single GFP Molecules in Solution. *Biophys. J.*; 78:2170-2179.
51. White J, Stelzer E. (1999) Photobleaching GFP reveals protein dynamics inside live cells. *Trends in Cell Biology*; 9:61-65.
52. Wallace W, Schaefer LH, Swedlow JR. (2001) A workingperson's guide to deconvolution in light microscopy. *Biotechniques*; 31:1076-8, 1080, 1082 passim.
53. Swedlow JR, Hu K, Andrews PD, Roos DS, Murray JM. (2002) Measuring tubulin content in *Toxoplasma gondii*: a comparison of laser-scanning confocal and wide-field fluorescence microscopy. *Proc Natl Acad Sci U S A*; 99:2014-9.
54. Magde D, Elson E, Webb WW. (1972) Thermodynamic Fluctuations in a Reacting System; Measurement by Fluorescence Correlation Spectroscopy. *Physical Review Letters*; 29:705 LP - 708.
55. Elliot L, Elson DM. (1974) Fluorescence correlation spectroscopy. I. Conceptual basis and theory. *Biopolymers*; 13:1-27.
56. Douglas Magde ELE, Watt W. Webb,. (1974) Fluorescence correlation spectroscopy. II. An experimental realization. *Biopolymers*; 13:29-61.
57. Webb W. (2001) Fluorescence Correlation Spectroscopy: Inception, Biophysical Experimentations, and Prospectus. *Appl. Opt.*; 40:3969-3983.
58. Schwille P, Korlach J, Webb WW. (1999) Fluorescence correlation spectroscopy with single-molecule sensitivity on cell and model membranes. *Cytometry*; 36:176-182.
59. Kohl T, Schwille P. (2005) Fluorescence correlation spectroscopy with autofluorescent proteins. *Adv Biochem Eng Biotechnol*; 95:107-142.
60. Feder TJ, Brust-Mascher I, Slattery JP, Baird B, Webb WW. (1996) Constrained diffusion or immobile fraction on cell surfaces: a new interpretation. *Biophys J*; 70:2767-2773.

61. Schwille P. (2001) Fluorescence correlation spectroscopy and its potential for intracellular applications. *Cell Biochem Biophys*; 34:383-408.
62. Gennerich A, Schild D. (2000) Fluorescence correlation spectroscopy in small cytosolic compartments depends critically on the diffusion model used. *Biophys J*; 79:3294-3306.
63. Wachsmuth M, Waldeck W, Langowski J. (2000) Anomalous diffusion of fluorescent probes inside living cell nuclei investigated by spatially-resolved fluorescence correlation spectroscopy. *J Mol Biol*; 298:677-689.
64. Lippincott-Schwartz J, Snapp E, Kenworthy A. (2001) Studying protein dynamics in living cells. *Nat Rev Mol Cell Biol*; 2:444-456.
65. Liebman PA, Entine G. (1974) Lateral diffusion of visual pigment in photoreceptor disk membranes. *Science*; 185:457-459.
66. Axelrod D, Koppel DE, Schlessinger J, Elson E, Webb WW. (1976) Mobility measurement by analysis of fluorescence photobleaching recovery kinetics. *Biophys J*; 16:1055-1069.
67. Edidin M, Zagyansky Y, Lardner TJ. (1976) Measurement of membrane protein lateral diffusion in single cells. *Science*; 191:466-468.
68. Phair RD, Misteli T. (2000) High mobility of proteins in the mammalian cell nucleus. *Nature*; 404:604-609.
69. Reits EAJ, Neefjes JJ. (2001) From fixed to FRAP: measuring protein mobility and activity in living cells. *3:E145-E147*.
70. Houtsmuller AB, Rademakers S, Nigg AL, Hoogstraten D, Hoeijmakers JH, Vermeulen W. (1999) Action of DNA repair endonuclease ERCC1/XPF in living cells. *Science*; 284:958-961.
71. Houtsmuller AB, Vermeulen W. (2001) Macromolecular dynamics in living cell nuclei revealed by fluorescence redistribution after photobleaching. *Histochem Cell Biol*; 115:13-21.
72. Klonis N, Rug M, Harper I, Wickham M, Cowman A, Tilley L. (2002) Fluorescence photobleaching analysis for the study of cellular dynamics. *Eur Biophys J*; 31:36-51.

73. Sprague BL, Pego RL, Stavreva DA, McNally JG. (2004) Analysis of Binding Reactions by Fluorescence Recovery after Photobleaching. *Biophys. J.*; 86:3473-3495.
74. Carrero G, Crawford E, Hendzel MJ, de Vries G. (2004) Characterizing fluorescence recovery curves for nuclear proteins undergoing binding events. *Bull Math Biol*; 66:1515-1545.
75. Houtsmuller AB. *Fluorescence Recovery after Photobleaching: Application to Nuclear Proteins*. Berlin / Heidelberg: Springer; 2005. 177-199 p.
76. Lakowicz JR. *Principles of fluorescence spectroscopy*. New York: Kluwer Academic/Plenum; 1999. xxiii, 698 p. p.
77. Bastiaens PI, Pepperkok R. (2000) Observing proteins in their natural habitat: the living cell. *Trends Biochem Sci*; 25:631-637.
78. Gordon GW, Berry G, Liang XH, Levine B, Herman B. (1998) Quantitative fluorescence resonance energy transfer measurements using fluorescence microscopy. *Biophys J*; 74:2702-2713.
79. de Laat WL, Jaspers NGJ, Hoeijmakers JHJ. (1999) Molecular mechanism of nucleotide excision repair. *Genes Dev.*; 13:768-785.
80. Sancar A. (1996) DNA Excision Repair. *Annual Review of Biochemistry*; 65:43-81.
81. Wood RD. (1999) DNA damage recognition during nucleotide excision repair in mammalian cells. *Biochimie*; 81:39-44.
82. Schärer OD. (2003) *Chemistry and Biology of DNA Repair*. *Angewandte Chemie International Edition*; 42:2946-2974.
83. Buschta-Hedayat N, Buterin T, Hess MT, Missura M, Naegeli H. (1999) Recognition of nonhybridizing base pairs during nucleotide excision repair of DNA. *PNAS*; 96:6090-6095.
84. Asahina H, Kuraoka I, Shirakawa M, Morita EH, Miura N, Miyamoto I, Ohtsuka E, Okada Y, K. T. (1994) The XPA protein is a zinc metalloprotein with an ability to recognize various kinds of DNA damage. *Mutat Res.*; 315:229-237.

85. Sugasawa K, Ng JMY, Masutani C, Iwai S, van der Spek PJ, Eker APM, Hanaoka F, Bootsma D, Hoeijmakers JHJ. (1998) Xeroderma pigmentosum group C protein complex is the initiator of global genome nucleotide excision repair. *Molecular Cell*; 2:223-232.
86. Sugasawa K, Okamoto T, Shimizu Y, Masutani C, Iwai S, Hanaoka F. (2001) A multistep damage recognition mechanism for global genomic nucleotide excision repair. *Genes Dev.*; 15:507-521.
87. Hoeijmakers JH, Egly JM, Vermeulen W. (1996) TFIIH: a key component in multiple DNA transactions. *Curr Opin Genet Dev.*; 6:26-33.
88. Matsunaga T, Mu D, Park C-H, Reardon JT, Sancar A. (1995) Human DNA Repair Excision Nuclease. *J. Biol. Chem.*; 270:20862-20869.
89. Sijbers AM, de Laat WL, Ariza RR, Biggerstaff M, Wei Y-F, Moggs JG, Carter KC, Shell BK, Evans E, de Jong MC. (1996) Xeroderma Pigmentosum Group F Caused by a Defect in a Structure-Specific DNA Repair Endonuclease. *Cell*; 86:811-822.
90. Nospikel T, Lalle P, Leadon SA, Cooper PK, Clarkson SG. (1997) A common mutational pattern in Cockayne syndrome patients from xeroderma pigmentosum group G: Implications for a second XPG function. *PNAS*; 94:3116-3121.
91. O'Donovan A, Davies AA, Moggs JG, West SC, Wood RD. (1994) XPG endonuclease makes the 3[prime] incision in human DNA nucleotide excision repair. *PNAS*; 91:432-435.
92. Waldmann TA. (1986) The structure, function, and expression of interleukin-2 receptors on normal and malignant lymphocytes. *Science*; 232:727-32.
93. Waldmann TA. (1991) The interleukin-2 receptor. *J Biol Chem*; 266:2681-2684.
94. Nakamura Y, Russell SM, Mess SA, Friedmann M, Erdos M, Francois C, Jacques Y, Adelstein S, Leonard WJ. (1994) Heterodimerization of the IL-2 receptor [beta]- and [gamma]-chain cytoplasmic domains is required for signalling. *J Biol Chem*; 269:330-333.
95. Damjanovich S, Bene L, Matko J, Alileche A, Goldman CK, Sharrow S, Waldmann TA. (1997) Preassembly of interleukin 2 (IL-2) receptor subunits on resting Kit 225 K6 T cells and their modulation by IL-2, IL-7, and IL-15: a

- fluorescence resonance energy transfer study. *Proc Natl Acad Sci U S A*; 94:13134-13139.
96. Vereb G, Meyer CK, Jovin TM. Novel microscope-based approaches for the investigation of protein - protein interactions in signal transduction. In: Heilmeyer Jr LMG, editor. *Interacting protein domains, their role in signal and energy transduction. NATO ASI series. Volume H102.* New York: Springer-Verlag; 1997. p 49-52.
 97. Nagy P, Jenei A, Kirsch AK, Szollosi J, Damjanovich S, Jovin TM. (1999) Activation-dependent clustering of the erbB2 receptor tyrosine kinase detected by scanning near-field optical microscopy. *J Cell Sci*; 112 (Pt 11):1733-1741.
 98. Liu P, Ying Y, Anderson RG. (1997) Platelet-derived growth factor activates mitogen-activated protein kinase in isolated caveolae. *Proc Natl Acad Sci U S A*; 94:13666-13670.
 99. Harder T, Simons K. (1999) Clusters of glycolipid and glycosylphosphatidylinositol-anchored proteins in lymphoid cells: accumulation of actin regulated by local tyrosine phosphorylation. *Eur J Immunol*; 29:556-562.

Chapter

2

Light Driven Dynamics of GFP Fluorescence Emission in Living Cells

S. M. Ibrahim, K. Jalink, W. G. van Cappellen,
G. Vámosi, G. Vereb, A.B. Houtsmuller

2.1 Abstract

Green fluorescent protein [1] and its color variants have revolutionised many aspects of cell biological research [2,3]. Probably the most important type of application is to visualise protein dynamics inside living cells, either by 2 or 3-dimensional time lapse imaging or by quantitative microscopic fluorescence assays such as fluorescence recovery after photobleaching [4], fluorescence correlation spectroscopy [5] and fluorescence resonance energy transfer [6]. In spite of the many obvious advantages of genetically encoded fluorescent protein tags, quantitative measurements using GFPs have been complicated by the photodynamic properties of the fluorophores. Upon excitation, most GFPs can be driven into roughly three different ‘dark states’. In addition to the triplet state (ns range) [7], GFP can also be driven into two longer range dark states, the so-called flickering (in the order of μs) [8], and ‘blinking’, which displays dark states that exist in the order of seconds. Where the first two have consequences for FCS and lifetime imaging [9] measurements, ‘blinking’ affects FRAP measurements. Although blinking has been investigated *in vitro* by immobilising enhanced green fluorescent protein EGFP in gels and applying single molecule microscopy, the blinking behaviour *in vivo* has not been investigated. Here, we show that in living cells the on-time is excitation intensity-dependent, whereas the time spent in the dark state [10] is independent of excitation intensity. This has consequences for the analysis of quantitative methods like FRAP.

2.2 Introduction

The green fluorescence protein and its variants [3] have become powerful tools for studying the structure and the dynamics of living cells due to their strong intrinsic visible fluorescence which is easily detectable by fluorescence spectroscopy

(reviewed in [1,11-15]). Methods and protocols to introduce the genes encoding fluorescent proteins fused to target proteins in a variety of common cell lines are well established [16]. The wide use of GFPs can be attributed to their minimal interference with cellular mechanisms and the ability of host cells to synthesize the fusion proteins on their own thereby enabling the visualization of the target protein non-invasively by fluorescence microscopy [1,11,14-16] GFPs are employed in fluorescence imaging and quantitative assays such as fluorescence recovery after photobleaching [4] and fluorescence correlation spectroscopy [5] to study the dynamic behaviour of proteins in living cells [14-18]. FRAP [17,19,20] and FCS [21,22] typically exploit changes in measured fluorescence intensities inside specified observation volumes to quantify dynamic processes. Effective interpretations of fluorescence data generated by these techniques require a good understanding of the photodynamics of the fluorescent-protein label to account for possible intrinsic fluctuations in fluorescence.

Fluorescence dynamics and single-molecule studies of GFPs have shown that this fluorophore under excitation alternates between an emissive “on-state” and a non-emissive “off-state” [23,24]. The resulting fluctuation in fluorescence is sometimes referred to as “blinking” and characterized by the lifetimes of the on- and off-states (on- and off-times respectively). Although the phenomenon is still the subject of many investigations, it has been attributed to the photophysical state of the chromophore as determined by changes in the chromophore environment and subtle structural variations in the protein. Switching between an “on” and an “off state” has been observed at varying degrees and frequencies for GFPs. Fast (ns range) fluctuations due to triplet state transitions [25-27] and the fluorescence flickers (μs range) revealed by FCS [28] are important in the interpretation of FCS data [29] while the long lived

(seconds time-range) dark states of GFPs (blinking) are not only relevant in single molecule studies but also in the interpretations of FRAP data.

Most studies on blinking of GFP and its mutants have been performed using single molecule techniques employing scanning near-field optical microscopy (SNOM), total internal reflection (TIR) wide-field microscopy, and fluorescence correlation spectroscopy (FCS) [10,28,30]. In these methods the studied GFP samples were either in solution (in the case of FCS), or immobilised in polyacrylamide, agarose or silica gels in single molecule studies. Although there are reported indications of the effect of blinking in photobleaching experiments using continuous laser excitations [10], there is as yet no reported quantitative approach to study the effect of the long-lived dark states on quantitative assays like FRAP in live cells.

To study the dynamics of GFP fluorescence in the living cell environment we employed a photobleaching protocol to synchronise [31] the transition of immobilised GFP to the dark state and then used fast confocal microscopy to characterize the light driven photodynamics of the fluorophore. With this method, we were able to characterize the blinking of enhanced green fluorescence protein (EGFP) in living HeLa cells. We found the on-time to be laser intensity dependent and the off-time constant irrespective of excitation intensity.

2.3 Materials and Methods

Microscopy

An inverted wide-field epifluorescence confocal laser scanning microscope system (Zeiss LSM410) equipped with an oil immersion 1.4 NA/63x objective with a heating collar was used. Cells grown on silica glass coverslip were transferred with the growth medium to a specially constructed sample dish and presented to the

microscope in a heated chamber placed on the microscope stage. The chamber and the objective lens were kept at 37°C.

Excitation was with the 488nm line of an Ar ion laser guided through an acousto-optical modulator (AOM) used to regulate excitation laser intensity. A 488 nm dichroic mirror and a 505-530 nm emission filter were used in the emission beampath. The confocal pinhole was set to a diameter of 20 μ m. Images were taken with the lens focussed to register maximum nuclear area. Measurements on a cell consisted of two sequential equatorial image scans with low laser intensity, separated by one higher intensity scan applied to drive the fluorophores' photophysical state. A fast scanning time with minimum delay between scans is essential for an accurate measurement of the recovery. A scanning time of 0.145s for 64x64 pixel images of the nucleus was achieved at an image resolution of 0.3125 μ m/pixel for the 63x lens objective used. All images were taken using a low monitoring irradiance of 0.48 μ W/ μ m² to avoid bleaching the fluorophores while still obtaining sufficient signal to background ratio. Typical integration time for imaging was 35.4 μ s per pixel. Image analysis was performed using a customized software developed locally in the LabVIEW (National Instruments, Austin, TX) environment.

Bleach protocol for the measurement of photo-induced fluorescence dynamics of immobilized GFP

The photo-induced fluorescence dynamics of immobilized EGFP expressed in the nuclei of HeLa cells transduced with histone H2B-EGFP (Fig. 2.1) was investigated using the imaging sequence depicted in Fig. 2.2A. The level of expression of the GFP in a cell under investigation was first determined by taking a pre-bleach image of the cell nucleus. The mean fluorescence intensity of this image, I_i corrected for the background was used to normalise all subsequent intensities measured on the cell.

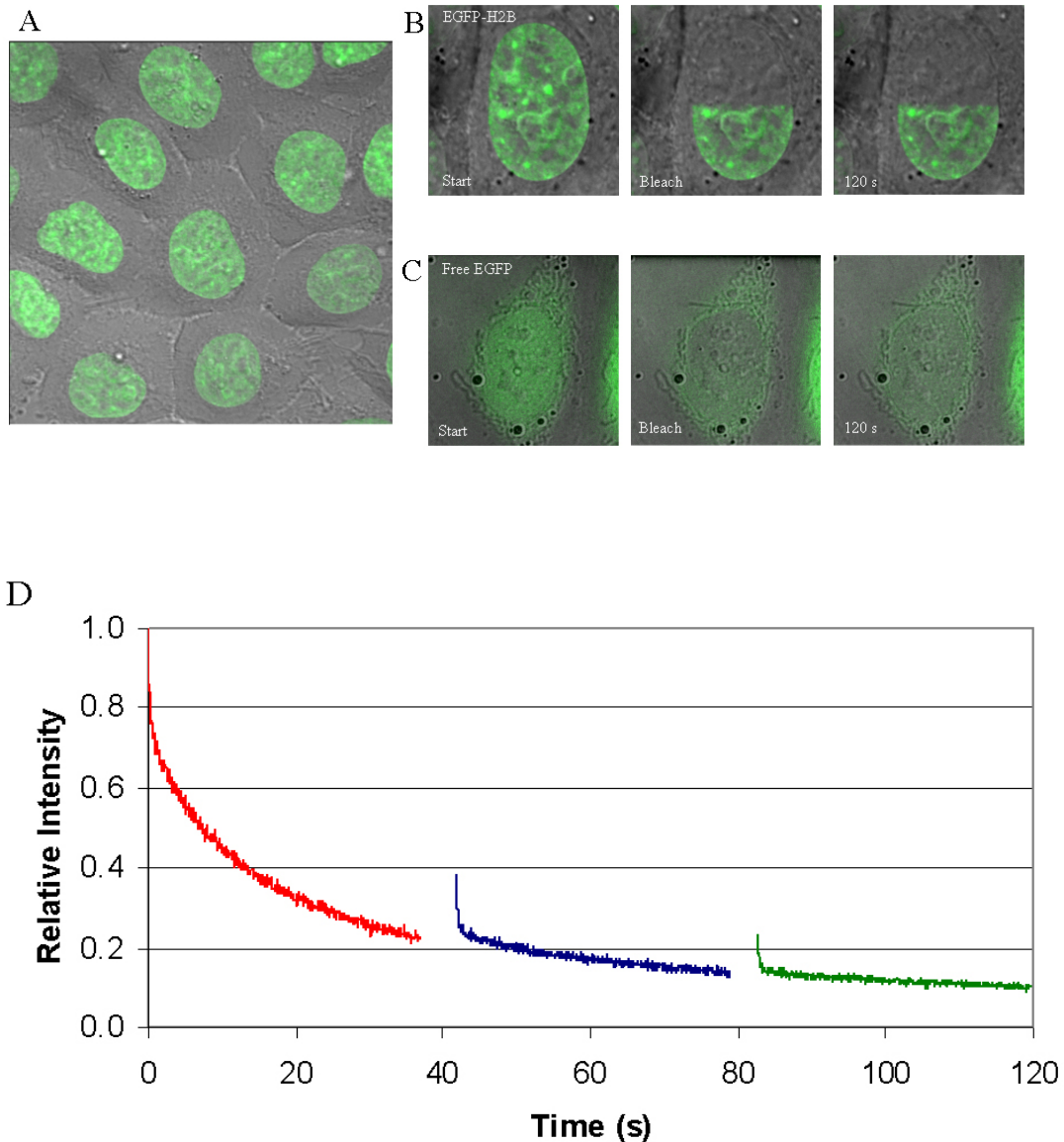


Fig. 2.1 Photobleaching of EGFP. (A) Confocal image of HeLa cells expressing GFP-tagged histone H2B. (B) H2B-GFP expressing HeLa-cell photobleached in one half of the nucleus. Images were taken immediately before and after photobleaching and at 120 s after photobleaching. Photobleaching was performed at high intensity ($148 \mu\text{W}/\mu\text{m}^2$), irreversibly bleaching all GFPs in that half. As expected, fluorescence intensities inside and outside the bleached region remained unchanged 120 s after bleaching [32]. Same experiment as in B with Hep3B cells expressing free EGFP resulted in quick redistribution of, and eventually reduced overall fluorescence within the nuclei upon bleaching. (D) Fluorescence decay obtained by continuously scanning a $1 \mu\text{m}$ wide strip spanning the nucleus of a living H2B-GFP expressing HeLa cell at the rate of 50 Hz at a relatively low intensity of $4.5 \mu\text{W}/\mu\text{m}^2$ for three 36 s periods separated by ~ 5 s intervals. Significant fluorescence recoveries were

observed after the pause periods, indicating that some EGFP molecules were reversibly bleached.

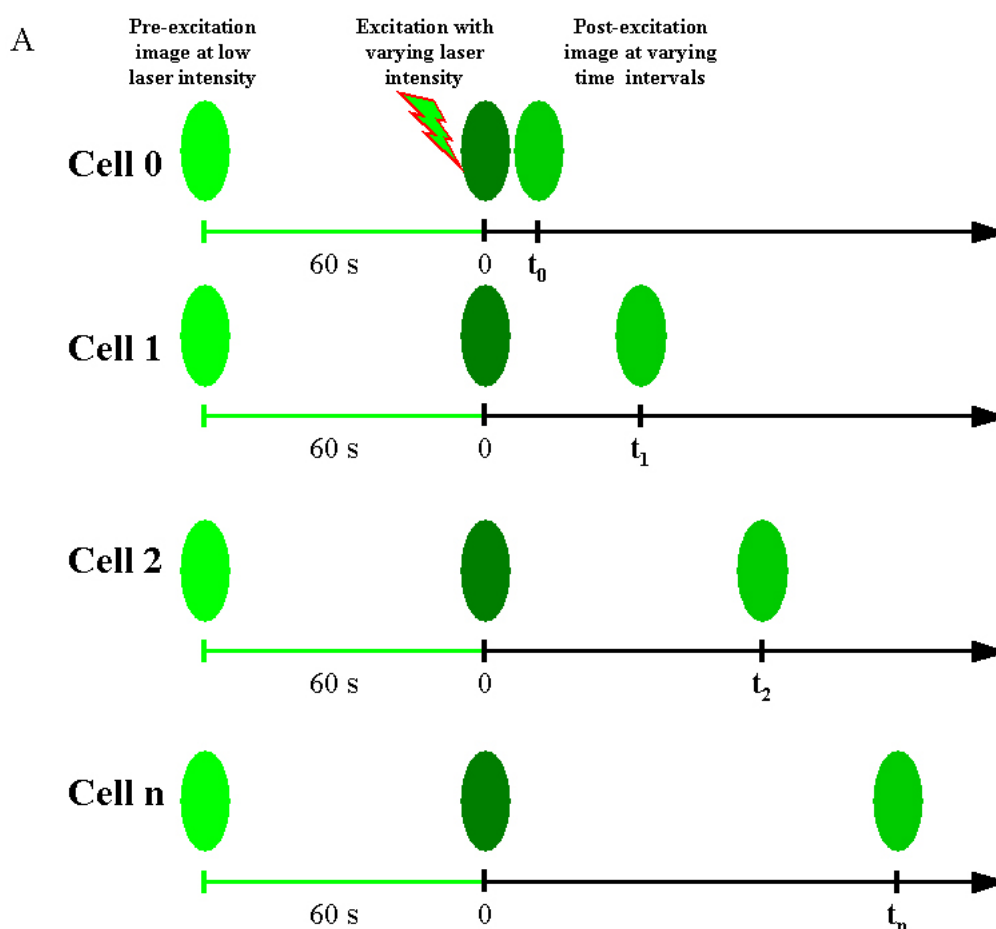


Fig. 2.2 Bleaching procedure for measurement of photo-induced fluorescence dynamics of immobilized GFP in living cells. (A) Schematic representation of the procedure: using a single scan of the entire cell nucleus the level of expression of the GFP in the cell under investigation is first determined. After 60 s the entire nucleus is bleached in a single scan at a specific laser intensity. A post-bleach image is taken at time t after bleaching to measure the mean fluorescence intensity of the cell after excitation. Every cell was imaged only twice: once before and once after bleaching. All images were taken with the low monitor laser irradiance of $0.48 \mu\text{W}/\mu\text{m}^2$. The post-bleach intensity was normalised to the pre-bleach intensity and the average of ten cells for each post-bleach time was obtained. The measurement was carried out for post-bleach times ranging from 0.6 to 200 s and for bleach intensities ranging from 2.6 to $122.0 \mu\text{W}/\mu\text{m}^2$.

After a pause of 60 s the cell was subjected to a bleach pulse of desired laser irradiance to induce the transition of susceptible fluorophores to the off-state. A post-bleach image was then taken at time t after the bleach to measure the mean fluorescence intensity of the cell after excitation. The post-bleach intensity, I_p (corrected for background) was normalised to the pre-bleach intensity, I_i and the average for ten cells (all with the same post-bleach time, t) was used to obtain the relative fluorescence intensity, I_t for this time. The measurement was carried out for post-bleach times ranging from 0.6 to 200 s to obtain the recovery profile of the fluorophore dark-state at the applied bleach irradiance. The procedure was repeated for bleach pulses ranging from 2.6 to 122.0 $\mu\text{W}/\mu\text{m}^2$.

Measurements on GFP-CAAX

Photobleaching experiments on GFP-CAAX expressed in membrane patches left by reseeded N15 neuroblastoma cells were carried out using a Leica TCS-SP confocal microscope equipped with $\times 63$ (NA 1.3) oil immersion objective. The 488 nm beam from an external ArKr laser (125 mW) was coupled into the back focal plane of the objective via the epifluorescence excitation port, using a 50/50 beam splitter, thus allowing simultaneous imaging and spot bleaching. Spots of $\sim 2.1 \mu\text{m}$ (full width half-maximum) were bleached in patches using 30 ms pulses from the ArKr laser during data collection in a line-scan mode at 125 Hz.

Evaluation of blink parameters

The recovery curves as obtained with the protocol described above were fitted to the function

$$I_t = I_0 + (I_f - I_0) \left[\frac{1}{2} + \frac{1}{\pi} \left(\tan^{-1} \left(\frac{t - t_{1/2}}{FWHM} \right) \right) \right] \quad (2.1)$$

where I_t is the post-excitation fluorescence intensity at time t . The first term, I_0 is the fluorescence intensity immediately after excitation while the second term is a cumulative Cauchy function with I_f being the intensity after equilibrium and $t_{1/2}$ the characteristic half-time for the Cauchy function; FWHM is full width at half maximum.

Blinking was characterised by the observed on-fraction, on-time, off-time and the rate constant of the transition between the dark and the bright states.

The on-fraction can be represented by the ratio

$$F_{\text{on}} = I_0/I_f \quad (2.2)$$

I_0 being the fraction of molecules fluorescent immediately after excitation and I_f the fraction of potentially fluorescent GFP molecules (not bleached) at the excitation intensity used.

2.4 Results

To study its blinking behaviour in living cells, we expressed EGFP coupled to histone H2B in HeLa cells (Fig. 2.1A). The histone H2B was chosen because it has been shown to be largely immobile (only 3% of H2B exchange within 6 min, ~40% with $t_{1/2} \approx 130$ min and the rest completely immobilised) [33-35]. Thus anchoring the fluorophore to the nucleosomal core assures immobility avoiding substantial diffusion related recovery of fluorescence in the time scale of the experiments. This was confirmed by irreversibly bleaching all the fluorophores in half of the nucleus of some of the HeLa cells by scanning (~10 scans) with very high intensity ($148 \mu\text{W}/\mu\text{m}^2$) laser beam and measuring the fluorescence intensities inside and outside the bleached regions by whole cell imaging at low intensity (Fig. 2.1B). The bleached half remained distinct even 120 s after bleaching with no significant change in the

fluorescence intensities inside and outside the bleached area (Fig. 2.1B). In contrast, bleaching portions of Hep3B cells expressing freely diffusing EGFP molecules resulted in reduced fluorescence intensities within the whole nucleus soon after bleaching (Fig. 2.1C).

We then investigated the photodynamic properties of EGFP using HeLa cells expressing EGFP-tagged H2B. Briefly, a 1 μm wide strip spanning the nucleus of a fixed HeLa cell was continuously scanned at a rate of 50 Hz with a intermediate laser irradiance of 4.5 $\mu\text{W}/\mu\text{m}^2$ for three consecutive periods of 36 s separated by ~ 5 s pauses. Photobleaching lead to exponential loss of emission falling to 22.8% in 36. However, when scanning was continued after a 5 s pause, significant fluorescence recovery (on average 15%) from the immobilized EGFP molecules was observed, indicating the presence of irradiation-induced ‘dark state’ molecules that (at least partly) returned to the excitable ground state (Fig. 2.1D).

Photo-induced fluorescence dynamics in the seconds time-scale

To further investigate the photo-induced reversible dark state of EGFP, the bleach protocol described in Materials and Methods (Fig. 2.2A) was applied to living HeLa cells expressing H2B-EGFP. Whole cell bleaching and rapid imaging employed in the procedure assured the exclusion of diffusion related recovery from the measured data (which in the case of H2B-EGFP is limited to 3% at the highest). Since repeated measurements after bleaching are expected to influence the equilibrium between dark and fluorescent states, cells selected for measurement were subjected to only one pre-bleach scan at low laser power (0.48 $\mu\text{W}/\mu\text{m}^2$) and only one post-bleach scan at a defined time interval after the bleach pulse. The monitor intensity of 0.48 $\mu\text{W}/\mu\text{m}^2$ was sufficient for taking pre- and post bleach images since no significant bleaching

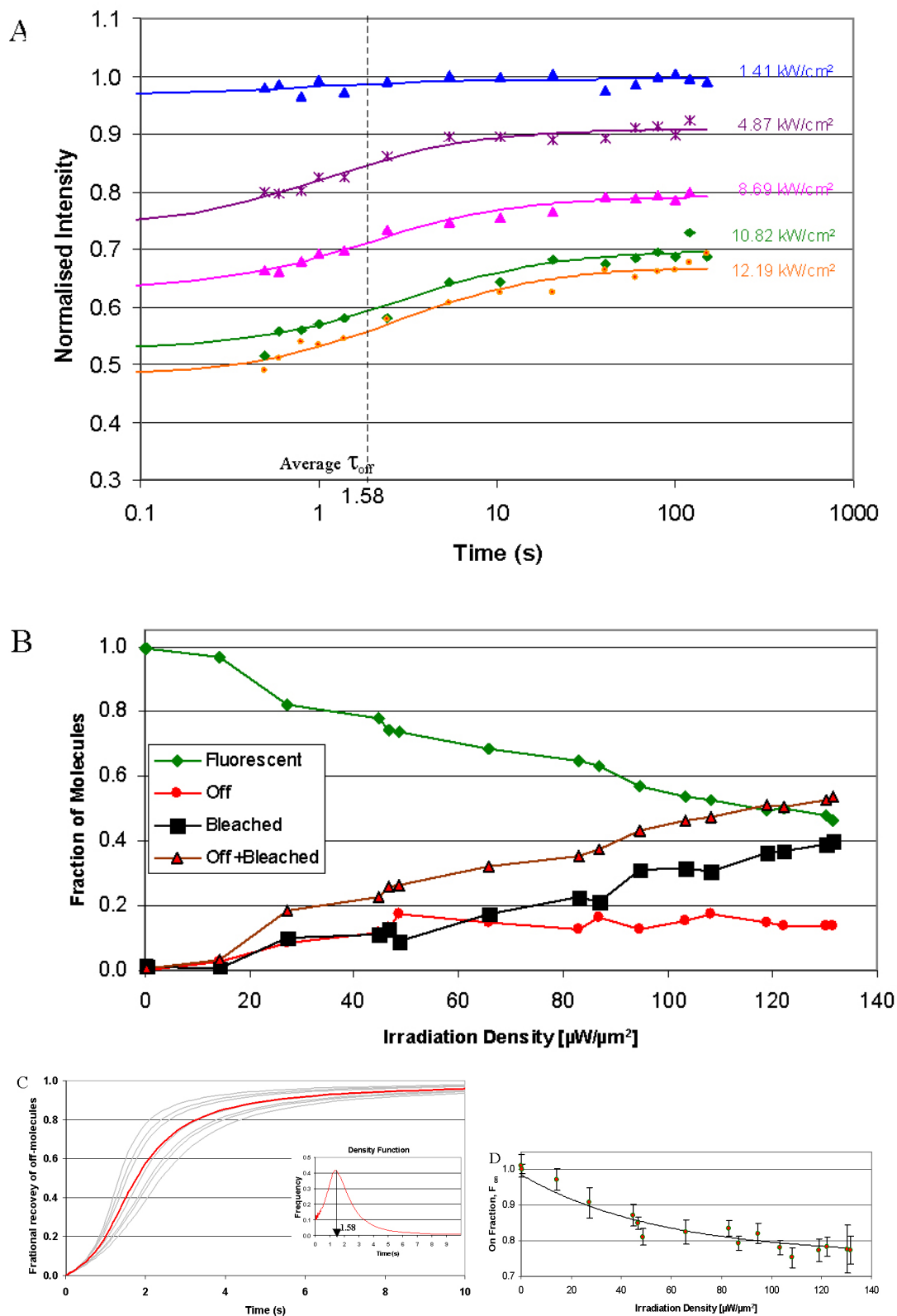


Fig. 2.3 Dependence of EGFP dark-state recovery kinetics on excitation density.

(A) Dark state recovery kinetics of GFP molecules in living H2B-EGFP expressing HeLa cells for five excitation intensities. The lines are the best fits of the recovery data to a cumulative Cauchy function as described in the text. (B) The fraction of molecules in the

different states (fluorescent, off and bleached) immediately after excitation are plotted against excitation intensity. (C) Normalised recovery from the dark state as a function of time for different irradiation intensities (grey) and the average for all the irradiation intensities (red). Inset is the derivative of the average curve. (D) Fraction of molecules in the on-state immediately after excitation (computed as fluorescent fraction in part B relative to the unbleached population of GFP, i.e. end-recovery intensity) as a function of irradiation intensity.

was observed (data not shown). A 60 s pause was applied after recording the prebleach image to allow the restoration of equilibrium between dark and fluorescent states [10]. Measurements were carried out at varying post-bleach times ranging from 0.6 to 200 s after bleaching at varying intensities ranging from 2.6 to 122 $\mu\text{W}/\mu\text{m}^2$. The fluorescence intensity immediately after bleaching, I_0 reflected the population of fluorophores in the on-state while subsequent post-bleach intensity I_t recorded after t s reflects the sum of this population and the fraction of molecules that recovered from the dark state after t s (Fig. 2.2A).

The recovery profiles (Fig. 2.3A) show that following a laser pulse EGFP fluorescence dropped to a minimum and increased sigmoidally with logarithmic time scale due to recovery of the dark state molecules. After 120 s, final post bleach intensities (I_f) were reached and after this period no further recovery of fluorescence was observed (data not shown). These final intensities are all less than the initial intensity before bleaching, due to intensity dependent irreversible bleaching of a fraction of the fluorophores. The fraction of fluorescence intensity not recovered, I_b represents the fraction of molecules permanently bleached at the bleach intensity. As expected, this irreversibly bleached fraction increased with bleach intensity (Fig. 2.3B). Conversely, the maximum post-bleach intensities (I_0) recorded immediately after bleaching decreased with bleach intensity. I_0 represents the fraction of molecules in the emissive state and when normalized to the final post bleach intensity I_f

determined after 120 s yields the on-fraction at the given bleach intensity. The on-fractions decreased with the bleach intensities (Fig. 2.3D). Interestingly, the fraction of molecules in the reversible dark state increased initially with intensity but saturated at $50 \mu\text{W}/\mu\text{m}^2$ (Fig. 2.3B).

On-time, Off-time and On-fraction

We then obtained estimates for the characteristic off-times corresponding to each bleach intensity, τ_{off} , (Fig. 2.3A) by fitting the data to Eqn. 2.1. Interestingly, $t_{1/2}$ values were independent of illumination intensity and yielded an average of 1.58 ± 0.23 s corresponding to a mean off-time of 2.28 ± 0.33 s (Fig. 2.3C). The on-fractions were calculated from the fitted values of I_0 and I_f as the ratio I_0/I_f . On-fractions were also determined from cell-pairs to substantiate the values calculated from recovery profiles. In these measurements, the bleach protocol (Material and Methods) was used on pairs of cells, where one cell was recorded immediately after bleaching and the other after 120 s (Fig. 2.3A). All images were taken at a monitor irradiance of $0.48 \mu\text{W}/\mu\text{m}^2$.

Accessibility of the dark state to bleaching

The recovery from dark state with time constant in the seconds range implies that during FRAP experiments GFP molecules contribute an additional mechanism to recovery of fluorescence. Such an additional component could be avoided if dark state molecules could be bleached by using very high bleach intensities. We therefore investigated whether or not a molecule in the dark state is able to absorb excitation light and thus is still susceptible to bleaching. To conduct these experiments we used small patches of the EGFP-tagged membrane protein CAAX. HEK-cells expressing EGFP-CAAX after transfection with EGFP-CAAX encoding plasmids when cultured

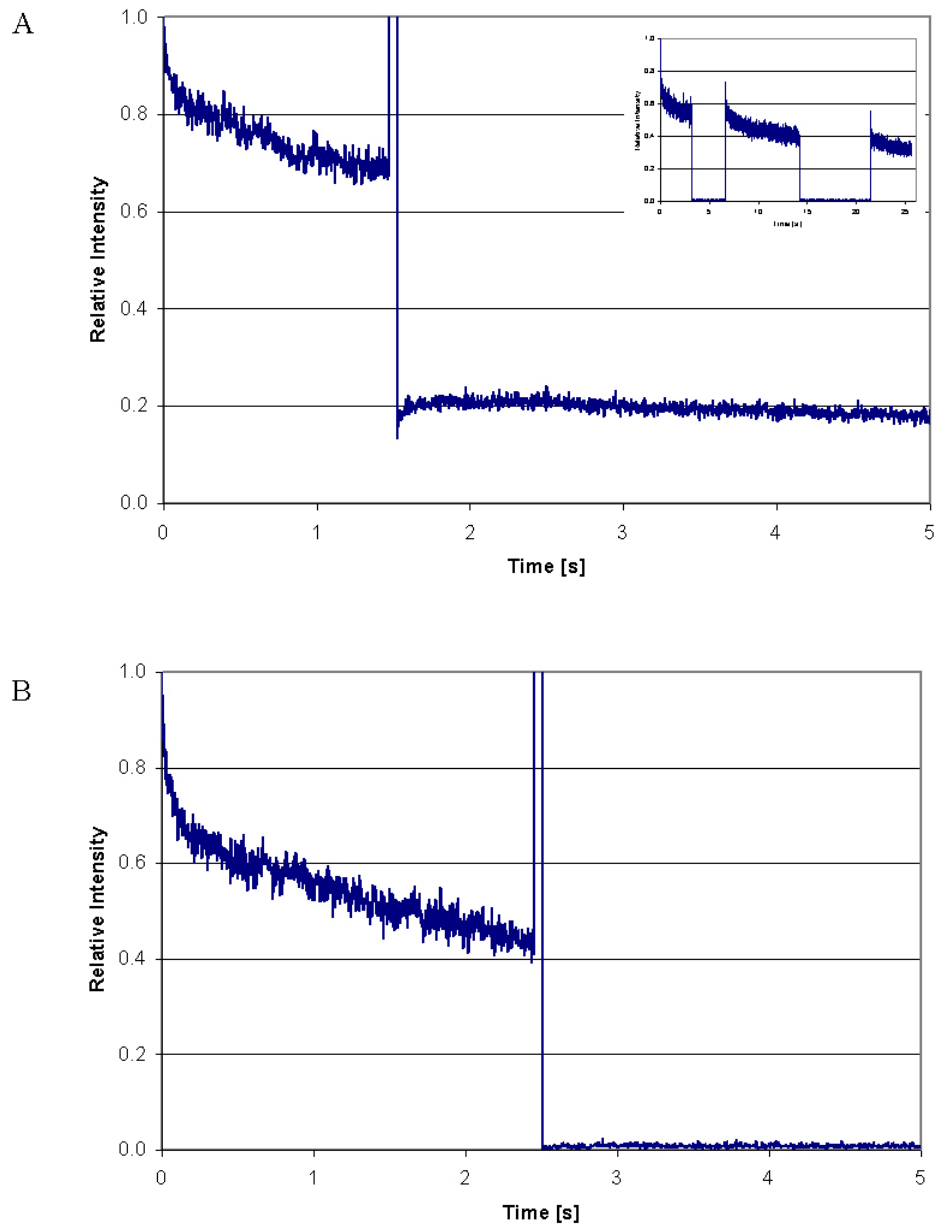


Fig. 2.4 Accessibility of GFP dark state to bleaching. (A) Fluorescence dynamics profile of a membrane patch subjected to a momentary high intensity bleach pulse of $20 \mu\text{W}/\mu\text{m}^2$ for 50 ms. Inset shows reversible photobleaching of GFP molecules in patches when illumination is paused for ~ 3.6 s during a continuous irradiation of the molecules using 2.5 ms pulses of $20 \mu\text{W}/\mu\text{m}^2$ laser power. (B) Fluorescence intensity profile of a patch subjected to a momentary bleach pulse of $6000 \mu\text{W}/\mu\text{m}^2$ for 50 ms after continuous scanning at $20 \mu\text{W}/\mu\text{m}^2$

on glass cover slips leave small protein patches on the coverslip as they move. The protein patches containing EGFP-CAAX are attached to the coverslip and do not

exchange with the medium (since otherwise they would gradually disappear), providing ensembles of immobilized EGFP molecules suitable for these experiments. Repeated monitoring of the patches at a laser intensity of $20 \mu\text{W}/\mu\text{m}^2$ showed that about 20% of the EGFP molecules are reversibly bleached (Fig. 2.4A inset, see also Fig. 2.2D). When patches were subjected to a bleach pulse at an intensity of $150 \mu\text{W}/\mu\text{m}^2$ after 1.5 s of continuous irradiation at $20 \mu\text{W}/\mu\text{m}^2$, the fluorescent intensity fell to 13% but recovered to 22% indicating a minimum of 16% of lost fluorescence is reversible (Fig 4A). However, when patches were subjected to a very strong bleach pulse ($6000 \mu\text{W}/\mu\text{m}^2$), the relative intensity dropped sharply to background level (Fig. 2.4B), indicating that the fraction in the dark-state was indeed efficiently and irreversibly bleached. A similar level of bleaching was observed for patches that had not previously been exposed to continuous irradiation (data not shown). These experiments suggest that EGFP molecules in the long-lived dark states are also susceptible to bleaching when exposed to a high flux laser irradiation.

2.5 Discussion

The environment of a fluorophore may have profound effects on its photophysical and photochemical properties. In living cells, these conditions are different from those in *in vitro* single molecule studies where the molecules under investigation are usually immobilised in a solid gel [10,28,30]. Moreover, the complex excited state dynamics of the GFP fluorophores makes the accurate prediction of their ensemble behaviour based on single molecule studies challenging. Therefore, we have studied in living cells the light induced fluorescence fluctuations of EGFP under conditions similar to those in quantitative assays employing the proteins as fluorescence probes.

The experimental setup utilising immobile H2B-EGFP allows investigation of blinking in living cells without significant diffusion related fluorescence recovery

We monitored the recovery of fluorescence from blinking EGFP molecules in HeLa cells expressing H2B-EGFP. The expression of EGFP in the cells follows the distribution of chromatin core histone H2B to which they are attached in the nucleus (Fig. 2.1A) ensuring their immobilization [33-35] as demonstrated by the absence of fluorescence redistribution 120 s after intensive repetitive bleaching of half of the nucleus of living HeLa cells expressing H2B-EGFP (Fig. 1B). If the fluorophores were mobile, bleached molecules would have dispersed over the nucleus soon after bleaching as in Hep3B cells expressing free EGFP molecules (Fig. 2.1C). To further discount mobility-related contributions to fluorescence recovery, whole cell imaging was employed.

By this strategy, we were able to induce blinking of susceptible EGFP molecules in the cells as evidenced by the recovery kinetics of the immobilized molecules (Fig. 2.3A).

EGFP on-times are excitation intensity dependent; off-times are independent of excitation intensity

The fraction of molecules in the emissive state decreases as the excitation intensity increases, while the population of molecules in off state initially increases with irradiance but saturates at about $50 \mu\text{W}/\mu\text{m}^2$. Similarly, the fraction of irreversibly bleached molecules increases with bleach intensity. The time an EGFP molecule remains in the on-state decreases with increasing excitation intensities while the lifetime of the off-state is, on average, 2.28 s irrespective of the excitation intensity. This is in agreement with the work of Garcia-Parajo [29] on the S65T mutant of GFP.

However, the off-times we found are much shorter than the 45 s reported by Peterman [8], who used single molecule studies on EGFP molecules immobilised in agarose gel at pH 8.

Blinking affects quantification of FRAP experiments

Although blinking of EGFP molecules may not be apparent when imaging larger cohorts of molecules, the phenomenon is not negligible if the proteins are subjected to excitation intensity variations [31], for instance in a FRAP experiment, or studied at the single molecule level, e.g. in FCS. Due to the large difference between the intensity used for monitoring and for the bleach pulse, blinking is expected to have effect on a FRAP experiment. The effect will be most notable in a situation where a large part or all of the proteins under investigation are immobile (or very slowly diffusing). After the bleach pulse, approximately 20 % of the bleached molecules in the bleached area will regain their fluorescent properties (Fig. 2.3A). The half-life of this recovery being 1.6 s, the FRAP curve (which is only due to recovery from the dark state) will fit to a model where ~80% of the molecules are immobile and the remaining ~20% (dependent on the exact bleach intensity) diffuses at a certain diffusion rate corresponding to a half-life of fluorescence recovery of 1.6 s. Since diffusion half-lives at a specific diffusion rate are dependent on the size and shape of the bleached area, the deduced diffusion coefficient will also depend on these data. In a typical strip FRAP experiment, an apparent diffusion coefficient corresponding to a half-life of ~1.6 s is approximately $0.5 \mu\text{m}^2/\text{s}$. Thus, in a situation where strip-FRAP is applied to nuclei in which 50% of the molecules are immobile, the effective diffusion coefficient of the freely diffusing fraction (50%) will be convoluted with a 10% fraction seemingly diffusing at a rate of $0.5 \mu\text{m}^2/\text{s}$. Proteins faster than this will appear slower and vice versa. In a scenario where all proteins are free to diffuse,

~20% of the bleached diffusing molecules will recover from the dark state. However, this will have more effect on the slower molecules than on the fast ones, since the latter are replaced at a faster rate than the blinking recovery rate.

Since the half-life of recovery due to blinking does not depend on the size of the bleached area whereas diffusion half-lives do may lead to erroneous interpretation of experiments with increasing size of the bleach area. Such experiment is the so-called mean square displacement test, which is frequently used to determine if molecules move by means other than diffusion. In free diffusion, the square root of the half-life of recovery is linearly dependent on the bleached area. Thus, any deviation from linearity may be interpreted as non-Brownian diffusion. However, since the recovery rate due to blinking is independent of the area, the phenomenon may add to the non-linearity.

In conclusion, quantification of phenomena that lead to slow protein mobility (transient immobilization, high viscosity of the medium, or being part of a large protein complex) with half-lives of recovery longer than ~1.5 s will be biased by blinking. In general, when no care is taken, mobile fractions (especially when a large fraction is immobile) and diffusion rates (especially slow diffusion) will be overestimated. Also, the mean square displacement test should be interpreted with care. Our experiments with very high laser intensity (6 mW/ μm^2) suggest that it is possible to effectively bleach all molecules in the focus of a laser beam, avoiding any effect of blinking behaviour of the fluorescent molecules used. However, this requires a special setup with high intensity lasers. Moreover, the application of very high laser intensities is unhealthy for a living cell. It is, however, possible to include blinking into explicit or Monte Carlo models used in the evaluation of FRAP recovery data.

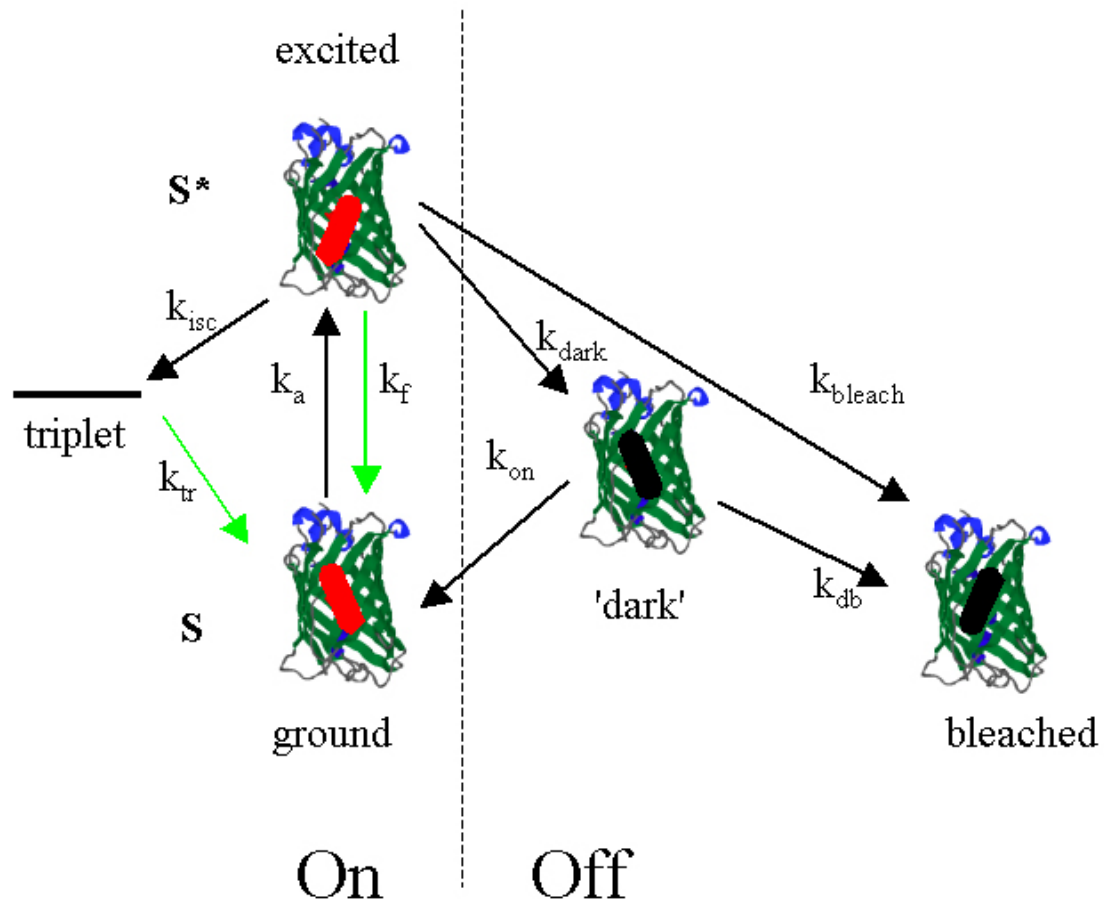


Fig. 2.5 Model describing the photo-induced fluorescence dynamics of EGFP in living cells. Following absorption of 488 nm light, the EGFP fluorophore in the ground state S is excited to singlet state level S^* (k_a). EGFP can then relax to any one of four possible states: by fluorescence to on-state (k_f), which is available to immediate excitation; by intersystem crossing to the triplet state (k_{isc}); to the non-emissive dark state (k_{dark}); or get permanently bleached (k_{bleach}). In the dark state, EGFP may be in a higher energy level than the ground state, but loses its energy probably in a non-emissive way (k_{on}). Although non-emissive, the dark state molecule may still absorb excitation light and get permanently photobleached (k_{db}). We were only able to show that this at least occurs at very high energy irradiation, but were not able to determine the rate at which this occurs at lower intensities. Green lines are processes involving photon emission.

A model for blinking of EGFP in living cells

The model presented in Fig. 2.5 suffices to explain our observations. Upon illumination by 488 nm laser light, the EGFP chromophore in the ground state is

driven to excited state, from where it can return to the ground state by emitting a photon. It is also possible that the excited molecule becomes photobleached and thereby loses its fluorescent capacity. The fluorophore can also adopt a temporary dark state after excitation (k_{dark}), during which it does not emit any photons. Probably, the energy level of the dark molecule is still above ground state [36] to which it will return (k_{on}) after an average 2.3 s corresponding to a half-life of 1.6 s. Surprisingly, although non-emissive, the dark molecule is able to absorb excitation light and undergo photobleaching. The fraction of molecules in the different states depends on the excitation intensity. A chromophore remains emissive when its transitions are within the singlet ground state and the excited singlet state (characterized by k_a and k_f). We consider the triplet state, T (characterized by k_{ISC} and k_{tr}) to be part of the excitation-emission cycle as the triplet state lifetimes are too short for our experiments to detect due to the long integration time. For this same reason, the short-lived protonation induced dark states could not be detected in our experiments and only the long-lived dark state could be identified.

Finally, we have shown in this work that blinking, the light induced fluorescence fluctuation, of EGFP molecules is measurable in bulk samples by variation of excitation laser intensity. We have found that the lifetime of the long-lived dark state of the chromophore is about 2.28 s irrespective of the excitation intensity while the on-time is dependent on the intensity used.

References

1. Tsien RY. (1998) The green fluorescent protein. *Ann. Rev. Biochem.*;67:509-544.

2. Tsien RY, Miyawaki A. (1998) BIOCHEMICAL IMAGING: Seeing the Machinery of Live Cells. *Science*; 280:1954-1955.
3. Bastiaens PI, Pepperkok R. (2000) Observing proteins in their natural habitat: the living cell. *Trends Biochem Sci*; 25:631-637.
4. Anderson CM, Georgiou GN, Morrison IE, Stevenson GV, Cherry RJ. (1992) Tracking of cell surface receptors by fluorescence digital imaging microscopy using a charge-coupled device camera. Low-density lipoprotein and influenza virus receptor mobility at 4 degrees C. *J Cell Sci*;101 (Pt 2):415-425.
5. Ahn HY, Hadizadeh KR, Seul C, Yun YP, Vetter H, Sachinidis A. (1999) Epigallocatechin-3 gallate selectively inhibits the PDGF-BB-induced intracellular signaling transduction pathway in vascular smooth muscle cells and inhibits transformation of sis-transfected NIH 3T3 fibroblasts and human glioblastoma cells (A172). *Mol Biol Cell*; 10:1093-1104.
6. Aoki K, Nakamura T, Matsuda M. (2004) Spatio-temporal Regulation of Rac1 and Cdc42 Activity during Nerve Growth Factor-induced Neurite Outgrowth in PC12 Cells. *J Biol Chem*;279:713-719.
7. Sekar RB, Periasamy A. (2003) Fluorescence resonance energy transfer (FRET) microscopy imaging of live cell protein localizations. *J Cell Biol*;160:629-633.
8. Hennink EJ, de Haas R, Verwoerd NP, Tanke HJ. (1996) Evaluation of a time-resolved fluorescence microscope using a phosphorescent Pt-porphine model system. *Cytometry*;24:312-320.
9. Bastiaens PI, Squire A. (1999) Fluorescence lifetime imaging microscopy: spatial resolution of biochemical processes in the cell. *Trends Cell Biol*;9:48-52.
10. Peterman EJG, Brasselet S, Moerner WE. (1999) The Fluorescence Dynamics of Single Molecules of Green Fluorescent Protein. *J. Phys. Chem. A*; 103: 10553-10560.
11. Cubitt AB, Heim R, Adams SR, Boyd AE, Gross LA, Tsien RY. (1995) Understanding, improving and using green fluorescent proteins. *Trends in Biochemical Sciences*; 20:448-455.

12. Palm GJ, Wlodawer A. (1999) Spectral variants of green fluorescent protein. *Methods Enzymol*;302:378-394.
13. Prendergast FG. (1999) Biophysics of the green fluorescent protein. *Methods Cell Biol*;58:1-18.
14. Lippincott-Schwartz J, Snapp E, Kenworthy A. (2001) Studying protein dynamics in living cells. *Nat Rev Mol Cell Biol*;2:444-456.
15. Zimmer M. (2002) Green fluorescent protein: applications, structure, and related photophysical behavior. *102*:759-781.
16. Lippincott-Schwartz J, Patterson GH. (2003) Development and use of fluorescent protein markers in living cells. *Science*;300:87-91.
17. Axelrod D, Koppel DE, Schlessinger J, Elson E, Webb WW. (1976) Mobility measurement by analysis of fluorescence photobleaching recovery kinetics. *Biophys J*;16:1055-1069.
18. Phair RD, Misteli T. (2001) Kinetic modelling approaches to in vivo imaging. *Nat Rev Mol Cell Biol*;2:898-907.
19. Verkman AS. (2002) Solute and macromolecule diffusion in cellular aqueous compartments. *Trends Biochem Sci*;27:27-33.
20. Misteli T. (2001) Protein dynamics: implications for nuclear architecture and gene expression. *Science*;291:843-847.
21. Webb W. (2001) Fluorescence Correlation Spectroscopy: Inception, Biophysical Experimentations, and Prospectus. *Appl. Opt.*;40:3969-3983.
22. Schwille P. (2001) Fluorescence correlation spectroscopy and its potential for intracellular applications. *Cell Biochem Biophys*;34:383-408.
23. Dickson RM, Cubitt AB, Tsien RY, Moerner WE. (1997) On/off blinking and switching behaviour of single molecules of green fluorescent protein. *Nature*;388:355-358.
24. Haupts U, Maiti S, Schwille P, Webb WW. (1998) Dynamics of fluorescence fluctuations in green fluorescent protein observed by fluorescence correlation spectroscopy. *PNAS*;95:13573-13578.

25. Johnson GD, Davidson RS, McNamee KC, Russell G, Goodwin D, Holborow EJ. (1982) Fading of immunofluorescence during microscopy: a study of the phenomenon and its remedy. *Journal of Immunological Methods*;55:231-242.
26. Widengren J, Rigler R, Mets Ål. (1994) Triplet-state monitoring by fluorescence correlation spectroscopy. *Journal of Fluorescence*;4:255-258.
27. Song L, Varma C, Verhoeven J, Tanke H. (1996) Influence of the triplet excited state on the photobleaching kinetics of fluorescein in microscopy. *Biophys. J.*; 70:2959-2968.
28. Schwille P, Kummer S, Heikal AA, Moerner WE, Webb WW. (2000) Fluorescence correlation spectroscopy reveals fast optical excitation-driven intramolecular dynamics of yellow fluorescent proteins. *PNAS*; 97:151-156.
29. Wachsmuth M, Waldeck W, Langowski J. (2000) Anomalous diffusion of fluorescent probes inside living cell nuclei investigated by spatially-resolved fluorescence correlation spectroscopy. *J Mol Biol*;298:677-89.
30. Garcia-Parajo MF, Segers-Nolten GMJ, Veerman J-A, Greve J, van Hulst NF. (2000) Real-time light-driven dynamics of the fluorescence emission in single green fluorescent protein molecules. *PNAS*; 97:7237-7242.
31. Zondervan R, Kulzer F, Orlinskii SB, Orrit M. (2003) Photoblinking of Rhodamine 6G in Poly(vinyl alcohol): Radical Dark State Formed through the Triplet. *J. Phys. Chem. A*;107:6770-6776.
32. Bini L, Pacini S, Liberatori S, Valensin S, Pellegrini M, Raggiaschi R, Pallini V, C TB. (2003) Extensive temporally regulated reorganization of the lipid raft proteome following T-cell antigen receptor triggering. *Biochem J*;369:301-309.
33. Lever MA, Th'ng JPH, Sun X, Hendzel MJ. (2000) Rapid exchange of histone H1.1 on chromatin in living human cells. *408*:873-876.
34. Kimura H, Cook PR. (2001) Kinetics of Core Histones in Living Human Cells: Little Exchange of H3 and H4 and Some Rapid Exchange of H2B. *J. Cell Biol.*; 153:1341-1354.

35. Mosammaparast N, Jackson KR, Guo Y, Brame CJ, Shabanowitz J, Hunt DF, Pemberton LF. (2001) Nuclear Import of Histone H2A and H2B Is Mediated by a Network of Karyopherins. *J. Cell Biol.*; 153:251-262.
36. Creemers TMH, Lock AJ, Subramaniam V, Jovin TM, Volker S. (2000) Photophysics and optical switching in green fluorescent protein mutants. *PNAS*; 97:2974-2978.

Chapter

3

**Dynamics of Nuclear Proteins:
Complementarity of Fluorescence Correlation
Microscopy and Recovery After Photobleaching
in Intracellular Mobility Measurements**

Shehu M. Ibrahim, Angelika Zotter, Karin A. Mattern,
Pascal Farla, Gert van Cappellen, Gyorge Vámosi,
Gyorge Vereb, Wim Vermeulen,
and Adriaan Houtsmuller.

3.1 Abstract

The dynamics of a cellular protein depends on its size, shape and function in the cellular environment. Fluorescence correlation spectroscopy (FCS) is a method well suited for the characterization of the diffusion properties of cellular proteins, but is largely insensitive to binding-related immobilization common to proteins in the nucleus, specifically those that bind either directly or indirectly to DNA. On the other hand, in fluorescence recovery after photobleaching (FRAP) experiments, an accurate evaluation of fluorescence recovery curves is only possible when the immobilization events are accounted for. We have used FCS in conjunction with FRAP to characterize the dynamics of functionally inert proteins of various sizes in the cell nucleus consisting of single fluorescent EGFPs fused to increasing numbers of the non-fluorescent mutants of the marker. The same methods were also used to determine the mobility of EGFP tagged, biologically active wild-type androgen receptor (AR) and an inactive mutant of the receptor (AR-D). In the FCS studies, good fits to the autocorrelation functions could be achieved using single- or multi-component anomalous diffusion models corrected for blinking of the EGFP marker. In contrast, FRAP recovery curves of the active AR could not be optimally fitted even when applying the anomalous fitting model. However, binding-related contributions to mobility could be used to explain the curves. Hence, FRAP could serve as a good indicator of the presence of binding, thereby facilitating a complete characterization of the dynamics of proteins when the two methods are combined.

3.2 Introduction

Live cell fluorescence microscopy experiments have shown that fluorescently tagged biologically active proteins involved in diverse nuclear functions such as gene transcription, RNA splicing and DNA replication and repair are often highly mobile in the cell nucleus [1-8]. In addition they may interact at high exchange rate with immobile binding sites, presumably on DNA. These conclusions are drawn mostly from studies on a large number of nuclear proteins by fluorescence recovery after photobleaching (FRAP) [9] (reviewed in [10-12]), and fluorescence correlation spectroscopy (FCS) [13,14]. In addition to the unexpectedly high mobility of many nuclear proteins, these studies suggest that nuclear transport of proteins is often energy independent and diffusion-mediated [1-4,7-10], though active directed transport of some proteins is possible in some cases [10].

FCS with its microscopic detection volume is capable of accurate determination of the diffusion coefficient and concentration of a protein in a localized spot [15]. The method is fast and diffusing species of sufficient disparity are distinguishable. However, the limitation of the sensitive volume to a minute spot makes the technique less suitable for the characterization of long range dynamic parameters such as binding rates involving long residence times. Immobile fluorescent molecules in the detection volume of an FCS system are susceptible to bleaching resulting in a high apparent number of molecules and faster than normal diffusion coefficients [11]. In the application of FCS to cellular protein dynamics, photobleaching of immobile fractions and autofluorescence in the area to be investigated is carried out before the measurement is commenced. Thus the accurate

in vivo characterization of cellular protein dynamics involving binding events by FCS alone is very challenging.

FRAP involves the measurement of the recovery of fluorescence in a bleached, relatively large, observation area (usually of several μm^2 in size) due to the influx of many unbleached fluorescent molecules from the unbleached region. The recovery kinetics (rate and shape) is affected by the mobility of many molecules over a longer range and time, as well as the interactions they undergo as they traverse the observation area. The long range and the multitude of parameters involved make the analysis of FRAP recovery kinetics very challenging. Simplified mathematical algorithms used to model FRAP recovery kinetics are only able to extract the apparent effective diffusion coefficients that may be weighted averages of two or more diffusing species or diffusion coupled with transient binding events [1,16,17]. However, if properly modeled, the diffusion coefficients, mobile and immobile fractions, as well as average residence times at binding sites of the labelled molecules can be extracted from a recovery profile [16-20]. In more rigorous evaluation of FRAP data, computer simulation of the FRAP process is applied to generate curves with varying diffusion coefficients and kinetic parameters [16,21]. The input parameters of the simulated curve that best fits the experimental curve are then ascribed to experimental data. The choice of parameters to associate with the experimental curve is influenced by a prior knowledge of some properties of the dynamics of the protein under investigation.

In this work, we demonstrate the complementarities of FCS and FRAP in the characterization of protein dynamics in the nucleus of living cells. The green fluorescent protein is functionally inert in the nucleus and therefore suitable for investigating the intranuclear mobility of macromolecules. We have investigated the

effect of the nuclear environment and molecular size on the mobility of the protein using various sizes of tandem constructs of the protein measured in solutions and when expressed in live cell nuclei. We propose a mathematical model for the extraction of binding parameters from FRAP measurements which we have tested on Monte Carlo simulation of some FRAP curves. We compare the dynamic properties of the tandem constructs of the EGFP obtained with FCS to those obtained using FRAP. We also compare the diffusion coefficients obtained by both methods for EGFP fusions of the wild-type androgen receptor (AR) and a non-active mutant of the receptor (AR-D), and show that the apparent discrepancies in the values obtained for EGFP-AR can be explained by the binding of the active receptor to DNA.

3.3 Materials and Methods

Assayed solutions

Stock solutions of rhodamine Rh6G and Alexa Fluor 488 (Molecular Probes, Inc., Willow Creek Road, Eugene, OR) were prepared by dissolving the dyes in DMSO at concentrations of 5 and 10 mM, respectively. The rEGFP used in this work was from Clontech (Clontech laboratories, Inc., Terra Bella Avenue, Mountain View, CA). EGFP-XPA protein was produced as previously described [22]. Dilutions of the assayed fluorophores were made in phosphate buffered saline solution (PBS).

Cell lines, cell culture and transfection conditions

Cell strains used in this study include Hep3B-cells stably expressing free EGFP or EGFP fused to increasing numbers of an EGFP variant in which glycine 67 was replaced by a valine [23]. This non-fluorescent EGFP(G67V) variant was designated NFP. Variants of the fusion proteins with two or more NFPs containing a triple

nuclear localisation signal (NLS) to facilitate transport to the nucleus were also made. CHO cells stably expressing EGFP-NFP_n-NLS were used for cellular experiment with these constructs. For the study of a functional DNA-binding protein, we used Hep3B-cells stably expressing the fusions of EGFP with the wild-type androgen receptor AR (EGFP-AR), or a fusion of EGFP with a mutant androgen receptor AR-D which cannot bind DNA due to a replacement of alanine 573 by an aspartate (EGFP-ARD) [24]. The cells were cultured in standard medium supplemented with 10% fetal calf serum, 100 i.u. penicillin and 100 U streptomycin per ml, and maintained in a humidified 5% CO₂ incubator at 37 °C.

Generation of EGFP-NFP_n and EGFP-NFP_n-NLS fusion constructs

NFP constructs were generated using the Quikchange Site-Directed Mutagenesis Kit (Stratagene, Cedar Creek, TX), and primers 5'-GTGACCACCCTGACCTACGTAGTGCAGTGCTTCAGCCGC-3' and 5'-GCGGCTGAAGCACTGCACTACGTAGTCAGGGTGGTCAC-3' and by removing the authentic start codon of the EGFP. The EGFP-NFP_n and EGFP-NFP_n-NLS constructs were generated by the insertion of multiple *PinAI-XmaCI* fragments containing NFP into the *XmaCI*-site of EGFP-C1 vector. In addition, an extra sequence encoding for a HisHA-tag at the N-terminus of EGFP (between the *NheI* and *NcoI* sites) was added. The EGFP-NFP_n-NLS constructs also contain three tandem copies of the SV40 T-antigen nuclear localization signal (NLS) inserted by cloning the *BglIII/BamHI*-fragment from pEYFP-Nuc (Clontech) in the *BamHI* site of EGFP-C1. They also contain a FLAG-tag at the C-terminus of the NLS (*BamHI* site).

Cell lines expressing the protein constructs were generated by the transfection of EGFP-NFP_n plasmid DNA into Hep3B and EGFP-NFP_n-NLS plasmid DNA into CHO cells using FugENE 6 transfection reagent (Roche, Indianapolis, IN). Stable clones were picked after selection with G418 Sulphate (Sigma, St. Louis, MO, 0.6

mg/ml active concentration). The molecular weights of the protein constructs expressed by the G418 resistant clones was checked by Western blotting using an anti-EGFP antibody (Ab290, Abcam, Cambridge, UK) and HRP-conjugated secondary antibody. The signal was visualized with Super Signal West Pico Luminol solution (Pierce, Rockford, IL).

Microscopy

Fluorescence autocorrelation measurements were performed on a Carl Zeiss LSM510 microscope upgraded to ConfoCor2/LSM510 combi. A combined setup enables easy positioning of the cells at the laser focus of the FCS head and images taken before and after FCS measurements aid in data interpretation [25,26]. For excitation, the 488 nm line of an Ar ion laser on the laser module was used at a tube current of 6.1 A. An additional shutter situated at the exit of the argon laser ensures complete blockage of the 458, 477 and 514 lines when the 488-line is being used. FCS measurements were performed at a laser power density of about $1.75 \mu\text{W}/\mu\text{m}^2$ using the C-Apochromat 40x water immersion objective (1.2 NA) with a band pass filter BP 505-550 nm (BP530-560 for Rh6G) and behind a 488 nm dichroic mirror at a detector pinhole setting of 70 μm .

Photobleaching experiments were performed on a Zeiss LSM-META confocal Microscope using a Plan-Neofluar 40x/1.3 NA oil-immersion objective. Excitation was by the 488-nm line of an Ar ion laser and EGFP fluorescence was detected by photomultiplier tubes (PMTs) after passing through a 505-550 nm band pass filter.

Both of the microscopes were equipped with a Zeiss 37-2 digital incubation system to keep cells under physiological conditions.

FCS measurement of liquid specimens

Dilute solutions of the assayed compounds (Rh6G, Alexa488, EGFP-chains) were prepared in PBS. 100-150 μl of the solution to be measured was then dropped onto a 24-mm silica glass coverslip mounted on a sample dish placed on the microscope stage. Five to ten repeated twenty-seconds-long FCS measurements were then carried out 200 μm above the glass. The autocorrelation functions were corrected for background obtained from measurements on clear PBS and then fitted to Eqn.3.1 for EGFP containing solutions and Eqn.3.3 for non-EGFP solutions to obtain the diffusion times and apparent number of molecules in the sample volume.

FCS measurement on cells

Cells for measurement were grown on 24-mm silica glass coverslips and then transferred to a sample dish with the growth medium replaced by phenol-red free medium. The dish was placed in a sample holder and mounted on the microscope stage in a heated chamber connected to a CO_2 supply. The chamber and the objective lens were kept at 37°C . With the aid of LSM imaging the cell to be studied was identified and the desired point for measuring positioned at the FCS beam. The location of the FCS center with respect to the LSM center was identified by focusing with a high laser intensity in FCS mode at a thin layer of precipitated Rh6G, and then examining the bleached spot in LSM mode.

Evaluation of autocorrelation curves

Autocorrelation curves measured from intracellular GFP tagged proteins in living cells are generally analysed using the Levenberg-Marquardt non-linear least-squares method to fit the data to a single- or multi-component anomalous diffusion model corrected for the triplet state and blinking fluctuations (Chapter 2) [27-29].

$$G(\tau) = a_0 + \frac{1}{\langle N \rangle} \cdot G_{tr} \cdot G_{bl} \cdot \sum_i^n \left[w_i \left(1 + \left(\frac{\tau}{\tau_{d,i}} \right)^{2/d_{w,i}} \right)^{-1} \left(1 + \frac{1}{S^2} \left(\frac{\tau}{\tau_{d,i}} \right)^{2/d_{w,i}} \right)^{-1/2} \right] \quad (3.1)$$

where the triplet state correction is given by

$$G_{tr}(\tau) = \frac{\left(1 - T + T e^{-\tau/\tau_r} \right)}{1 - T} \quad (3.1a)$$

and the blinking correction by

$$G_{bl}(\tau) = \frac{\left(1 - \omega_{bl} + \omega_{bl} e^{-\tau/\tau_{bl}} \right)}{1 - \omega_{bl}} \quad (3.1b)$$

$\langle N \rangle$ in equation 1 is the average number of molecules in the detection volume, the diffusional autocorrelation time, $\tau_{d,i}$ of the i -th diffusing species represents the average time it takes the molecule of a weight fraction w_i to traverse the detection volume described by the structure parameter, $S = \omega_z/\omega_{xy}$ (ratio of axial radius ω_z to the lateral radius ω_{xy} of the ellipsoid forming the detection volume). $d_{w,i}$ denotes the anomaly parameters of the diffusing components and a_0 is an offset to compensate for the nonzero baseline of the autocorrelation function arising from drifts in the fluorescence signal.

In the triplet term, G_{tr} , T denotes the equilibrium molar fraction of fluorophores in the triplet state [13,29-31] and τ_{tr} is the triplet lifetime. The “blinking term”, G_{bl} accounts for the conformational fluctuations between fluorescent and dark state formation. ω_{bl} is the fraction of fluorophores in the detection volume in the dark state and τ_{bl} is the corresponding relaxation time.

The diffusion time can be converted to a diffusion coefficient (D) using the equation:

$$D_i = \frac{\omega_{xy}^2}{4\tau_{d,i}} \quad (3.2)$$

The radii ω_{xy} and ω_z are obtained by calibrating the system with a dilute solution of a dye of known concentration and diffusion coefficient. Rh6G of molecular mass 0.479 kDa is commonly used for its small size and photostability. In such dilute solution (~10 nM), diffusion is simply Brownian and of a single component. Eqn.3.1 then simplifies to

$$G(\tau) = a_0 + \frac{1}{\langle N \rangle} \cdot G_{tr} \cdot \left(1 + \left(\frac{\tau}{\tau_d}\right)\right)^{-1} \left(1 + \frac{1}{S^2} \left(\frac{\tau}{\tau_d}\right)\right)^{-1/2} \quad (3.3)$$

The diffusion time, τ_d obtained from a Levenberg-Marquardt non-linear least-squares method fit to Eqn.3.3 and the diffusion coefficient of Rh6G ($280 \mu\text{m}^2/\text{s}$) are used in Eqn.3.2 to obtain ω_{xy} . An estimate of ω_z can then be obtained from the fit result of S or rigorously determined from measurements of a series of dilute concentrations of the dye. For a given concentration of dye, the average number of molecules in the detection volume can be expressed in terms of the dimensions of the ellipsoidal sensitive volume in the optical plane and the molar concentration c :

$$N = N_A c \pi^{3/2} \omega_{xy}^2 \omega_z \quad (3.4)$$

N_A is Avogadro's number. Thus, $\omega_{xy}^2 \omega_z$ can be derived from the slope of a plot of apparent number of particles, N against dye concentration.

FCS System Calibration

We calibrated the FCS system by evaluating the autocorrelation curves obtained for measurements on different concentrations of Rh6G solutions. Autocorrelation curves obtained at the excitation laser power of $2.88 \mu\text{W}/\mu\text{m}^2$ could be fitted well with the single component model of Eqn.3.3 producing a scatter residual plot randomly distributed about zero (Fig. 3.1 inset). This shows that the observation volume of our instrument is Gaussian in three dimensions [32] as confirmed by the absence of a strong maximum in the plot of count rate per molecule (cpm) as a function of detector pinhole diameter (Fig. 3.1) [33].

Typical calibration measurements on 20, 38, 76, 80 and 100 nM Rh6G solutions in buffer yielded an average diffusion time of $30.6 \pm 1.1 \mu\text{s}$ and the slope of the plot of apparent number of particles, N, versus dye concentration ($N/C \text{ M}^{-1}$) was 0.117 (plot not shown). Using these in Eqn.3.1 and Eqn.3.3, we calculated the radial and axial radii to be $0.185 \mu\text{m}$ and $1.02 \mu\text{m}$ respectively, resulting in a structural parameter, S of 5.53. For subsequent fittings using equations Eqn.3.1 and Eqn.3.3, S was fixed at this value. We used this to fit the autocorrelation curves we obtained from measurements on a 30 nM solution of Alexa488 in PBS to recover a diffusion coefficient of $220 \mu\text{m}^2/\text{s}$ and a triplet time of $4.2 \mu\text{s}$. The diffusion coefficient is close to $230 \mu\text{m}^2/\text{s}$ obtained by Bacia et al. for Alexa488 in water [31].

Accurate analysis of the autocorrelation curves of EGFP-tagged nuclear proteins requires knowledge of the nonfluorescent-triplet and -blinking state parameters (τ_{tr} and ω_{tr} , and τ_b and ω_b , respectively) associated with the GFP. To determine these parameters we analysed a solution of rEGFP in buffer and fitted the autocorrelation curves with Eqn.3.1 for a single component keeping the structural parameter, S fixed at the value of 5.53. For a 23 nM solution we obtained a triplet

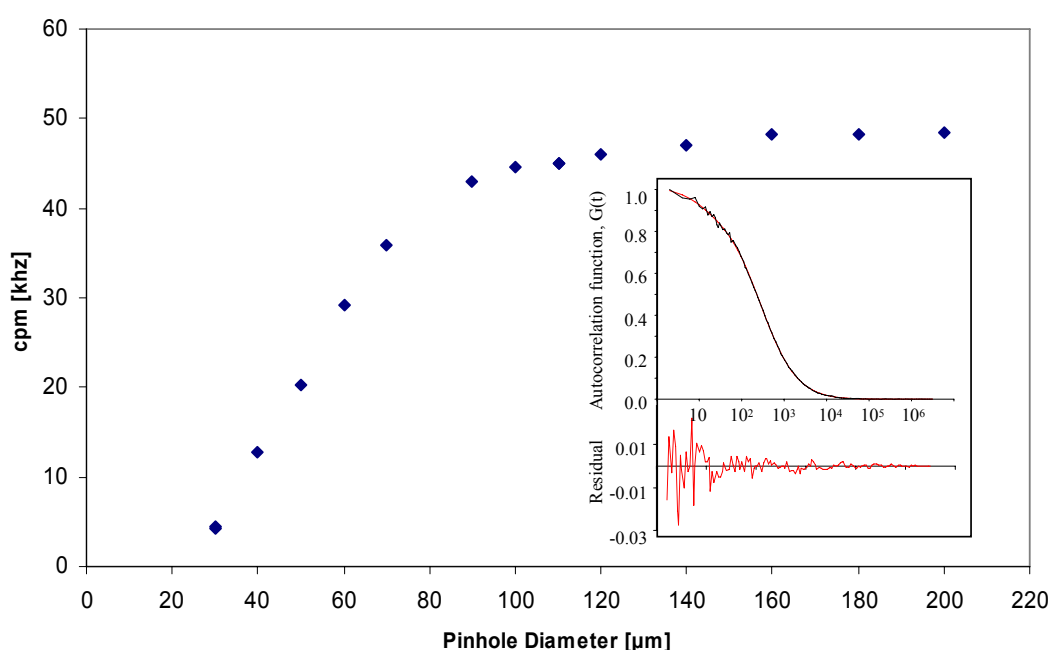


Fig. 3.1 Dependence of detector count rate (cpm) on pinhole setting. Detector count rate from a nanomolar concentration rhodamine 6G solution plotted against the pinhole diameter. Inset is the autocorrelation function (top panel) of measured FCS fluorescence of the solution at the usual pinhole setting of 70 μm. The ACF was fitted (red line) to equation 1 and the fit parameters used for calibrating the sensitive volume of the setup. Inset bottom panel is the residual of the fit.

time of 9.4 +/- 0.6 μs with a triplet fraction of 0.15 +/- 0.08 and a blinking relaxation time of 296 +/- 15 μs with a fraction of 0.12 +/- 0.4. The diffusion coefficient of 86.35

+/-3.31 $\mu\text{m}^2/\text{s}$ recovered for EGFP in buffer along with the blink parameters in the single component fit are comparable with previous results [13,29,34,35].

The blink parameters were appropriately substituted into Eqn.3.1 to fit the measured autocorrelation curves of a solution of EGFP-XPA diluted in PBS. The diffusion coefficient of 54.6 $\mu\text{m}^2/\text{s}$ obtained for the protein is in conformity with expected diffusion coefficient of a 54-kDa protein in PBS.

Fluorescence recovery after photobleaching (FRAP)

Cells for photobleaching experiments were chosen to minimize cell-to-cell nuclear size variation. Using the cropping function of the microscope cells were centred, aligned upright and focussed for an equatorial 512 x 512 pixel (38.4 μm x 38.4 μm) image of 2 μm optical slice thickness recorded at zoom 6 and pinhole setting of 160 μm . With the same settings the FRAP experiments were carried out with the use of the bleach-control macro provided with the Zeiss LSM software. The program was set to measure the average fluorescence intensity of a 10 pixel (0.7 μm) strip spanning the entire nucleus every 21 milliseconds for 4 s at a monitor laser power of 0.8%, followed by a bleach-scan of the strip at 100% laser power and then monitoring the post-bleach intensity of the strip every 21 ms for 20 to 60 s at the low laser intensity. Mean fluorescence intensities of the bleached region were corrected for background taken from non-expressing cells. FRAP data for 10 to 60 cells were averaged to obtain a mean recovery curve for each cell line.

Analysis of FRAP-data

FRAP data were analysed with a custom-written LabView program employing the nonlinear Levenberg-Marquardt algorithm for the general model accounting for both

free and anomalous (hindered) diffusion [36]. In the absence of directed transport and assuming that recovery after bleaching is solely due to a single diffusing species, the fluorescence intensity f_t at any time for a Gaussian laser beam can be approximated [36]] by the equation:

$$f_t = \frac{f_0 + f_\infty (t/t_{1/2})^\alpha}{1 + (t/t_{1/2})^\alpha} \quad (3.6)$$

where f_0 is the fluorescence intensity immediately after photobleaching, f_∞ is the maximum recovered intensity attainable after a long time, $t_{1/2}$ is the time to half of the maximum recovery (i.e. $(f_\infty + f_0)/2$), and α is the anomaly parameter [36], which in the FRAP formalism has a value of 1 for free diffusion, and smaller than 1 for hindered diffusion.

The mobile fraction (percentage recovery of fluorescence) is determined by

$$R = \frac{f_\infty - f_0}{f^0 - f_0} \quad (3.7a)$$

while the immobile fraction is given by

$$\text{Im} = \frac{f^0 - f_\infty}{f^0 - f_0} \quad (3.7b)$$

The 3-dimensional diffusion coefficient of the mobile molecules is obtained from the half-time of recovery, $t_{1/2}$ by

$$D = \frac{\gamma \omega^2}{6t_{1/2}} \quad (3.8)$$

where ω is the bleached width and γ , the bleach parameter is obtained as described by Wolf et.al [37].

However, if a fraction, q of the molecules undergoes reversible-binding events with a fast binding rate compared to the diffusion (high turn over), then the calculated effective diffusion coefficient would be reduced by a factor of $(1+q)$ [17], so that the measurable effective diffusion coefficient becomes

$$D_{eff} = D/(1+q) \quad (3.10)$$

On the other hand, if the binding and dissociation rates are slow compared to diffusion, the resulting FRAP curve is said to exhibit biphasic behaviour [17,38] (a fast diffusion phase and a slow turnover phase) and the fluorescence intensity at time, t on the recovery curve can be written as

$$f_t = \frac{k}{1+k} f_{imm} + \frac{1}{1+k} f_{free} \quad (3.11)$$

where the bound fraction, $v = k/(1+k)$ and $k = k_b/k_d$ is the ratio of the binding and dissociation rates. If the dissociation is exponential with a rate constant k_b then the concentration of released molecules diffusing in and out of the observation volume is

$$c_b = \left[v(1 - e^{-k_d t}) \frac{(t/t_{1/2})^\alpha}{1 + (t/t_{1/2})^\alpha} \right] \quad (3.12a)$$

while the concentration of freely diffusing molecules is given by

$$c_d = (1 - \nu) \frac{(t/t_{1/2})^\alpha}{1 + (t/t_{1/2})^\alpha} \quad (3.12b)$$

Thus if the fluorescence intensity increases from f_0 to f_∞ after equilibrium, then the fluorescence intensity at any time during the experiment can be written as

$$f_t = f_0 + (f_\infty - f_0) \left[(1 - \nu) \frac{(t/t_{1/2})^\alpha}{1 + (t/t_{1/2})^\alpha} + \nu(1 - e^{-k_d t}) \frac{(t/t_{1/2})^\alpha}{1 + (t/t_{1/2})^\alpha} \right]$$

or

$$f_t = f_0 + (f_\infty - f_0)(1 - \nu e^{-k_d t}) \frac{(t/t_{1/2})^\alpha}{1 + (t/t_{1/2})^\alpha} \quad (3.13)$$

Eqn.3.13 enables the estimation of important biological information such as average residence time of the bound molecules ($t_r = 1/k_d$) and the steady state proportions of bound, $\frac{k}{1+k}$ and free, $\frac{1}{1+k}$ molecules contributing to the recovery dynamics.

3.4 Results

Characterization of functionally inert EGFP-chains expressed in CHO-cells

We used fluorescence correlation spectroscopy and fluorescence recovery after photobleaching to study the mobility of EGFP and fusions of EGFP with increasing numbers of a non-fluorescent EGFP(G67V)-mutant NFP, which we termed EGFP-chains. Since the constructs have no function in the host nuclei, they make an ideal set of proteins to study the properties of the cell nucleus with respect to macromolecular mobility. Moreover they facilitate a comparison between FCS and FRAP analyses in live cells.

Table 1: Composition and molecular weights of tandem GFP constructs.

Protein	Molecular weights of constituents [kDa]				
	linker	GFP	H _A + Flag	NLS	Total
EGFP	1 x 2	1 x 26.8	1 x 4.5	0 x 3	33.3
EGFP-NFP	2 x 2	2 x 26.8	1 x 4.5	0 x 3	62.1
EGFP-NLS	1 x 2	1 x 26.8	1 x 4.5	1 x 3	36.3
EGFP-NFP-NLS	2 x 2	3 x 26.8	1 x 4.5	1 x 3	65.1
EGFP-NFP₂-NLS	3 x 2	4 x 26.8	1 x 4.5	1 x 3	93.9
EGFP-NFP₃-NLS	4 x 2	5 x 26.8	1 x 4.5	1 x 3	122.7
EGFP-NFP₄-NLS	5 x 2	6 x 26.8	1 x 4.5	1 x 3	151.5

Each construct is made up of a fluorescent EGFP (MW = 26.8 kDa) tagged to a number of non-fluorescent mutants of the protein (NFP, MW = 26.8 kDa). The fluorescent EGFP has a H_A with a flag (MW = 4.5 kDa) at one end and a linker (MW = 2kDa) through which it is fused to an NFP at the other end. Fusions of NFPs and NFP to NLS (MW = 3kDa) are also achieved by linkers.

We first characterised the integrity, expression levels and subcellular distribution of the fusion proteins by Western blotting and confocal microscopy (Fig. 3.2). We were able to fuse a maximum of four NFPs to EGFP and express the intact fusion product in CHO-cells (Fig 3.2F). As expected, EGFP (MW, 33 kDa, Table 1) and the twice as large EGFP-NFP (MW=62 kDa) were able to pass the nuclear envelope both with (Fig. 3.2 A and B) and without (Fig. 3.3 A and B) a nuclear localisation signal, although the larger construct without NLS migrated to the nucleus to a lesser extent. EGFP-NFP₂, EGFP-NFP₃, and EGFP-NFP₄ were not able to sufficiently pass the nuclear envelope. To facilitate the uptake of these into the host nuclei three tandem copies of the SV40 T-antigen nuclear localization signal (NLS) were fused to the ends of these constructs, after which efficient nuclear transport was observed (Fig. 3.2 C-E). To investigate the effect of the presence of the triple-NLS, EGFP and EGFP-NFP were also fused to the triple-NLS. All EGFP-chains carrying an NLS were stably expressed in CHO cells. The NLS-free EGFP and EGFP-NFP were investigated after transient transfection to Hep3B-cells.

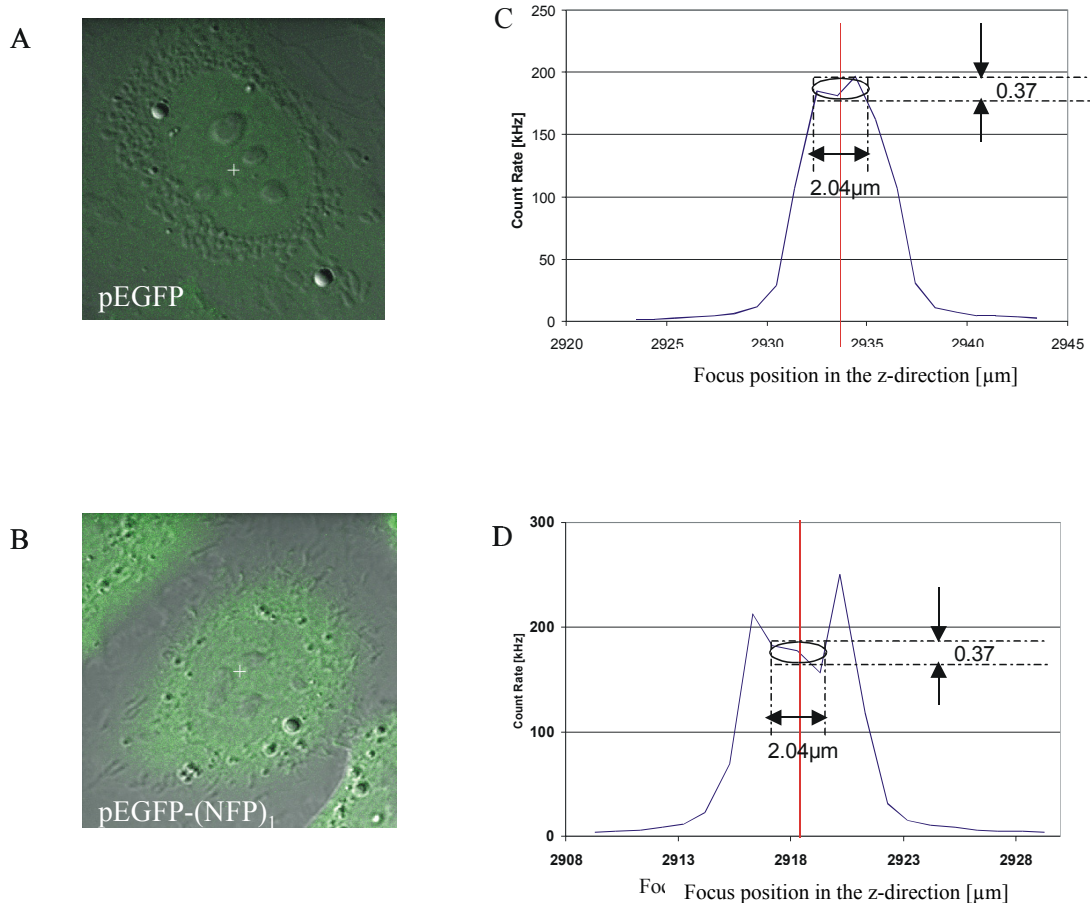


Fig. 3.2 Reduced nuclear uptakes of tandem constructs of EGFP. (A and B) Confocal optical sections of Hep3B cells expressing EGFP (A) and EGFP-NFP (B) At the marked position in the nucleus (white cross) fluorescence scans of the cells along the optical axis were made to obtain the expression levels across the compartments of a resting cell. (C and D) Fluorescence intensity profiles across the cells. Fluorescence intensities were measured at marked positions in the nucleus (crosses) of panel A (C) and panel B (E) as a function of objective position as the piezoelectric positioner moved the objective along the optical axis. Ellipses representing the sensitive volume of the setup are superimposed on the fluorescence traces for easy visualization of the FCS measuring positions. The fluorescence intensity profiles show higher fluorescence in the cytoplasm than the nucleus for the Hep3B cell expressing the larger EGFP-NFP implying better nuclear uptake of the smaller.

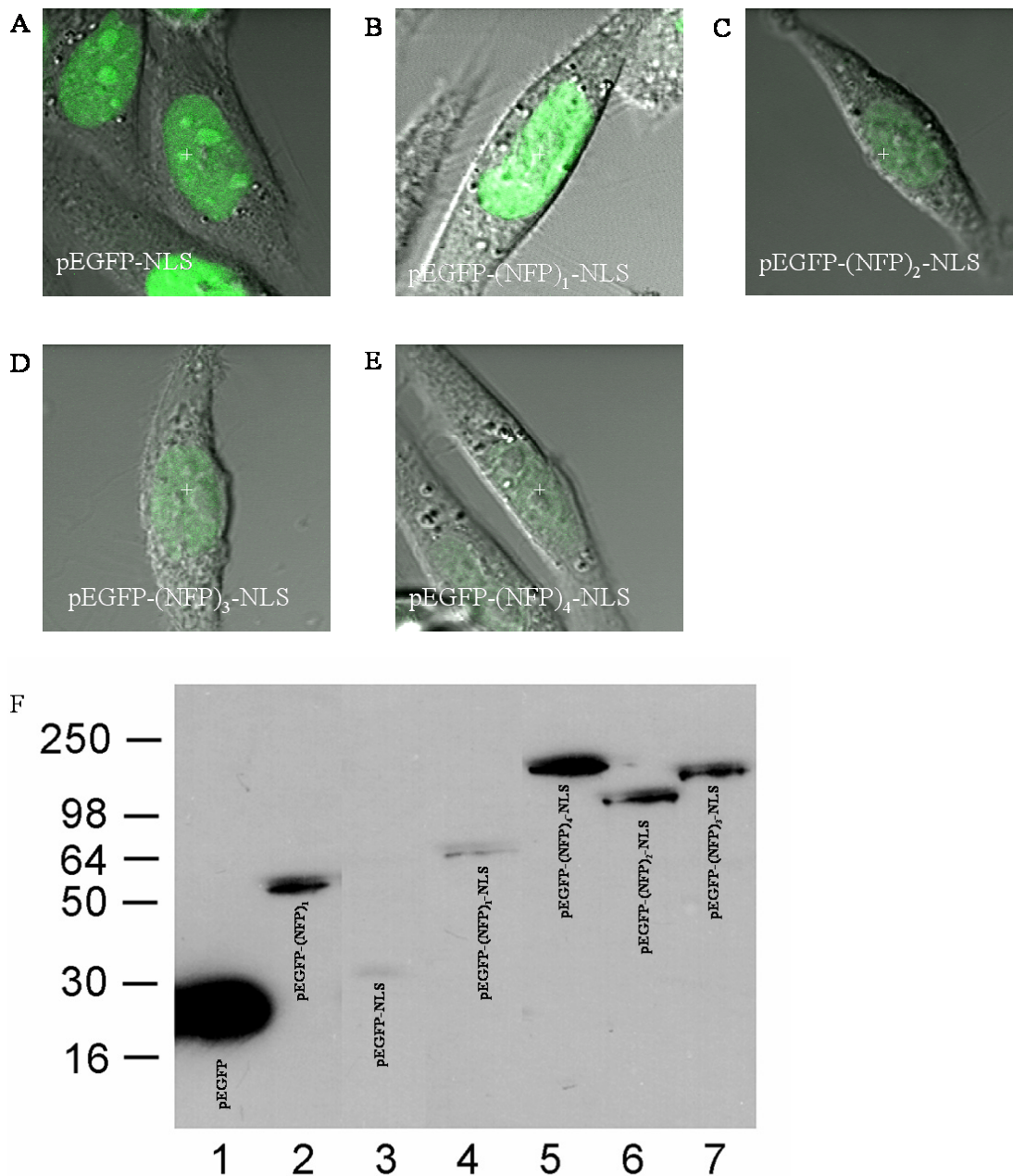


Fig. 3.3 CHO cells expressing tandem constructs of EGFP appended with NLS. Confocal optical sections of CHO cells expressing (A) EGFP-NLS, (B) EGFP-NFP-NLS, (C) EGFP-NFP₂-NLS, (D) EGFP-NFP₃-NLS, and (E) EGFP-NFP₄-NLS. The marked positions (crosses) represent the positions at which FCS measurements were carried out. (F) Stable cell lines containing EGFP-NFP_n or EGFP-NFP_n-NLS constructs express protein of the expected increasing sizes. Western blot of whole-cell extracts of Hep3B cells expressing EGFP (lane 1) or EGFP-NFP₁ (lane 2), and of CHO cells expressing EGFP-NLS (lane 3), EGFP-NFP₁-NLS (lane 4), EGFP-NFP₄-NLS (lane 5), EGFP-NFP₂-NLS (lane 6), EGFP-NFP₃-NLS (lane 7).

FCS analysis of the nuclear mobility of EGFP-chains in living CHO-cells

We then investigated the mobility of EGFP-chains in the nuclei of living cells by FCS. We avoided the nucleoli during these measurements and took care that the microscope objective was also adjusted properly in the z-direction to ensure that the focal volume of the laser was within the nucleus (Figs. 3.3 C and D). Fluorescence autocorrelation curves collected for the various EGFP-chains at the respective marked positions in Figs. 3.2 and 3.3 are shown in Fig. 3.4A. The triplet and blinking parameters established earlier for the fluorescent EGFP ($\tau_{tr} = 9.4\mu\text{s}$, $\omega_{tr} = 0.15$; $\tau_b = 286\ \mu\text{s}$ and $\omega_b = 0.12$) were used in fitting the autocorrelation curves. Interestingly, curves of the NLS-free EGFP and EGFP-NFP fitted best to a one component diffusion model (Eqn.3.1) with good residuals (Fig. 3.4A), whereas the autocorrelation curves for the NLS-appended constructs required fitting to two component model to obtain good residuals (Fig. 3.4A inset). The single EGFP protein showed the highest diffusion coefficient of $29.8 \pm 1.3\ \mu\text{m}^2/\text{s}$ (Table 2). Two- component analysis of the autocorrelation curves of EGFP-NLS suggested that a fast component of $71 \pm 17\%$ had a diffusion coefficient of $27.4 \pm 2.5\ \mu\text{m}^2/\text{s}$, similar to the NLS-free EGFP, whereas the slow component had a diffusion coefficient of $2.5 \pm 1.4\ \mu\text{m}^2/\text{s}$. EGFP-NFP, EGFP-NFP₂, EGFP-NFP₃, and EGFP-NFP₄ had increasingly slower diffusion coefficient, but a somewhat higher anomaly parameters (Table 2). This clearly shows that the size of a protein can in principle be determined from its diffusion coefficient. In addition, the slow components obtained from NLS-appended EGFP-chains were not dependent on their size, suggesting that their mobility is reduced to more or less the same extent by the NLS. This is most likely due to transient interactions of the triple-NLS used here with immobile structures in the nucleus.

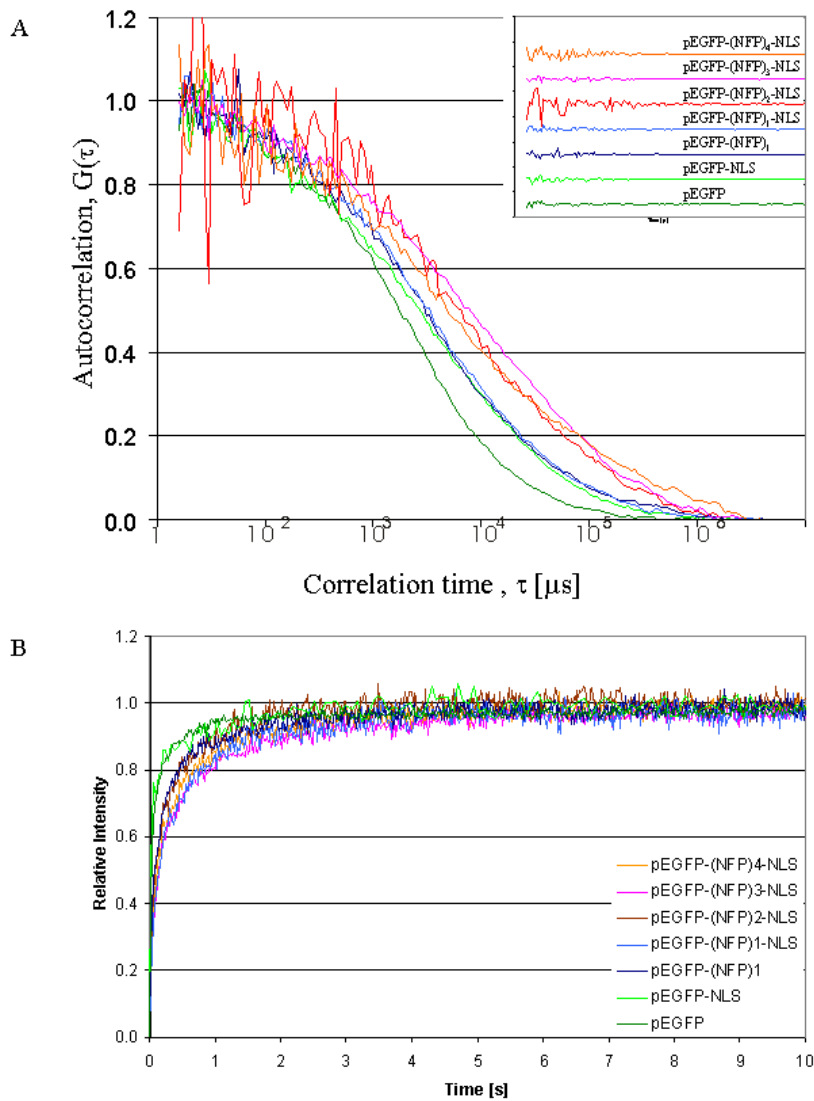


Fig. 3.4. FCS and FRAP analysis of cells expressing tandem constructs of GFP of increasing sizes. Normalized autocorrelation functions of fluorescence measured from the marked positions in Fig. 3.3 from Hep3B cells expressing EGFP (dark green), EGFP-NFP (light green), and in Fig. 3.4 from CHO cells expressing EGFP-NLS (dark blue), EGFP-NFP-NLS (light blue), EGFP-NFP₂-NLS (red), EGFP-NFP₃-NLS (purple), EGFP-NFP₄-NLS (orange). The correlation functions could be described by the anomalous diffusion model of Eqn.3.1 with corrections for EGFP blinking and triplet state. Inset panel shows the corresponding fit residuals. Inset shows the corresponding fit residuals. (B) FRAP analysis of same cell lines as used in panel A.

Table.2 FCS analysis of intranuclear mobility of EGFP-chains in living cells.

Protein	MW [kDa]	ω_1 [%]	D_1 ($\mu\text{m}^2/\text{s}$)	D_2 ($\mu\text{m}^2/\text{s}$)	dw_1	dw_2
EGFP	33.3	-	29.8 ± 1.3	-	2.2 ± 0.1	-
EGFP-NLS	36.3	71 ± 17	27.4 ± 2.5	2.5 ± 1.4	2.4 ± 0.4	1.9 ± 0.2
EGFP-NFP	62.1	-	18.6 ± 1.8	-	2.8 ± 0.3	-
EGFP-NFP-NLS	65.1	82 ± 5	17.6 ± 1.7	1.3 ± 0.5	2.6 ± 0.2	1.9 ± 0.3
EGFP-NFP₂-NLS	93.9	68 ± 14	13.0 ± 0.5	0.8 ± 0.5	2.6 ± 0.4	2.2 ± 0.2
EGFP-NFP₃-NLS	122.7	76 ± 4	11.5 ± 1.8	1.4 ± 0.6	3.1 ± 0.7	2.9 ± 1.0
EGFP-NFP₄-NLS	151.5	71 ± 8	8.7 ± 2.3	0.8 ± 0.4	2.6 ± 0.4	2.4 ± 0.3

FCS diffusion parameters are presented as mean \pm SEM. Data was obtained by fitting the autocorrelation curves obtained from FCS measurement on EGFP and EGFP-NFP expressed in Hep3B cells and constructs with NLS appendage in CHO cells to one- or two- component diffusion model of Eqn.3.1. Indexes 1 and 2 refer to the fast and slow components. D_1 and D_2 are the diffusion constants, ω_1 is the fraction of constructs associated with the fast component and dw is the anomaly parameter which in FCS formalism is 2 for Brownian diffusion

FCS analysis of the mobility of EGFP-chains in aqueous solution

To assess the effect of the nuclear environment on the mobility of the constructs, nuclear extracts were obtained of the cells expressing the various EGFP-chains, diluted 5 times and the mobility of the chains was determined by FCS. EGFP had roughly three times higher diffusion coefficient than in the living cell nucleus ($81.21 \mu\text{m}^2/\text{s}$), similar to that of the purified recombinant EGFP in aqueous solution. The diffusion coefficients obtained for increasingly long EGFP chains showed an inverse cube root dependence on their molecular weight (Fig. 3.5A). The ratio of measured intranuclear-to-invitro diffusion coefficient also showed an inverse dependence on molecular weight (Fig. 3.5B) indicating that the effect of the nuclear environment increases with size.

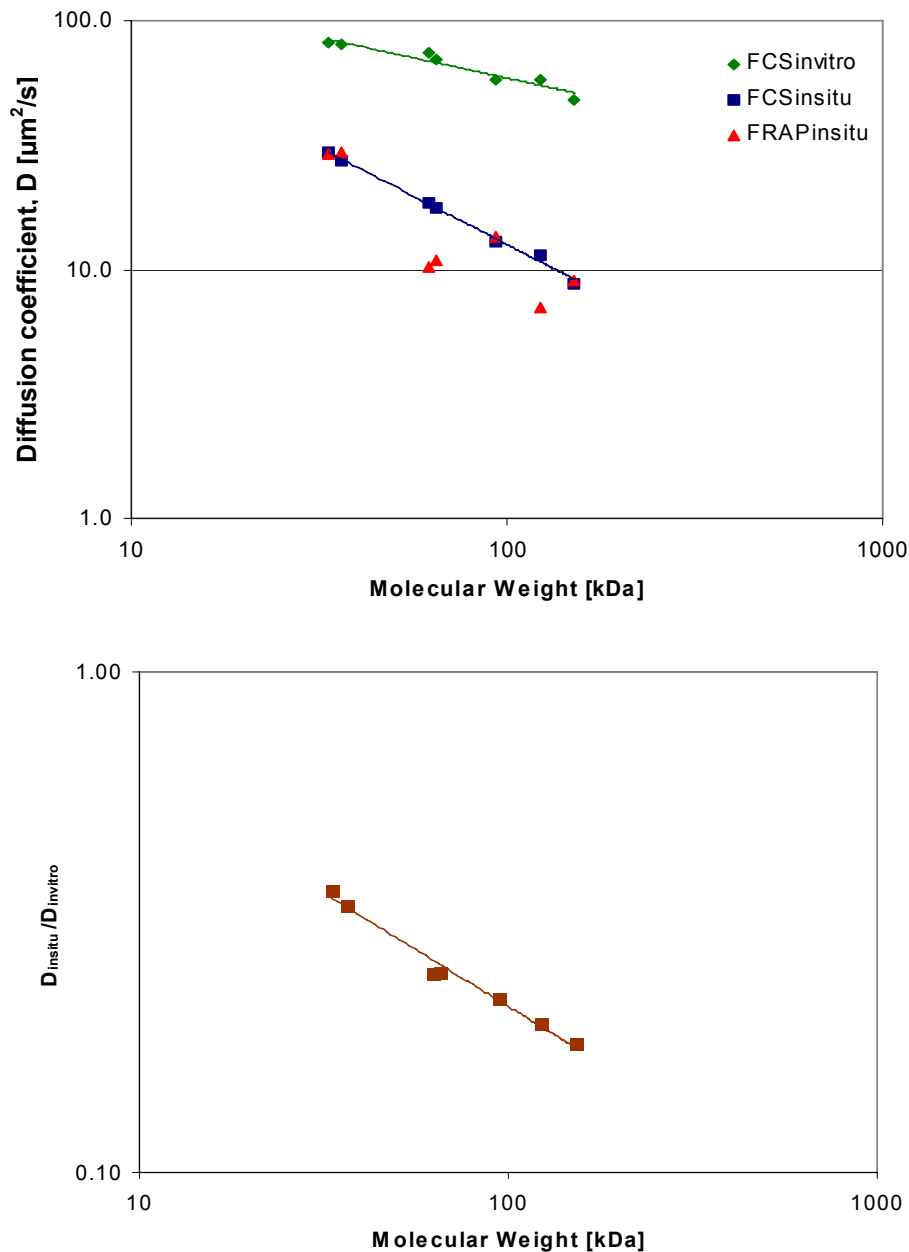


Fig. 3.5 Effect of protein molecular weight on in-vitro and intranuclear mobility of GFP constructs. (A) Diffusion coefficients of the extracts of GFP constructs in dilute solution of PBS measured by FCS (green), the fast components of intranuclear diffusion coefficients of the constructs in Hep3B and CHO cells measured by FCS (blue) and the measured intranuclear effective diffusion coefficients of the proteins measured by FRAP (red) plotted as function of the molecular weights. (B) The ratios of intranuclear to in-vitro diffusion coefficients measured by FCS plotted as function of the molecular weights.

Evaluation of the mathematical FRAP model

To enable a comparison between FCS and FRAP, the dynamics of the proteins was also studied using FRAP. Prior to the analysis of experimental data, we evaluated the accuracy of the mathematical model (Eqn.3.13) in extracting the mobility parameters from experimental FRAP-curves. We analyzed computer simulated FRAP recovery curves for different combinations of the typical FRAP mobility parameters: diffusion coefficients, immobile fractions and durations of immobilization. The Monte Carlo simulation program goes through loops representing 20 ms integration times used in the FRAP the experiments. The mobility parameters serve as the input to the program together with the laser power, the size of the cell nucleus and dimensions of the sampled region of interest. Using these inputs the program simulates the position of fluorescent molecules (about 30,000 in an ellipsoid representing a cell nucleus) relative to the position of the observation strip to mimic the measured fluorescence intensities in each loop. Good fits to the simulated curves were obtained (Fig. 3.6) and the recovered parameters agreed with the simulated values (Fig 3.7). The equation was particularly effective in evaluating the durations of immobilization.

FRAP analysis of the nuclear mobility of EGFP-chains in living CHO-cells

We performed FRAP experiments on the transfected CHO cells that were used for the FCS measurements. Fluorescence recovery curves obtained for the respective constructs are shown in Fig. 3.4B. Modelling the recovery curve obtained for EGFP and EGFP-NLS with simple Brownian recovery (Eqn.3.6) produced a poor fit at the beginning of recovery (Fig. 3.8A) but the fit was improved using the anomalous diffusion model (Fig. 3.8B, Table 3). However, the larger constructs required modifying the diffusion equation to account for transient immobilisation before good

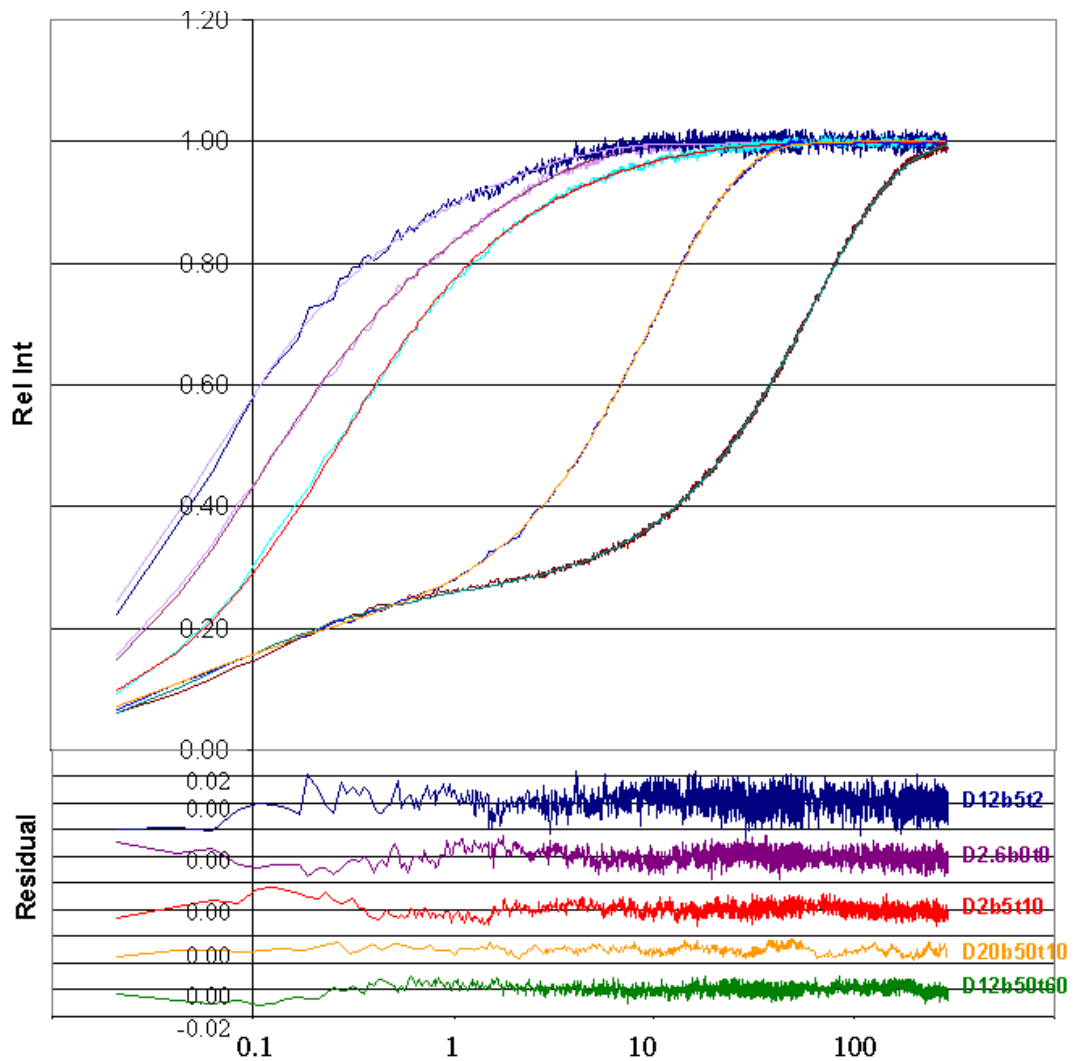


Fig. 3.6 Monte Carlo simulated FRAP curves for free diffusion and free diffusion with immobilized fraction. (A) Monte Carlo simulated FRAP curves for a free diffusion with diffusion coefficient D of $2.6 \mu\text{m}^2/\text{s}$ with no binding (D2.6b0t0); D of $2.06 \mu\text{m}^2/\text{s}$, 5% bound fraction and residence time of 10 s (D2b5t10); D of $12.0 \mu\text{m}^2/\text{s}$, 5% bound fraction and residence time of 2 s (D12b5t2); D of $20.0 \mu\text{m}^2/\text{s}$, 50% bound fraction and residence time of 10 s (D20b50t10); and D of $12.0 \mu\text{m}^2/\text{s}$, 50% bound fraction and residence time of 60 s (D12b50t60) were fitted (smooth curves) nonlinearly using Eqn.3.13 with $\alpha = 1$. The panel at the bottom shows the corresponding residuals of the fits.

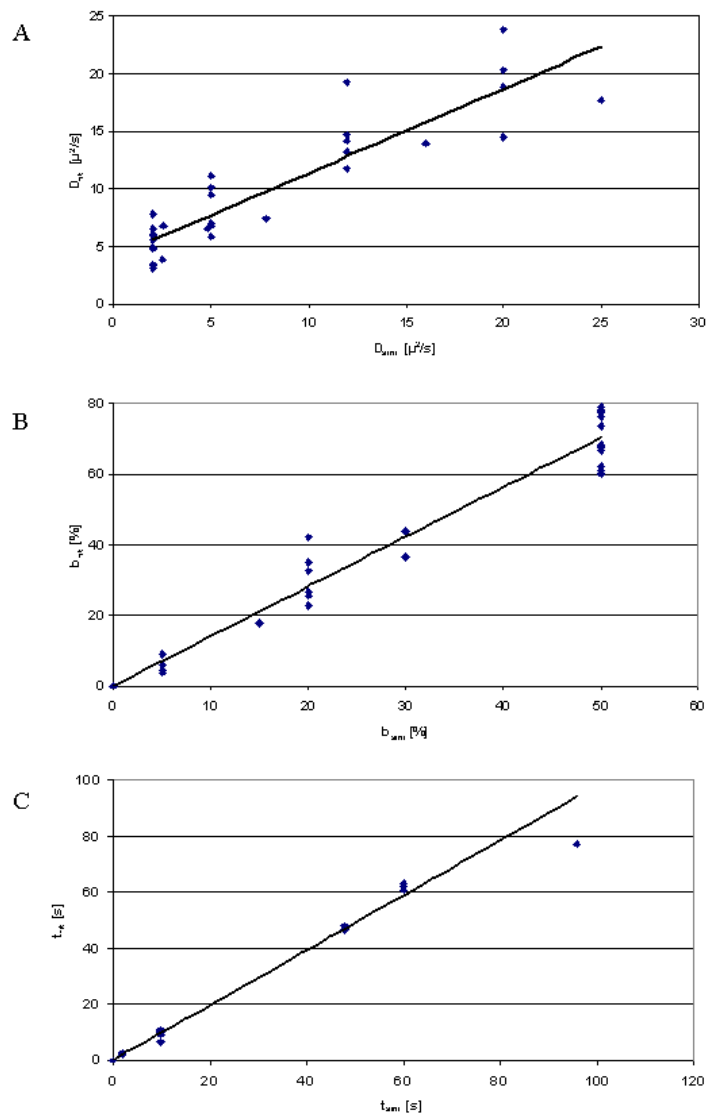


Fig. 3.7 Accuracy of recovered binding parameters from nonlinear fits of simulated Monte Carlo FRAP curves. (A-C) Plots of recovered (fit) versus simulated (sim) parameters for (A) diffusion coefficients (D vs D), (B) bound fractions (b_f vs b) and residence times (t vs t_{sim}).

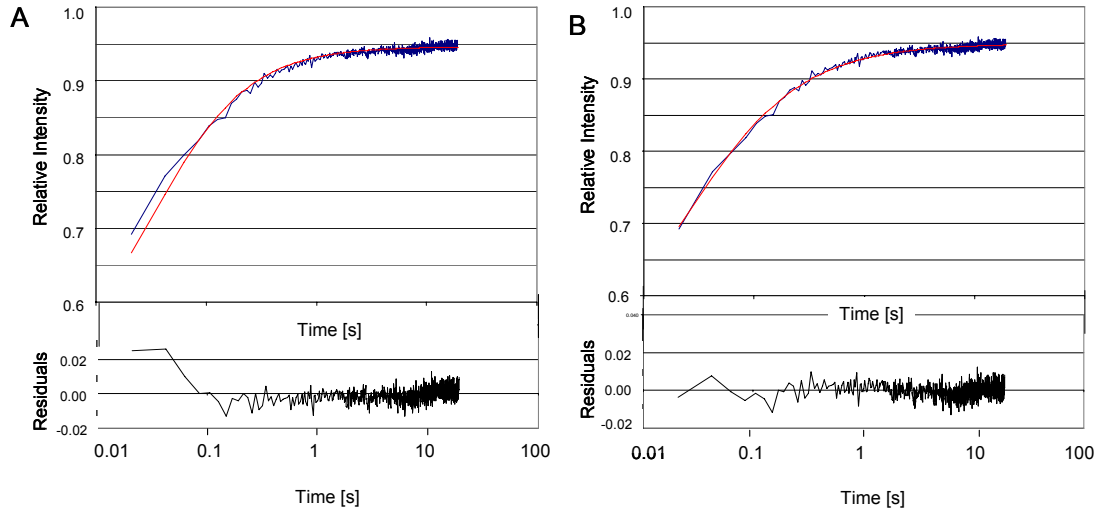


Fig. 3.8 Goodness of fit in mathematical modeling of FRAP recovery curves. (A) Fitting the recovery curve obtained for EGFP expressed in Hep3B to a simple Brownian model resulted in a poor fit, especially at the beginning of the recovery curve (bottom). (B) The diffusion of EGFP could be described well by the anomalous diffusion model.

fits to the recovery kinetics could be obtained (Table 3). The recovery curves did not show large variations in the anomaly parameter, with EGFP-NFP₁ deviating the most from simple Brownian diffusion, and EGFP-NLS and EGFP-NFP₂-NLS showing the least anomaly (α closest to 1). The effective diffusion coefficients measured for EGFP, EGFP-NLS, EGFP-NFP₂-NLS and EGFP-NFP₄-NLS (29.2 ± 1.6 , 29.6 ± 5.1 , 13.5 ± 1.7 and $9.0 \pm 1.7 \mu\text{m}^2/\text{s}$ respectively) agree with values obtained from FCS (Fig 3.5) but the apparent diffusion coefficients extracted for EGFP-NFP₁, EGFP-NFP₁-NLS and EGFP-NFP₃-NLS (10.2 ± 0.8 , 10.9 ± 0.7 , and $7.0 \pm 0.4 \mu\text{m}^2/\text{s}$ respectively) are slower than the fast components measured by FCS for these proteins. This indicates that the constructs with an even number of protein units experience some transient obstruction that slows down their apparent diffusion rates. Using Eqn.3.10 and assuming that diffusion coefficients obtained from FCS represent the intranuclear diffusion rates of the proteins, we deduced that in addition to the one-second-duration

restriction to mobility experienced by a subpopulation (10, 19 and 14 % for EGFP-NFP₁, EGFP-NFP₁-NLS and EGFP-NFP₃-NLS respectively) of these proteins, a further 74, 50 and 55 percent of the proteins, respectively, experience brief obstructions to their movements.

Table.3 FRAP analysis of intranuclear mobility of EGFP-chains in living cells.

Protein	MW [kDa]	α	D_{eff} ($\mu\text{m}^2/\text{s}$)	Bound [%]	Residence time [s]
EGFP	33.3	0.97 \pm0.04	29.2 \pm1.6	-	-
EGFP-NLS	36.3	0.98 \pm0.15	29.6 \pm 5.1	-	-
EGFP-NFP₁	62.1	0.90 \pm0.03	10.2 \pm 0.8	10 \pm 2	1.1 \pm 0.1
EGFP-NFP₁-NLS	65.1	0.97 \pm0.04	10.9 \pm .70	19 \pm 1	1.2 \pm 01
EGFP-NFP₂-NLS	93.9	0.98 \pm0.09	13.5 \pm 1.7	25 \pm 3	0.8 \pm 0.1
EGFP-NFP₃-NLS	122.7	0.96 \pm0.19	7.0 \pm 0.4	14 \pm 8	2.1 \pm 0.5
EGFP-NFP₄-NLS	151.5	0.97 \pm0.04	9.0 \pm 2.3	19 \pm 2	1.3 \pm 0.1

The FRAP diffusion parameters are presented as mean \pm SEM. Data was obtained by fitting the recovery curves obtained from FRAP measurement on EGFP and EGFP-NFP expressed in Hep3B cells and constructs with NLS appendage in CHO cells to anomalous diffusion model of Eqn.3.6 (for the smallest constructs i.e. EGFP and EGFP-NLS) or the anomalous diffusion model corrected for binding (in the case of the larger constructs. D_{ef} is the apparent diffusion coefficient extracted from the recovery curve, α is the anomaly parameter which in FRAP formalism is 1 for Brownian diffusion.

FCS and FRAP analysis of androgen receptor mobility in living Hep3B-cells

We then combined the FRAP and FCS methods to study the dynamics of androgen receptors (AR) in Hep3B cells. Two Hep3B cell lines stably expressing either the GFP-tagged wild-type AR (AR-A) or the GFP-tagged non-DNA-binding mutant (AR-D) were investigated. AR-D has a mutation in the DNA binding domain (DBD). The autocorrelation curves obtained by FCS measurements proteins are shown in Fig. 3.9A. The autocorrelation curves obtained for Hep3B cells expressing GFP-tagged wild-type AR showed a longer tail than those expressing the mutant

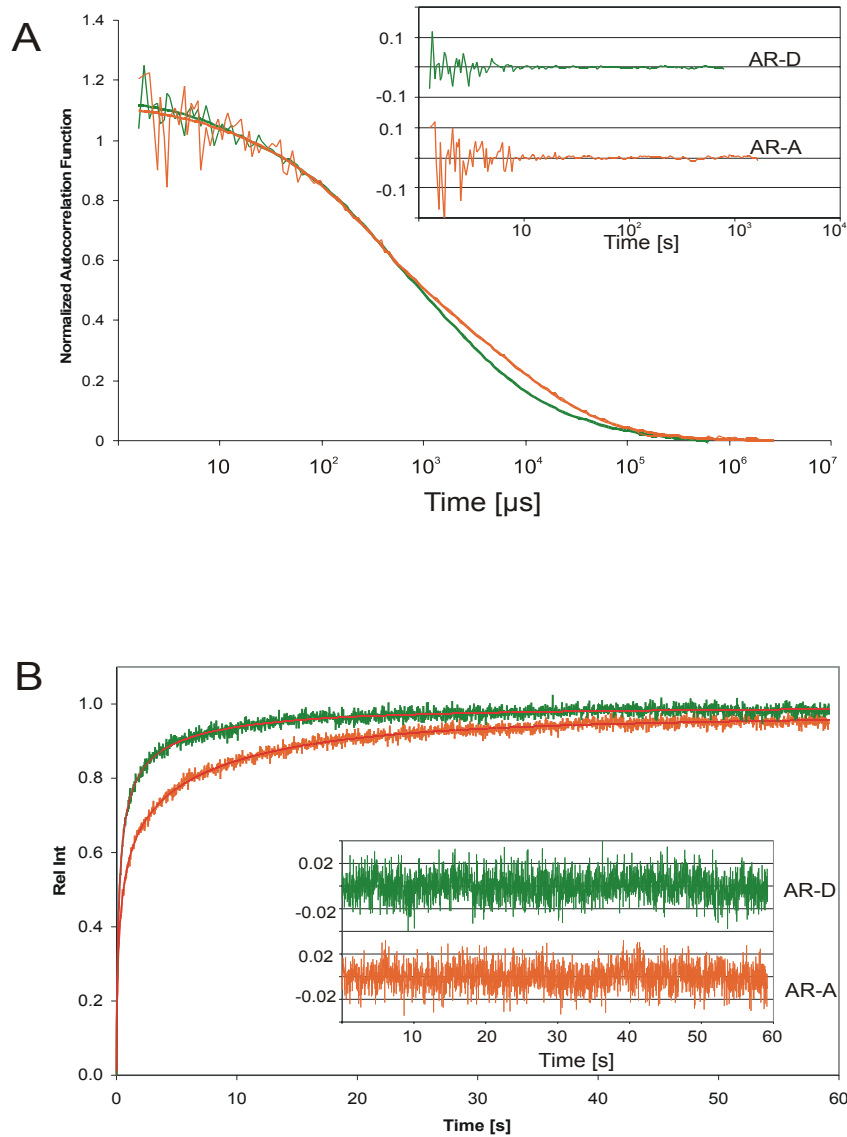


Fig. 3.9 Complementary use of FCS and FRAP reveal a bound fraction of agonistic liganded GFP-ARs in Hep3B cells. (A) Autocorrelation functions measured from Hep3B cells expressing wild-type AR (AR-A; orange) and those expressing the non-DNA-binding mutant AR (AR-D; green). The autocorrelation function from the mutant fitted well to a one component model (Eqn.3.1) whereas the wild type data could only be fitted to two components (materials and methods: Eqn.3.1). (B) FRAP analysis of the same cell lines as in A. The FRAP curve for the mutant, AR-D (green) fitted well to the one component anomalous diffusion model of Eqn.3.6 but the curve from the wild type-expressing cell line could only be fitted by immobilization coupled with anomalous diffusion model of Eqn.3.13 indicating that a fraction of the wild type AR is transiently bound (corresponding residuals are shown in the inset).

form. This is either due to multiple diffusing species or transient binding. The diffusion coefficient ($7.8 \pm 1.2 \mu\text{m}^2/\text{s}$) obtained by fitting the autocorrelation curves from the mutant AR-D with a one component model (Eqn.3.1) and the fast component of diffusion ($7.7 \pm 1.3 \mu\text{m}^2/\text{s}$) evaluated from fitting the autocorrelation curves from the wild-type AR-A to two components (Eqn.3.1) agree with the diffusion coefficient obtained for EGFP-NFP₄ ($8.7 \pm 2.3 \mu\text{m}^2/\text{s}$). The diffusion coefficient obtained for the 28 % slow component of the wild type AR-A is $0.5 \mu\text{m}^2/\text{s}$, less than one-tenth the value for the faster component. This indicates that the second component is due to transient immobilization of ARs as a result of binding events.

FRAP experiments were then conducted on both cell lines and the recovery curves evaluated by modeling them to the anomalous diffusion equations Eqn.3.6 and Eqn.3.13. Eqn.3.6 was sufficient to model the recovery curve obtained for AR-D and no improvement in the residual was observed by fitting the curve to Eqn.3.13. On the other hand recovery curves from cells expressing AR-A could only be satisfactorily modeled using Eqn.3.13, using the anomalous diffusion model corrected for binding activities (Fig. 3.9B).

3.5 Discussion

We have, in this work demonstrated the complementary of FCS and FRAP in the measurement of protein dynamics in the living cell. As model systems we used functionally inert tandem constructs of the GFP and the biologically active AR. The results presented have shown that a well calibrated FCS system with its sub-femtoliter observation volume is well suited to accurate determination of protein mobility in living cells, and that the minute differences in diffusion rate of the increasingly large EGFP-chains are distinguishable both with FCS as well as with FRAP measurements.

We also showed that quantitative measurement of long range immobilisation events, to which FCS is essentially blind, is well possible using complementary FRAP experiments.

The mobility of the inert EGFP-chains we investigated showed an inverse cube-root dependency on molecular weight. We also found that the nucleoplasm is three times more viscous than water as revealed by the difference between the diffusion coefficients measured in aqueous solution and those measured in the nucleus of living cells. However, the effect of nuclear architecture and collisions with other macromolecules shifts the size dependence of mobility as large molecules may undergo more interactions than smaller ones. The shape of a protein also affects its mobility as the conformation of a protein affects the frequency of its interaction with other nuclear structures. The anomaly parameters measured for the even-numbered GFPs are higher especially when the model with one diffusing component respective autocorrelation curves were modelled with one diffusing component is used. The fusion of a nuclear localisation signal to the EGFP constructs complicated their dynamics in the nucleus. The NLS probably binds frequently to and is released from immobile structures leading to a second component in FCS curves and resulting in slower effective diffusion in FRAP. This is revealed in FCS measurements as the autocorrelation curves measured for NLS-appended GFPs required fitting to two components for a good fit. When longer duration binding occurs as in the case of androgen receptors, bleaching of the immobile fraction complicates the autocorrelation curve, thus prebleaching of the immobile fraction is recommended before measurement.

The analytical method described here for FRAP is a combination of known methods; the mathematical analytical approach described is a combination of the

approach described in Feder et al. [36] to evaluate diffusion and the approaches of Carrero et al. [17,38,39] and Sprague et al [16,40] to evaluate binding. It was tested on simulated FRAP curves and worked quite well. The advantage is that it is quite simple. The drawback of this and any other analytical methods is that experimental results not only depend on molecular mobility, but also on the shape and size of the photobleached volume which is hard to model analytically. Using Monte-Carlo simulations could circumvent the problem but are rather time consuming. For FCS this is not the case, the shape and size of the small confocal volume are easily determined.

In summary, FCS provides a sensitive method for diffusion measurements although in live cells it is difficult to apply. Not only finding the appropriate place to measure, but also the mobility of the cell challenges its application. Binding of the diffusing species can also present a problem for evaluation. Complementary FRAP experiments can be used to extract these binding times. In addition, photobleaching of molecules with little or no mobility are of special concern. In order to avoid contributions of photobleaching to the autocorrelation function, the immobile and slowly moving fluorophores may be photodegraded by illumination prior to the measurement. However, in that case only the more mobile fraction of molecules can be analysed by FCS. Therefore, combining FCS and FRAP experiments seems to be the optimal approach for studying protein mobility in living cells.

References

1. Houtsmuller AB, Rademakers S, Nigg AL, Hoogstraten D, Hoeijmakers JH, Vermeulen W. (1999) Action of DNA repair endonuclease ERCC1/XPF in living cells. *Science*;284:958-61.
2. Hoogstraten D, Nigg AL, Heath H, Mullenders LH, van Driel R, Hoeijmakers JH, Vermeulen W, Houtsmuller AB. (2002) Rapid switching of TFIIH

- between RNA polymerase I and II transcription and DNA repair in vivo. *Mol Cell*;10:1163-74.
3. Rademakers S, Volker M, Hoogstraten D, Nigg AL, Mone MJ, van Zeeland AA, Hoeijmakers JHJ, Houtsmuller AB, Vermeulen W. (2003) Xeroderma Pigmentosum Group A Protein Loads as a Separate Factor onto DNA Lesions. *Mol. Cell. Biol.*;23:5755-5767.
 4. Phair RD, Misteli T. (2000) High mobility of proteins in the mammalian cell nucleus. *Nature*; 404:604-9.
 5. Huang S, Deerinck TJ, Ellisman MH, Spector DL. (1998) The Perinucleolar Compartment and Transcription. *J. Cell Biol.*; 143:35-47.
 6. Snaar S, Wiesmeijer K, Jochemsen AG, Tanke HJ, Dirks RW. (2000) Mutational Analysis of Fibrillarin and Its Mobility in Living Human Cells. *J. Cell Biol.*;151:653-662.
 7. Pederson T. (2000) Diffusional protein transport within the nucleus: a message in the medium.2:E73-E74.
 8. Shopland LS, Lawrence JB. (2000) Seeking Common Ground in Nuclear Complexity.150.1.F1. *J. Cell Biol.*;150:1F-4.
 9. Misteli T. (2001) Protein dynamics: implications for nuclear architecture and gene expression. *Science*;291:843-7.
 10. Axelrod D, Koppel DE, Schlessinger J, Elson E, Webb WW. (1976) Mobility measurement by analysis of fluorescence photobleaching recovery kinetics. *Biophys J*;16:1055-69.
 11. Lippincott-Schwartz J, Snapp E, Kenworthy A. (2001) Studying protein dynamics in living cells. *Nat Rev Mol Cell Biol*;2:444-56.
 12. Verkman AS. (2002) Solute and macromolecule diffusion in cellular aqueous compartments. *Trends Biochem Sci*;27:27-33.
 13. Schwille P, Haupts U, Maiti S, Webb WW. (1999) Molecular dynamics in living cells observed by fluorescence correlation spectroscopy with one- and two-photon excitation. *Biophys J*;77:2251-65.

14. Wachsmuth M, Weidemann T, Muller G, Hoffmann-Rohrer UW, Knoch TA, Waldeck W, Langowski J. (2003) Analyzing Intracellular Binding and Diffusion with Continuous Fluorescence Photobleaching. *Biophys. J.*;84:3353-3363.
15. Webb W. (2001) Fluorescence Correlation Spectroscopy: Inception, Biophysical Experimentations, and Prospectus. *Appl. Opt.*;40:3969-3983.
16. Sprague BL, Pego RL, Stavreva DA, McNally JG. (2004) Analysis of Binding Reactions by Fluorescence Recovery after Photobleaching. *Biophys. J.*;86:3473-3495.
17. Carrero G, Crawford E, Hendzel MJ, de Vries G. (2004) Characterizing fluorescence recovery curves for nuclear proteins undergoing binding events. *Bull Math Biol*;66:1515-45.
18. Houtsmuller AB, Vermeulen W. (2001) Macromolecular dynamics in living cell nuclei revealed by fluorescence redistribution after photobleaching. *Histochem Cell Biol*;115:13-21.
19. White J, Stelzer E. (1999) Photobleaching GFP reveals protein dynamics inside live cells. *Trends in Cell Biology*;9:61-65.
20. Klonis N, Rug M, Harper I, Wickham M, Cowman A, Tilley L. (2002) Fluorescence photobleaching analysis for the study of cellular dynamics. *Eur Biophys J*;31:36-51.
21. Houtsmuller AB. *Fluorescence Recovery after Photobleaching: Application to Nuclear Proteins*. Berlin / Heidelberg: Springer; 2005. 177-199 p.
22. Segers-Nolten GMJ, Wyman C, Wijgers N, Vermeulen W, Lenferink ATM, Hoeijmakers JHJ, Greve J, Otto C. (2002) Scanning confocal fluorescence microscopy for single molecule analysis of nucleotide excision repair complexes. *Nucl. Acids Res.*;30:4720-4727.
23. Cubitt AB, Heim R, Adams SR, Boyd AE, Gross LA, Tsien RY. (1995) Understanding, improving and using green fluorescent proteins. *Trends in Biochemical Sciences*;20:448-455.
24. Farla P, Hersmus R, Geverts B, Mari PO, Nigg AL, Dubbink HJ, Trapman J, Houtsmuller AB. (2004) The androgen receptor ligand-binding domain

- stabilizes DNA binding in living cells. *Journal of Structural Biology: Recent Advances in Light Microscopy*;147:50-61.
25. Brock R, Jovin TM. (1998) Fluorescence correlation microscopy (FCM)-fluorescence correlation spectroscopy (FCS) taken into the cell. *Cell Mol Biol (Noisy-le-grand)*;44:847-56.
 26. Brock R, Vamosi G, Vereb G, Jovin TM. (1999) Rapid characterization of green fluorescent protein fusion proteins on the molecular and cellular level by fluorescence correlation microscopy. *PNAS*;96:10123-10128.
 27. Schwille P, Korch J, Webb WW. (1999) Fluorescence correlation spectroscopy with single-molecule sensitivity on cell and model membranes. *Cytometry*;36:176-82.
 28. Gennerich A, Schild D. (2000) Fluorescence correlation spectroscopy in small cytosolic compartments depends critically on the diffusion model used. *Biophys J*;79:3294-306.
 29. Wachsmuth M, Waldeck W, Langowski J. (2000) Anomalous diffusion of fluorescent probes inside living cell nuclei investigated by spatially-resolved fluorescence correlation spectroscopy. *J Mol Biol*;298:677-89.
 30. Widengren J, Mets Ü, Rigler R. (1995) Fluorescence correlation spectroscopy of triplet states in solution: A theoretical and experimental study. *J. Phys. Chem.*;99:13368-13379.
 31. Bacia K, Schwille P. (2003) A dynamic view of cellular processes by in vivo fluorescence auto- and cross-correlation spectroscopy. *Methods*;29:74-85.
 32. Hess ST, Sheets ED, Wagenknecht-Wiesner A, Heikal AA. (2003) Quantitative Analysis of the Fluorescence Properties of Intrinsically Fluorescent Proteins in Living Cells. *Biophys. J.*;85:2566-2580.
 33. Krouglova T, Vercammen J, Engelborghs Y. (2004) Correct Diffusion Coefficients of Proteins in Fluorescence Correlation Spectroscopy. Application to Tubulin Oligomers Induced by Mg²⁺ and Paclitaxel. *Biophys. J.*; 87:2635-2646.

34. Rusu L, Gambhir A, McLaughlin S, Radler J. (2004) Fluorescence Correlation Spectroscopy Studies of Peptide and Protein Binding to Phospholipid Vesicles. *Biophys. J.*;87:1044-1053.
35. Hess ST, Webb WW. (2002) Focal Volume Optics and Experimental Artifacts in Confocal Fluorescence Correlation Spectroscopy. *Biophys. J.*;83:2300-2317.
36. Feder TJ, Brust-Mascher I, Slattery JP, Baird B, Webb WW. (1996) Constrained diffusion or immobile fraction on cell surfaces: a new interpretation. *Biophys J*;70:2767-73.
37. Wolf DE, Edidin M. Methods of measuring diffusion and mobility of molecules in surface membranes. In: Baker P, editor. *Techniques in Cellular Physiology*. Volume 1. Amsterdam: Elsevier/North Holland Biomedical Press; 1981. p 1-14.
38. Carrero G, McDonald D, Crawford E, de Vries G, Hendzel MJ. (2003) Using FRAP and mathematical modeling to determine the in vivo kinetics of nuclear proteins. *Methods*;29:14-28.
39. Carrero G, Crawford E, Th'ng J, de Vries G, Hendzel MJ. (2004) Quantification of protein-protein and protein-DNA interactions in vivo, using fluorescence recovery after photobleaching. *Methods Enzymol*; 375:415-42.
40. Sprague BL, McNally JG. (2005) FRAP analysis of binding: proper and fitting. *Trends in Cell Biology*; 15:84-91.

Chapter

4

In the absence of DNA damage the nuclear mobility of most nucleotide excision factors is mainly determined by their molecular size

Angelika Zotter, Shehu M. Ibrahim, P.O. Mari, Bart Geverts,

Jan H. J. Hoeijmakers, Wim Vermeulen

and Adriaan B. Houtsmuller

4.1. Abstract

Many crucial cellular reactions take place within the cell nucleus. To facilitate these reactions, the cell often employs complex assemblies of proteins to interact with DNA, which in most cases, is packed into chromatin. The sites of protein action are often randomly dispersed throughout the nucleus, specifically in the case of DNA damage. Considering the crowded nuclear environment, it is still not completely understood how chromatin-transacting proteins move through the nucleus, assemble into functional complexes and onto DNA, and act synchronically at their respective sites of need. To study the movement of functional nuclear proteins in the living cell, we employed the well-characterized multi-subunit nucleotide excision repair (NER) machinery as a paradigm. Systematic comparison of mobility parameters of diverse functional, physiologically expressed GFP-tagged NER subunits in the absence of induced DNA damage revealed that the mobility of each factor is mainly determined by its molecular size. Only the 10 subunit TFIIH complex, which has an additional function in transcription initiation, and the primary NER damage sensor XPC, showed significant retention indicative of biological action also in the absence of NER-inducing DNA damage.

4.2. Introduction

Understanding complex cellular processes requiring the assembly of multiple proteins is of fundamental importance in biological research. How these multiple components reach their respective targets in an ordered and timely fashion is a matter of debate and has led to controversies in models describing these processes [1]. Particularly, nuclear DNA transacting processes are thought to be restricted by space occupancy in the nucleoplasm due to molecular crowding.

It has been hypothesized that nuclear factors reside in pre-assembled holo-complexes or modules to facilitate their timely assembly when required at sites of action. Some nuclear proteins and RNAs have also been shown to accumulate consistently in distinct nuclear compartments believed to be specialized centers for DNA replication [2], transcription [3-5], RNA processing [6,7], or ribosome biogenesis [8] (reviewed in [9]). The purpose of such distinct nuclear assemblies could be to enable resident enzymes to carry out their vital functions (e.g. replication) in a concerted manner. However, the association of nuclear factors with these structures has been shown to be far from static, in fact they generally seem to be highly dynamic [10-13]. Whether these “nuclear factories” themselves are kept in place via attachment to a nuclear matrix is still a matter of controversy [14-16] (reviewed in [16-19]; [20]).

Similarly, the manner of subnuclear translocation in order to assemble at such structures, or other sites of action, is still under debate. Studies on numerous nuclear bodies such as RNP particles, and chromosome fibers have shown that the movement of some nuclear solutes is largely diffusion-based but in some cases rely on energy-dependent processes [21] (reviewed in [22]). Many nuclear proteins observed, though showing random movement independent of ATP-based energy, still exhibit substantially slower mobility than inert solutes like GFP [23]. Therefore, it has been suggested that

nuclear protein mobility is mainly determined by stop-and-go binding events [23]. Likewise, the impact of chromatin structure on protein mobility, especially a “sieving effect” for larger nuclear solutes, is still under debate ([24,25]; reviewed in [26]).

To explore the nature of nuclear protein mobility, we chose the nucleotide excision repair (NER) complex as a model system. NER is a highly conserved multi-step and multi-subunit DNA repair pathway, specialized in the removal of UV-induced DNA damage. The NER pathway has been extensively studied *in vitro*, resulting in a detailed model for its core reaction (reviewed in [27-30]). To clarify the *in vivo* functioning and organization of the NER machinery, several subunits of the NER complex have been tagged with GFP in our lab, and have been introduced into corresponding NER defective mutant cell lines. Their functionality was tested by their capability to restore UV resistance to the respective complemented cell lines, and cells were selected for expression at physiological levels. Within this background, DNA repair factors have been shown to move throughout the nucleus as distinct proteins or smaller multimeric subunits of a complex, and to assemble step by step at their active sites as individual factors that transiently interact only at DNA damage sites [12,31-34]. But in what manner do NER proteins move about to efficiently find their target regions, and assemble as complexes at DNA damage sites in the living cell?

In order to find out what factors determine their mobility within the nucleus, we compared the mobility of different NER proteins in cells that were not subjected to UV irradiation. In these cells, DNA damage was minimal, and therefore also the activity of the NER enzymes we investigated. Using confocal photobleaching techniques in cells stably expressing GFP-tagged NER proteins at physiologically relevant concentrations, combined with mathematical fitting methods, we attempted to reconstruct the nuclear dynamics of functional nuclear proteins in a state of inactivity. As an additional control

and comparison, we included in our measurements exogenous proteins of comparable size, but with no defined cellular function.

4.3. Results

Distribution of NER factors within the cell

All GFP-tagged NER factors were stably expressed in mammalian cells carrying inactivating mutations in their respective NER gene. Cell populations with physiological expression levels of the fusion protein were selected. In addition, fusion proteins were tested for their biological activity before being used in our protein dynamics studies. The GFP-tagged NER factors ERCC1 and XPA used in these experiments were predominantly localized in the nuclei of mammalian cells, as described before [31,32]. Also XPG-GFP is homogeneously distributed throughout nuclear space with reduced fluorescent signal within the nucleoli, both when expressed in CHO cells as well as SV40-immortalized human fibroblasts [35]. XPB-GFP in transcriptionally active cells showed additional accumulation in nucleoli [12], next to an overall homogeneous nuclear distribution. XPC-GFP showed an inhomogeneous nuclear distribution that largely mimicked the non-uniform distribution of genomic DNA or chromatin in interphase mammalian nuclei [36]. As a control for nuclear protein dynamics measurements, we used free EGFP and the hybrid molecule EGFP-NFP. NFP (non-fluorescent protein), is an EGFP variant in which the fluorophore has been made non-fluorescent by a single mutation (S65V; see materials and methods).

Nuclear mobility of GFP-tagged NER factors.

In previous experiments [12,31,32,36], we have determined the mobilities of a number of different GFP-tagged NER factors by using various FRAP techniques. The corresponding

measurements were performed over a period spanning several years, in which experimental conditions, such as microscopic settings and laser intensities, as well as the type of microscope used, varied. This hampered proper comparison of mobility parameters of the different GFP-tagged NER factors. To systematically determine mobilities of distinct nuclear proteins and comprehensively analyze the factors that influence their differential mobility, we used a FRAP procedure optimized to accurately visualize diffusion of small proteins within the nucleus of living cells (Materials and Methods). Importantly, the monitoring laser power was chosen sufficiently low as to avoid significant bleaching due to monitoring. This important improvement has been made possible by the higher sensitivity of modern detectors.

To assess the mobility of GFP-tagged NER proteins in the absence of UV-induced DNA damage, we examined untreated mammalian cells at physiological temperature (37°C). Using the same microscope and laser settings, we directly compared the mobility of the following GFP-tagged NER proteins (see also Table 1): the relatively small lesion verification factor XPA (58kDa); the 3'-endonuclease XPG (161kDa); the 5'-endonuclease ERCC1 (as part of a stable dimer with XPF, 163kDa); the damage sensor XPC (as a heterotrimeric complex of XPC, hHR23B and CEN2, about 229 kDa); and the helicase XPB (as integral part of the ten-subunit TFIIH complex, 480-510 kDa).

In direct comparison (Fig. 4.1A), XPG-EGFP (161kDa) showed a slightly but significantly slower redistribution after photobleaching than EGFP-XPA (58 kDa). In addition, ERCC1/XPF-GFP (163 kDa) exhibited a similar pattern of redistribution to the equally-sized XPG-EGFP. GFP-tagged XPB, as an integral subunit of a large multi-protein complex, exhibited a clearly slower mobility than the previously mentioned NER proteins. Together, these data point towards protein mobility being determined mostly by size and shape of the examined nuclear factors. XPC-EGFP, on the other hand, showed

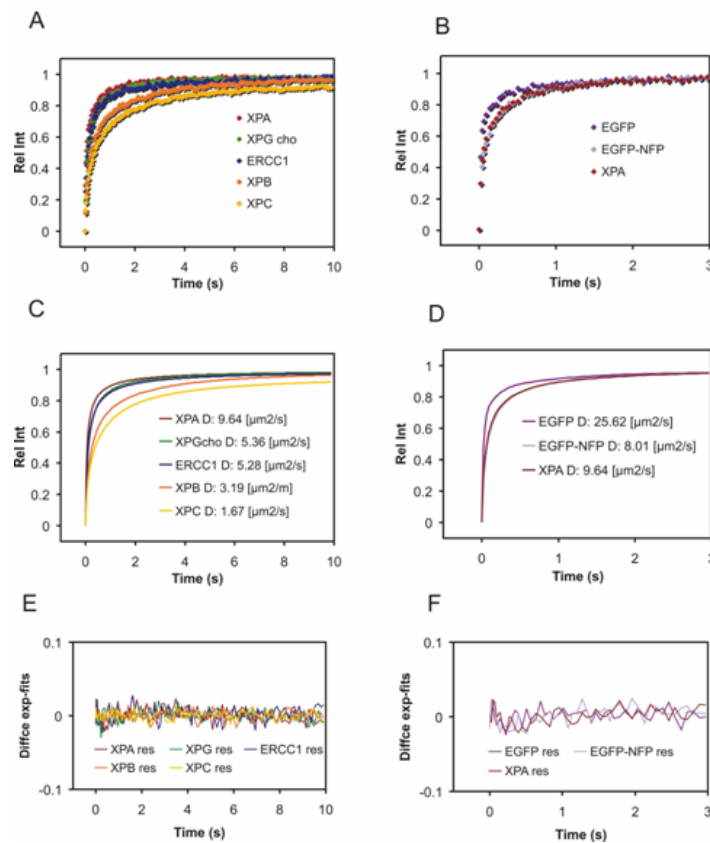


Fig. 4.1. Comparative FRAP analysis of DNA repair factors. (A-B) Graphical representation of experimental data obtained for the GFP-tagged NER factors XPA, XPG, ERCC1, XPB, and XPC (A) and GFP proteins that do not have cellular functions, plotted together with functional EGFP-XPA (B). Normalised fluorescence was calculated as $I_{\text{norm}} = (I_t - I_0) / (I_{\text{before}} - I_0)$, where I_t is the measured intensity at time t , I_{before} is the pre-bleach intensity, I_0 is the fluorescence directly after the bleach pulse. (C-D) Graphical representation of the corresponding mathematical fits for the obtained FRAP curves in (A-B). FRAP fitting curves for the functional NER factors [37] and GFP proteins (plotted together with XPA) (D) are given with the corresponding effective diffusion coefficients. (E-F) Residuals representing the quality of the fits.

a significantly different mobility. Surprisingly, it appeared to be even slower than XPB, though it is part of a complex much smaller than TFIIH, with an estimated molecular mass of only 229 kDa. Clearly, this protein moves much slower than expected on the basis of its molecular size.

Mobility of GFP-variants within mammalian cell nuclei.

To further investigate the nature of NER protein mobility, we included the biologically inert EGFP and EGFP-NFP molecules in our measurements. Since these relatively small exogenous proteins do not perform any defined function within the cell, we could assume that their nuclear mobility is mainly determined by diffusion depending on molecular size and shape of the solute, and the viscosity of the nucleoplasm. Accordingly, we observed a slower mobility of the double-sized EGFP (EGFP-NFP), as compared to single EGFP (see Fig. 4.1B). Moreover, comparing the recovery pattern of the equally-sized molecules EGFP-NFP and XPA-EGFP revealed that these proteins, in spite of their entirely different physical properties and biological functions, show equal nuclear mobilities (Fig. 4.1B). These results strongly suggest that not molecular interactions, but rather the size of a molecule determine the overall mobility of EGFP molecules as well as functional NER factors.

Mathematical analysis of nuclear protein mobility

To quantify the observed differences in protein mobility, we fitted the obtained FRAP recovery curves to a mathematical equation describing 2-dimensional Brownian diffusion (see Materials and Methods). Considering that dense nuclear structures could constrain random motion and hence affect otherwise free mobility (resulting in anomalous diffusion, “corralled diffusion”), we express the determined mobilities of all nuclear factors as an “effective diffusion” rate (D_{eff}).

In this way, the following effective diffusion coefficients were obtained for the inert control molecules EGFP and EGFP-NFP: D_{eff} EGFP (27 kDa), $25.6 \mu\text{m}^2/\text{s}$; D_{eff} EGFP-NFP (54kDa), $8.0 \mu\text{m}^2/\text{s}$ (see also Table 1 and Fig. 4.1D). Notably, EGFP has a significantly higher mobility rate than the double-sized protein EGFP-NFP. Furthermore, analysis of the NER protein EGFP-XPA (58 kDa) mobility curve resulted in a D_{eff} very

similar to the one obtained for EGFP-NFP ($9.6 \mu\text{m}^2/\text{s}$; see Table 1). Equally, most of the other NER factors analyzed produced D_{eff} corresponding to their respective molecular weight (see Table 1). Importantly hereby, the equally-sized proteins XPG and ERCC1/XPF produced very similar D_{eff} (5.4 and $5.3 \mu\text{m}^2/\text{s}$, respectively), which were

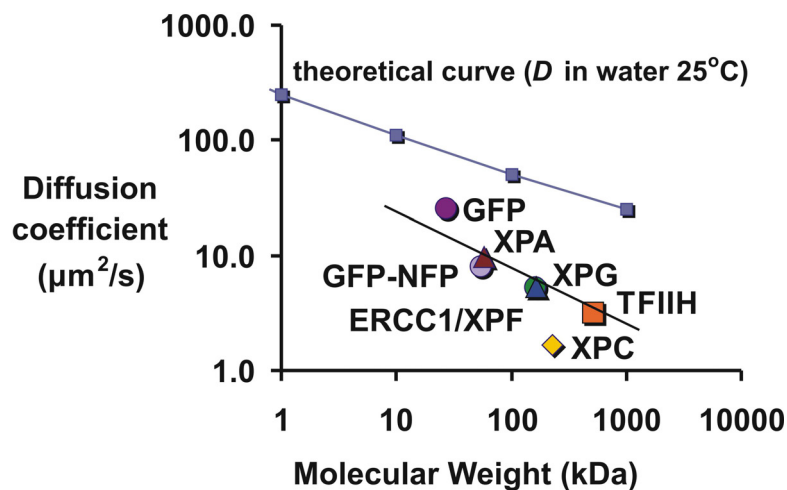


Fig. 4.2. Molecular mass dependence of intra-nuclear diffusion coefficient of NER protein
Measured effective diffusion coefficients of nuclear proteins are plotted in log against their calculated molecular weight.

Table.1 FRAP and FCS analysis of intranuclear mobility of functionally inert and biologically active nuclear factors in living cells

Protein	MW [kDa]	Nuclear function	D [$\mu\text{m}^2/\text{s}$]	bound fraction	transient retention
EGFP	27	none	25.6	-	10.40%
EGFP-NFP	54	none	8	-	43.00%
EGFP-XPA	58	NER lesion verification	9.6	-	-
ERCC1-GFP	163 ¹	5' endonuclease	5.3	-	24.10%
XPG-EGFP	161	3' endonuclease	5.4	-	10.40%
XPB-EGFP	410-510 ²	helicase	3.2	8.8% (2.90 s)	14.70%
XPC-EGFP	229 ³	NER lesion recognition factor	1.7	9.1% (1.23 s)	63.60%

¹⁾ in complex with XPF; ²⁾ as part of TFIIH complex +/-CAK; ³⁾ in complex with hHR23B + centrosome component

significantly different from the smaller factor XPA ($9.6 \mu\text{m}^2/\text{s}$) and the large TFIIH complex ($3.2 \mu\text{m}^2/\text{s}$). The recovery curve of XPC, however, despite its good fit to equations for Brownian diffusion, produced a strikingly low D_{eff} ; this strongly suggests that not only diffusional parameters restrict the overall mobility of this protein. Rather, transient interactions of a significant fraction of XPC with immobile nuclear structures even in unchallenged cells may contribute to the observed slow mobility[38]. These interactions are in the range of maximally a few seconds.

To visualize the relationship between the obtained diffusion rates and molecular weight of the measured fusion proteins, the log of the measured D_{eff} s was plotted against the log of the predicted MW (Fig. 4.2). This graph clearly demonstrates the size-dependent mobility of biologically inactive proteins, as well as NER proteins (not actively engaged in NER), in the cell nucleus. Also XPB-GFP showed mobility consistent with the diffusion of a stable complex in the range of 500 kDa, indicating that its mobility is mainly determined by diffusion. Apparently, the previously demonstrated contribution of transient binding of a fraction of TFIIH molecules to transcription initiation sites [12] is too small to be revealed with this adapted strip-FRAP procedure alone. XPC-EGFP mobility, on the other hand, deviates substantially from what would be expected from its molecular size. Ignoring the most plausible possibility that XPC's mobility is retarded by transient DNA binding and using the inverse cube-root dependence of D_{eff} on molecular mass suggests that XPC would be part of a complex in the range of several MDa. Together, these results imply that findings using FRAP technique are not in all cases a sole reflection of the molecular size but may be influenced by shape as well as by transient interactions.

Complementary FCS analysis to uncover transient protein immobilization:

To further characterize the mobility of nuclear proteins we compared our FRAP results with data obtained from fluorescence correlation spectroscopy (FCS) measurements. In FCS, only a volume less than 1 femto-liter inside the nucleus is monitored. Therefore, data obtained with this method reflect the diffusion of nuclear proteins in the nucleosol, largely excluding the influence of globally distributed binding sites and large obstacles. Analysis of diffusion parameters obtained by both, FRAP and FCS, could be used to discover transiently bound protein fractions which can not be detected with either of these methods alone.

Using mobility parameters determined by FRAP and FCS, we found for some proteins analyzed very shortly immobile fractions (see Table 1). The calculated time frames for this immobilisation (<1s) correspond to anomalous (corralled) diffusion which could be due to sterical hindrance by dense nuclear structures and be influenced by the molecular shape of the protein. Only XPB and XPC yielded transiently bound fractions in time frames indicative of biological activity. For XPB, we calculated a fraction of about 9% immobilized for about 3 s, which corresponds to the previously described engagement of the TFIIH complex in Polymerase I and II transcription [12]. XPC, surprisingly, showed an equal percentage of immobilized protein as XPB, but for only a little more than 1 second (see Table 1). Considering its substantially slower recovery after photobleaching even compared to the large TFIIH complex, this result was puzzling. On the other hand, XPC additionally showed a very large transiently immobilisation fraction, accounting for nearly 2/3 of the available protein. Perhaps XPC exhibits a general “stickiness”, very short DNA-binding in order to probe continuously for DNA damage, which could account for its slow redistribution. The immobilization in this case might be too short to be temporally resolved with our methods.

4.4 Discussion

How nuclear processes function in their required precision and efficiency in an environment that is believed to be relatively crowded is a question of fundamental importance. The nature of protein motion in order to arrive at randomly dispersed sites of their enzymatic action is of special interest in the case of cellular emergency functions such as DNA repair.

To analyze the nuclear mobility of DNA-interacting proteins background we chose the NER machinery as a model system. This system provided several crucial advantages: the multi-protein NER machinery has already been extensively studied *in vitro*, resulting in a profound knowledge of its core reaction [27,39]; the GFP-tagged NER core factors used in this study were expressed in physiologically relevant amounts in corresponding mutant cell lines and have been shown to be functional in NER [12,31,32,35,36]; the NER machinery can be switched on (by inducing global or local NER-specific DNA damage) or, importantly, be studied in a situation where DNA repair is at a minimum *i.e.* in the absence of UV-induced DNA damage. Therefore, NER proteins are an excellent model system to study the behavior of nuclear proteins when they are not exerting their primary function.

By tagging various NER proteins with GFP and expressing them at physiologically relevant levels in corresponding mutant cell lines that lack the protein under investigation, we could study the molecular mobility of each of the subunits separately. Using the same microscope and the same settings for all of the factors measured facilitated a direct comparison of the only slightly divergent protein mobilities. Moreover, by combining two different novel microscopic approaches and mathematical

analysis, we could establish individual mobility parameters for each of the factors examined.

Our results show that individual NER subunits, in the absence of DNA damage, exhibit passive diffusion at a rate mainly determined by their molecular size or that of the protein complex they are a stable part of. Only the helicase XPB and the lesion recognition factor XPC showed partial immobilization in time frames consistent with biological function.

XPB is an integral part of the ten-subunit TFIIH complex [40], that besides NER also functions in RNA polymerase I and II transcription initiation (Iben et al., 2002; Wang et al., 1994; van Vuuren et al., 1994). Concomitantly, the mobility parameters of XPB are consistent with the diffusion of a protein complex the size of TFIIH. We found that only a small percentage (9%) of the TFIIH pool is immobilized for a short time also in cells not subjected to DNA damage. These data are in concordance with earlier studies that already suggested transient binding of TFIIH to transcription sites [12]. The fact that redistribution of XPB is further slowed down at lower temperatures [12] indicates that the observed transient immobilization of TFIIH is due to its involvement in a temperature dependent process in which it gets immobilised, most likely binding to DNA.

Despite the very slow redistribution of the damage recognition factor XPC, we found that its calculated immobilized fraction (9%, equal to XPB) is relatively small, and the time of immobilization very short (a little more than 1s). However, an additional large fraction (about 2/3) of the XPC pool is transiently retained for even less than 1s. This short stalling could be either interpreted as constrained, “corralled”, diffusion, or as very short immobilization events at immobile nuclear structures. XPC has been shown to be additionally slowed down at lower temperatures, indicating temperature-dependent binding or dissociation of this protein [36]. We hypothesize therefore, that most of the

nuclear XPC pool might be engaged in continuous probing of DNA for NER damage, also in unchallenged cells. It might attach to distorted or perhaps partly remodeled patches of chromatin and dissociate quickly from these structures if no damage is detected. Another indication of this is the fact that XPC, unlike the other NER factors, is not homogeneously distributed throughout the nucleus but rather co-localizes with DNA-dense regions [36]. The retention time of XPC could be too short to be resolved by our combined methods, which would explain the outcome of our calculations. The percentage of stalled XPC could also be underrated since very densely distributed binding sites for XPC might have influenced FCS measurements. The FCS data therefore may not only represent free diffusion of the XPC complex, but also be influenced by transiently bound molecules. Consequently, the obtained data might not contribute as much to resolving immobilized fractions of XPC undetected by FRAP measurements. There might be two or more pools of transiently immobilized protein, which we could not resolve with our combined methods (indicated also by the biphasic FCS autocorrelation curve (Fig. 4.3)). Therefore, we cannot exclude the possibility that XPC (in complex with hHR23B and CEN1) has an additional function within the cell nucleus. Association of XPC with DNA might be facilitated by the UV-damaged DNA binding factor XPE [41]. Determination of the mobility of this newly characterized damage recognition protein in unchallenged cells might therefore be of special interest.

In summary, our study presents the first direct mobility comparison of functional NER proteins within the nucleus of mammalian cells in a unchallenged condition. Our data show that chromatin-transacting proteins that are not engaged in their respective function are freely mobile throughout the nucleus. Our results therefore provide further

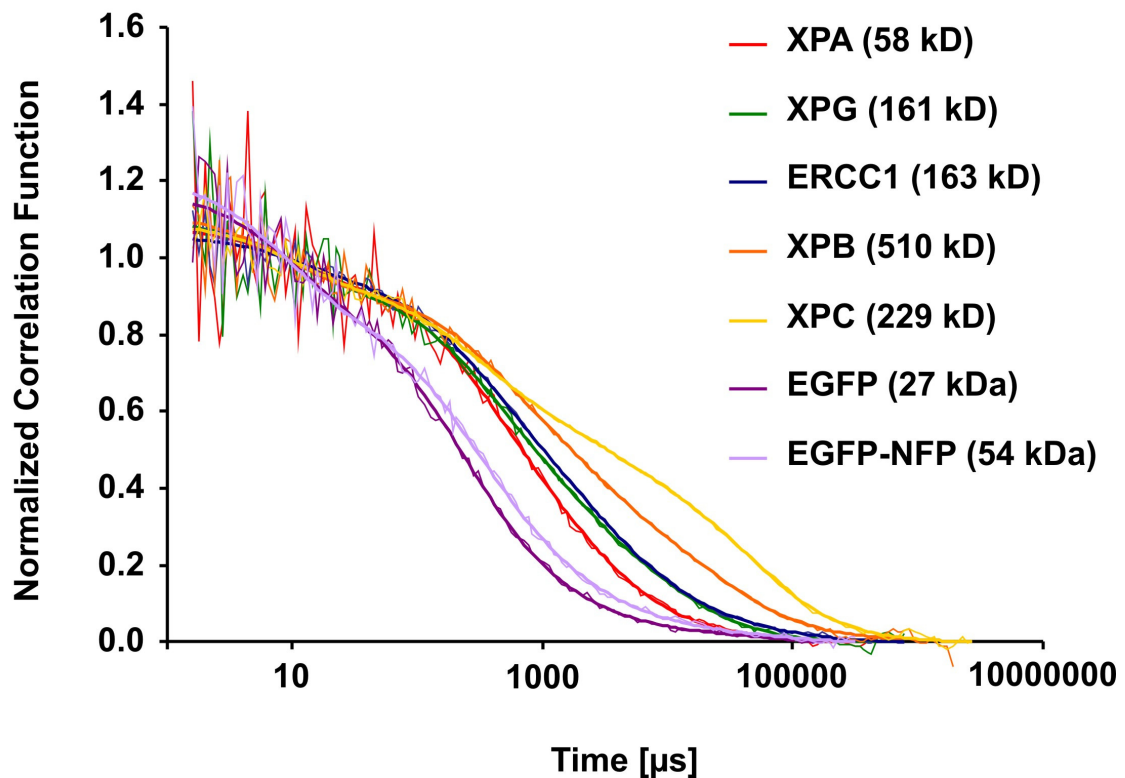


Fig. 4.3. FCS autocorrelation curves of the diverse nuclear proteins. The normalized correlation function is plotted against time. Molecular sizes of the proteins (or complexes they are a stable part of) are given in kilodaltons.

support for a general model of chromatin-transacting processes in which free diffusion and random collision allows the efficient formation of functional and adaptable protein complexes directly at the site of need. Individual factors can hereby be easily exchanged or used for multiple actions within one or more processes, rendering a cell capable of adapting quickly and efficiently to environmental or internal challenges.

4.5. Materials and Methods

Cell lines

Cell lines used in this study were the simian virus 40 (SV40)- immortalized human fibroblasts XP20S (XP-A), stably expressing EGFP-XPA (clone 40; Rademakers et al., 2003), XPCS2BA (XP-B; Vermeulen et al., 1994) stably expressing XPB-EGFP [12], XP20MA (XP-C), stably expressing XPC-EGFP, the Chinese hamster ovary (CHO) cell lines 43-3B (ERCC1) expressing GFP-ERCC1, and UV135 (XP-G) stably expressing XPG-EGFP, CHO cell lines (WT) stably expressing EGFP, and HeLa cells (WT) stably expressing EGFP-NFP. All cell lines were cultured in a 1:1 mixture of DMEM/Ham's F10 medium containing Ultra-Glutamine (Cambrex Corporation, New Jersey, USA), supplemented with antibiotics and 10% FCS at 37°C in an atmosphere of 5% CO₂.

EGFP constructs and the generation of stably expressing cell lines

Full-length human XPC and full-length human XPG were tagged on the C-terminus with EGFP by in-frame ligation into the His₆HA-EGFP-N1 vector, a derivative of the pEGFP-N1 vector from CLONTECH. In this vector, polyhistidine (His₆) and hemagglutinin [42] were added at the C-terminus of EGFP. SV40-transformed XP20MA (XP-C) cells, as well as the CHO cell line UV135 (XP-G), were transfected with the corresponding plasmids, following selection with 0.3mg/ml of G418 (gentamycin), and subsequently for UV resistance (three times irradiation with 4J/m² UV with 1-day interval). An equal procedure was applied for the other NER constructs used here [12,31,32]. All the corrected cell lines were tested for functionality and physiological expression levels [12,31,32]. EGFP and EGFP-NFP expressing cell lines were generated by transfection with a dT-EGFPx-FLAG tag plasmid and subsequent selection with G418.

Confocal Microscopy

Three days prior to experiments, cells were seeded onto 24mm glass coverslips. Imaging and FRAP experiments were performed on a Zeiss LSM 510 equipped with a 60-mW Ar laser (488 nm) and a 40x, 1.2-n.a., oil immersion lens (Zeiss, Oberkochen, Germany). The microscope was equipped with an objective heater. Unless stated otherwise, living cells were examined at 37°C.

Fluorescence Recovery after Photobleaching

Diffusion measurements were performed by FRAP analysis at high time resolution (Strip-FRAP). A strip spanning the nucleus was photo-bleached for 20ms at 100% laser intensity (140-180 μ W, argon laser at 488 nm). Recovery of fluorescence within the strip was monitored with 20ms intervals at low laser intensity (550-650 nW), to avoid photobleaching by the probe beam. Measurements were performed at 37°C, using a heated stage with feedback temperature control. Raw data were corrected for background and fluctuations in the monitoring laser power. The half time of recovery, $t_{1/2}$, was obtained by a fitting method for Brownian Diffusion (based on the findings of Feder et al., 1996), following the equation $F(t) = (F_0 + F_\infty(t/t_{1/2})^\alpha) / (1 + (t/t_{1/2})^\alpha)$; F_0 is the fluorescence intensity at time $t=0$, F_∞ is the intensity towards infinite time, $t_{1/2}$ is the half time for recovery and α is the anomaly time exponent. The FRAP $t_{1/2}$ were converted to effective diffusion coefficients by the $D = (\omega^2 \gamma) / (2t_{1/2})$, where ω is the strip width, and γ is the bleach parameter.

Fluorescence autocorrelation measurements

Fluorescence autocorrelation measurements were performed on a Carl Zeiss LSM510 microscope upgraded to ConfoCor2/LSM510 combi. A combined setup enabled easy

positioning of the cells in the laser focus of the FCS and the acquisition of images before and after FCS measurements to aid in data interpretation. For excitation, the 488 nm line of an Ar ion laser on the laser module was used at a tube current of 6.1 A. FCS measurements were performed at a laser power density of about $1.75 \mu\text{W}/\mu\text{m}^2$ using the C-Apochromat 40x water immersion objective lens (1.2 NA) with a band pass filter BP 505-550 nm (BP530-560 for Rh6G) at a detector pinhole setting of 70 μm .

Cells for FCS measurement were grown on 24-mm silica glass coverslips and then transferred to a sample dish with the growth medium replaced by phenol-red free medium. The dish was placed in a sample holder and presented to the microscope stage in a heated chamber supplied with CO_2 . The chamber and the objective lens were kept at a temperature of 37°C . With the aid of LSM imaging the desired area of a cell was selected and positioned within the FCS laser focus by a centering-macro controlling the microscope stage. The coordinates of the location of the FCS center with respect to the LSM center were determined by bleaching a hole into a thin layer of Rh6G in FCS mode and then examining the Rh6G film in LSM mode.

References

1. Misteli T. (2005) Concepts in nuclear architecture. *BioEssays*;27:477-487.
2. Hozak P, Jackson DA, Cook PR. (1994) Replication factories and nuclear bodies: the ultrastructural characterization of replication sites during the cell cycle. *J Cell Sci*;107 (Pt 8):2191-2202.
3. Kimura H, Tao Y, Roeder RG, Cook PR. (1999) Quantitation of RNA polymerase II and its transcription factors in an HeLa cell: little soluble holoenzyme but significant amounts of polymerases attached to the nuclear substructure. *Mol Cell Biol*;19:5383-5392.

4. Francastel C, Magis W, Groudine M. (2001) Nuclear relocation of a transactivator subunit precedes target gene activation. *Proc Natl Acad Sci U S A*;98:12120-12125.
5. Pombo A, Jackson DA, Hollinshead M, Wang Z, Roeder RG, Cook PR. (1999) Regional specialization in human nuclei: visualization of discrete sites of transcription by RNA polymerase III. *Embo J*;18:2241-2253.
6. Smith KP, Moen PT, Wydner KL, Coleman JR, Lawrence JB. (1999) Processing of endogenous pre-mRNAs in association with SC-35 domains is gene specific. *J Cell Biol*;144:617-629.
7. Sacco-Bubulya P, Spector DL. (2002) Disassembly of interchromatin granule clusters alters the coordination of transcription and pre-mRNA splicing. *J Cell Biol*;156:425-436.
8. Dundr M, Hoffmann-Rohrer U, Hu Q, Grummt I, Rothblum LI, Phair RD, Misteli T. (2002) A kinetic framework for a mammalian RNA polymerase in vivo. *Science*;298:1623-1626.
9. Jackson DA. (2003) The principles of nuclear structure. *Chromosome Res*;11:387-401.
10. Lamond AI, Spector DL. (2003) Nuclear speckles: a model for nuclear organelles. *Nat Rev Mol Cell Biol*;4:605-612.
11. Phair RD, Misteli T. (2000) High mobility of proteins in the mammalian cell nucleus. *Nature*;404:604-609.
12. Hoogstraten D, Nigg AL, Heath H, Mullenders LH, van Driel R, Hoeijmakers JH, Vermeulen W, Houtsmuller AB. (2002) Rapid switching of TFIIH between RNA polymerase I and II transcription and DNA repair in vivo. *Mol Cell*;10:1163-1174.
13. Kimura H, Sugaya K, Cook PR. (2002) The transcription cycle of RNA polymerase II in living cells. *J Cell Biol*;159:777-782.
14. Philimonenko VV, Flechon JE, Hozak P. (2001) The nucleoskeleton: a permanent structure of cell nuclei regardless of their transcriptional activity. *Exp Cell Res*;264:201-210.

15. Nickerson J. (2001) Experimental observations of a nuclear matrix. *J Cell Sci*;114:463-474.
16. Pederson T. (2000) Half a century of "the nuclear matrix". *Mol Biol Cell*;11:799-805.
17. Cook PR. (1999) The organization of replication and transcription. *Science*;284:1790-795.
18. Bode J, Goetze S, Heng H, Krawetz SA, Benham C. (2003) From DNA structure to gene expression: mediators of nuclear compartmentalization and dynamics. *Chromosome Res*;11:435-445.
19. Barboro P, D'Arrigo C, Mormino M, Coradeghini R, Parodi S, Patrone E, Balbi C. (2003) An intranuclear frame for chromatin compartmentalization and higher-order folding. *J Cell Biochem*;88:113-120.
20. Philimonenko AA, Jackson DA, Hodny Z, Janacek J, Cook PR, Hozak P. (2004) Dynamics of DNA replication: an ultrastructural study. *J Struct Biol*;148:279-289.
21. Calapez A, Pereira HM, Calado A, Braga J, Rino J, Carvalho C, Tavanez JP, Wahle E, Rosa AC, Carmo-Fonseca M. (2002) The intranuclear mobility of messenger RNA binding proteins is ATP dependent and temperature sensitive. *J Cell Biol*;159:795-805.
22. Carmo-Fonseca M, Platani M, Swedlow JR. (2002) Macromolecular mobility inside the cell nucleus. *Trends Cell Biol*;12:491-495.
23. Phair RD, Scaffidi P, Elbi C, Vecerova J, Dey A, Ozato K, Brown DT, Hager G, Bustin M, Misteli T. (2004) Global nature of dynamic protein-chromatin interactions in vivo: three-dimensional genome scanning and dynamic interaction networks of chromatin proteins. *Mol Cell Biol*;24:6393-6402.
24. Misteli T. (2001) Protein dynamics: implications for nuclear architecture and gene expression. *Science*;291:843-847.
25. Shav-Tal Y, Darzacq X, Shenoy SM, Fusco D, Janicki SM, Spector DL, Singer RH. (2004) Dynamics of single mRNPs in nuclei of living cells. *Science*;304:1797-1800.

26. Verkman AS. (2002) Solute and macromolecule diffusion in cellular aqueous compartments. *Trends Biochem Sci*;27:27-33.
27. de Laat WL, Jaspers NGJ, Hoeijmakers JHJ. (1999) Molecular mechanism of nucleotide excision repair. *Genes Dev.*;13:768-785.
28. Araujo SJ, Tirode F, Coin F, Pospiech H, Syvaoja JE, Stucki M, Hubscher U, Egly J-M, Wood RD. (2000) Nucleotide excision repair of DNA with recombinant human proteins: definition of the minimal set of factors, active forms of TFIIH, and modulation by CAK. *Genes Dev.*;14:349-359.
29. de Boer J, Hoeijmakers JH. (2000) Nucleotide excision repair and human syndromes. *Carcinogenesis*;21:453-460.
30. Schärer OD. (2003) Chemistry and Biology of DNA Repair. *Angewandte Chemie International Edition*;42:2946-2974.
31. Houtsmuller AB, Rademakers S, Nigg AL, Hoogstraten D, Hoeijmakers JH, Vermeulen W. (1999) Action of DNA repair endonuclease ERCC1/XPF in living cells. *Science*;284:958-961.
32. Rademakers S, Volker M, Hoogstraten D, Nigg AL, Mone MJ, van Zeeland AA, Hoeijmakers JHJ, Houtsmuller AB, Vermeulen W. (2003) Xeroderma Pigmentosum Group A Protein Loads as a Separate Factor onto DNA Lesions. *Mol. Cell. Biol.*;23:5755-5767.
33. Volker M, Mone MJ, Karmakar P, van Hoffen A, Schul W, Vermeulen W, Hoeijmakers JHJ, van Driel R, van Zeeland AA, Mullenders LHF. (2001) Sequential Assembly of the Nucleotide Excision Repair Factors In Vivo. *Molecular Cell*;8:213-224.
34. Mone. (2004) In vivo dynamics of chromatin-associated complex formation in mammalian nucleotide excision repair. *Proc Natl Acad Sci U S A*.
35. Zotter A, Luijsterburg MS, Warmerdam DO, Ibrahim S, Nigg A, van Cappellen WA, Hoeijmakers JHJ, van Driel R, Vermeulen W, Houtsmuller AB. (2006) Recruitment of the Nucleotide Excision Repair Endonuclease XPG to Sites of UV-induced DNA Damage Depends on Functional TFIIH. *Mol. Cell. Biol.*:MCB.00695-706.

36. Hoogstraten D, Nigg AL, van Cappellen WA, Hoeijmakers JH, Houtsmuller AB, Vermeulen W. (in preparation) DNA-damage sensing in living cells by xeroderma pigmentosum group C.
37. Bini L, Pacini S, Liberatori S, Valensin S, Pellegrini M, Raggiaschi R, Pallini V, C TB. (2003) Extensive temporally regulated reorganization of the lipid raft proteome following T-cell antigen receptor triggering. *Biochem J*;369:301-309.
38. Hoogstraten D, Nigg AL, van Cappellen WA, Hoeijmakers JH, Houtsmuller AB, Vermeulen W. (2003) DNA-damage sensing in living cells by xeroderma pigmentosum group C. in preparation.
39. Riedl T, Hanaoka F, Egly J-M. (2003) The comings and goings of nucleotide excision repair factors on damaged DNA. *EMBO J.*;22:5293-5303.
40. Giglia-Mari G, Coin F, Ranish JA, Hoogstraten D, Theil A, Wijgers N, Jaspers NGJ, Raams A, Argentini M, van der Spek PJ and others. (2004) A new, tenth subunit of TFIIH is responsible for the DNA repair syndrome trichothiodystrophy group A. *Nat Genet*;36: 714 -719.
41. Moser J, Volker M, Kool H, Alekseev S, Vrieling H, Yasui A, van Zeeland AA, Mullenders LH. (2005) The UV-damaged DNA binding protein mediates efficient targeting of the nucleotide excision repair complex to UV-induced photo lesions. *DNA Repair (Amst)*;4:571-582.
42. Ha T. (2001) Single-molecule fluorescence resonance energy transfer. *Methods*;25:78-86.

Chapter

5

Recruitment of the Nucleotide Excision Endonuclease XPG to sites of UV-induced Damage Depends on Functional TFIIH.

Angelika Zotter, Martijn S. Luijsterburg, Daniël O. Warmerdam,
Shehu Ibrahim, Alex Nigg, Wiggert A. van Cappellen,
Jan H. J. Hoeijmakers, Roel van Driel ,
Wim Vermeulen
and Adriaan B. Houtsmuller

Mol Cell Biol. 2006

5.1. Abstract

The structure-specific endonuclease XPG is an indispensable core protein of the nucleotide excision repair (NER) machinery. XPG cleaves the DNA strand at the 3' side of the DNA damage. XPG binding stabilizes the NER pre-incision complex and is essential for the 5' incision by the ERCC1/XPF endonuclease. We have studied the dynamic role of XPG in its different cellular functions in living cells. We have created mammalian cell lines that lack functional endogenous XPG and stably express EGFP-tagged XPG. Life cell imaging shows that in undamaged cells XPG-EGFP is uniformly distributed throughout the cell nucleus, diffuses freely and is not stably associated with other nuclear proteins. XPG is recruited to UV-damaged DNA with a $t_{0.5}$ of 200 s and is bound for 4 min in NER complexes. Recruitment requires functional TFIIH, although some TFIIH mutants allow slow XPG recruitment. Remarkably, binding of XPG to damaged DNA does not require the DDB2 protein, which is thought to enhance damage recognition by NER factor XPC. Together, our data present a comprehensive view of the *in vivo* behaviour of a protein that is involved in a complex chromatin associated process.

5.2. Introduction

Nucleotide excision repair (NER) is a versatile DNA repair mechanism that removes different types of helix-distorting damage from the genome, including UV light-induced DNA damage, such as cyclobutane pyrimidine dimers (CPD) and 6-4 photoproducts (6-4 PP) [10, 22]. The severe clinical features of three photo-hypersensitive hereditary NER disorders underscore its biological importance: the cancer-prone syndrome, the neuro-developmental conditions Cockayne syndrome (CS) and trichothiodystrophy (TTD) [28]. The multi-step NER process requires the coordinated actions of at least 25 polypeptides

[11]. The general *modus operandi* for NER comprises the following steps: 1) recognition of DNA damage, 2) unwinding around the lesion, 3) dual incision on both sides of the damage, 4) removal of the excised oligonucleotide, and 5) filling the generated gap by DNA polymerase and ligase [5]. Two different modes of NER exist, i.e. transcription-coupled NER (TC-NER) and global genome NER (GG-NER) [21]. TC-NER removes lesions exclusively from the transcribed strand of active genes, whereas GG-NER repairs damage at any other position in the genome. GG-NER protects against damage-induced mutagenesis and can thus be considered a cancer-preventing process, whereas TC-NER primarily promotes cellular survival and therefore may counteract aging [30]. The damage sensor for 6-4 PP in GG-NER is the heterotrimeric XPC/HR23B/centrin2 complex [48, 60]. In addition, the UV-damaged DNA binding protein (UV-DDB) assists XPC in the recognition of CPD [9, 61] and facilitates 6-4 PP repair [33]. In TC-NER lesions are detected by stalled elongating RNA polymerase II [54]. After lesion-detection the two NER sub-pathways funnel into a common mechanism. Damage sensing is followed by the recruitment of the ten-subunit TFIIH complex [13], which utilizes its helicase components XPB and XPD to locally unwind the DNA around the lesion. The structure-specific endonuclease XPG subsequently binds and promotes formation of an open DNA complex around the lesion [8]. The next proteins that bind to the repair complex are the single-stranded DNA (ssDNA) binding Replication Protein A (RPA) and the damage verification factor XPA, which play an important role in the correct positioning of the 3' endonuclease XPG and the 5' endonuclease ERCC1/XPF [4]. After dual incision a stretch of ~30 nucleotides ssDNA containing the damage is released, after which the replication factors RPA, PCNA and DNA polymerase δ/ϵ fill in the resulting gap [45]. In the last step the newly synthesized DNA is sealed by DNA ligase I and the original chromatin structure is restored by chromatin assembly factor I (CAF I) [15].

In vitro studies have resulted in a number of models for the assembly of the NER complex onto damaged DNA, proposing a completely pre-assembled holo-complex [50], a partly pre-assembled NER complexes [16-19], and the sequential assembly of individual NER factors, assuming conflicting assembly sequences [41, 48, 62, 63]. Assembly studies in intact cultured cells using locally damaged nuclei support the sequential assembly scenario [60]. We have previously studied the *in vivo* kinetics of the NER components ERCC1/XPF [24, 31], TFIIH [23, 31], XPA [40], XPC [38], and CSB [54]. Together, these studies culminate to a model in which NER factors move freely throughout the nucleus and are incorporated one-by-one into repair complexes after the induction of DNA damage. However, the above-mentioned studies could not unambiguously identify the precise role of XPG, including at what stage the protein is incorporated in the NER complex. Therefore, we have carried out a comprehensive *in vivo* analysis of the behavior of XPG in DNA repair.

5.3. Results

Generation of cell lines stably expressing functional XPG-EGFP

To study the nuclear distribution and dynamics of the XPG protein in living cells we tagged the protein with enhanced green fluorescent protein (EGFP). EGFP was fused to the carboxy-terminus of human XPG (Fig. 5.1A), resulting in an XPG-EGFP fusion protein, which was stably expressed in XPG-deficient human fibroblasts (XPCS1RO-Sv) and in Chinese Hamster Ovary cells (UV135). Fluorescently tagged XPG is predominantly located in the nucleus of both cell types in which it is uniformly distributed, with nucleoli being less populated (Fig. 5.1B). These observations are in

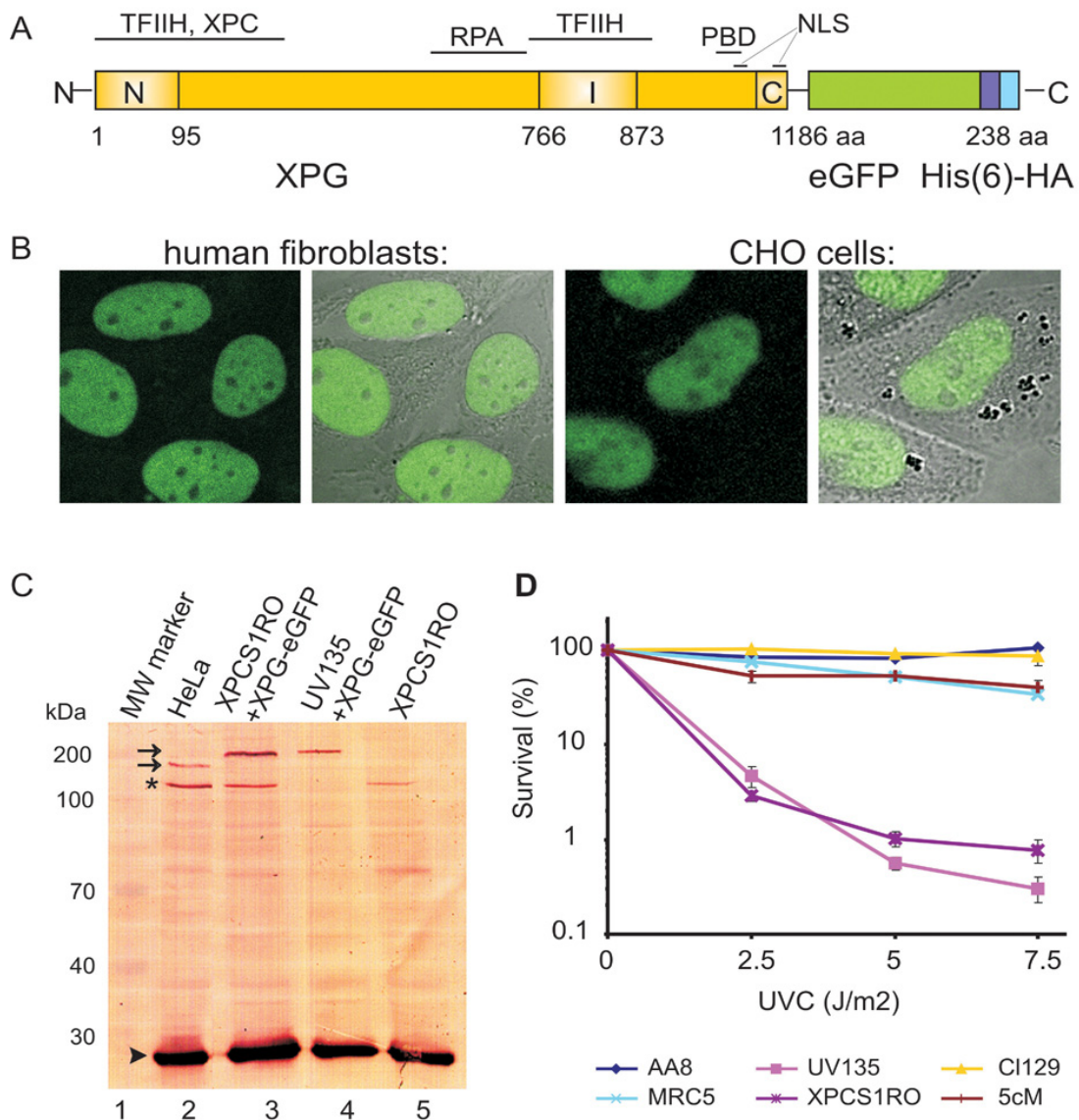


Fig. 5.1. Expression and functionality of XPG-EGFP. (A) Schematic representation of the XPG-EGFP-His(9)-HA fusion gene with the N-terminal and C-terminal nuclease domains (N and C, respectively) and different interaction domains indicated. I, Internal domain; PBD, PCNA binding domain; NLS, probable nuclear localization signal; aa, amino acids. (B) Localization of the XPG fusion protein in human fibroblasts (left two images, showing the fluorescence signal and an overlay of fluorescence and phase contrast) and CHO cells (right two images). XPG-EGFP is present mainly in the nucleus, except in the nucleoli. (C) Immuno-blot, probed with monoclonal anti-XPG, of 40 μ g of whole-cell extract from HeLa (lane 2), human XPCS1RO-Sv (XP-G) expressing XPG-EGFP (lane 3), CHO (UV135) cells expressing XPG-EGFP (lane 4) and untransfected XPCS1RO-Sv (lane 5). The molecular mass of protein markers is indicated in kilodaltons (kDa). EGFP-tagged XPG migrates slower than endogenous XPG (upper and lower

arrow, respectively). No XPG protein was detected in the human fibroblasts in which the severely truncated XPG-mRNA is probably highly unstable or not recognized. Chinese hamster XPG cannot be detected with our anti-XPG serum. Loading control: PCNA (arrowhead), asterisk indicates cross-reacting non-specific band only present in human cell extracts. (D) UV-survival of repair-proficient human MRC5 cells (wild type; light blue line), XPCS1RO cells (violet line), XPCS1RO cells stably expressing XPG-EGFP (clone 5cM; brown line), wild type CHO cells (AA8; dark blue line), XPG-deficient CHO cells (UV135; purple line), and UV135 cells expressing XPG-EGFP (clone 129; yellow line). The transfected cell lines show a correction of UV sensitivity to the wild type level.

accordance with earlier findings for fixed cells [6, 53, 60]. Immuno-blot analysis of whole cell extracts of both cell types, using anti-XPG antibodies, showed that XPG-EGFP migrates in SDS-PAGE with a mobility corresponding to the expected size of the full-length fusion protein (~180 kDa, Fig. 5.1C [36]). Labeling with anti-EGFP antibodies did not reveal the presence of any other GFP-containing polypeptides in the crude extracts (data not shown). This implies that all microscopy-based studies in this paper truly reflect the behavior of XPG-EGFP. The Western blot in Fig. 5.1C indicates that XPG-EGFP is expressed at about the same level as endogenous XPG in wild type (HeLa) cells. Importantly, XPG-EGFP was able to restore normal UV-sensitivity of XPG cells (Fig. 5.1D), showing that the fusion protein is functional in NER when expressed at physiologically levels.

Mobility of XPG-EGFP in the nucleus

XPG has been reported to interact with other DNA repair proteins and with transcription factors and might therefore be part of a larger protein complex [42]. To investigate whether XPG either moves freely through the nucleoplasm, is part of a larger complex, or is bound to immobile nuclear structures, we used FRAP (Fluorescence Recovery after Photo-bleaching; Fig. 5.2A). XPG-EGFP molecules in a specific nuclear region are

bleached by a short light pulse, followed by monitoring the kinetics and extent of recovery of fluorescence due to the diffusion of non- bleached XPG-EGFP molecules into the bleached area. In non-UV irradiated living cells, monitored at 37°C, essentially all XPG-EGFP was mobile. The same redistribution kinetics were found for XPG-EGFP in CHO cells (Fig. 5.2B) and in human fibroblasts (Fig. 5.2C), indicating that XPG-EGFP mobility is independent of cell type and organism. Curve fitting shows that the effective diffusion coefficients (D_{eff}) of XPG-EGFP in CHO cells and human fibroblasts are very similar, i.e. $6.1 \pm 1.5 \mu\text{m}^2/\text{s}$ and $4.0 \pm 0.8 \mu\text{m}^2/\text{s}$, respectively (Fig. 5.2B and 5.2C). These diffusion coefficients were significantly different than other NER-GFP fusions (XPA, TFIIH) tested in parallel (A.zotter unpublished data and [23, 40]). Using combined FLIP and FRAP [23] we showed that the mobility of XPG is the same at 27° and 37°C (Fig. 5.2D). Similar results have been obtained for other NER factors [24, 40], except for TFIIH [23] in which temperature-sensitive mobility was thought to be due to binding to transcription complexes. Together, this indicates that XPG in undamaged cells is not part of a larger complex, e.g. with TFIIH as has been suggested elsewhere [1, 19], and does not interact with immobile nuclear components, such as chromatin.

In vivo assembly of XPG-EGFP into the NER complex

Analysis of the *in vivo* kinetics of NER complex assembly has shown that incorporation of TFIIH and ERCC1/XPF into the pre-incision complex is not diffusion-limited [31]. Association of the ERCC1/XPF incision factor depended on the presence of functional TFIIH [31]. To determine how XPG-EGFP is incorporated into the repair complex *in vivo*, we analyzed its recruitment kinetics in nuclei that had been locally UV-irradiated (Fig. 5.3A, [31]). XPG-EGFP accumulation in the damaged area reached a plateau after

about 10 min (Fig. 5.3B). This plateau reflects a pseudo steady state in which DNA repair takes place at a constant rate and the number of XPG molecules that are incorporated into

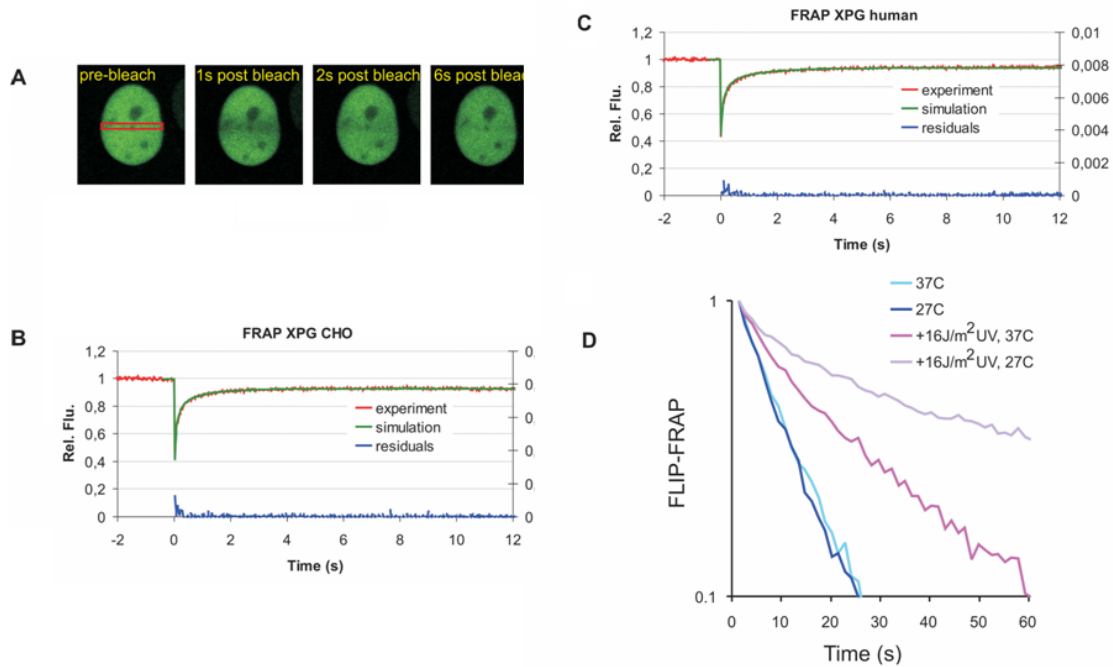


Fig. 5.2. FRAP analysis of XPG mobility. (A) Example of FRAP analysis to determine effective diffusion coefficients in non UV-irradiated cells. A strip (red rectangle) spanning the nucleus containing EGFP-tagged protein is bleached at high laser intensity. Subsequently, fluorescence recovery after photobleaching is monitored in the strip. (B-C) Graphical representation of FRAP analysis of EGFP-XPG in non-UV irradiated CHO cells (B) and human fibroblasts (C), the mean relative fluorescence (flu. after bleaching/flu. before bleaching) is plotted against the indicated time in seconds. Red lines: experimental data; green lines: simulated curves; blue lines at the bottom of each graph represent residuals which are a measure for the quality of the fits. (D) Simultaneous FLIP/FRAP analysis of XPG mobility in the nucleus of CHO cells. A small area at one pole of the nucleus is bleached for 1 s, subsequently fluorescence is monitored in time in the bleached (FRAP) and unbleached area (FLIP). The difference in EGFP intensity between the two areas after the bleach pulse is plotted on a log scale as a function of time. Light blue line, XPG redistribution at 37°C; dark blue line, XPG redistribution at 27°C; purple line, XPG redistribution in UV irradiated cells at 37°C; violet line, XPG redistribution in UV irradiated cells at 27°C. Experiments on UV-irradiated cells were performed between 10 min and 30 min after global UV-C irradiation.

repair complexes per unit time equals the number of molecules that are released after a repair event. The rate of incorporation of XPG-EGFP was the same in CHO cells and in

human fibroblasts, with a $t_{0.5}$ of ~ 200 s for both cell types (Fig. 5.3B). This shows that the absence of the DDB2 subunit of the UV-DDB protein in CHO cells has no effect on the

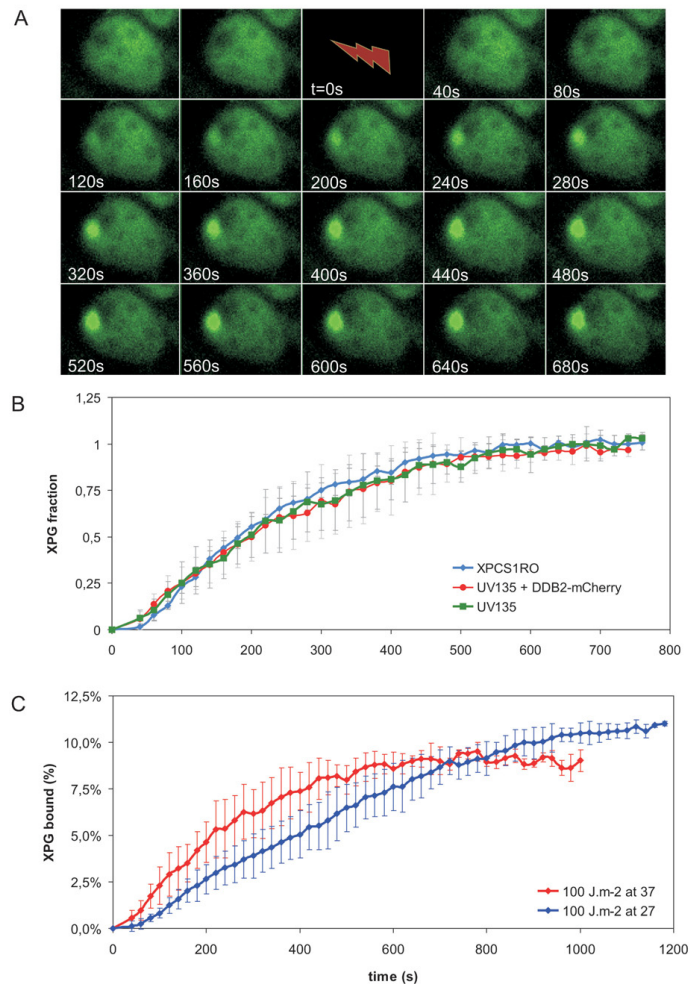


Fig. 5.3. Accumulation of XPG-EGFP after local UV-DNA damage. (A) Time-lapse series of XPG-EGFP expressed in CHO UV135 cells prior and immediately after UV-C irradiation (100 J/m^2). After taking pre-irradiation images cells were irradiated for 39s (lightning arrow), subsequently images were taken with 20s interval. (B) Incorporation kinetics of XPG-EGFP in CHO cells (UV135 – green line, $n=5$), CHO cells transfected with DDB2-mCherry (UV135 + DDB2 – red line, $n=5$) and human fibroblasts (XPCS1RO – blue line, $n=5$) at UV-damaged areas after 100 J/m^2 UV-C. The local relative accumulation of XPG-EGFP was measured versus time. (C) Incorporation kinetics of XPG-EGFP in UV135 cells at 37°C (red line, $n=5$) and 27°C (blue line, $n=5$). The local accumulation of XPG-EGFP was measured and plotted as a percentage of the total EGFP fluorescence of the cell nucleus (37°C $n=11$, 27°C $n=20$) versus time after start of UV irradiation. Error bars represent SD between different experiments.

kinetics of incorporation of XPG in NER complexes that assemble on UV-damaged DNA. To investigate the role of DDB2 more directly, we transfected CHO cells that stably express XPG-EGFP transiently with DDB2 fused to the red fluorescent protein mCherry [44]. Subsequently, binding of XPG-EGFP was measured in cells that also expressed DDB2-mCherry. The rate of incorporation of XPG-EGFP was the same in transfected and non-transfected cells, i.e. with and without expression of DDB2 (Fig. 5.3B). Our experiments show that DDB2 does not changes the incorporation kinetics of XPG into the NER pre-incision complex.

Table 5.1 Human cell-lines used for local damage induction

Cell strain	TFIIH mutation	Affected function	Syndrome	Reference
C5RO	none		wild type	
XPCS1BA	F99S in XPB	unknown	mild XP/CS	(57)
XP131MA	frame-shift 742 in XPB	helicase activity	XP/CS	(8)
XP6BE	R638W in XPD	p44 interaction	XP	(39)
XPCS2	G602D in XPD	helicase activity	XP	(58)
TTD1BEL	R722W in XPD	p44 interaction	TTD	(52)

Binding of XPG depends on the presence of functional TFIIH

The rate of binding of XPG-EGFP to the nascent NER complex is temperature-dependent. The initial rate of XPG-EGFP incorporation at 37°C is about 1.5%/min and at 27°C about 0.5%/min (Fig. 5.3C). Analogous to previous studies of the *in vivo* kinetics of incorporation of ERCC1/XPF it is likely that the temperature-dependent step in NER complex formation is the DNA unwinding process, catalyzed by the helicase activity of TFIIH [43]. Previous studies, using fixed cells and *in vitro* NER assembly, were not conclusive about the question whether XPG incorporation required functional TFIIH [6, 41, 53]. To determine whether XPG binding depends on functional TFIIH, we measured the UV-induced accumulation of XPG (using a specific antibody) at different time points after local UV-irradiation in various cell lines mutated in the TFIIH helicases XPB or XPD (Table 1) and in wild-type cells. Accumulation of XPG, measured 10 min after local UV-induced DNA damage, was strongly reduced in all TFIIH mutants tested, in comparison to wild type cells. In contrast, XPC, which binds to DNA damage before TFIIH, accumulated normally in all mutants (Fig. 5.4). However, some XPG accumulation was observed in all mutant TFIIH cell lines 30 min after local UV damage, except in TTD cells (Fig. 5.4). These results show that functional TFIIH is required for normal XPG binding. However, several TFIIH mutants still support what seems a slow or limited XPG incorporation in the NER complex.

XPG-EGFP is transiently immobilized by UV-damaged DNA

In addition to the binding (i.e. pre-steady state) kinetics of XPG-EGFP into the nascent NER complex, we have analyzed the steady state kinetics and the nuclear redistribution after UV damage. Different UV-C doses have been employed, i.e. 2, 4, 8, and 16 J/m².

Whole cell exposure to UV-light induces a uniform distribution of DNA lesions in the nucleus. This did not result in a detectable redistribution of XPG-EGFP, in contrast to the

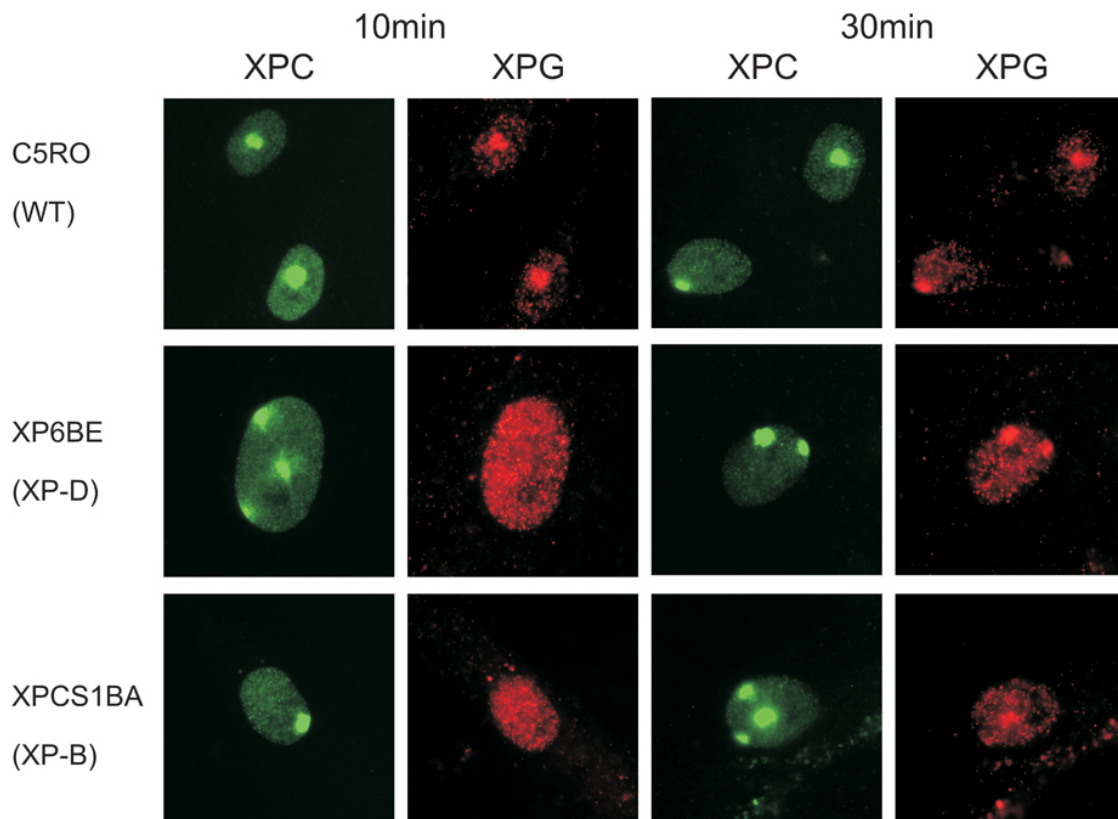


Fig. 5.4. Accumulation of XPC and XPG after local UV-damage in human wild-type cells (C5RO) and various TFIIH mutants: 10 min (columns 1 and 2) and 30 min after UV-irradiation (columns 3 and 4). Columns 1 and 3, immunofluorescence labeling with anti-XPC antibody (green); columns 2 and 4, labeling with anti-XPG antibody (red).

study by Park *et al.* that reported the formation of XPG foci upon UV irradiation in fixed cells [37]. However, these XPG foci could be the result of the fixation procedure. FRAP analyses performed between 10 and 45 min after UV-treatment (when incorporation of XPG is in steady state), showed incomplete fluorescence recovery in human fibroblasts and in CHO cells within the time frame of 8 seconds after photobleaching (Fig. 5.5A and 5B, compare to untreated cells). This indicates that maximally 20-30% of the XPG-EGFP molecules are immobile. The mobility of unbound XPG-EGFP did not change upon UV

irradiation, as shown by the recovery plots of Fig. 5.5C and 5D. This demonstrates that the XPG molecules that do not participate in NER have the same mobility and therefore the same molecular size before and after UV irradiation. Similar to other NER factors [23, 24, 40] we conclude that the observed immobilization of XPG-EGFP reflects its incorporation in the NER complex.

Despite exhibiting similar total cellular fluorescence intensities (representing the expression levels of XPG-EGFP), human fibroblasts showed less XPG-EGFP immobilization at a NER-saturating UV dose than CHO cells, i.e. 20% and 30%, respectively (Fig. 5.5E and 5F). Furthermore, a quantitatively different response to UV-dose was observed for both cell types. While in human cells a larger fraction of the XPG-EGFP molecules was immobilized at low UV-doses (saturating at 8J/m^2) CHO cells show a significant increase in immobilized XPG-EGFP up to 16J/m^2 (Fig. 5.5E and 5F). This shows that the fraction of immobilized XPG-EGFP of the total cellular amount of XPG is different in both cell types. This is probably due to the fact that the concentration of other NER factors is different. If cells were cultured at 27°C instead of at 37°C , a significantly larger fraction of XPG-EGFP was immobilized at the same UV dose in both cell lines (Fig. 5.5E and 5F), indicating that at any given time point more XPG-EGFP molecules participate in NER events. Combined FRAP and FLIP at 27°C instead of 37°C , confirmed a decrease in mobility of XPG-EGFP after UV-irradiation (Fig. 5.2D). This implies that the dissociation of XPG-EGFP from the NER complex (presumably after dual incision) is temperature-dependent, resulting in a longer residence time at lower temperature and thus increased immobilization.

In addition to a role in NER, XPG has been shown to be involved in base excision repair of oxidative DNA lesions *in vitro* [26]. To investigate a possible role of XPG in BER *in vivo* we treated cells with ionizing radiation or paraquat. Both procedures induce

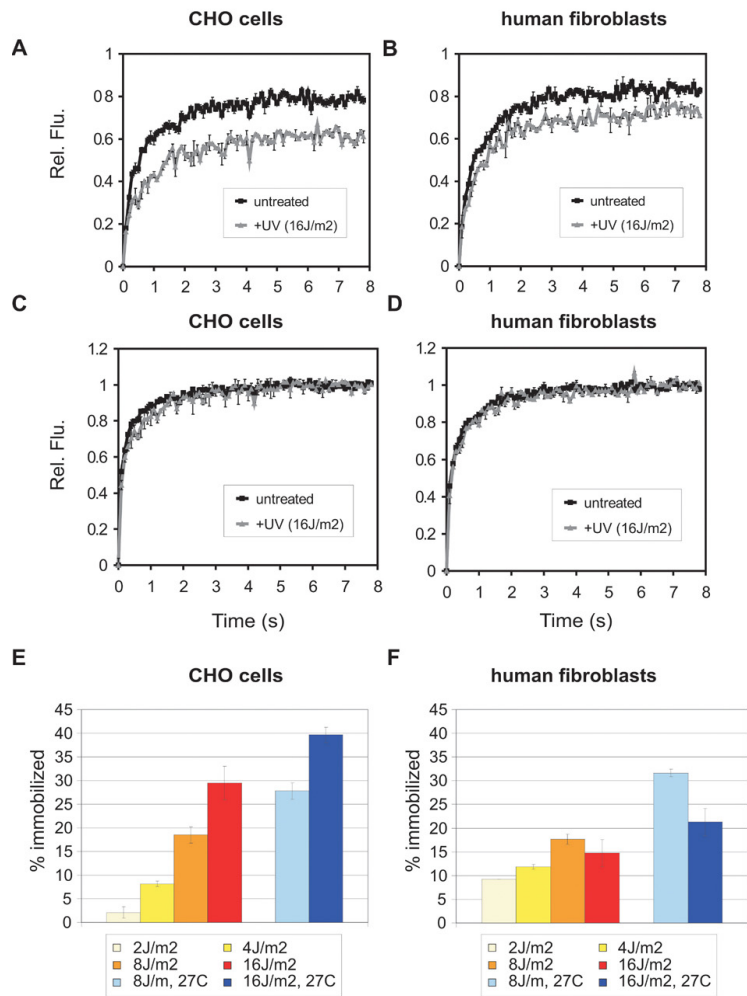


Fig. 5. 5. FRAP analysis of UV-treated and untreated cells to visualize DNA damage-dependent immobilization of XPG-EGFP. (A, B) FRAP recovery curves (normalized to pre-bleach intensity set to one) in CHO cells and human fibroblasts, respectively. Black curves: XPG-EGFP recovery in untreated cells (as a reference); grey curves: recovery in UV irradiated cells. (C, D) FRAP recovery curves (normalized to maximum recovery post-bleach set to one) of XPG-EGFP in CHO cells and human fibroblasts, respectively. Black curves: XPG recovery in untreated cells (as a reference); grey curves: recovery in UV irradiated cells. (E, F) Immobilized XPG-EGFP fractions in CHO cells and human fibroblasts, respectively, in response to different UV doses. Light blue and dark blue bars depict measurements in cells cultured at 27°C, after 8 and 16J/m² UV, respectively. Error bars show the standard error of the mean.

oxidative lesions that are removed by BER. After treatment with these agents, we did not observe increased immobilization of XPG-EGFP (data not shown), suggesting that XPG does not play a major role in BER. However, we cannot rule out that the number of lesions introduced by these procedures is too low to detect changes in XPG-EGFP immobilization or that the kinetics of XPG in BER are different and do not result in detectable immobilization of XPG. Besides a role in BER, it has been suggested that XPG associates with transcription bubbles containing stalled RNAPII molecules together with TFIIH and CSB [42]. In addition, the *S. cerevisiae* XPG homolog Rad 2 has been shown to be required for RNAPII activity [27]. We showed that the mobility of TFIIH, which is involved in RNAPI and RNAPII activity, is affected by treatment with transcription inhibitors (e.g. 5,6-dichloro-1-D-ribofuranosyl benzimidazole or DRB [23, 25]). We did not observe any effect on XPG-EGFP mobility after treatment with DRB (data not shown) and were thus not able to confirm a role of XPG in transcription bubbles *in vivo* [42]. It cannot be excluded that the interaction of XPG with transcription bubbles is too transient or involves only a very small fraction of molecules escaping detection.

The residence time of XPG-EGFP in the NER complex is in the order of minutes

To determine the residence time of XPG in a NER complex we applied a FRAP variant on locally damaged cells. Briefly, an elongated area distant from the local damage is bleached. Subsequently, the fluorescence redistribution is monitored (Fig. 5.6A). The time required to re-establish the pre-irradiation distribution of XPG-EGFP is a measure for the mean residence time of molecules in the NER complex. A new equilibrium between bleached and non-bleached molecules was reached with a $t_{0.9}$ of approximately 3 to 4 minutes. (Fig. 5.6B), reflecting the residence time of XPG in the NER complex. This value is similar to the measured residence time of other components of the NER complex [23, 24, 40].

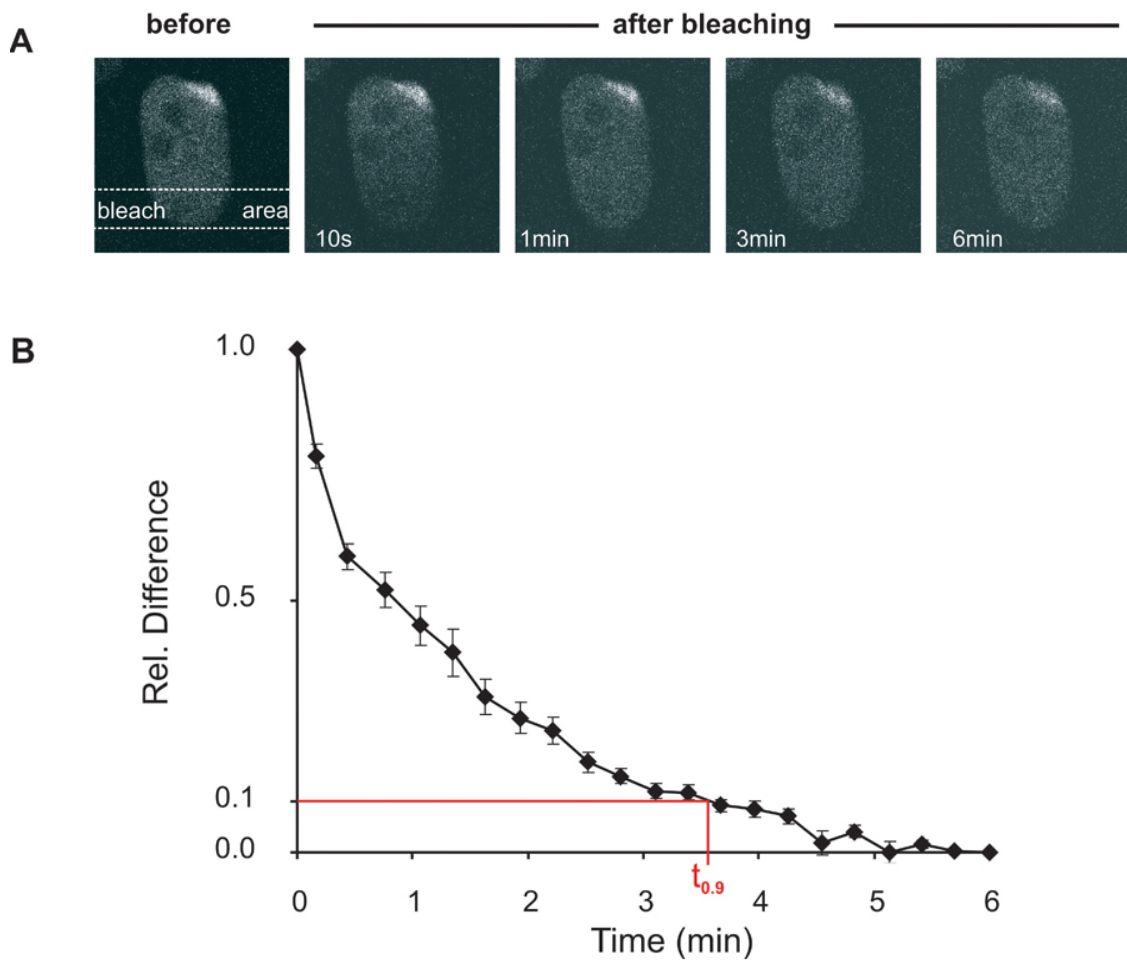


Fig. 5.6. FLIP analysis of locally UV-damaged areas in the nucleus. (A) A strip opposite a locally damaged area in the nucleus is bleached and the redistribution of bleached and unbleached XPG-EGFP is monitored in time. (B) FLIP curve of the locally damaged nucleus. The relative difference between redistribution in the damaged versus the non-damaged area is plotted in time. Error bars depict the standard error of the mean.

5.4. Discussion

The endonuclease XPG is a multi-functional nuclear protein. It plays a central role in nucleotide excision repair (NER) of helix-distorting DNA damage and is thought to be involved in transcription, transcription-coupled repair of non-helix distorting DNA lesions and in base excision repair (BER) [26, 27, 42]. In the NER complex XPG carries

out the incision at the 3' side of the damage and stabilises the protein complex on the locally unwound DNA [5]. In this study we present a comprehensive analysis of the dynamic behaviour of XPG inside the nucleus of living CHO cells and human fibroblasts that do not contain functional endogenous XPG and that stably express human XPG-EGFP at levels similar to endogenous XPG in wild type cells (Fig. 5.1). Since these cells show normal UV-resistance, the XPG-EGFP is fully functional.

XPG only interacts with NER components on damaged DNA

Evidence has been presented that XPG associates with TFIIH [1, 19, 34]. Our FRAP measurements on cells expressing functional XPG-EGFP show that *in vivo* in undamaged cells the majority of the protein is not associated with TFIIH, because of the observed difference in mobility rate and differential dependence of the mobility on temperature. Importantly, also after UV damage the XPG molecules that are not engaged in DNA repair show the same *in vivo* mobility, indicating that XPG only interacts with other nuclear components if it binds to the NER complex that assembles on damaged DNA (Fig. 5.5). This is supported by the finding that other NER proteins show apparent diffusion rates that are different from what is observed here for XPG-EGFP [14, 23, 24, 40]. Moreover, the mobility of TFIIH differs at 27 and 37°C, whereas that of XPG-EGFP is temperature independent (Fig. 5.2). Also the kinetics of incorporation of these two proteins into the NER complex is different ($t_{0.5}$ of 200 s for XPG and 110 s for TFIIH (Fig. 5.3 and [31])). The observation that endonuclease XPG does not associate with nuclear components except in the DNA damage-induced NER complex, supports the notion that this protein is only involved in DNA repair.

The dynamics of XPG engagement in NER

After UV-induced DNA damage XPG-EGFP is incorporated into the NER complex with a $t_{0.5}$ of incorporation of about 200 s at 37°C (Fig. 5.3). CHO cells and human fibroblasts show the same assembly rate. This rate of incorporation is somewhat lower than that of XPC and TFIIH ($t_{0.5}$ is 100 and 110 s, respectively [31, 38]) and significantly lower than the 5' endonuclease ERCC1/XPF ($t_{0.5}$ is 65 s [31]). A quantitative model has been proposed that is able to at least partly explain these differences in rates of incorporation [38]. After about 5 min, XPG incorporation into NER complexes reaches a steady state. FRAP experiments show that the protein remains incorporated for about 3.5 min (Fig. 5.6). This is similar to what has been found for XPA (4 to 6 min), TFIIH (4 min) and ERCC1/XPF (4 min) [23, 24, 40] and probably reflects the time required by the NER complex to repair a DNA lesion. XPC has a significantly lower residence time (1-2 min), probably because it leaves the NER complex before repair is complete (Hoogstraten and Vermeulen, unpublished results, [38]) in line with *in vitro* studies [41]. Under steady state condition, at the highest UV doses used here (16 J.m⁻²), maximally about 30% of the XPG-EGFP molecules are associated with a NER complex and therefore engaged in NER (Fig. 5.5). Similar values have been obtained for ERCC1/XPF, XPA and TFIIH [23, 24, 40]. These results support a model in which the NER complex assembles from its individual components on a time scale of minutes, remains intact for 3 to 4 min (maybe except for XPC) during which the actual repair takes place and subsequently dissociates allowing its components to reassemble on another lesion.

Although the dynamic behaviour of XPG is largely the same in CHO cells and in human fibroblasts, a difference is observed in the degree of XPG immobilization under steady state conditions at high UV dose (16 J.m⁻²). In CHO cells an almost two-fold larger fraction of the XPG-EGFP molecules becomes engaged in NER than observed for

human fibroblasts (at 37°C 20% and 30%, respectively (Fig. 5.6)). The simplest explanation is that the expression levels of XPG and/or other NER proteins differ in the two cell types. Alternatively, the endogenous truncated, non-functional XPG protein that is present in the human fibroblasts may compete with the functioning of XPG-EGFP, resulting in a lower immobilized fraction. The XPG mutation in CHO UV135 cells is unknown but can be considered a null mutation, since XPG mRNA can hardly be detected in these cells [29].

DDB2 (p48) does not affect the rate of XPG incorporation kinetics

The kinetics of incorporation of XPG into the NER complex and its residence time in the NER complex are the same in CHO cells and in human fibroblasts (Fig. 5.3, Fig. 5.6). This is remarkable, since CHO cells lack functional DDB2 (p48), which is a subunit of the UV-DDB complex that is thought to enhance the association of the damage recognition protein XPC with DNA lesions, in particular pyrimidine dimers [33, 49, 51]. Since XPC binding precedes incorporation of XPG into the NER complex, it was expected that XPG binding in CHO cells would be slower than in human fibroblasts, which contain endogenous DDB2. Expression of DDB2 in CHO cells did not result in accelerated binding of XPG to UV-induced DNA damage (Fig. 5.3). These results indicate that UV-DDB does not significantly increase the rate of binding of XPG to UV-damaged DNA.

Recruitment of XPG requires functional TFIIH

Previous experiments showed that the incorporation of core NER factors into the NER complex occurs in a specific sequence [40, 60]. However, the precise timing of XPG incorporation could not be established unambiguously. Here we show that incorporation of XPG into the NER complex is temperature-dependent (Fig. 5.3). The same has been

found for ERCC1/XPF, whereas binding of TFIIH and XPC are temperature-independent ([31], M.S. Luijsterburg and R. Van Driel, unpublished data). This was interpreted that binding of ERCC1 requires an enzyme activity, i.e. the helicase activity of the TFIIH subunits XPB and XPD [31]. Therefore, our data suggests that also XPG binding requires TFIIH helicase activity, indicating that TFIIH binding must precede XPG incorporation. Studies in cell lines that have a mutated *XPB* or *XPD* gene show that impairment of TFIIH function severely affects XPG incorporation into the NER complex (Fig. 5.4, Table 1).

Comparison of the effect of different TFIIH mutation indicates which parts of the TFIIH molecule are important for XPG binding. XP/TTD cells [47, 55, 56], which carry a C-terminal R722W substitution in XPD [46], exhibit the most severe reduction of XPG recruitment. This suggests that XPD plays an important role in the recruitment of XPG to sites of UV damage in vivo. Recent findings demonstrate that the stability of the TFIIH complex is severely affected in TTD cells (D. Hoogstraten and W. Vermeulen, unpublished data) [2, 13]. Therefore, it is conceivable that impaired recruitment of XPG in TTD cells is due to the compromised stability, rather than a direct interaction of XPG with the C-terminus of XPD. A recent study demonstrated that phosphorylation of S751 of XPB controls the 5' incision by ERCC1/XPF, whereas the 3' incision by XPG is unaffected [3]. Accordingly, our experiments show that XPG binding is only moderately affected in the XPB mutant, which has a truncated C-terminal domain, lacking the serine 751 residue (Fig. 5.4). This suggests that another part of the TFIIH complex controls the 3' incision by XPG, possibly the N-terminal PH-fold of p62, which has been shown to interact directly with XPG [12]. Nonetheless, our results unambiguously show that stable recruitment of XPG to the pre-incision complex depends on functional TFIIH.

Summarising, our results unfold a consistent and simple picture for the dynamic behaviour of XPG in living CHO cells and human fibroblasts. The protein diffuses freely as a monomer, not showing any prominent interactions other than the nascent NER complex that is formed in UV-damaged cells after binding of XPC and TFIIH. The in vivo dynamics of the XPG protein are remarkably similar in human cells and Chinese hamster cells, showing that major differences in genetic background hardly affect XPG behaviour.

5.5. Materials and Methods

Cell lines

Cell lines used in this study were simian virus 40 (SV-40)-immortalized human fibroblasts MRC5 (NER-proficient), XPCS1RO (XPG-deficient); HeLa cells (NER-proficient), CHO AA8 (NER-proficient), CHO UV135 (XPG-deficient), 3T3 cells (inducible EGFP expression) and the primary human fibroblasts C5RO (NER-proficient), XPCS1BA (XPB-deficient), XP131MA (XPB-deficient), XP6BE (XPD-deficient), XPCS2 (XPD-deficient) and TTD1BEL (XPD-deficient). All cell lines were cultured in a 1:1 mixture of DMEM/Ham's F10 medium containing Ultra-Glutamine (Cambrex Corporation, New Jersey, USA) supplemented with antibiotics and 10% FCS at 37°C in an atmosphere of 5% CO₂.

Generation of cells expressing XPG-EGFP and construction of DDB2-mCherry

EGFP-tagged XPG was generated by in-frame ligation of full length human XPG cDNA into a EGFP N1 vector (Clontech Laboratories, California, USA)). This resulted in a fusion gene under control of a cytomegalovirus promoter encoding an XPG-EGFP hybrid polypeptide. The fusion gene was expressed in the XPG-deficient CHO cell line UV135

and the XPG-deficient SV40-transformed human fibroblast cell line, XPCS1RO-Sv [7]. After subsequent rounds of selection on the presence of the neomycin resistance gene (by G418-resistance selection) and UV-irradiation (to select for functional XPG expression) stable expressing clones were isolated for each of the cell types. The pDDB2-eYFP [33] plasmid was digested with *AgeI* and *BsrGI* in order to replace the eYFP for mCherry [44] to yield pDDB2-mCherry

Immunoblot analysis and UV survival

Cell extracts were generated by sonication, separated by sodium dodecyl sulfate polyacrylamide gel (8%) electrophoresis and transferred to nitrocellulose membranes. Expression of the fusion protein was analyzed by immunoblotting with a mouse monoclonal anti-XPG antibody (IB5 T.C., 1:100 in PBS/0.05% Tween-20; a gift from Dr. J.M. Egly), followed by a secondary antibody (goat anti-mouse conjugated with alkaline phosphatase (Biosource International, California, USA) and detection using bromo-4-chloro-3-indolyl phosphate (BCIP) and nitro blue tetrazolium (NBT). As loading control, mouse monoclonal anti-PCNA antibody (Dako, Glostrup, Denmark) at a dilution of 1:1000 was used. For UV-survival experiments, cells were exposed to different UV doses 2 days after seeding. Survival was determined 3 days after UV-irradiation by measuring cell proliferation with the aid of [³H] thymidine pulse-labeling at 37°C, as described previously [20]

Immunofluorescence

Cells were grown on 24 mm glass coverslips and fixed with 3% paraformaldehyde in PBS with 0.3% Triton X-100 for 20 min at room temperature (RT). Coverslips were washed three times for 10 min with phosphate-buffered saline (PBS) containing 0.1% Triton X-100, and were subsequently incubated for 1 h with PBS containing 1% BSA.

Cells were incubated at RT with the primary antibody for 1.5 - 2h in a moist chamber. Subsequently, coverslips were washed three times for 10 min with PBS-Triton X-100 and 5 min with PBS 1% BSA. Incubation with the secondary antibody was for 30 min – 1 h at RT (dark chamber) followed by extensive washing with PBS 1% BSA and finally PBS. Samples were embedded in Vectashield (Vector Laboratories, California, USA) mounting medium containing 0.1 mg of DAPI (4'-6'-diamidino-2-phenylindole) per ml. Primary antibodies used for immunolabeling were: mouse monoclonal antibody against XPG (8H7, Lab Vision Fremont, California, United States, 1:2000), and affinity-purified rabbit monoclonal antibody against XPC [35]. Secondary antibody: cy3-conjugated goat anti-mouse antiserum and FITC-conjugated anti-rabbit antiserum (Both from Jackson ImmunoResearch Laboratories, West Grove, Pennsylvania, USA). All antibodies were diluted in PBS containing 0.15% glycine and 0.5% bovine serum albumin. Fluorescence microscopy images were obtained with a Leica DMRBE microscope (Leica Microsystems, Wetzlar, Germany) equipped with epifluorescence optics, a PL-FLUOTAR 100x, 1.3-numerical aperture oil immersion lens and a Hamamatsu (Hamamatsu Photonics, Hamamatsu City, Japan) dual mode cooled CCD camera.

Confocal imaging

Digital images of EGFP-expressing living cells were obtained using a Zeiss LSM 410 microscope equipped with a 60-mW Ar laser (488 nm) and a 40x, 1.3-numerical aperture oil immersion lens and a Zeiss LSM 510 equipped with a 60-mW Ar laser (488 nm) and a 40x, 1.2-n.a., or 63x Planapochromat, n.a. 1.4, oil immersion lens (Zeiss, Oberkochen, Germany). Both microscopes were equipped with an objective heater. Unless stated otherwise, living cells were examined at 37°C.

UV irradiation.

For induction of global UV DNA damage, cultured cells on coverslips were rinsed with PBS and irradiated with a Phillips TUV lamp (254 nm) at a dose rate of $\sim 0.8 \text{ J/m}^2/\text{s}$. To induce local UV-damage, cells were UV-irradiated through an polycarbonate filter (Millipore Billerica, Massachusetts, USA) with pores of $5 \mu\text{m}$ diameter, as described previously [32, 60]. At indicated time points after filter removal the cells were either microscopically examined, or fixed with 2% paraformaldehyde and further processed for immuno-histochemistry as described above. For kinetic measurements on locally UV-damaged cells that express XPG-EGFP were grown to confluency in glass bottom dishes (MatTek, Ashland, Massachusetts, USA). Local UV-irradiation was performed as described [31]. Briefly, a petridish was filled with microscopy medium (137 mM NaCl, 5,4 mM KCl, 1,8 mM CaCl_2 , 0,8 mM MgSO_4 , 20 mM D-glucose and 20 mM HEPES) and a small piece of Alcian blue-coated filter ($5 \mu\text{m}$ pores) was sunk onto the cells. A glass ring was carefully placed on top of the filter after which the petridish was sealed with a lid containing a quartz window. The cells were transferred to an Zeiss Axiovert 200 M microscope with a 37° incubator and an objective heater, to ensure the appropriate temperature for this live cell experiment. Subsequently, irradiation was performed using a homemade box, containing four UV lamps (Philips TUV 9W PL-S) above the microscope stage. The UV dose rate was measured to be 3 W.m^{-2} at 254 nm. Cells were irradiated for 39 s, resulting in a UV dose of 100 J.m^{-2}

FRAP and fluorescence loss in photobleaching (FLIP)

For all experiments cells were seeded onto 24 mm glass coverslips three days prior to the experiments.

FRAP experiments. Using a Zeiss LSM510 META confocal microscope, equipped with a 60 mW Argon laser and a 40x oil immersion lens (1.2 n.a.), mobility measurements were performed by FRAP analysis at high time resolution (Strip-FRAP; [23], modified). A strip spanning the nucleus was photo-bleached for 20 ms at 100% laser intensity (120-160 μ W, argon laser at 488nm). Recovery of fluorescence within the strip was monitored with 20 ms intervals at low laser intensity (450-750nW) to avoid photobleaching by the probe beam. Measurements were performed at 37°C, using a heated stage with feedback temperature control. Raw data were corrected for background and fluctuations in the monitoring laser power.

Fluorescence Loss in Photobleaching (FLIP).

To determine the residence time of XPG at locally UV-irradiated areas local UV irradiation was applied as described above. Using a Zeiss LSM 410 microscope equipped with a 60 mW Argon laser (488 nm) and a 40x, 1.3 n.a. oil immersion lens, a strip was bleached (at 100% 488 nm) for 5 s near the edge of the nucleus opposite to the local damage site. Redistribution of fluorescence was monitored over time (at 488 nm). Evaluation was performed by comparing the loss of fluorescence of bound protein over time (in local damaged area) versus non-bound protein (outside the damaged area) of EGFP-tagged protein. The residence time of XPG in a NER complex was calculated as described elsewhere [24]

Combined FLIP-FRAP analysis.

Using a Zeiss LSM510 META confocal microscope, equipped with a 60-mW Argon laser and a 40x oil immersion lens (1.2 n.a.), a 2 μ m (30-pixel) strip spanning the cell nucleus at one pole was bleached for 1s at a laser power of 120-160 μ W. Redistribution of fluorescence throughout the nucleus was recorded at low laser power (1.6-1.9 μ W),

keeping monitoring bleaching to a minimum (<5 %). We compared the difference between the fluorescence in the bleached and the unbleached area (at a distance of 150 pixels = 10.2 μm) of the nucleus, and plotted the fluorescence values against time. Unless otherwise specified, measurements were performed at 37°C, using a heated stage with feedback temperature control. At least 9 independent measurements were averaged to form a single mobility curve. Redistribution of fluorescence was corrected for lateral cell movement. Rotating cells, or cells moving out of focus were excluded from evaluation.

FRAP analysis

For analysis of FRAP data, FRAP curves were normalized to pre-bleach values and the best fitting curve (least squares) was picked from a large set of computer simulated FRAP curves in which three parameters representing mobility properties were varied: diffusion rate (ranging from 0.04 to 25 $\mu\text{m}^2/\text{s}$), immobile fraction (0, 10, 20, 30, 40, 50 %) and time spent in immobile states, ranging from very short residence times (0.02, 0.04, 0.08, ..., 1 s) to relatively long residence times (2, 4, 8, 16, 32, 64, 128, ∞ s). Monte Carlo computer simulations used to generate FRAP curves were based on a model of diffusion in an ellipsoid volume representing the cell nucleus, and simple binding kinetics representing binding to immobile elements in the cell nucleus. Simulations were performed at unit time steps corresponding to the experimental sample rate of 21 ms. Diffusion was simulated by each step deriving novel positions $M(x+ dx, y+ dy, z+ dz)$ for all mobile molecules $M(x, y, z)$, where $dx = G(r_1)$, $dy = G(r_2)$ and $dz = G(r_3)$, r_i is a random number ($0 \leq r_i \leq 1$) chosen from a uniform distribution, and $G(r_i)$ is an inversed cumulative Gaussian distribution with $\mu = 0$ and $\sigma^2 = 6Dt$, where D is the diffusion coefficient and t is time measured in unit time steps. Immobilization was based on simple binding kinetics described by: $k_{on}/k_{off} = F_{imm} / (1 - F_{imm})$, where F_{imm} is the relative number of immobile

molecules. The chance for each particle to become immobilized (representing chromatin-binding) was defined as $P_{immobilise} = k_{on} = k_{off} \cdot F_{imm} / (1 - F_{imm})$, where $k_{off} = 1 / t_{imm}$, and t_{imm} is the average time spent in immobile complexes measured in unit time steps; the chance to release was $P_{mobilise} = k_{off} = 1 / t_{imm}$. The FRAP procedure was simulated on the basis of an experimentally derived 3D laser intensity profile providing a chance based on 3D position for each molecule to get bleached during simulation of the bleach pulse.

Assembly at local damaged sites

For analyzing the dynamics of NER complex assembly cells were kept on an Axiovert 200M microscope stage at the appropriate temperature, using a temperature-controlled microscope chamber. The objective (Zeiss Apochromat 100X) was temperature-controlled with an objective heater. One image was taken to determine the position and the GFP fluorescence intensity of the cells (monochromator at 470 nm, bandwidth 20 nm). A reflection image of the filter was obtained moving up in the z-direction. Images of the cells and the filter were overlaid to determine which nuclei are located under a filter pore. The distance between cells and filter was measured with a Piezo electrical element and had to be less than 7 μm to obtain a well-defined damaged area. CHO cells were transiently transfected with DDB2-mCherry with lipofectamine 2000 (Invitrogen, Breda, the Netherlands) according to the manufacturer's instructions. The cells were irradiated ($100 \text{ J}\cdot\text{m}^{-2}$) and images were collected at 20 s interval for 30 minutes to allow EGFP accumulation in the locally damaged area to reach a plateau level. DDB2-mCherry accumulation was monitored with $550 \pm 20 \text{ nm}$. The accumulation of XPG-EGFP at sites of local damage was quantified with Object-Image software [59]. A macro was written to determine the centre of gravity of the fluorescent spot at every time point. Next, the average fluorescence intensity was measured in a region of $20 \mu\text{m}^2$ around the centre of gravity for every time point. The average intensity of the entire nucleus, except the

damaged area, was also measured, representing the unbound protein pool. The EGFP signal in the undamaged area was subtracted from the damaged area. The resulting value represents the NER-related bound protein fraction. All values were corrected for photo bleaching. Time courses were normalized with respect to the plateau level. Start of the UV irradiation was defined as $t=0$. Assembly curves were normalized to 1 or to the bound fraction calculated by the equation: $\text{Bound (\%)} = (I_{\text{spot}} - I_{\text{outspot}}) * \text{pixels}_{\text{spot}} / (I_{\text{nucleus}} - I_{\text{background}}) * \text{pixels}_{\text{nucleus}}$, where I_{spot} and I_{outspot} are the average pixel intensities inside the damaged spot and outside the spot, respectively. I_{nucleus} is the average pixel intensity of the nucleus, including the spot and $I_{\text{background}}$ is the average pixel intensity outside the cell.

5.7. Acknowledgement

This work was supported by grants of the Netherlands Organisation for Scientific Research (NWO): NWO-CW 700.98.302 (AZ); ZonMW 912-03-012 (MSL), 917-46-364 (WV) and 901-01-229.

The DDB2-EYFP plasmid was kindly provided by Dr. L.H. Mullenders and the mCherry cDNA was kindly provided by Dr. R.Y. Tsien.

The authors would like to thank A. Theil and N. Wijgers for technical assistance, N.O.E. Vischer (Center for advanced microscopy (CAM)/UvA) for valuable assistance with data analysis. Dr. J. Goedhart (CAM) for critical reading of the manuscript and Drs. E.M.M. Manders and T.W.J. Gadella (CAM) for support.

References

1. Araujo, S. J., E. A. Nigg, and R. D. Wood. (2001) Strong functional interactions of TFIIH with XPC and XPG in human DNA nucleotide excision repair, without a preassembled repairosome. *Mol Cell Biol* 21:2281-2291.

2. Botta, E., T. Nardo, A. R. Lehmann, J. M. Egly, A. M. Pedrini, and M. Stefanini. (2002) Reduced level of the repair/transcription factor TFIIH in trichothiodystrophy. *Hum Mol Genet* 11:2919-2928.
3. Coin, F., J. Auriol, A. Tapias, P. Clivio, W. Vermeulen, and J. M. Egly. (2004) Phosphorylation of XPB helicase regulates TFIIH nucleotide excision repair activity. *Embo J* 23:4835-4846.
4. de Laat, W. L., E. Appeldoorn, K. Sugasawa, E. Weterings, N. G. Jaspers, and J. H. Hoeijmakers. (1998) DNA-binding polarity of human replication protein A positions nucleases in nucleotide excision repair. *Genes Dev* 12:2598-2609.
5. de Laat, W. L., N. G. Jaspers, and J. H. Hoeijmakers. (1999) Molecular mechanism of nucleotide excision repair. *Genes Dev* 13:768-785.
6. Dunand-Sauthier, I., M. Hohl, F. Thorel, P. Jaquier-Gubler, S. G. Clarkson, and O. D. Scharer. (2005) The spacer region of XPG mediates recruitment to nucleotide excision repair complexes and determines substrate specificity. *J Biol Chem* 280:7030-7037.
7. Ellison, A. R., T. Nospikel, N. G. Jaspers, S. G. Clarkson, and D. C. Gruenert. (1998) Complementation of transformed fibroblasts from patients with combined xeroderma pigmentosum-Cockayne syndrome. *Exp Cell Res* 243:22-28.
8. Evans, E., J. G. Moggs, J. R. Hwang, J. M. Egly, and R. D. Wood. (1997) Mechanism of open complex and dual incision formation by human nucleotide excision repair factors. *Embo J* 16:6559-6573.
9. Fitch, M. E., S. Nakajima, A. Yasui, and J. M. Ford. (2003) In vivo recruitment of XPC to UV-induced cyclobutane pyrimidine dimers by the DDB2 gene product. *J Biol Chem* 278:46906-46910.
10. Friedberg, E. C. (2001) How nucleotide excision repair protects against cancer. *Nat Rev Cancer* 1:22-33.
11. Friedberg, E. C. (2005) Suffering in silence: the tolerance of DNA damage. *Nat Rev Mol Cell Biol* 6:943-953.
12. Gervais, V., V. Lamour, A. Jawhari, F. Frindel, E. Wasielewski, S. Dubaele, J. M. Egly, J. C. Thierry, B. Kieffer, and A. Poterszman. (2004) TFIIH contains a PH

- domain involved in DNA nucleotide excision repair. *Nat Struct Mol Biol* 11:616-622.
13. Giglia-Mari, G., F. Coin, J. A. Ranish, D. Hoogstraten, A. Theil, N. Wijgers, N. G. Jaspers, A. Raams, M. Argentini, P. J. van der Spek, E. Botta, M. Stefanini, J. M. Egly, R. Aebersold, J. H. Hoeijmakers, and W. Vermeulen. (2004) A new, tenth subunit of TFIIH is responsible for the DNA repair syndrome trichothiodystrophy group A. *Nat Genet* 36:714-719.
 14. Giglia-Mari, G., C. Miquel, A. F. Theil, P. O. Mari, D. Hoogstraten, J. M. Ng, C. Dinant, J. H. Hoeijmakers, and W. Vermeulen. (2006) Dynamic Interaction of TTDA with TFIIH Is Stabilized by Nucleotide Excision Repair in Living Cells. *PLoS Biol* 4:e156.
 15. Green, C. M., and G. Almouzni. (2003). Local action of the chromatin assembly factor CAF-1 at sites of nucleotide excision repair in vivo. *Embo J* 22:5163-5174.
 16. Guzder, S. N., P. Sung, L. Prakash, and S. Prakash. (1996) Nucleotide excision repair in yeast is mediated by sequential assembly of repair factors and not by a pre-assembled repairosome. *J Biol Chem* 271:8903-8910.
 17. Guzder, S. N., P. Sung, L. Prakash, and S. Prakash. (1999) Synergistic interaction between yeast nucleotide excision repair factors NEF2 and NEF4 in the binding of ultraviolet-damaged DNA. *J Biol Chem* 274:24257-24262.
 18. Guzder, S. N., P. Sung, L. Prakash, and S. Prakash. (1997) Yeast Rad7-Rad16 complex, specific for the nucleotide excision repair of the nontranscribed DNA strand, is an ATP-dependent DNA damage sensor. *J Biol Chem* 272:21665-21668.
 19. Habraken, Y., P. Sung, S. Prakash, and L. Prakash. (1996) Transcription factor TFIIH and DNA endonuclease Rad2 constitute yeast nucleotide excision repair factor 3: implications for nucleotide excision repair and Cockayne syndrome. *Proc Natl Acad Sci U S A* 93:10718-10722.
 20. Hamel, B. C., A. Raams, A. R. Schuitema-Dijkstra, P. Simons, I. van der Burgt, N. G. Jaspers, and W. J. Kleijer. (1996) Xeroderma pigmentosum--Cockayne syndrome complex: a further case. *J Med Genet* 33:607-610.

21. Hanawalt, P. C. (2000) DNA repair. The bases for Cockayne syndrome. *Nature* 405:415-416.
22. Hoeijmakers, J. H. (2001) Genome maintenance mechanisms for preventing cancer. *Nature* 411:366-374.
23. Hoogstraten, D., A. L. Nigg, H. Heath, L. H. Mullenders, R. van Driel, J. H. Hoeijmakers, W. Vermeulen, and A. B. Houtsmuller. (2002) Rapid switching of TFIIH between RNA polymerase I and II transcription and DNA repair in vivo. *Mol Cell* 10:1163-1174.
24. Houtsmuller, A. B., S. Rademakers, A. L. Nigg, D. Hoogstraten, J. H. Hoeijmakers, and W. Vermeulen. (1999) Action of DNA repair endonuclease ERCC1/XPF in living cells. *Science* 284:958-961.
25. Iben, S., H. Tschochner, M. Bier, D. Hoogstraten, P. Hozak, J. M. Egly, and I. Grummt. (2002) TFIIH plays an essential role in RNA polymerase I transcription. *Cell* 109:297-306.
26. Klungland, A., M. Hoss, D. Gunz, A. Constantinou, S. G. Clarkson, P. W. Doetsch, P. H. Bolton, R. D. Wood, and T. Lindahl. (1999) Base excision repair of oxidative DNA damage activated by XPG protein. *Mol Cell* 3:33-42.
27. Lee, S. K., S. L. Yu, L. Prakash, and S. Prakash. (2002) Requirement of yeast RAD2, a homolog of human XPG gene, for efficient RNA polymerase II transcription. implications for Cockayne syndrome. *Cell* 109:823-834.
28. Lehmann, A. R. (2003) DNA repair-deficient diseases, xeroderma pigmentosum, Cockayne syndrome and trichothiodystrophy. *Biochimie* 85:1101-1111.
29. MacInnes, M. A., J. A. Dickson, R. R. Hernandez, D. Learmonth, G. Y. Lin, J. S. Mudgett, M. S. Park, S. Schauer, R. J. Reynolds, G. F. Strniste, and et al. (1993) Human ERCC5 cDNA-cosmid complementation for excision repair and bipartite amino acid domains conserved with RAD proteins of *Saccharomyces cerevisiae* and *Schizosaccharomyces pombe*. *Mol Cell Biol* 13:6393-6402.
30. Mitchell, J. R., J. H. Hoeijmakers, and L. J. Niedernhofer. (2003) Divide and conquer: nucleotide excision repair battles cancer and ageing. *Curr Opin Cell Biol* 15:232-240.

31. Mone, M. J., T. Bernas, C. Dinant, F. A. Goedvree, E. M. Manders, M. Volker, A. B. Houtsmuller, J. H. Hoeijmakers, W. Vermeulen, and R. van Driel. (2004) In vivo dynamics of chromatin-associated complex formation in mammalian nucleotide excision repair. *Proc Natl Acad Sci U S A* 101:15933-5937.
32. Mone, M. J., M. Volker, O. Nikaido, L. H. Mullenders, A. A. van Zeeland, P. J. Verschure, E. M. Manders, and R. van Driel. (2001) Local UV-induced DNA damage in cell nuclei results in local transcription inhibition. *EMBO Rep* 2:1013-1017.
33. Moser, J., M. Volker, H. Kool, S. Alekseev, H. Vrieling, A. Yasui, A. A. van Zeeland, and L. H. Mullenders. (2005) The UV-damaged DNA binding protein mediates efficient targeting of the nucleotide excision repair complex to UV-induced photo lesions. *DNA Repair (Amst)* 4:571-582.
34. Mu, D., C. H. Park, T. Matsunaga, D. S. Hsu, J. T. Reardon, and A. Sancar. (1995) Reconstitution of human DNA repair excision nuclease in a highly defined system. *J Biol Chem* 270:2415-2418.
35. Ng, J. M., W. Vermeulen, G. T. van der Horst, S. Bergink, K. Sugawara, H. Vrieling, and J. H. Hoeijmakers. (2003) A novel regulation mechanism of DNA repair by damage-induced and RAD23-dependent stabilization of xeroderma pigmentosum group C protein. *Genes Dev* 17:1630-1645.
36. O'Donovan, A., A. A. Davies, J. G. Moggs, S. C. West, and R. D. Wood. (1994) XPG endonuclease makes the 3' incision in human DNA nucleotide excision repair. *Nature* 371:432-435.
37. Park, M. S., J. A. Knauf, S. H. Pendergrass, C. H. Coulon, G. F. Strniste, B. L. Marrone, and M. A. MacInnes. (1996) Ultraviolet-induced movement of the human DNA repair protein, Xeroderma pigmentosum type G, in the nucleus. *Proc Natl Acad Sci U S A* 93:8368-8373.
38. Politi, A., M. J. Mone, A. B. Houtsmuller, D. Hoogstraten, W. Vermeulen, R. Heinrich, and R. van Driel. (2005) Mathematical Modeling of Nucleotide Excision Repair Reveals Efficiency of Sequential Assembly Strategies. *Mol Cell* 19:679-690.

39. Protic-Sabljić, M., S. Seetharam, M. M. Seidman, and K. H. Kraemer. (1986) An SV40-transformed xeroderma pigmentosum group D cell line: establishment, ultraviolet sensitivity, transfection efficiency and plasmid mutation induction. *Mutat Res* 166:287-294.
40. Rademakers, S., M. Volker, D. Hoogstraten, A. L. Nigg, M. J. Mone, A. A. Van Zeeland, J. H. Hoeijmakers, A. B. Houtsmuller, and W. Vermeulen. (2003) Xeroderma pigmentosum group A protein loads as a separate factor onto DNA lesions. *Mol Cell Biol* 23:5755-5767.
41. Riedl, T., F. Hanaoka, and J. M. Egly. (2003) The comings and goings of nucleotide excision repair factors on damaged DNA. *Embo J* 22:5293-5303.
42. Sarker, A. H., S. E. Tsutakawa, S. Kostek, C. Ng, D. S. Shin, M. Peris, E. Campeau, J. A. Tainer, E. Nogales, and P. K. Cooper. (2005) Recognition of RNA polymerase II and transcription bubbles by XPG, CSB, and TFIIH: insights for transcription-coupled repair and Cockayne Syndrome. *Mol Cell* 20:187-198.
43. Schaeffer, L., R. Roy, S. Humbert, V. Moncollin, W. Vermeulen, J. H. Hoeijmakers, P. Chambon, and J. M. Egly. (1993) DNA repair helicase: a component of BTF2 (TFIIH) basic transcription factor. *Science* 260:58-63.
44. Shaner, N. C., R. E. Campbell, P. A. Steinbach, B. N. Giepmans, A. E. Palmer, and R. Y. Tsien. (2004) Improved monomeric red, orange and yellow fluorescent proteins derived from *Discosoma* sp. red fluorescent protein. *Nat Biotechnol* 22:1567-1572.
45. Shivji, M. K., V. N. Podust, U. Hubscher, and R. D. Wood. (1995) Nucleotide excision repair DNA synthesis by DNA polymerase epsilon in the presence of PCNA, RFC, and RPA. *Biochemistry* 34:5011-5017.
46. Stefanini, M., P. Lagomarsini, S. Giliani, T. Nardo, E. Botta, A. Peserico, W. J. Kleijer, A. R. Lehmann, and A. Sarasin. (1993) Genetic heterogeneity of the excision repair defect associated with trichothiodystrophy. *Carcinogenesis* 14:1101-1105.
47. Stefanini, M., W. Vermeulen, G. Weeda, S. Giliani, T. Nardo, M. Mezzina, A. Sarasin, J. I. Harper, C. F. Arlett, J. H. Hoeijmakers, and et al. (1993) A new

- nucleotide-excision-repair gene associated with the disorder trichothiodystrophy. *Am J Hum Genet* 53:817-821.
48. Sugasawa, K., J. M. Ng, C. Masutani, S. Iwai, P. J. van der Spek, A. P. Eker, F. Hanaoka, D. Bootsma, and J. H. Hoeijmakers. (1998) Xeroderma pigmentosum group C protein complex is the initiator of global genome nucleotide excision repair. *Mol Cell* 2:223-232.
 49. Sugasawa, K., Y. Okuda, M. Saijo, R. Nishi, N. Matsuda, G. Chu, T. Mori, S. Iwai, K. Tanaka, and F. Hanaoka. (2005) UV-induced ubiquitylation of XPC protein mediated by UV-DDB-ubiquitin ligase complex. *Cell* 121:387-400.
 50. Svejstrup, J. Q., Z. Wang, W. J. Feaver, X. Wu, D. A. Bushnell, T. F. Donahue, E. C. Friedberg, and R. D. Kornberg. (1995) Different forms of TFIIH for transcription and DNA repair: holo-TFIIH and a nucleotide excision repairsome. *Cell* 80:21-28.
 51. Tang, J. Y., B. J. Hwang, J. M. Ford, P. C. Hanawalt, and G. Chu. (2000) Xeroderma pigmentosum p48 gene enhances global genomic repair and suppresses UV-induced mutagenesis. *Mol Cell* 5:737-744.
 52. Taylor, E. M., B. C. Broughton, E. Botta, M. Stefanini, A. Sarasin, N. G. Jaspers, H. Fawcett, S. A. Harcourt, C. F. Arlett, and A. R. Lehmann. (1997) Xeroderma pigmentosum and trichothiodystrophy are associated with different mutations in the XPD (ERCC2) repair/transcription gene. *Proc Natl Acad Sci U S A* 94:8658-8663.
 53. Thorel, F., A. Constantinou, I. Dunand-Sauthier, T. Nospikel, P. Lalle, A. Raams, N. G. Jaspers, W. Vermeulen, M. K. Shivji, R. D. Wood, and S. G. Clarkson. (2004) Definition of a short region of XPG necessary for TFIIH interaction and stable recruitment to sites of UV damage. *Mol Cell Biol* 24:10670-10680.
 54. van den Boom, V., E. Citterio, D. Hoogstraten, A. Zotter, J. M. Egly, W. A. van Cappellen, J. H. Hoeijmakers, A. B. Houtsmuller, and W. Vermeulen. (2004) DNA damage stabilizes interaction of CSB with the transcription elongation machinery. *J Cell Biol* 166:27-36.

55. Vermeulen, W., E. Bergmann, J. Auriol, S. Rademakers, P. Frit, E. Appeldoorn, J. H. Hoeijmakers, and J. M. Egly. (2000) Sublimiting concentration of TFIIH transcription/DNA repair factor causes TTD-A trichothiodystrophy disorder. *Nat Genet* 26:307-313.
56. Vermeulen, W., S. Rademakers, N. G. Jaspers, E. Appeldoorn, A. Raams, B. Klein, W. J. Kleijer, L. K. Hansen, and J. H. Hoeijmakers. (2001) A temperature-sensitive disorder in basal transcription and DNA repair in humans. *Nat Genet* 27:299-303.
57. Vermeulen, W., R. J. Scott, S. Rodgers, H. J. Muller, J. Cole, C. F. Arlett, W. J. Kleijer, D. Bootsma, J. H. Hoeijmakers, and G. Weeda. (1994) Clinical heterogeneity within xeroderma pigmentosum associated with mutations in the DNA repair and transcription gene ERCC3. *Am J Hum Genet* 54:191-200.
58. Vermeulen, W., M. Stefanini, S. Giliani, J. H. Hoeijmakers, and D. Bootsma. (1991) Xeroderma pigmentosum complementation group H falls into complementation group D. *Mutat Res* 255:201-208.
59. Vischer, N. O., P. G. Huls, R. I. Ghauharali, G. J. Brakenhoff, N. Nanninga, and C. L. Woldringh. (1999) Image cytometric method for quantifying the relative amount of DNA in bacterial nucleoids using *Escherichia coli*. *J Microsc* 196 (Pt 1):61-68.
60. Volker, M., M. J. Mone, P. Karmakar, A. van Hoffen, W. Schul, W. Vermeulen, J. H. Hoeijmakers, R. van Driel, A. A. van Zeeland, and L. H. Mullenders. (2001) Sequential assembly of the nucleotide excision repair factors in vivo. *Mol Cell* 8:213-224.
61. Wakasugi, M., A. Kawashima, H. Morioka, S. Linn, A. Sancar, T. Mori, O. Nikaido, and T. Matsunaga. (2002) DDB accumulates at DNA damage sites immediately after UV irradiation and directly stimulates nucleotide excision repair. *J Biol Chem* 277:1637-1640.
62. Wakasugi, M., and A. Sancar. (1998) Assembly, subunit composition, and footprint of human DNA repair excision nuclease. *Proc Natl Acad Sci U S A* 95:6669-6674.

63. Wakasugi, M., and A. Sancar. (1999) Order of assembly of human DNA repair excision nuclease. *J Biol Chem* 274:18759-18768.

Chapter

6

Translational Mobility of EGF Receptor Fusion Proteins over Short and Long Distances – Complementarity of Fluorescence Correlation Microscopy and FRAP in Cellular Diffusion Measurements

G. Vámosi, S. M. Ibrahim, E. Friedländer, R. Brock,
V. Majewski, T. M. Jovin, S. Damjanovich,
and G. Vereb

6.1 Abstract

The translational mobility of epidermal growth factor receptor-green fluorescent protein fusion proteins (EGFR-GFP) transfected into Chinese hamster ovary cells was measured by fluorescence correlation microscopy (FCM) and fluorescence recovery after photobleaching (FRAP). For both stimulated and unstimulated receptors, at least three distinct molecular processes contributed to the autocorrelation functions. Five models taking account of different photophysical as well as diffusional processes were compared with respect to their ability to describe the experimental data. No clear distinction could be made between anomalous diffusion and free Brownian diffusion. The inclusion of a protonation-dependent blinking term greatly increased the reliability of fitting the diffusion constants. A significant decrease in receptor mobility upon stimulation was observed independent of the model of fit. In contrast, the specific fluorescence per molecule did not change. These observations are best explained by a signaling dependent attachment of the receptors to slowly moving or stationary molecular structures such as to the underlying cytoskeleton or larger receptor aggregates that were already photobleached. FRAP measurements of unstimulated receptors yielded diffusion constants smaller by a factor of ~ 10 in comparison to those derived from the autocorrelation measurements. When only the first few seconds of the FRAP recovery curves were fitted, the diffusion constants converged towards those determined by FCM. FCM probes molecular movements over short distances, whereas in FRAP recovery of fluorescence results from diffusion of molecules over longer distances and may therefore be subject to a large number of diffusional barriers. The two techniques complement each other in the determination of molecular mobilities over long and short temporal and spatial scales. Limitations of cellular FCM measurements in resting and stimulated cells are discussed. A method to measure the axial and lateral dimensions of the detection volume directly is presented.

6.2 Introduction

The epidermal growth factor receptor (EGFR) is a member of the erbB receptor family. Binding of epidermal growth factor (EGF) to this 170 kDa receptor induces activation of the tyrosine kinase catalytic domain resulting in autophosphorylation of the receptor C-terminal domain as well as phosphorylation of signal transduction proteins [1].

Although it is generally accepted that a receptor dimer in complex with a ligand is responsible for inducing the signal transduction cascade, the exact mechanism of EGFR activation is still under debate. Two models have been proposed. According to the conformational activation model [2], ligand binding increases kinase activity by inducing an as yet uncharacterized conformational change in the transmembrane segment of signaling competent receptors that are present as preformed dimers. This model is supported by FRET data [2] as well as data from Stern and coworkers [3] demonstrating that a point mutation in the transmembrane domain can enhance kinase activity even without binding of EGF. Recently it has been shown by chemical crosslinking followed by sucrose gradient centrifugation that EGFR has the ability to form dimers even in the absence of ligand [4] and the authors also presented evidence for EGF inducing a twist of the juxtamembrane domain of the receptor upon binding. Transmembrane domains of the EGFR were found to dimerize when expressed in *E. coli* [5].

The second model is that of ligand-induced allosteric receptor dimerization [6]. Data coherent with this model include the following observations. Upon incubation of cells with EGF, oligomerization was detected by electron microscopy of immunogold labeled EGFR [7]. Bivalent anti-EGFR antibodies capable of inducing dimerization of the receptors were able to induce activation in the absence of EGF [8]. Chemical crosslinking could also induce kinase activity [9, 10]. Furthermore, the activation kinetics of solubilized receptors has a second order concentration dependence [6]. Recently, titration

calorimetry and small-angle X-ray scattering led to the formulation of a model in which the extracellular domain of EGFR dimerizes only after binding an EGF molecule. [11]. Contradictory to this, single molecule tracking revealed that EGFR dimers occupied by one EGF molecule were pre-formed before binding the second EGF [12].

In order to investigate the molecular details of the activation event, a number of luminescence techniques have been employed. Fluorescence resonance energy transfer (FRET; [13]) has been applied in probing the proximity or mobility of receptors or receptor subunits [2, 14-16]. Receptor mobility was determined by fluorescence recovery after photobleaching (FRAP; [17, 18]) or single particle tracking [19, 20]. In most cases, the reporter group was introduced in the form of labeled ligands or Fab-fragments specific for the extracellular domain. Attachment of the reporter group to the ligand limits the scope of analytical questions to activated receptors, while anti-receptor Fab-fragments suffer from rather low affinity and possible interference with activation. In contrast, the generation of active receptor - green fluorescent protein (GFP) fusion proteins for endogenous labeling obviates both of these problems.

In this paper, fluorescence correlation microscopy (FCM, [21-24]) and fluorescence recovery after photobleaching (FRAP; [17, 25]) were employed to investigate activation-induced changes in receptor mobility and aggregation in molecular detail. Chinese hamster ovary (CHO) cells stably transfected with an EGFR-GFP fusion protein served as model system. The analysis of the GFP fusion proteins is less obtrusive than the labeling strategies employed previously in that the intact receptor is examined in living cells without interference from the addition of reporter groups to the ligand-binding domain.

Fluorescence correlation spectroscopy (FCS) derives information on molecule number and diffusion rates from temporal fluctuations arising from passage of molecules

through femtoliter confocal detection volumes. In addition, changes in molecular aggregation can be detected from the fluorescence per molecule (fpm) calculated by dividing the total fluorescence by the average number of molecules. Photophysical processes affecting the quantum yield may contribute additional components to the temporal autocorrelation function. For GFP pH-dependent and independent protonation equilibria causing dark state formation (“blinking”) contribute two components in the upper microsecond time range [26]. Fluorescence correlation microscopy (FCM) integrates the FCS modality into a microscope system with high-sensitivity digital imaging and micropositioning in order to perform FCS measurements in different locations or compartments of living cells [22, 27]. In FCS, the mean residence time of a molecule in the detection volume needs to be short with respect to the total measurement time. Otherwise, the molecules may be bleached at the laser powers required for recording autocorrelation functions. In living cells measurement times of several minutes may be hampered by cellular movements. This cellular characteristic limits FCS to the analysis of particles having a diffusion coefficient of 10^{-10} cm²/s or larger. In FRAP, information on molecular mobility is derived from recovery curves of fluorescence after locally bleaching fluorophores with a high intensity laser pulse. While in FCS fluctuations may arise from molecules moving about in the immediate vicinity of the detection volume, only, in FRAP recovery results from diffusion of molecules over relatively long distances.

In our measurements, autocorrelation functions for EGFR-GFP fusion proteins in both resting and stimulated cells were best described by functions consisting of at least three components with time constants in the upper millisecond, lower millisecond to upper microsecond and lower microsecond time range. Five different models were employed to fit the autocorrelation functions: (i) a model containing two diffusional components and one triplet term, (ii) a model assuming a triplet term, two GFP blinking

terms and one diffusional component, models assuming a triplet term with one freely diffusing component and one anomalous diffusing component with (iii) or without (iv) a blinking term, or (v) a model including a triplet term, a blinking term and anomalous diffusion for both the slow and the fast component. Inclusion of a blinking term significantly improved the quality of the fits. Fits assuming either Brownian diffusion or anomalous diffusion described the experimental data equally well.

Upon EGF stimulation, observed decrease in receptor mobility was significantly more than, that expected for receptor dimerization. The number of diffusing species decreased by only ~22 %, and the average fluorescence intensity per molecule remained almost unchanged. These observations are best explained by possible attachment to immobile or large structures of low mobility such as the membrane-proximal actin cytoskeleton, , or by hindrance of receptor diffusion by actin polymerization [28, 29]. The diffusion constants derived from the autocorrelation functions were larger than the ones derived from FRAP by a factor of ~10. Only when considering very short recovery time intervals did the diffusion constants derived from FRAP approach those from FCS measurements. Considering the local nature of FCS measurements in comparison to the long-range plasma membrane characteristics reflected by FRAP, the large diffusion constant derived from the FCS measurements is evidence of a high molecular mobility in membrane microdomains.

To our knowledge this is the first systematic comparison of the information obtained by both FCS and FRAP on receptor diffusion. Here we show that the two techniques arrive at complementary descriptions of membrane organization on the submicrometer as well as the micrometer scale.

6.3. Materials and methods

Cell culture

A431 epidermoid carcinoma cells, Chinese hamster ovary (CHO) cells and transfected CHO cells stably expressing the fusion protein of the epidermal growth factor receptor and the F64L, S65T mutant of GFP (EGFP) [23] were grown in a 5% CO₂ humidified atmosphere at 37°C in DMEM supplemented with 10% FCS. Two different subclones of the transfected CHO cells, differing with respect to the level of EGFR-GFP expression were used. F1-10 expressed an estimated 2×10^4 receptors per cell and F1-4 an estimated 10^6 receptors per cell. For EGF stimulation, 8 or 50 nM murine EGF (IC Chemikalien, Ismaning, Germany) was used.

Western blot analysis of tyrosine phosphorylation after receptor stimulation with EGF

Tyrosine phosphorylation of cellular proteins was determined in Western blots of EGF-stimulated and control cell lysates. Aliquots containing lysates of 4×10^6 cells were boiled in nonreducing SDS-PAGE sample buffer for 10 min. Proteins were separated electrophoretically on a Bio-Rad minigel apparatus (Bio-Rad, Richmond, VA) using a 10% gel and were transferred to PVDF-Imobilon P membranes (Millipore). Membranes blocked by Tween20-PBS (TPBS) containing 1% BSA were incubated overnight with 10 ng/ml SC-508-HRP peroxidase-conjugated anti-phosphotyrosine antibody (PY20, Santa Cruz Biochemicals) in TPBS-1% BSA. After washing three times in TPBS and once in PBS, membranes were developed with ECL reagents (Amersham Pharmacia Biotech), exposed onto Fuji X-ray film and digitized at 1200 dpi. Total protein of the membrane was determined by amido-black staining.

Measurement of Ca²⁺ responses upon EGF stimulation

Intracellular Ca²⁺ concentrations were measured by fluorescence microscopy using the Calcium indicator dye Fura-2 (Molecular Probes, Eugene, OR) [30]. The ratio I_{340}/I_{380} of the fluorescence intensities excited at 340 and 380 nm is independent of dye concentration and is a monotonously increasing function of Ca²⁺ concentration. F1-10, A431 and CHO cells were grown on 25 mm diameter round coverslips in DMEM. Before the experiment, cells were starved for 12 hours in serum-free medium. Cells were loaded with 2 µg/ml Fura-2-AM for 30 minutes at 37 °C, washed twice with HBS (containing, in mM: 135 NaCl, 5 KCl, 1 MgCl₂, 1.8 CaCl₂, 5 glucose, 10 HEPES, pH 7.4) and imaged with an Attofluor Digital Ratio Imaging System (Atto Instruments, Rockville, MD) with a time resolution of 0.2 frames per second. Spectral ranges were 340 ± 12.5 nm and 380 ± 12.5 nm for excitation and larger than 520 nm for emission. After 100 seconds 0, 8 or 50 nM EGF was administered, and at 400 seconds 2 µg/ml of ionomycin was added to permeabilize the plasma membranes for Ca²⁺. To display activation-induced temporal changes in Ca²⁺ concentration ratio images (I_{334}/I_{380}) corrected for field flatness were calculated, and the average ratio of regions-of-interest (ROIs) covering the inside of each cell were graphed versus time.

Fluorescence correlation microscopy

Measurement of fluorescence autocorrelation

For the measurement of fluorescence autocorrelation, the instrument described in [22, 23] was used. Cells were grown on 12 mm diameter round coverslips in DMEM, washed twice in HBS with 0.1% BSA and allowed to equilibrate at 25°C for 30 min. FCS measurements were performed using a water immersion objective (Zeiss C-Apochromat 40×, NA 1.2) at defined positions of the plasma membrane. First, the lateral position of

the laser focus in the sample was determined by detection of focally excited fluorescence with a CCD camera. Cells were then continuously visualized by the camera in transmission or wide-field fluorescence illumination mode, and the cell was positioned in the x- and y-dimension with respect to the position of the focus using a high-precision motorized x-y stage (Märzhäuser, Wetzlar, Germany). Transmission and wide-field fluorescence images were recorded (Fig. 6.1A). Positioning of the focal volume along the optical axis (z) was achieved by a Pifoc piezoelectric lens positioner (Physik Instrumente, Waldbronn, Germany). The profile of fluorescence intensity along the optical axis was recorded by scanning the focus through the cell. In cells expressing the EGFR-GFP fusion protein, the plasma membrane was apparent as peaks of fluorescence intensity proximal and distal to the coverslip. Measurements were carried out in the upper (distal) cell membrane (see Fig. 6.1B) over 60-200 seconds. A series of 3-10 consecutive measurements was acquired at each position. After about every fifth measurement the focal position was confirmed by recording a fluorescence profile. For assessing the effect of receptor stimulation on autocorrelation functions, EGF was added at a final concentration of 50 nM by carefully pipetting 200 μ l of 250 nM stock solution to the 800 μ l buffer already on the cells. Data presented are those from experiments where no displacement of the membrane with respect to the confocal detection volume was observed during the series of measurements. For excitation, the 488 nm line of an Ar ion laser (2313-150MLYV, Uniphase, Eching, Germany) at laser power densities of 0.7-1.4 kW/cm² was used. Emission was detected through a dichroic mirror (500 DRLP, Omega Optical, Brattleboro, VT, USA) and a 515-545 nm bandpass filter (Delta Light & Optics, Lyngby, Denmark).

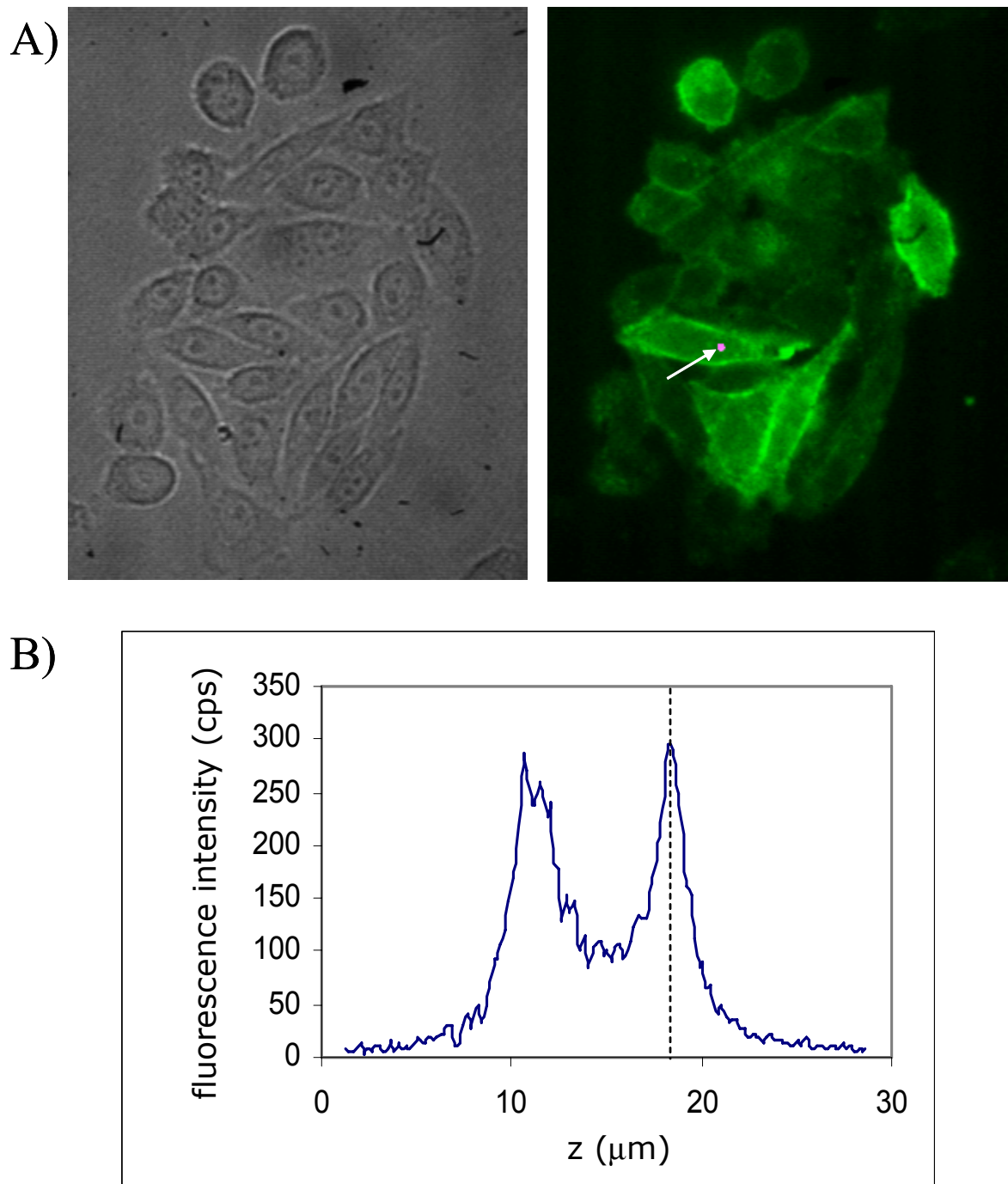


Fig. 6.1 Localization of the epidermal growth factor receptor (EGFR) in Chinese hamster ovary (CHO) (A) Transmission and fluorescence image of CHO F1-10 cells. The spot at the arrowhead indicates the focal volume during an FCS measurement. (B) Fluorescence intensity profile across the cell. Fluorescence intensity vs. objective position was detected as the piezoelectric focus positioner approached the objective towards the sample. The dashed line indicates the upper membrane (distal from the cover plate), where the FCS measurements in this example were performed.

Evaluation of autocorrelation curves

Autocorrelation curves calculated on-line by the ALV-5000/E correlator board (ALV Laserbetriebsgesellschaft, Langen, Germany) were fitted assuming five different models.

Two distinct components with free diffusion plus a triplet component

$$G(\tau) = a_0 + \frac{1}{N} G_{\text{triplet}} \cdot \left[w_1 \left(1 + \frac{\tau}{\tau_{d,1}} \right)^{-1} \left(1 + \frac{\tau}{S^2 \tau_{d,1}} \right)^{-1/2} + (1 - w_1) \left(1 + \frac{\tau}{\tau_{d,2}} \right)^{-1} \left(1 + \frac{\tau}{S^2 \tau_{d,2}} \right)^{-1/2} \right] \quad (6.1a)$$

$$\text{and } G_{\text{triplet}}(\tau) = \frac{\left(1 - T + T e^{-\tau/\tau_{tr}} \right)}{1 - T} \quad (6.1b)$$

where N is the number of molecules in the detection volume, $\tau_{d,1}$ and $\tau_{d,2}$ are the diffusional autocorrelation times of the diffusing species, w_1 is the weight of the first species with $w_1 = \nu_1 F_1^2 / (\nu_1 F_1 + \nu_2 F_2)^2$, ν_1 and ν_2 denoting the relative molar fractions, and F_1 and F_2 the fluorescence efficiencies of species 1 and 2. The structure parameter, S , denotes the ratio of the axial vs. radial diameters of the ellipsoid-shaped detection volume (defined by the surface of e^{-2} detection efficiency relative to the center of the illuminated spot), τ is the “lag” time; a_0 is an offset to compensate for the nonzero baseline of the autocorrelation function arising from a drift in the fluorescence signal (e. g. due to photobleaching). Correction for triplet state formation was included in all the models. In the triplet term, G_{triplet} , T denotes the equilibrium molar fraction of fluorophores in the triplet state [31, 32] and τ_{tr} is the triplet lifetime.

One component with free diffusion plus protonation-dependent blinking of GFP and triplet state formation

The model assumes that two protonation mechanisms are simultaneously present in EGFP [26, 33]:

$$\mathbf{G}(\tau) = a_0 + \frac{1}{N} \cdot \mathbf{G}_{triplet} \cdot \mathbf{G}_{prot}^{(2)} \cdot \left[\left(1 + \frac{\tau}{\tau_d} \right)^{-1} \left(1 + \frac{\tau}{S^2 \tau_d} \right)^{-1/2} \right] \quad (6.2a)$$

$$\text{and } \mathbf{G}_{prot}^{(2)}(\tau) = \frac{\left(1 - \Theta_{c,1} + \Theta_{c,1} e^{-\tau/\tau_{c,1}} - \Theta_{c,2} + \Theta_{c,2} e^{-\tau/\tau_{c,2}} \right)}{1 - \Theta_{c,1} - \Theta_{c,2}} \quad (6.2b)$$

$$\mathbf{G}_{prot}^{(2)}(\tau) = \left(1 - \Theta_{c,1} + \Theta_{c,1} e^{-\tau/\tau_{c,1}} - \Theta_{c,2} + \Theta_{c,2} e^{-\tau/\tau_{c,2}} \right)$$

where $G_{prot}^{(2)}$ is the “blinking term” accounting for protonation-dependent dark state formation with two different mechanisms, $\Theta_{c,1}$ and $\Theta_{c,2}$ are the average fractions of fluorophores in the detection volume being in the dark state due to the corresponding protonation mechanism, and $\tau_{c,1}$ and $\tau_{c,2}$ are the corresponding relaxation times.

Two diffusional components; fast diffusing species 1 with free, and slowly diffusing species 2 with anomalous diffusion and triplet correction

$$\mathbf{G}(\tau) = a_0 + \frac{1}{N} \cdot \mathbf{G}_{triplet} \times \left[w_1 \left(1 + \frac{\tau}{\tau_{d,1}} \right)^{-1} \left(1 + \frac{\tau}{S^2 \tau_{d,1}} \right)^{-1/2} + (1 - w_1) \left(1 + \left(\frac{\tau}{\tau_{d,2}} \right)^{2/d_{w,2}} \right)^{-1} \left(1 + \frac{1}{S^2} \left(\frac{\tau}{\tau_{d,2}} \right)^{2/d_{w,2}} \right)^{-1/2} \right] \quad (6.3)$$

Here $d_{w,2}$ is the anomaly parameter of the slowly diffusing component [33, 34], with a value equal to two for free diffusion and larger than two for obstructed diffusion.

Fast diffusing component with free, and slowly diffusing component with obstructed diffusion, GFP blinking with one component and triplet correction

$$G(\tau) = a_0 + \frac{1}{N} \cdot G_{triplet} \cdot G_{prot}^{(1)} \times \left[w_1 \left(1 + \frac{\tau}{\tau_{d,1}} \right)^{-1} \left(1 + \frac{\tau}{S^2 \tau_{d,1}} \right)^{-1/2} + (1 - w_1) \left(1 + \left(\frac{\tau}{\tau_{d,2}} \right)^{2/d_{w,2}} \right)^{-1} \left(1 + \frac{1}{S^2} \left(\frac{\tau}{\tau_{d,2}} \right)^{2/d_{w,2}} \right)^{-1/2} \right] \quad (6.4a)$$

$$\text{and } G_{prot}^{(1)}(\tau) = \frac{(1 - \Theta_c + \Theta_c e^{-\tau/\tau_c})}{1 - \Theta_c} \quad (6.4b)$$

where $G_{prot}^{(1)}$ is a “blinking term” assuming a single protonation mechanism, Θ_c is the fraction of fluorophores in the detection volume being in the protonation-dependent dark state and τ_c is the corresponding chemical relaxation time. As the characteristic time constants of the two proposed protonation mechanisms are separated by less than an order of magnitude [26], only one component was included in this and the following models.

Two species with anomalous diffusion and GFP blinking with one component and triplet correction

$$G(\tau) = a_0 + \frac{1}{N} \cdot G_{triplet} \cdot G_{prot}^{(1)} \times \left[w_1 \left(1 + \left(\frac{\tau}{\tau_{d,1}} \right)^{2/d_{w,1}} \right)^{-1} \left(1 + \frac{1}{S^2} \left(\frac{\tau}{\tau_{d,1}} \right)^{2/d_{w,1}} \right)^{-1/2} + (1 - w_1) \left(1 + \left(\frac{\tau}{\tau_{d,2}} \right)^{2/d_{w,2}} \right)^{-1} \left(1 + \frac{1}{S^2} \left(\frac{\tau}{\tau_{d,2}} \right)^{2/d_{w,2}} \right)^{-1/2} \right] \quad (6.5)$$

where $d_{w,1}$ and $d_{w,2}$ denote the anomaly parameters of the diffusing components.

Weighted least squares fitting for all models applying the Levenberg-Marquardt algorithm was performed using a program written in LabVIEW environment (National Instruments, Austin, TX, USA). The reciprocal of the variance of 5 residuals around each data point (differences between the actual data points and the values of the test function calculated with properly selected initial parameters) served as statistical weight for the respective data point in the fit procedure.

Table 1 summarizes the terms included in the different models.

Table 1

	<i>Model</i>				
	#1	#2	#3	#4	#5
Triplet	Yes	yes	yes	yes	yes
Blinking components	-	two	-	one	one
Fast diffusion	Free	-	free	free	anomalous
Slow diffusion	Free	free	anomalous	anomalous	anomalous

Background correction

For cells expressing very few EGFR-GFP fusion proteins ($N \leq 1$), background fluorescence was comparable to the signal from the EGFR-GFP molecules. In the presence of such background an aberrantly high number of molecules N is derived from the amplitude of the autocorrelation function. To correct for the background fluorescence a correction factor was used [35]:

$$G_{corr}(\tau) = \left(1 - \frac{I_B}{I_{tot}}\right)^2 (G(\tau) - a_0) + a_0 \quad (6.6)$$

I_B is the uncorrelated background intensity (cellular autofluorescence and dark current of the photodiodes), and I_{tot} is the total intensity including the signal and the background. $G(\tau)$ is any of the autocorrelation functions listed above and a_0 is the offset term described in the previous sections.

Diffusion constants were derived from the diffusional autocorrelation times according to

$$D = \frac{\omega_{xy}^2}{4\tau_D} \quad (6.7)$$

where ω_{xy} is the radius of the e^{-2} ellipsoid in the plane perpendicular to the optical axis.

Experimental determination of the dimensions of the ellipsoid of the confocal detection volume

For calculating the diffusion constant D from the diffusional autocorrelation time, knowledge of ω_{xy} is necessary. In order to calibrate the size of the detection volume, the autocorrelation functions of a concentration series of fluorescein solutions (1, 2, 5, 10 nM) were measured. Autocorrelations were fitted to the single-component free diffusion model including a triplet term, which yielded the number of molecules, N (Fig. 6.2A). For a single diffusing species, the average number of molecules in the detection volume can be expressed in terms of the dimensions of the e^{-2} ellipsoid in the optical plane and the molar concentration c :

$$N = N_A c \pi^{3/2} \omega_{xy}^2 \omega_z, \quad (6.8)$$

from which the product $\omega_{xy}^2 \omega_z$ can be derived (N_A is Avogadro's number). The axial radius of the ellipsoid, ω_z was determined experimentally by adsorbing ethidium bromide to the surface of a coverslip from a 10 μ M solution of the dye. Fluorescence intensity was recorded while the distance of the objective from the adsorbed dye layer was continuously changed by the piezoelectric focus positioner of the microscope (Fig. 6.2B). The intensity profile was fitted to a Lorentzian function:

$$I(z) = I_b + \frac{2Aw}{\pi((4z - z_0)^2 + w^2)} \quad (6.9)$$

where I_b is the background intensity, A is a constant, z is the coordinate of the objective and z_0 is the location of the peak. The width parameter w was used as an approximation for ω_z . Then ω_{xy} was calculated from the previously determined product $\omega_{xy}^2 \omega_z$ and w . Typical dimensions for the instrument used were $\omega_{xy} = 0.34 \pm 0.04 \mu\text{m}$ and $\omega_z = 2.43 \pm 0.58 \mu\text{m}$ yielding an experimentally determined structure factor S of ~ 7.1 .

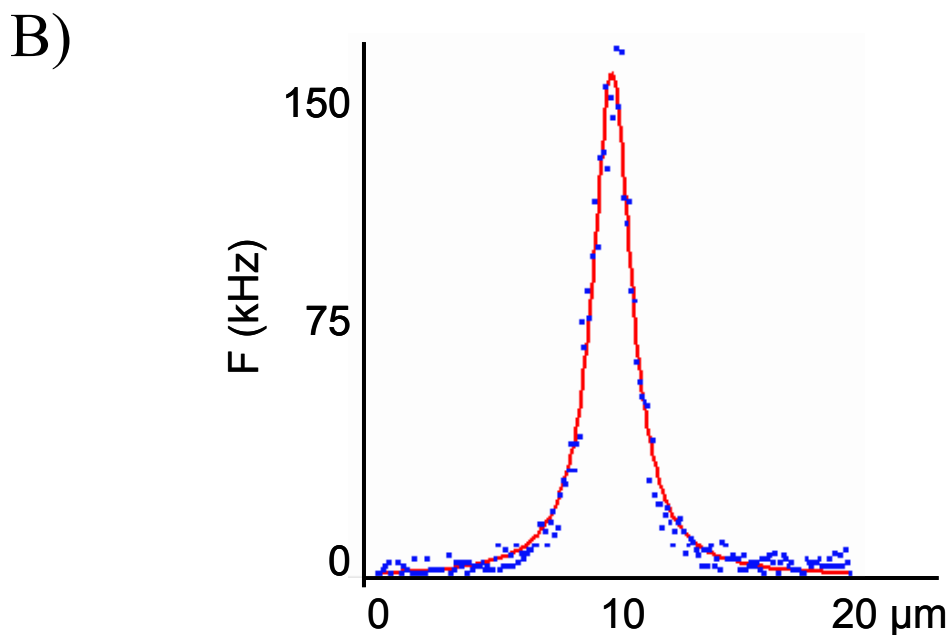
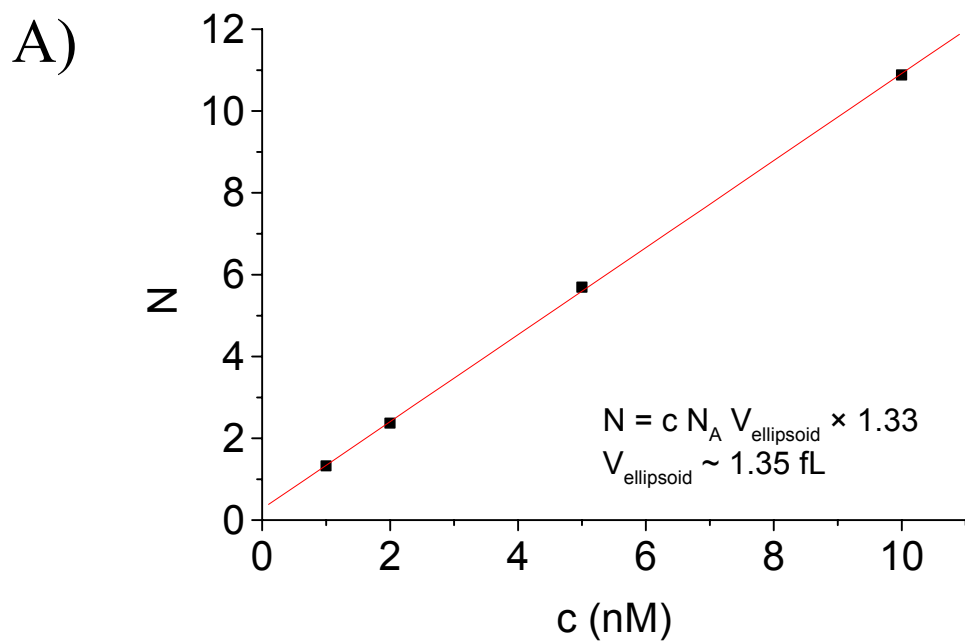


Fig. 6.2. Calibration of the sensitive volume in the FCM. The apparent number of molecules present in the sensitive volume was determined with a concentration series of fluorescein solutions. (A) The volume of the e-2 ellipsoid derived from the slope of the straight line was 1.35 fL. (B) Fluorescence intensity profile of an ethidium bromide layer adhering to the coverslip as a function of objective position. The curve was fitted with a Lorentzian, the width of which yielded the axial radius, $\omega_z=2.22 \mu\text{m}$ in this experiment, of the e-2 ellipsoid.

Statistical analysis of data derived from autocorrelation functions

To test the significance of changes in the autocorrelation functions upon receptor stimulation by EGF and of the difference of the value of the anomaly parameters d_w from 2, two-sided, paired t-tests were carried out at a level of confidence $\alpha=0.95$.

Fluorescence recovery after photobleaching (FRAP)

FRAP measurements were performed using a custom-made instrument based on a Leica fluorescence microscope. The beam of a 488 nm argon ion laser was splitted with a half-mirror and focused to a diffraction-limited spot with a 40× (N.A.=0.5) dry objective. The beam diameter was determined to be 375 nm by comparing the e^{-2} diameter of the intensity profile of the beam to the image of microbeads of known diameter projected to a screen. Laser output was 40 mW, attenuation of the beam for monitoring was $10^4\times$. Excitation power density in the illuminated spot was $<0.5 \text{ kW/cm}^2$. An electromechanical shutter wheel was used to block the main beam path during monitoring. Bleaching time was 200 ms, preceded and followed by 200 ms dead time for protecting the cooled photomultiplier used for sampling the recovery kinetics at 5 - 50 Hz. Emission was detected through the half-mirror and a 500 nm longpass filter (Schott). Data were fitted with a custom-written LabView program employing the linearization method described in [36] for free Brownian diffusion and a nonlinear Levenberg-Marquardt algorithm for the general model accounting for both free and anomalous (hindered) diffusion [37]. Assuming that there is no directional flow and that recovery after bleaching is due to diffusion of a single component only, the fluorescence intensity f_i at any time for a Gaussian laser beam is given by the equation:

$$f_t = \frac{f_0 + f_\infty (t/t_{1/2})^\alpha}{1 + (t/t_{1/2})^\alpha} \quad (6.10)$$

where f_0 is the fluorescence intensity immediately after photobleaching, f_∞ is the maximum recovered intensity attainable after a long time, $t_{1/2}$ is the time of recovery to $(f_\infty + f_0)/2$, and α is the anomaly parameter [37], which in the FRAP formalism has a value of one for free diffusion, and smaller than one for hindered diffusion. The mobile fraction (percentage recovery of fluorescence) is determined by

$$R = \frac{f_\infty - f_0}{f^0 - f_0} \quad (6.11)$$

and the diffusion constant by

$$D = \frac{\gamma \omega^2}{4t_{1/2}} \quad (6.12)$$

where f_0 is the fluorescence intensity before bleaching, ω is the radius of the laser beam at e-2 height of the Gaussian beam at the point of focus on the membrane and the coefficient γ is a function of bleaching:

$$\gamma = a + b(f_0 / f^0)^c \quad (6.13)$$

The constants a , b and c were determined to be $a=0.512281$, $b=0.474267$ and $c=-0.415823$ according to [38]. Under our experimental conditions, γ was 1.147 ± 0.073 (mean \pm S.D, $n=314$).

6.4. Results

Signaling competence of EGFR-GFP fusion proteins

Previously, the capacity of the EGFR-GFP fusion proteins to bind ligand and to internalize was assessed by fluorescence microscopy [23, 39, 40]. Here, the functionality

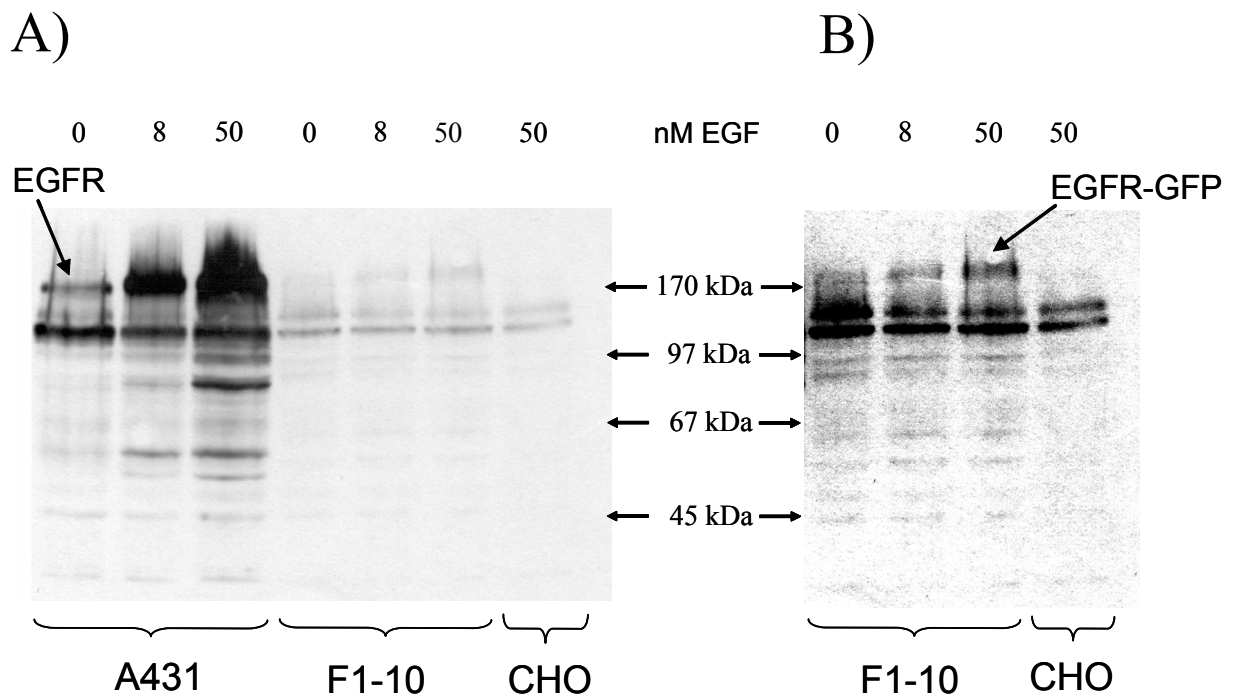


Fig. 6.3. Tyrosine phosphorylation evoked by EGF stimulation. (A) Anti-phosphotyrosine Western blot of A431, F1-10 and CHO cells in rest, and stimulated with 8 or 50 nM EGF. (B) Contrast-enhanced image of the lanes for F1-10 and CHO from the blot in A.

of the fusion proteins to induce downstream signaling was assessed by analysis of ligand-induced tyrosine phosphorylation of cellular proteins and detection of calcium signaling upon receptor stimulation with EGF.

Tyrosine phosphorylation

Signal transduction is initiated by activation of the tyrosine kinase and subsequent phosphorylation of tyrosine residues in the receptor C-terminal domain and down-stream substrates. Lysates of ligand-treated and control cells were probed for tyrosine phosphorylated proteins by Western blot (Fig. 6.3). The human epidermoid carcinoma cell line A431 served as a positive control. In A431 cells, as well as F1-10 cells, ligand-induced tyrosine phosphorylation of bands with ~170-190 kDa molecular weight,

corresponding to the EGFR was dose-dependent. Due to its larger molecular weight, the mobility of the EGFR-GFP fusion protein was smaller than that of the native EGF receptor. Other proteins at ~60, 65, 90 and 100 kDa were also phosphorylated in a dose-dependent manner. In non-transfected CHO cells only two weak bands with 100 and 110 kDa molecular weight were present, and although these were also present in A431 and F1-10, their phosphorylation state did not change upon EGF treatment. The F1-10 cell line expresses only 2×10^4 copies of the EGFR-GFP fusion protein compared to 2×10^6 EGFRs in A431 cells. For this reason, the intensity of the band corresponding to the receptor was much weaker in F1-10 than in A431 cells.

Calcium response

Phospholipase C γ is one of the early down-stream effectors of EGF receptor signaling. Activation of this enzyme by docking on phosphotyrosine residues of EGFR leads to the generation of diacylglycerol and release of inositol-trisphosphate, eliciting an increase of intracellular calcium [41]. The aim of the Ca²⁺ measurements was not an absolute determination of Ca²⁺ concentration, but the mere demonstration of the presence of Ca²⁺ responses and illustration of their relative magnitude for different cells and different conditions. Changes in intracellular calcium were detected by ratiometric imaging of the fluorescence of the Ca-indicator dye Fura-2 excited at 340 and 380 nm. For both A431 cells and F1-10 cells, stimulation with 50 nM EGF led to an increase in intracellular calcium Fig. 6.4. At 8 nM EGF a calcium response was detectable in A431 cells, only. CHO negative controls did not exhibit an increase in intracellular calcium at any EGF concentration.

Fluorescence autocorrelation measurements

Characterization of the bleachable fraction of receptor molecules

Fluorescence autocorrelation measurements were performed on cells expressing about 2×10^4 of the EGFR-GFP fusion proteins. When the laser excitation was switched on, even at low illumination intensities (0.7-1.4 kW/cm²), a considerable fraction of the EGFR-GFP was photobleachable. Photobleaching distorts the autocorrelation curves by mimicking the presence of a component with a long diffusional autocorrelation time. In addition, the fraction of bleached molecules is not detectable by FCS, limiting the analysis of diffusion rates and receptor numbers to molecules diffusing sufficiently fast to escape bleaching.

To address whether the bleached molecules were either immobile or diffusing too slowly to escape bleaching, intermittent 15-second bleaching periods were applied with pauses of either 10 - 15 s or 50 - 200 s and fluorescence was recorded (Fig. 6.5A). The count traces after longer pauses (3rd and 6th count traces) resembled the original bleaching curve (2nd count trace). Monitoring of the fluorescence intensity with a laser power of 1.3 kW/cm² before and after the bleaching intervals (1st and 5th count traces) showed that the total count rate decreased by only ~28% (from 62 to 45 kHz) over the first three 15-second bleaching periods (2nd, 3rd and 4th count traces), whereas the transient decreases during the individual bleaching periods were much larger, 85 ± 3 %. This discrepancy between transient and total reduction of fluorescence showed that the majority of the bleachable molecules are mobile on a longer time scale.

At lower laser intensities, however, the acquisition of autocorrelation functions was hampered by movements of the plasma membrane over the long acquisition times

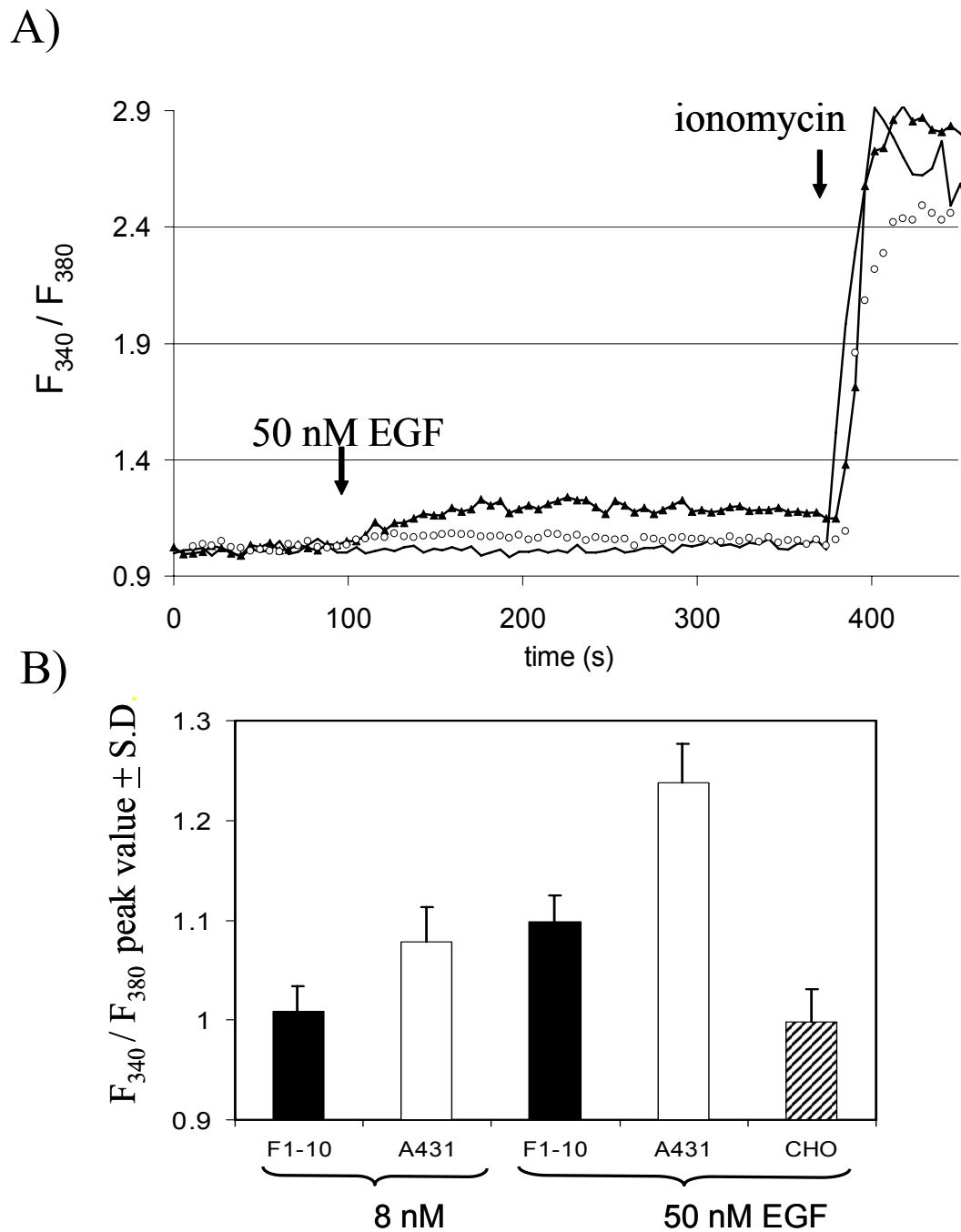


Fig. 6.4. Calcium signals induced by EGF stimulation. (A) Calcium response curves of Fura-2 loaded cells after EGF stimulation. Changes in intracellular calcium concentration are indicated by the ratio of Fura-2 fluorescence excited at 340 and 380 nm (F_{340}/F_{380}). The time of adding EGF, and ionomycin (2 mg/ml, for calibration) are marked with arrows. Typical responses of native CHO, F1-10 and A431 cells are shown with solid line, circles and closed triangles, respectively. (B) Average peak values with SDs of fluorescence ratios ($n = 10 - 30$). The resting value characteristic for unstimulated cells was ~ 1 , corresponding to an intracellular Ca^{2+} concentration of 80-120 nM.

necessary to acquire autocorrelation functions. In order to avoid the continuous decrease of intensity during the autocorrelation measurements, the fraction of molecules with low mobility was eliminated by pre-bleaching the sample using an illumination intensity of 13 kW/cm² for 100-200 seconds, until the fluorescence was constant (Fig. 6.5B). The remaining intensity was 26 ± 16 % SD (n=21) of the original one, i.e. the mobility of ~74% of the receptors was too low to escape photobleaching. The cell-to-cell variability of the bleachable fraction seemed to correlate with the initial fluorescence intensity; the higher the initial intensity, the higher the bleachable fraction.

In Fig. 6.5A count traces at 13 kW/cm² and 1.3 kW/cm² are shown. The fluorescence intensity at the lower laser power is much higher than 10% of the signal recorded at the higher laser power. This nonlinear dependence of emission intensity on illumination power density is also indicative of the presence of photobleaching, which is more pronounced at higher laser power, where considerable bleaching occurs even after reaching a steady signal level due to a dynamic equilibrium between photobleaching and re-population by diffusion. Although the illuminated spot

Dependence of apparent diffusional autocorrelation times on laser power

Photobleaching has a twofold effect on autocorrelation functions. First, the number of molecules in the detection volume is reduced. Second, photodestruction reduces the period, during which a fluorophore emits photons in the detection volume. The latter phenomenon leads to a decrease of the diffusional autocorrelation time [42] and thereby to overestimating the diffusion constant. The higher the excitation laser power, the stronger this effect. Fig. 6.6 shows the correlation times and the weights of the components obtained from autocorrelation curves fitted according to model 1 (a slow and a fast diffusion component plus triplet state) as a function of illumination intensity. The

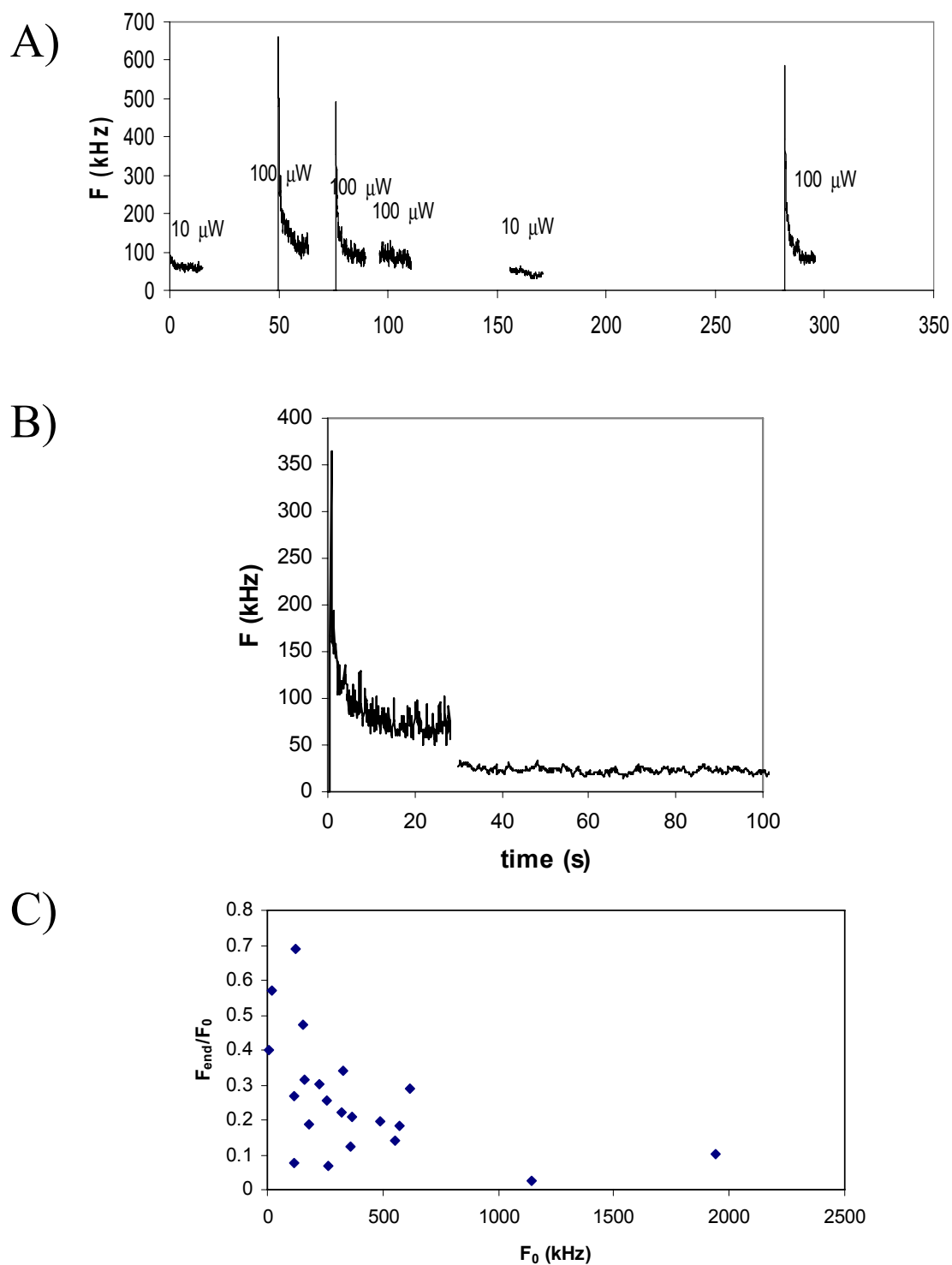


Fig. 6.5. Repetitive bleaching of EGFR-GFP reveals fast and slow diffusing EGFRs. (A)

Count traces during repetitive bleaching and monitoring intervals. Count rate was monitored at a

laser power of $10 \mu\text{W}$, while bleaching was done with $100 \mu\text{W}$ corresponding to power densities

of 1 and $10 \text{ kW}/\text{cm}^2$, respectively. See text for details. (B) Pre-bleaching of low mobility and

immobile EGFR- GFPs. During the 30-s bleach is confined to a relatively small fraction of the total cell surface area, a decrease of the overall fluorescence intensity of the cell was observed after completion of the FCS experiments. With typically 20 minutes of cumulative focal illumination at 0.9-1.3 kW/cm² of power density, a decrease of about 20% of total fluorescence per cell was derived from wide-field fluorescence images and integration over all pixels of one cell. Neighboring cells showed no such decrease.. (C) Relative decrease of fluorescence intensity vs. initial intensity at illumination with 100 μW intensity for 30 s.

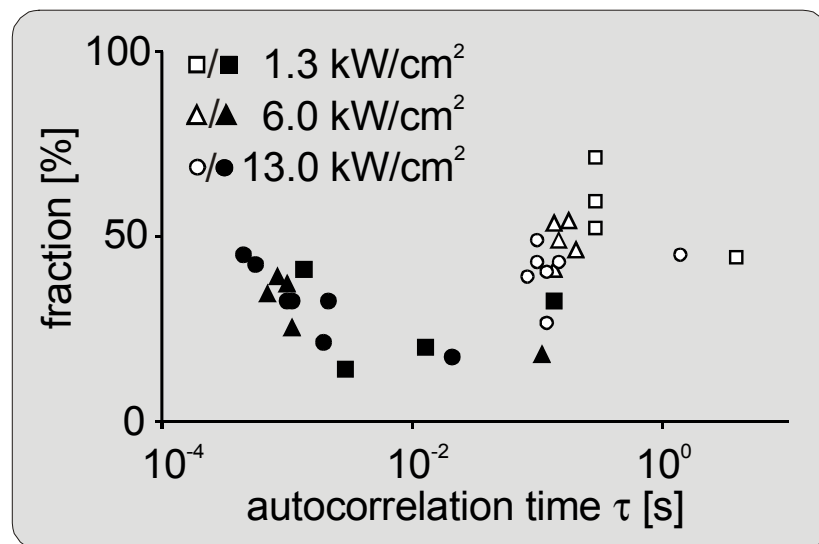


Fig. 6.6. Dependence of the autocorrelation functions on the laser illumination intensity. Autocorrelation curves were fitted according to model 1 (a slow and a fast diffusion component plus triplet state). The correlation time of the fast component (open symbols) is largely unaffected by illumination intensity, whereas the slow diffusion correlation time component (filled symbols) is negatively correlated with laser power.

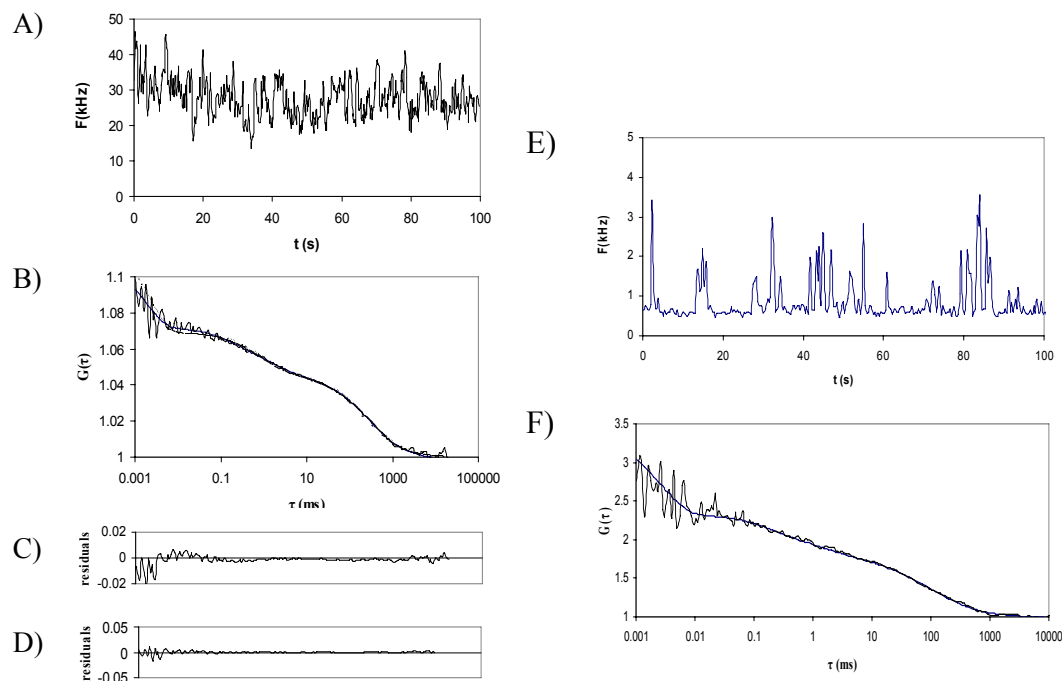


Fig. 6.7 FCS measurement done on a resting F1-10 cell. The pre-bleached sample has a steady running average of fluorescence intensity. (A) Autocorrelation curve and nonlinear fits. Model 1 (dashed line) assumes triplet state and two diffusing components with free Brownian diffusion. Model 5 (solid line) considers triplet state formation, GFP blinking and two diffusing components also allowing obstructed diffusion. (B) Residuals of model 1. In the 0.1-10 ms regime the fit is poor. (C) Residuals according to model 5 show a better fit in the fast regime, indicating the presence of GFP blinking. The anomaly parameter of the fast diffusing component was 2.25, referring to obstructed diffusion, whereas for the slow component it was ~ 2 , the values characteristic for free diffusion. (D) Count trace recorded from an F1-10 cell with very low expression level. Background intensity was assessed to be ~ 0.5 kHz. (E) Autocorrelation curve and nonlinear fit according to model 5. The high amplitude refers to a low molecule concentration: the mean number of molecules in the detection volume was ~ 0.12 , corresponding to a receptor concentration of 0.14 nM.

apparent correlation time of the fast component was barely affected by laser power; the time spent in the illuminated volume was too short compared to the bleaching time constant. In contrast, the correlation time of the slow component was negatively correlated with the illumination intensity. In addition, the relative fraction of the slow

component decreased with increasing laser power. To minimize this photobleaching effect, the lowest laser power sufficient for recording autocorrelation functions with a good signal-to-noise ratio was employed over a measurement time at which movements of the plasma membrane did not distort the autocorrelation measurements.

Analysis of autocorrelation functions

The autocorrelation functions acquired from EGFR-GFP expressing cells consisted of multiple components, implying that fluctuations resulting from several photophysical and/or diffusion processes were present, simultaneously (Fig. 6.7). In order to identify the mode of molecular diffusion and the nature of the photophysical processes of the EGFR-GFP fusion proteins, a series of different models were employed for fitting the autocorrelation functions.

The simplest model reasonably fitting the autocorrelation functions assumed two components diffusing by free Brownian diffusion (Eqn.6.1). Averages of fitted parameters from 12 independent measurements in different cells are given in Table 2. The characteristic autocorrelation time constant in the microsecond domain was fitted by a triplet term, yielding a fraction of molecules in the triplet state of $T = 0.56 \pm 0.13$, and a triplet lifetime of $\tau_{tr} = 2.3 \pm 1.2 \mu\text{s}$. In this model, the decay of the autocorrelation function in the lower millisecond domain was attributed to a fast diffusion process. The slow diffusion time was attributed to the diffusion of EGFR-GFP fusion proteins in the plasma membrane.

The expression level of the EGFR-GFP fusion proteins in F1-10 cells had a rather broad distribution. In some cases the number of molecules in the detection volume was significantly smaller than one (Fig. 6.7 E and F). In these cases correction for uncorrelated background was indispensable for the correct determination of N (Eqn.6.6).

The background was derived from the baseline of the count traces. With a detection volume of 1.46 fL, the concentration of the receptors was as low as 0.15 nM.

Table 2

Fit parameters of resting and stimulated cells		
	Mean±SD	
	Before EGF	After EGF
D_1 (cm ² /s)*	$2.69 \pm 0.94 \times 10^{-7}$	$1.92 \pm 1.09 \times 10^{-7}$
D_2 (cm ² /s)*	$1.07 \pm 0.35 \times 10^{-9}$	$0.69 \pm 0.58 \times 10^{-9}$
w_1	0.33 ± 0.05	0.36 ± 0.11
T	0.55 ± 0.12	0.57 ± 0.15
τ_{tr} (μs)	2.0 ± 0.8	2.6 ± 1.5
Mse	4.2	5.9

Data are presented as mean ± S.D. from twelve independent experiments. Those measurements were selected, in which cell movements did not influence the position of the plasma membrane with respect to the detection volume in measurements immediately before and after stimulation with 50 nM EGF. Indexes 1 and 2 refer to the fast and slow components. D_1 and D_2 are the diffusion constants, w_1 is the relative contribution of the fast component, T and τ_{tr} are the triplet fraction and lifetime, and mse is the mean squared error of the nonlinear fits. The asterisk denotes parameters that changed significantly after EGF treatment ($p < 0.05$).

As an alternative to fitting the experimental data in the fast regime (10^{-4} - 10^{-2} s) by free diffusion, terms describing protonation-dependent fluorescence fluctuations were included in the autocorrelation function. EGFP is known to undergo protonation leading to a dark, non-fluorescent state by two different mechanisms: an external, pH-dependent process and an internal, pH-independent one, in which a proton in the GFP molecule is translocated [26, 33]. Autocorrelation data were fitted according to Eqn.6. 2, which takes these two protonation mechanisms, triplet state formation and a single diffusing species into account. The characteristic time constants of blinking obtained from the fits were 400 ± 290 μs and 5 ± 3 ms.

Analysis of autocorrelation functions assuming diffusional constraints in the cytoplasm and the plasma membrane

In a number of cases, the model with two distinct freely diffusing components (Eqn.6.1) failed to describe the data in the time domain of either the slow membrane-located or the fast cytoplasmic component. Plasma membrane proteins may be subject to local hindrances to their diffusion, caused by membrane domains [43, 44] or the membrane-proximal actin cytoskeleton, the so-called terminal web [45]. A model of anomalous diffusion had been proposed that accounts for the resulting non-linearity of the root mean-square displacement with time [33, 34]. Different models assuming obstructed diffusion were employed for fitting the data (Eqns.6.3, 6.4 and 6.5). The anomaly parameter d_w expresses the degree of non-linearity. For free Brownian diffusion this value equals two in the corresponding autocorrelation function, for obstructed diffusion this value is larger than 2. If $d_w > 2$, the slope of the autocorrelation function around the diffusion correlation time is smaller than in the case of free diffusion. Therefore an extended sloping tail region of the autocorrelation curve can be fitted when assuming the anomalous diffusion model [46]. However, the shape of the function has a weak dependence on the anomaly parameter d_w , implying that the fitted value of this parameter may carry considerable error. For this reason, the quality of fits assuming anomalous diffusion was evaluated for each component separately, limiting the flexibility of the fitted curve. Three models of obstructed diffusion, successively including more components, were tested: (i) model 3 assuming triplet state formation, free diffusion of the fast component and obstructed diffusion of the slow component (Eqn.6.3), (ii) model 4 assuming GFP blinking in addition to the terms in model 3 (Eqn.6.4), and finally (iii) model 5 with triplet state formation, GFP blinking and two components with obstructed

Table 3

Fit parameters of resting and stimulated cells (mean±SD)						
	Model 3		Model 4		Model 5	
	free + obstructed		blinking + free + obstructed		blinking +obstructed+obstructed	
	Before EGF	After EGF	Before EGF	After EGF	Before EGF	After EGF
D_1 (10^{-7} cm ² /s)	2.90±1.44	2.58±1.01	1.98±0.98	1.68±0.98	1.97±0.83	1.63±0.94
D_2 (10^{-9} cm ² /s)	1.06±0.45*	0.66±0.28*	1.17±0.52*	0.68±0.30*	1.17±0.51*	0.66±0.30*
w_1	0.304±0.06	0.33±0.10	0.29±0.05	0.34±0.12	0.30±0.06	0.36±0.12
$d_{w,1}$	n.a.	n.a.	n.a.	n.a.	2.12±0.38	2.43±0.35**
$d_{w,2}$	2.26±0.11**	2.24±0.10**	2.04±0.15	1.99±0.15	2.02±0.14	1.96±0.16
T	0.58±0.11	0.57±0.06				
τ_{tr} (10^{-7} s)	2.82±1.05	3.22±0.74				
θ_c	n.a.	n.a.	0.10±0.03	0.09±0.01	0.09±0.01	0.09±0.01
τ_c (10^{-4} s)	n.a.	n.a.	1.78±0.17	1.85±0.24	1.81±0.21	1.87±0.22
mse	4.6	5.8	3.3	4.78	3.5	3.5

Data are presented as mean \pm S.D. from twelve independent experiments with autocorrelation recorded immediately before and after stimulation with 50 nM EGF, in which cell movements did not influence the position of the detection volume.

* D_2 changed significantly after EGF stimulation (p values of two-tailed paired t-tests, model 3: p=0.033, model 4: p=0.0023 model 5: p=0.0016)

** $d_{w,1}$ and $d_{w,2}$ in model 3, and $d_{w,1}$ in model 5 differed significantly from 2 (p<0.001), i.e. the diffusion of the respective components can be described by a model of obstructed diffusion (D : diffusion constant, w : weight of diffusion component, d_w : anomaly parameter, T : triplet fraction, τ_{tr} : triplet lifetime, θ_c : fraction of the protonation-dependent dark species, τ_c : chemical relaxation time of the protonation process, mse: mean squared error of nonlinear fits).

diffusion (Eqn.6.5). Mathematically (i) and (ii) are equivalent to fixing the value of the anomaly parameter of the fast component to two.

The fitted parameters obtained for models 3 to 5 (Eqns.6.3, 6.4, and 6.5) are summarized in Table 3. For model 3, the anomaly parameter $d_{w,2}$ of the slow component was slightly but significantly larger than 2. However, for many of the measurements model 3 failed to fit the data in the 0.1-1 ms range. The implementation of a term for a

single dark species due to protonation in model 4 greatly improved the quality of the fit, especially in the ms range (see mean squared errors of the fits in Table 3). On EGF-stimulated cells, the introduction of the anomaly parameter for the fast component, $d_{w,l}$ in model 5 further reduced the mean standard error of the fits. In resting cells $d_{w,l}$ was close to two, while it was significantly larger than 2 in stimulated cells. In contrast, the mean value of the anomaly parameter was close to two for the slow component in this model.

FCM measurements on EGF-stimulated cells

In resting cells, the EGFR-GFP fusion proteins showed a relatively uniform distribution (Fig. 6.8A). Stimulation with EGF led to receptor aggregation and internalization within 5 min which was still apparent even 30 min after stimulation (Fig. 6.8B). To record the autocorrelation function for a cell, the spot for measurement was photobleached (for about 200 s) at a laser irradiance of 13 kW/cm² until the fluorescence signal stabilizes. Consecutive autocorrelation curves were then taken at 1.3 kW/cm². EGF was added to the medium (large volume to allow for quick and thorough mixing) at regular intervals during the course of the experiment increasing the EGF concentration of the medium up to a final concentration of 50 nM. Each EGF addition was followed by autocorrelation measurements on the stimulated cell at the same spot where the previous measurements had been carried out. Fit values to autocorrelation measurements taken directly before and after adding 50 nM EGF to the cells are shown in Tables 2 and 3. For all models, the diffusion constants decreased upon stimulation with EGF (Fig. 6.9A). In addition, EGF caused a decrease of the number of molecules N in the detection volume (Fig 9B). The average ratio of the apparent number of molecules after and before EGF incubation was 0.78.

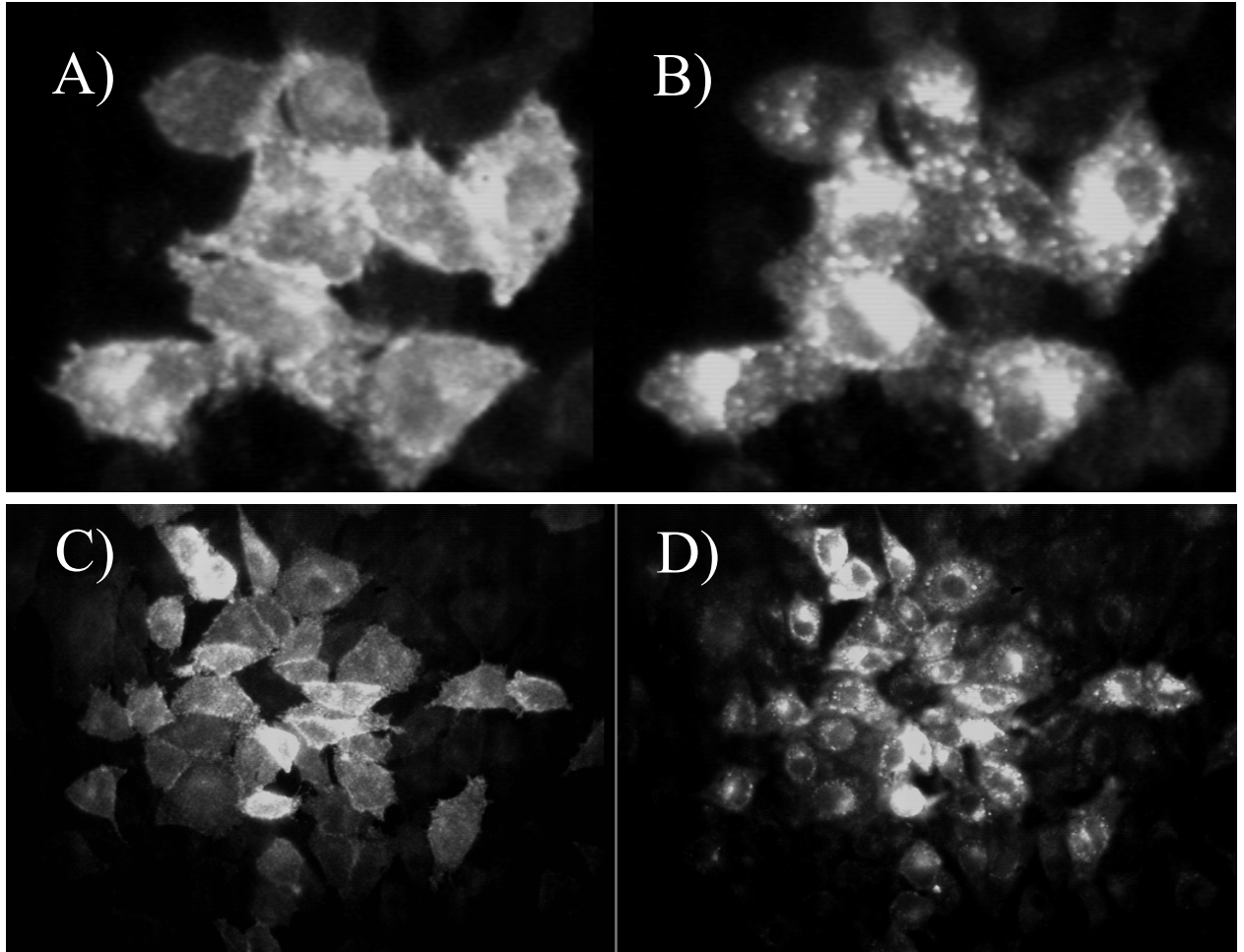


Fig. 6.8

Fluorescence images of F1-10 cells taken before (A, C) and ~30 minutes after EGF stimulation (B, D). In resting cells the distribution of receptors is more uniform than in stimulated cells, in which the distribution is more granulated. Note the translocation of receptors from the membrane to the cytoplasm.

Receptor oligomerization was further evaluated by calculating the fluorescence per molecule, fpm , normalized to laser power. The fpm is obtained by dividing the background corrected fluorescence F by the background corrected number of molecules N and the laser power P : $fpm = FN^{-1}P^{-1}$. The mean fluorescence decreased after stimulation, but only to the same extent as the number of molecules N . Consequently, the mean fluorescence per molecule was unaffected: the ratio of the fpm values after and before stimulation was close to 1 (0.94 ± 0.36) (Fig. 6.9C, D).

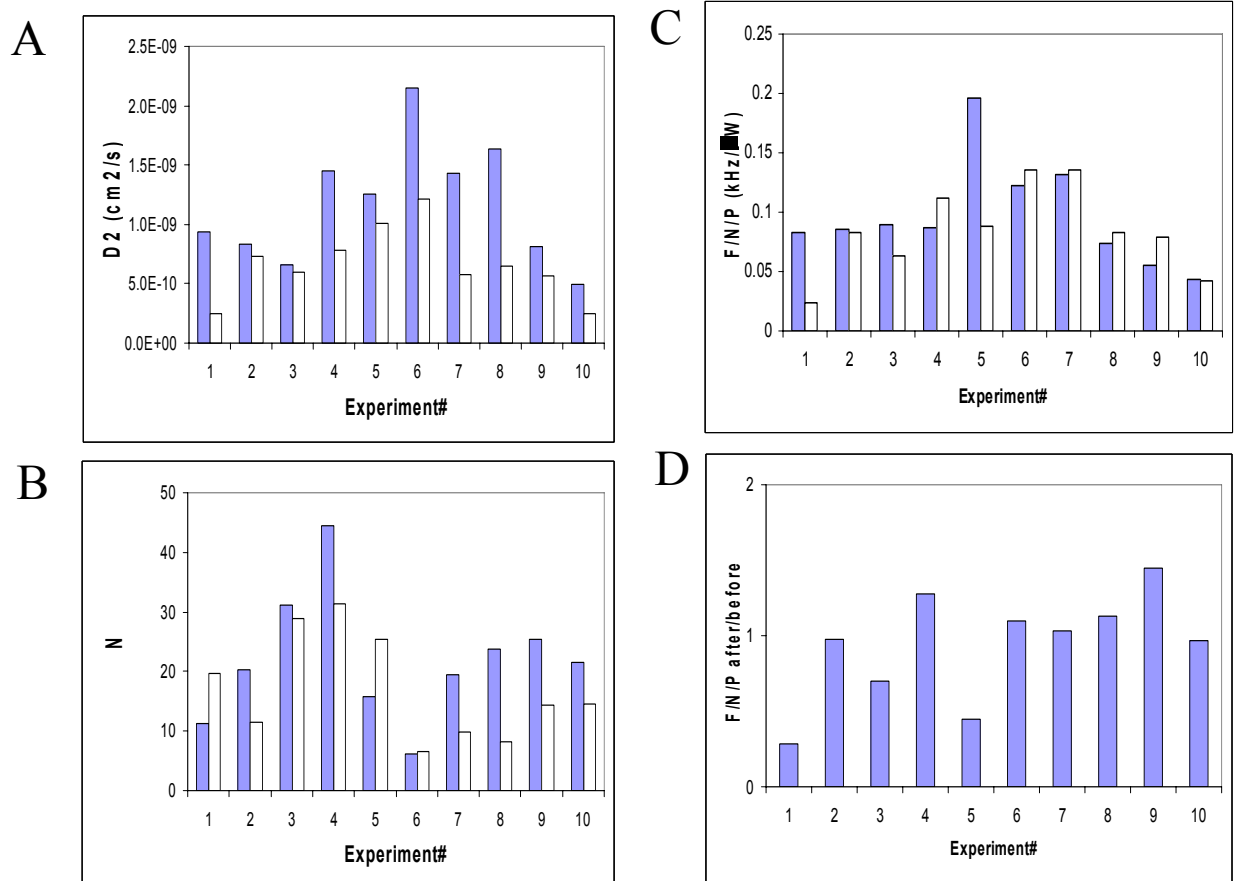


Fig. 6.9. Effect of EGF stimulation on F1-10 cells. Closed bars: before treatment, open bars: after treatment. (A) The change of $D2$ upon stimulation by 50 nM EGF. (B) The change of the apparent number of independently moving particles in the detection volume, N . (C) Effect of EGF treatment on the normalized specific fluorescence per molecule. F is the fluorescence intensity in kHz, N is the average number of molecules in the detection volume and P is the laser power. (D) Ratio of $F/N/P$ values after and before stimulation. Apart from a few outliers the value is around 1.

FRAP measurements of EGFR-GFP fusion proteins

In contrast to FCS, FRAP has already been employed for the analysis of molecular mobilities of receptors and intracellular molecules in a variety of systems [17, 47-49]. In earlier FRAP measurements, analysis of EGFR diffusion has been limited to stimulated receptors, visualized by incubation of EGF receptors with fluorescently labeled ligands.

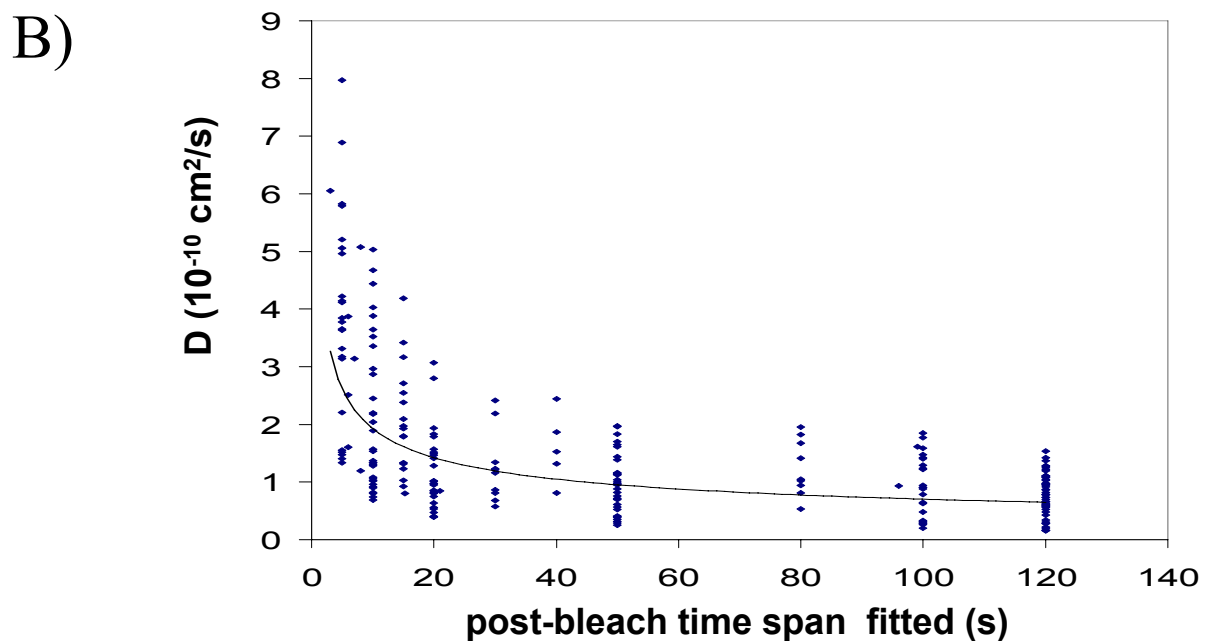
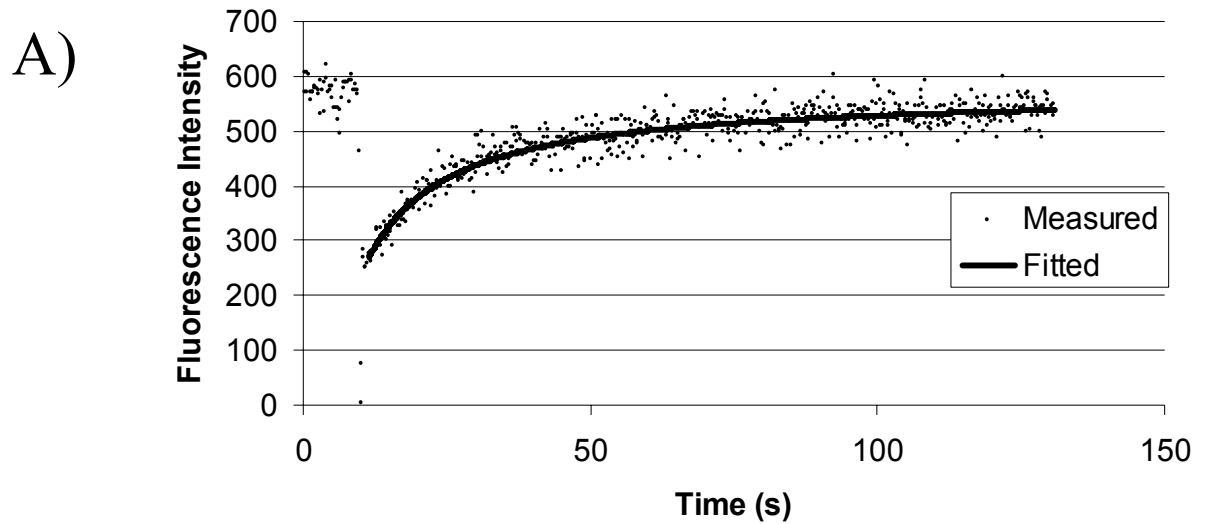


Fig. 6.10 Typical FRAP data and fit. (A) Dependence of fitted diffusion constant on the time span used for fitting FRAP data. Data are fitted to the free diffusion model ($\alpha=1$). The same 51 recovery curves, sampled at 50Hz, are fitted taking into account various time spans after the bleach pulse. The shorter the fitted period, the higher the diffusion coefficient.

The availability of the endogenously labeled EGFR-GFP fusion proteins allowed for determining the diffusion constant of unstimulated receptors. In our measurements on F1-4 cells the unbleached fraction f_0/f^0 was $52.3 \pm 13.6 \%$, and the mobile fraction R was 84.9 ± 15.2 (mean \pm S.D., n=314). The diffusion constants derived from FRAP recovery curves (Fig. 6.10A) obtained by fitting the entire recovery time span (120 - 130 s) using a free Brownian diffusion model (Fig. 6.10B) were considerably slower ($8.7 \times 10^{-11} \text{ cm}^2/\text{s}$) than those obtained from FCS experiments (see also table 4). Limiting the evaluation of the recovery curve to the first five seconds after the photobleaching pulse increased the values obtained for D to an average of $3.3 \times 10^{-10} \text{ cm}^2/\text{s}$. When the same recovery curves were fitted with a model for anomalous diffusion (making the assumption that $f_\infty = f^0$) the diffusion constant was found to be $9.0 \pm 3.3 \times 10^{-11} \text{ cm}^2/\text{s}$ and the anomaly parameter $\alpha = 0.6 \pm 0.3$.

6.5 Discussion

Functional characterization of EGFR-GFP fusion proteins

The functionality of the EGFR-GFP fusion proteins with respect to early signaling events was confirmed by anti-phosphotyrosine Western blot analysis and Ca-signalling. Western-blot analysis of tyrosine-phosphorylated proteins probed for the activation of the receptor itself, and also for the propagation of the signal to down-stream targets. The latter was also confirmed by Ca-imaging.

The significantly weaker calcium response of F1-10 cells compared to A431 cells can be explained by the lower expression level of the receptor. An additional factor might be the reduced ligand binding affinity of the chimeric EGFR-GFP, which may be as low as one-tenth of that of the native receptor (B. Defize personal communication). The decrease in the affinity can be attributed to either conformational change induced by the presence of the linker region and of the GFP moiety assuming the model of predimerized receptors or by sterical hindrance in the formation of the 2:2 receptor-ligand complex. Nonetheless, the induction of Ca-signaling and tyrosine phosphorylation of proteins other than the

EGFR-GFP confirms the ability of the fusion protein to elicit downstream signaling also in CHO cells. The ability to be engulfed by membrane ruffles when liganded with microbead-linked EGF [39] and eventually be internalized in a Cbl- and Grb2-dependent manner [40] provides further evidence for the functionality of the chimeras.

Table 4

	FCS	FRAP				
cell	F1-10	F1-4	F1-4, 50Hz sampling			
parameter	all	all	fit to 120 s	fit to 5 s	anomalous	generic
D (cm ² /s×10 ⁻¹⁰)	10.70	0.87	0.78	3.27	0.90	0.71
S.D.	4.00	0.46	0.36	2.59	0.33	0.31
n	26	314	51	39	51	51
α	-	-	-	-	0.6	0.8

Diffusion constants determined for the EGFR-GFP fusion protein using FCS and FRAP on resting cells.

FCS data were evaluated according to model 5 (a fast and a slow species with anomalous diffusion, one blinking term plus triplet correction). All FRAP recovery curves were fitted to the Brownian diffusion model first, resulting in diffusion constants an order of magnitude lower than those derived from FCS. Measurements that were sampled at a high (50 Hz) frequency were used to fit both the whole recovery curve (120s), and also the initial parts of the same curves. Results for fitting the first 5 seconds are presented in the table. (Not all 51 curves could be fitted unambiguously over this short time span). Further models used for fitting were the anomalous diffusion model either with fixing $f_{\infty} = f^0$ or leaving the value of f_{∞} free (generic).

Effect of bleaching on autocorrelation measurements

In all cells, a strong decrease of fluorescence was observed in the first few seconds of illumination. Recovery of this fluorescence in the absence of laser excitation indicated that this decaying signal originated from a fraction of receptors with little mobility. However, when the laser power was reduced to a level at which bleaching could be almost completely avoided, the time required to obtain an autocorrelation curve increased resulting in a dominance of movements of the plasma membrane in the autocorrelation function.

Apparently, a fraction (~75%) of receptors has a diffusion rate too low to be distinguished from cellular movements by FCM, while a second fraction with higher mobility may be distinguished. For this reason, the fraction of receptors with little mobility was prebleached at higher excitation intensities and autocorrelation functions were recorded at laser powers as low as possible for obtaining autocorrelation functions with good signal-to-noise ratios. This protocol confines the quantification of receptor numbers and diffusion to the fraction of receptors with higher mobility.

After several minutes of laser illumination at a single spot on the membrane, the extent of overall depletion of fluorescence in the cell derived from integrating all pixel-intensities was orders of magnitude larger (20%) than the percentage of the illuminated area out of the total cell surface area (~0.01%). This means that not only those receptors located in the membrane domain initially overlapping with the focal volume were bleached, but also receptors from more distant membrane regions could cross domain boundaries and reach the illuminated area within the time span of the measurements

The large fraction of receptors with low mobility demonstrates a practical limitation of FCS in cellular studies set forth by the sensitivity of the method to the displacement of the membrane with respect to the detection volume. These factors prevent measurements of diffusion times slower than a few seconds (in our case τ_d s longer than a few seconds). For investigating such slow diffusion processes FRAP may be a more adequate approach.

Evaluation of autocorrelation functions

Diffusion constants were derived from the diffusion autocorrelation times based on a direct determination of the dimensions of the detection volume. The method employed here differs from the usual practice of relying on calibration measurements on

compounds of known diffusion constants [49]. This direct method of determining the dimensions of the detection volume and the structure parameter, S , yielded identical values to those obtained from the amplitude and shape of the autocorrelation curve from a fluorescein solution.

Autocorrelation functions for EGFR-GFP fusion proteins in both resting and stimulated cells consisted of at least three components with time constants in the upper millisecond, lower millisecond to upper microsecond and lower microsecond time range. While the slowest component was assigned to diffusion of receptors in the plasma membrane, it was uncertain whether the component in the lower millisecond time range resulted from cytoplasmic diffusion of proteolytic fragments of the EGFR-GFP fusion protein, from protonation-dependent blinking of GFP or from a superposition of both processes. The fastest process was assigned to triplet state transitions.

Five different models were employed to fit the autocorrelation functions: (i) a model containing two diffusional components and one triplet term, (ii) a model assuming a triplet term, two GFP blinking terms and one diffusional component, models assuming a triplet term with one freely diffusing component and one anomalously diffusing component with (iii) or without (iv) a blinking term, or (v) a model including a triplet term, a blinking term and anomalous diffusion for both the slow and the fast component.

Fitting the autocorrelation functions with a model assuming two protonation-dependent photophysical transitions in the sub-millisecond to millisecond time-range and no diffusion term (model 2), yielded time constants of $400 \pm 290 \mu\text{s}$ and $5 \pm 3 \text{ ms}$. The faster term is in good agreement with the time constants of protonation equilibria determined in previous studies. The time constant of the external, pH-dependent mechanism was found to be $300 \mu\text{s}$ at pH 7 and $45 \mu\text{s}$ at pH 5, while the time constant of the internal process was $340 \mu\text{s}$ [26]. Thus, the time constant in the upper microsecond

time range likely corresponds to a superposition of both the internal and external protonation processes. However, the slower component has a time constant more than an order of magnitude larger than that of the protonation processes. For this reason, the autocorrelation curve in the sub-millisecond to millisecond time-range cannot be explained by these processes alone. Instead, one has to consider the presence of diffusing GFP-containing species other than the EGFR-GFP in the membrane observed through the slow (sub-second) term of the autocorrelation functions.

The identity of this faster diffusing species may be delineated from the dependence of the weights of the slow and the fast components on the position of the detection volume. In the cytoplasm of resting cells, the fast component contributed 59 ± 8 % to the autocorrelation function, compared to only 33 ± 5 % when the beam waist was placed on the plasma membrane. The presence of the faster component in the latter case originated likely from the ellipsoidal shape of the sensitive volume with a longitudinal axis of about $2.4 \mu\text{m}$, extending into the cytoplasm. Conversely, the detection of the slow component for placement of the detection volume in the cytoplasm was probably caused by the same factor, especially when considering that these cells are generally $<5\mu\text{m}$ thick at areas outside the nucleus.

The diffusion constant of the faster, cytoplasmic component is $2.7 \pm 0.9 \times 10^{-7}$ cm^2/s , which is in range with the values reported previously for free cytoplasmic GFP using FCS ($D = 1.7 \pm 0.4 \times 10^{-7}$ cm^2/s [50] and $1.25 \pm 0.13 \times 10^{-7}$ cm^2/s [33]). However, Western blot analysis has shown that in the F1-10 cells there is no free GFP. Thus the faster component could either be attributed to EGFR-GFP fusion proteins being transported in vesicles, to free cytoplasmic EGFR-GFP that have lost their signal sequence, or other fluorescent molecules native to the cytoplasm. Of these possibilities the first can probably be excluded as the diffusion constant of integral membrane proteins

in intracellular membranes is comparable to that in the cytoplasmic membrane [51, 52] and the speed of vesicular traffic is even slower than that [53].

Depending on the number and nature of components included in the different models, different diffusion constants were obtained. Comparison of the diffusion constants obtained with the different models revealed a dependence of the diffusion constant on the number and nature of components included in each model. The diffusion constant of the fast component in models 4 and 5 was ~30% lower than the one obtained with model 3, which did not include a blinking term. In models 4 and 5 this term had an average characteristic time constant of ~0.18 ms. Without this blinking term, the fast diffusion term compensated for the poor fit in the sub-millisecond time range and thus converged to a smaller value. Evidently, inclusion of the blinking term critically affected the determination of diffusion times.

The molecular details of the diffusion mechanism were addressed by testing models assuming free Brownian diffusion as well as anomalous diffusion [34]. Anomalous diffusion describes a non-linear dependence of the mean-square displacement on time. Such a dependency may occur when diffusion is hindered e.g. by collisions with inert obstacles such as small membrane domains or molecular aggregates from which the receptor is excluded. In this case, the diffusion constant is time-dependent: the short-range diffusion coefficient is higher than the long-range one (anomalous subdiffusion). The longer the time interval over which molecular displacement is analyzed, the more pronounced the discrepancy between the mean square displacement for Brownian diffusion and that of the hindered diffusion. For short time intervals, the diffusion constant approaches that of unhindered diffusion. On the other hand, if the diffusion of the receptors is restricted to membrane domains of similar size to that of the detection volume, d_w values between 1 and 2 are expected.

As did diffusion constants, the anomaly parameters also showed variability in the measurements. In model 5, the values of $d_{w,1}$ and $d_{w,2}$ ranged between 1.76 - 2.97 and 1.7-2.30 for the fast and slow components, respectively. Values larger than 2, especially in the case of the fast component, may relate to obstructed diffusion mechanism with various local diffusion conditions in the accidentally selected and probed volume elements. Wachsmuth et al reported values of $d_w > 2$ for the diffusion of GFP and GFP-beta-galactosidase in AT-1 and COS-7 cells [33]. Values less than 2, if not caused by the uncertainty in the fitting procedure, may be due to corralled diffusion due to membrane domains with sizes comparable to that of the detection volume. An alternative explanation could be directed diffusion (or vesicle trafficking). However, it should be emphasized that the mean of $d_{w,2}$ did not differ significantly from 2; therefore the assumption of an anomalous diffusion mechanism is not fully convincing unless there is considerable micro-heterogeneity in the system.

For describing the diffusion of GFP receptor fusion proteins in the plasma membrane model 5 – assuming a slow and a fast non-Brownian diffusion component, plus GFP blinking and triplet correction – seems to be the most adequate. The inclusion of a protonation term and a fast diffusion time are indispensable to attain satisfactory fits throughout the millisecond to second time range. The use of the anomalous diffusion model is not fully convincing; however, if kept in a relatively narrow range around 2, the value of the anomaly parameter affects the fitted diffusion correlation time to a moderate extent only, so it does not compromise other parameters of the fit. The determination whether or not anomalous diffusion behavior occurs here and whether it can be detected by FCS remains open and deserves further investigation.

Effects of receptor stimulation on autocorrelation measurements

After stimulation of receptors with EGF, a significant decrease of the slow diffusion coefficient corresponding to a decrease in receptor mobility was observed. This decrease of the diffusion constants was independent of the model used for the fit. This finding illustrates the robustness of the evaluation of slow (intramembrane) diffusion times. At first sight the decrease of the diffusion constants and of the number of molecules is consistent with receptor aggregation and downregulation. However, the two-fold decrease of D exceeds the theoretically predictable value for dimerization (assuming spherical molecules this would be by a factor of $\sim\sqrt[3]{2} = 1.26$). This discrepancy hints at immobilization or at least hindering in motion of the EGFR-GFP fusion proteins. This may be due to interaction with static structures e.g. with the underlying cytoskeleton, which was observed in A431 cells upon stimulation with EGF (van Bergen en Henegouwen PMP et al, J. Cell. Biochem. 1989, 39:445-465). Alternatively, receptors could oligomerize instead of dimerizing. However, in the case of oligomerization a decrease of the number of independently diffusing particles by a factor larger than two would be expected, but this decrease is only 22%. The constancy of the normalized fluorescence per molecule also indicates that, at least in the first few minutes of activation, the aggregate size of EGFRs does not change significantly. These findings may reflect activation of the receptors according to the conformational activation model (not involving a change in the aggregation state of the receptor) rather than by induced receptor dimerization or oligomerization. However, we have to keep in mind that the chromophore of a large fraction of the receptors is bleached and therefore not subject of the FCS studies. Thus, it is equally plausible that receptor aggregation / dimerization occurs, but it is only reflected by the decrease in diffusion constant, as the detected EGFR-GFP molecules, or preformed dimers adhere to the more slowly moving higher

order clusters that are already photobleached in the pre-bleach period and thus do not contribute to the specific fluorescence per particle value.

Complications in cellular FCM

For FCM measurements of EGFR-GFP fusion proteins, photobleaching of molecules with little or no mobility, as well as movements of the plasma membrane are of special concern. In order to avoid contributions of photobleaching to the autocorrelation function, the immobile and slowly moving fluorophores may be photodestructed by high intensity illumination prior to the measurement. However, in that case only the more mobile fraction of molecules can be analyzed by FCM. The motion of the plasma membrane along the optical axis results in slow fluctuations of the detected signal with large amplitude. This motion contributes an additional component to the autocorrelation function and hampers the determination of the number of diffusible molecules in the detection volume. Estimates on the rate and amplitude of membrane mobility were derived from the repeated acquisition of fluorescence profiles along the optical axis Fig. 6.11. This motion can be as fast as several hundred nanometers per minute, and can cover a z-range of more than a micron. In our analyses, only those cells were included, which did not perform such motions as suggested by the congruency of the intensity profiles before and after the measurement, and by the relatively smooth fluorescence vs. time count traces with little or no low-frequency drift.

Comparison of FCS and FRAP analysis

Earlier reports on the lateral diffusion coefficients of EGFRs determined by FRAP are available for several cell types (e.g. $D = 4.5\text{-}8.2 \times 10^{-10} \text{ cm}^2/\text{s}$ at $15\text{-}37^\circ\text{C}$ on A431 cells [54], $D = 1.8 \times 10^{-10} \text{ cm}^2/\text{s}$, on fibroblasts and $D = 4.1 \times 10^{-10} \text{ cm}^2/\text{s}$ on keratinocytes [55]). Our FRAP experiments, depending on the exact evaluation method, yielded somewhat

lower diffusion coefficients, $0.7-0.9 \times 10^{-10}$ cm²/s, when fitting throughout the whole 120-140 s of the measurement. This discrepancy may be due to the different cell types used in earlier and the present experiments. When fitting only the first five seconds of the FRAP recovery curve, the derived diffusion coefficient is higher than that for the whole curve: $\sim 3.3 \times 10^{-10}$ cm²/s. Even this value is slower (by a factor of ~ 3) than the mean diffusion coefficients derived from FCS, which are ~ 1.2 and 0.7×10^{-9} cm²/s for resting and stimulated cells, respectively. To understand this discrepancy, the different nature of the experiments must be considered: in FCS the local environment of a relatively small area of the membrane is probed, which may be smaller than the diameter of a membrane domain. Therefore mainly diffusion inside a membrane microdomain determines the diffusion correlation time. In FRAP the long range diffusion rate of unbleached molecules arriving from more distant areas and having to cross domain boundaries is also examined. Thus, the rate of long-range receptor motion is not only affected by the intradomain diffusion rate, but also by the rate of crossing domain boundaries [45, 49]. It also has to be kept in mind that in the FCS measurements receptors with low mobility were pre-bleached to avoid artifacts in the autocorrelation function, so the motion of this fraction of the molecules was not subject of the FCS studies.

When the autocorrelation functions were fitted with models including a blinking term and two anomalous diffusion components, the average anomaly parameter of the membrane diffusion term was close to two, possibly signifying free Brownian diffusion. In contrast, for FRAP measurements the anomaly parameter lesser than unity hinted at the possibility of obstructed diffusion. The analysis of only the first few seconds of the recovery curve yielded a higher diffusion coefficient than the total recovery curve, i.e. the diffusion coefficient was time (or distance) dependent, corroborating the assumption of an anomalous diffusion mechanism. Obstructed diffusion can result from either molecular

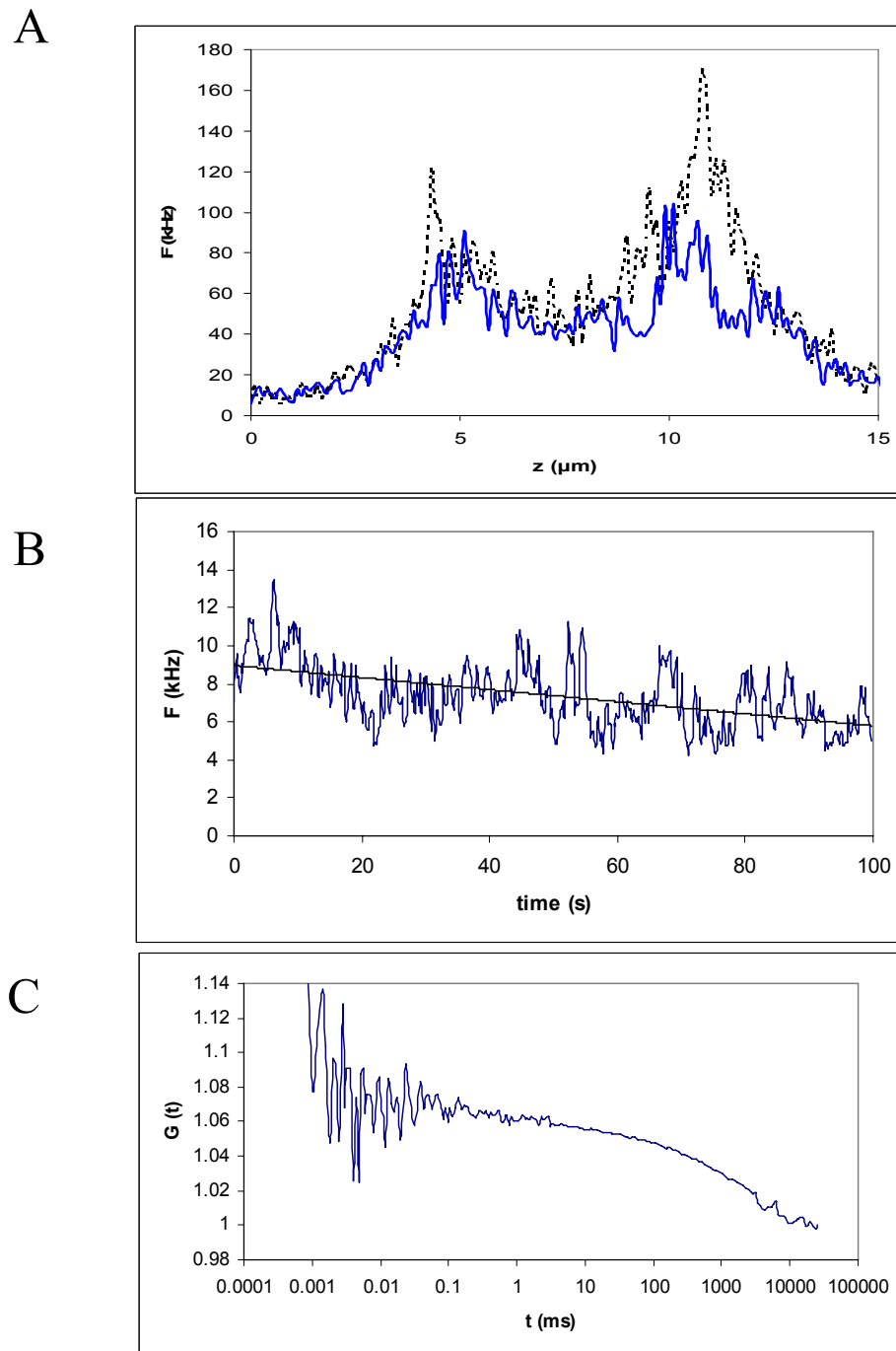


Fig. 6.11 Effect of macroscopic motion of the cell membrane on an FCS measurement. Disparate z-profiles before (dashed line) and after (solid line) an FCS measurement show that the cell membrane has undergone macroscopic motion between the two z-scans. The vertical dotted line denotes the focus position during the FCS measurement. (A) The count trace recorded during the FCS measurement displays large fluctuations and a decreasing trend as the membrane is moving out of the focus. (B) This appears in the autocorrelation function as a long "diffusion time"

interactions (binding to immobile structures or large complexes), frequent collisions with densely packed obstacles or corraling due to boundaries between distinct membrane domains [37, 43, 56]. If the last possibility applies, and the diameter of membrane domains significantly exceeds that of the illuminated spot, the manifestation of obstructed diffusion during the measurement depends on the position of the sensitive volume relative to the domain boundaries. If the boundary lies within the detection volume, the anomalous nature of diffusion may be observed, but otherwise it may not be detected. The presence of membrane domain boundaries affects the autocorrelation function only if the domain is comparable in size to that of the detection volume.

The uncertainty of detecting anomalous diffusion in the FCS measurements may originate from the fact that fluctuations resulting from molecular movements in the immediate vicinity of the detection volume are detected. In contrast, in FRAP the recovery of fluorescence results from diffusion of molecules over short as well as longer distances. Molecules therefore may encounter a large number of diffusion barriers. Thus the short-range diffusion of molecules in FCS will be hardly affected by boundaries and heterogeneities in membrane organization. Only if a diffusion barrier lies within the detection volume, or if membrane microdomains are comparable in size with the detection volume, may anomalous diffusion be observed. The diffusion constant and anomaly parameter may also depend on the size of the membrane domain and the position of the detection volume with respect to the domain boundaries: in a larger domain, diffusion may occur faster than in a smaller one, in which the observable mobility is more strongly dependent on the rate of crossing membrane domain boundaries, also called hop diffusion [45, 57, 58]. The large standard deviation of the

slow diffusion constant and the anomaly parameter in the FCS measurements may reflect the microheterogeneity of the plasma membrane.

6.6 Conclusions

Because a significant fraction of the membrane-located receptors appears to be immobile on the time-scale of the FCS measurement, it was necessary to pre-bleach the sample until a dynamic equilibrium between bleaching and re-population processes of the illuminated area were established; otherwise the drift of fluorescence intensity would have compromised the autocorrelation data. On the other hand, the finite photostability of the dyes involves a technical limitation of FCS: diffusible species with too long diffusion times (in our system >1 s) cannot be reliably analyzed because of the too long exposure to laser illumination and consequent photodestruction. In addition to photobleaching, which in principle can be treated mathematically, long diffusion times necessitate longer recording times, during which the position of the plasma membrane can change due to active or passive motions of the cell. Thus, for the investigation of such slow diffusion processes FRAP might be more adequate.

The details of the selected model, such as the involvement of correction terms for photophysical processes like protonation dependent GFP “blinking” or triplet state formation may significantly affect the nonlinear fit estimates of faster diffusion times, which are in the same time range, and may even change the conclusions concerning the diffusion mechanism (free or obstructed) of the slow diffusing species by distorting the shape of the autocorrelation function. However, this does not question the validity of the comparison of slow (membrane-related) diffusion times under different treatment conditions: a consequent evaluation of the slow diffusion constants with different models yielded similar numerical D_2 values, and a convincing decrease in the mobility of EGFR-

GFP evoked by EGF stimulation. Hence we can say that the slow diffusion correlation time is a fairly robust parameter, which is hardly influenced by the model so long as the other terms are reasonably well fitted. The decreased mobility of EGFR-GFP is best explained by attachment of the receptors to slowly moving or stationary molecular structures such as to the underlying cytoskeleton or larger receptor aggregates that were already photobleached, since the specific fluorescence per molecule did not change, and the number of fluorescing molecules in the observation volume only decreased by 22%.

Our FCS measurements report on the microheterogeneity of local diffusion conditions both in terms of mobility and the effect of obstacles hindering diffusion as reflected by the large SD of the values of the diffusion constants and the anomaly parameters. This indication of the microdomain structure of the cell membrane and its influence on the motion of cell surface receptors is further supported by the anomalous nature of diffusion reported by FRAP data. Our analysis also shows that FCS and FRAP can provide complementary information on the local (few hundred nm) and long-range (several microns) diffusion properties of plasma membrane receptors.

6.6 Acknowledgements

The cooperation between T.M.J., G. Vámosi and G. Vereb was supported by the DAAD-MÖB joint grant for exchange of researchers No. 91/1997 and by FP5 QLRT-1999-3126. This work was supported by grants ETT 117/2001, OTKA T037831, F025210, TS 040773, T030411, and the Alexander von Humboldt Foundation. R. B. was recipient of a doctoral fellowship from the Studienstiftung des deutschen Volkes. The authors thank Drs. Donna Arndt-Jovin, Jörg Langowski and Malte Wachsmuth for valuable discussions and critical reading of the manuscript.

References

1. Yarden, Y., (2001) The EGFR family and its ligands in human cancer. signalling mechanisms and therapeutic opportunities. *Eur J Cancer*. 37 Suppl 4: p. S3-8.
2. Gadella, T.W., Jr. and T.M. Jovin, (1995) Oligomerization of epidermal growth factor receptors on A431 cells studied by time-resolved fluorescence imaging microscopy. A stereochemical model for tyrosine kinase receptor activation. *J Cell Biol*. 129(6): p. 1543-1558.
3. Stern, D.F. and M.P. Kamps, (1988) EGF-stimulated tyrosine phosphorylation of p185neu: a potential model for receptor interactions. *Embo J*. 7(4): p. 995-1001.
4. Moriki, T., H. Maruyama, and I.N. Maruyama, (2001) Activation of preformed EGF receptor dimers by ligand-induced rotation of the transmembrane domain. *Journal of Molecular Biology*. 311(5): p. 1011-1026.
5. Mendrola, J.M., et al., (2002) The Single Transmembrane Domains of ErbB Receptors Self-associate in Cell Membranes. *J. Biol. Chem*. 277(7): p. 4704-4712.
6. Yarden Y, S.J., (1987) Self-phosphorylation of epidermal growth factor receptor: evidence for a model of intermolecular allosteric activation. *Biochemistry* 26(5): p. 1434-1442.
7. Nico van Belzen, P.J.R.W.J.H.S.W.d.L.A.J.V.J.B., (1988) Direct visualization and quantitative analysis of epidermal growth factor-induced receptor clustering. *Journal of Cellular Physiology*. 134(3): p. 413-420.
8. Spaargaren, M., et al., (1991) Antibody-induced dimerization activates the epidermal growth factor receptor tyrosine kinase. *J. Biol. Chem*. 266(3): p. 1733-1739.
9. Cochet, C., et al., (1988) Demonstration of epidermal growth factor-induced receptor dimerization in living cells using a chemical covalent cross-linking agent. *J. Biol. Chem*. 263(7): p. 3290-3295.
10. Fanger BO, S.J., Staros JV., (1989) High-yield trapping of EGF-induced receptor dimers by chemical cross-linking. *FASEB J*. . 3(1): p. 71-75.

11. Lemmon, M.A., et al., (1997) Two EGF molecules contribute additively to stabilization of the EGFR dimer. *Embo J.* 16(2): p. 281-294.
12. Sako, Y., S. Minoghchi, and T. Yanagida, (2000) Single-molecule imaging of EGFR signalling on the surface of living cells. *Nat Cell Biol.* 2(3): p. 168-172.
13. Stryer, L., (1978) Fluorescence energy transfer as a spectroscopic ruler. *Ann Rev Biochem.* 47: p. 819-846.
14. Jovin, T.M. and D.J. Arndt-Jovin, *FRET microscopy: Digital imaging of fluorescence resonance energy transfer. Application in cell biology.*, in *Cell Structure and Function by Microspectrofluorimetry*, E. Kohen and J.G. Hirschberg, Editors. 1989, Academic Press: San Diego, CA. p. 99-115.
15. Damjanovich, S., et al., (1995) Structural hierarchy in the clustering of HLA class I molecules in the plasma membrane of human lymphoblastoid cells. *Proceedings of the National Academy of Sciences of the United States of America.* 92(4): p. 1122-1126.
16. Bastiaens, P.I. and T.M. Jovin, (1996) Microspectroscopic imaging tracks the intracellular processing of a signal transduction protein: fluorescent-labeled protein kinase C beta I. *Proc Natl Acad Sci U S A.* 93(16): p. 8407-8412.
17. Edidin, M., Y. Zagyansky, and T.J. Lardner, (1976) Measurement of membrane protein lateral diffusion in single cells. *Science.* 191(4226): p. 466-468.
18. Jacobson, K., et al., (1982) Fluorescence photobleaching in cell biology. *Nature.* 295(5847): p. 283-284.
19. Anderson, C.M., et al., (1992) Tracking of cell surface receptors by fluorescence digital imaging microscopy using a charge-coupled device camera. Low-density lipoprotein and influenza virus receptor mobility at 4 degrees C. *J Cell Sci.* 101 (Pt 2): p. 415-425.
20. Kusumi, A., Y. Sako, and M. Yamamoto, (1993) Confined lateral diffusion of membrane receptors as studied by single particle tracking (nanovid microscopy). Effects of calcium-induced differentiation in cultured epithelial cells. *Biophys J.* 65(5): p. 2021-2040.
21. Magde, D., E.L. Elson, and W.W. Webb, (1974) Fluorescence correlation spectroscopy. II. An experimental realization. *Biopolymers.* 13(1): p. 29-61.

22. Brock, R. and T.M. Jovin, (1998) Fluorescence correlation microscopy (FCM)-fluorescence correlation spectroscopy (FCS) taken into the cell. *Cell Mol Biol (Noisy-le-grand)*. 44(5): p. 847-856.
23. Brock, R., et al., (1999) Rapid characterization of green fluorescent protein fusion proteins on the molecular and cellular level by fluorescence correlation microscopy. *Proc Natl Acad Sci U S A*. 96(18): p. 10123-128.
24. Schwille, P., et al., (1999) Molecular dynamics in living cells observed by fluorescence correlation spectroscopy with one- and two-photon excitation. *Biophys J*. 77(4): p. 2251-2265.
25. Lippincott-Schwartz, J., E. Snapp, and A. Kenworthy, (2001) Studying protein dynamics in living cells. *Nat Rev Mol Cell Biol*. 2(6): p. 444-456.
26. Haupts, U., et al., (1998) Dynamics of fluorescence fluctuations in green fluorescent protein observed by fluorescence correlation spectroscopy. *PNAS*. 95(23): p. 13573-13578.
27. Brock, R., M.A. Hink, and T.M. Jovin, (1998) Fluorescence Correlation Microscopy of Cells in the Presence of Autofluorescence. *Biophys. J*. 75(5): p. 2547-2557.
28. Wiegant, F.A.C., Blok, F. J., Defize, L. H. K., Linnemans, W. A. M., Verkley, A. J., and Boonstra, J., (1986) Epidermal growth factor receptors associated to cytoskeletal elements of epidermoid carcinoma (A431) cells. *J. Cell Biol*. 103: p. 87-94.
29. Gronowski, A.M. and P.J. Bertics, (1995) Modulation of epidermal growth factor receptor interaction with the detergent-insoluble cytoskeleton and its effects on receptor tyrosine kinase activity. *Endocrinology*. 136(5): p. 2198-2205.
30. Grynkiewicz, G., M. Poenie, and R.Y. Tsien, (1985) A new generation of Ca²⁺ indicators with greatly improved fluorescence properties. *J Biol Chem*. 260(6): p. 3440-3450.
31. Widengren, J. and Ü. Mets, (1994) Triplet state monitoring by fluorescence correlation spectroscopy. *J. Fluorescence*. 4: p. 255-258.

32. Widengren, J., Ü. Mets, and R. Rigler, (1995) Fluorescence correlation spectroscopy of triplet states in solution: A theoretical and experimental study. *J. Phys. Chem.* 99: p. 13368-13379.
33. Wachsmuth, M., W. Waldeck, and J. Langowski, (2000) Anomalous diffusion of fluorescent probes inside living cell nuclei investigated by spatially-resolved fluorescence correlation spectroscopy. *J Mol Biol.* 298(4): p. 677-689.
34. Saxton, M.J., (1994) Anomalous diffusion due to obstacles: a Monte Carlo study. *Biophys. J.* 66(2): p. 394-401.
35. Axelrod, D., et al., (1976) Mobility measurement by analysis of fluorescence photobleaching recovery kinetics. *Biophys J.* 16(9): p. 1055-1069.
36. van Zoelen, E.J., L.G. Tertoolen, and S.W. de Laat, (1983) Simple computer method for evaluation of lateral diffusion coefficients from fluorescence photobleaching recovery kinetics. *Biophys. J.* 42(1): p. 103-108.
37. Feder, T.J., et al., (1996) Constrained diffusion or immobile fraction on cell surfaces: a new interpretation. *Biophys. J.* 70(6): p. 2767-2773.
38. Wolf, D.E., and M. Edidin. (1981) Methods of Measuring Diffusion and Mobility of Molecules in Surface membranes. In *Techniques in Cellular Physiology. Vol. P1/1, Pt. 105.*, ed. P.F. Baker. Elsevier/North-Holland Biomedical, Amsterdam. 1-14
39. Brock, R. and T.M. Jovin, (2001) Heterogeneity of signal transduction at the subcellular level: microsphere-based focal EGF receptor activation and stimulation of Shc translocation. *J Cell Sci.* 114(Pt 13): p. 2437-2447.
40. Waterman H, K.M., Rubin C, Shtiegman K, Lavi S, Elson A, Jovin T, Yarden Y., (2002) A mutant EGF-receptor defective in ubiquitylation and endocytosis unveils a role for Grb2 in negative signaling. *EMBO J.* 21(3): p. 303-313.
41. Margolis, B., et al., (1989) EGF induces tyrosine phosphorylation of phospholipase C-II: A potential mechanism for EGF receptor signaling. *Cell.* 57(7): p. 1101-1107.
42. Widengren J, R.R., (1996) Mechanisms of photobleaching investigated by fluorescence correlation spectroscopy. *Bioimaging.* 4(3): p. 149-157.

43. Edidin, M., (1993) Patches and fences: probing for plasma membrane domains. *J Cell Sci Suppl.* 17: p. 165-169.
44. Edidin, M., (2001) Shrinking patches and slippery rafts: scales of domains in the plasma membrane. *Trends Cell Biol.* 11(12): p. 492-496.
45. Kusumi, A. and Y. Sako, (1996) Cell surface organization by the membrane skeleton. *Curr Opin Cell Biol.* 8(4): p. 566-574.
46. Nagle, J.F., (1992) Long tail kinetics in biophysics? *Biophys. J.* 63(2): p. 366-370.
47. Damjanovich, S., et al., (1983) Distribution and mobility of murine histocompatibility H-2Kk antigen in the cytoplasmic membrane. *Proc Natl Acad Sci U S A.* 80(19): p. 5985-5989.
48. Edidin, M., et al., (1988) Lateral diffusion measurements give evidence for association of the Tac peptide of the IL-2 receptor with the T27 peptide in the plasma membrane of HUT-102-B2 T cells. *J. Immunol.* 141(4): p. 1206-1210.
49. Edidin, m., *Mobility and proximity in biological membranes*, in *Mobility and proximity in biological membranes*, S. Damjanovich, M. Edidin, and L. Tron, Editors. 1994, CRC Press. p. 109-135.
50. Brock, R., I.H. Hamelers, and T.M. Jovin, (1999) Comparison of fixation protocols for adherent cultured cells applied to a GFP fusion protein of the epidermal growth factor receptor. *Cytometry.* 35(4): p. 353-362.
51. Cole, N.B., Smith CL, Sciaky N, Terasaki M, Edidin M, Lippincott-Schwartz J., (1996) Diffusional mobility of Golgi proteins in membranes of living cells. *Science.* 273(5276): p. 797-801.
52. Wagner, M.L. and L.K. Tamm, (2001) Reconstituted Syntaxin1A/SNAP25 Interacts with Negatively Charged Lipids as Measured by Lateral Diffusion in Planar Supported Bilayers. *Biophys. J.* 81(1): p. 266-275.
53. Oheim, M. and W. Stuhmer, (2000) Tracking chromaffin granules on their way through the actin cortex. *European Biophysics Journal.* V29(2): p. 67-89.
54. Schlessinger, J., (1983) Lateral and rotational diffusion of EGF-receptor complex: relationship to receptor-mediated endocytosis. *Biopolymers.* 22(1): p. 347-353.

55. Lirvall, M., et al., (1996) Uvb Radiation Affects the Mobility of Epidermal Growth Factor Receptors in Human Keratinocytes and Fibroblasts. *Bioscience Reports*. 16(3): p. 227-238.
56. Dietrich, C., et al., (2002) Relationship of lipid rafts to transient confinement zones detected by single particle tracking. *Biophys J*. 82(1): p. 274-284.
57. Sako, Y. and A. Kusumi, (1995) Barriers for lateral diffusion of transferrin receptor in the plasma membrane as characterized by receptor dragging by laser tweezers: fence versus tether. *J Cell Biol*. 129(6): p. 1559-1574.
58. Tomishige, M., Y. Sako, and A. Kusumi, (1998) Regulation Mechanism of the Lateral Diffusion of Band 3 in Erythrocyte Membranes by the Membrane Skeleton. *J. Cell Biol*. 142(4): p. 989-1000.

Chapter

7

Cholesterol-dependent clustering of IL-2R α and its colocalization with HLA and CD48 on T lymphoma cells suggests their functional association with lipid rafts

G. Vereb, J. Matkó, G. Vámosi, S. M. Ibrahim, E. Magyar,
S. Varga, J. Szöllősi, A. Jenei, R. Gáspár,
T. A. Waldmann and S. Damjanovich

Proc Natl Acad Sci U S A. 2000, 97: 6013-8

7.1 Abstract

Immunogold staining and electron microscopy show that IL-2 receptor α subunits exhibit non-random surface distribution on human T lymphoma cells. Analysis of inter-particle distances reveals that this clustering on a few hundred nm scale is independent of the presence of IL-2 and of the expression of the IL-2R β subunit. Clustering of IL-2R α is confirmed by confocal microscopy, yielding the same average cluster size, \sim 600-800 nm, as electron microscopy. HLA class I and II, and CD48 molecules also form clusters of the same size. Disruption of cholesterol-rich lipid rafts with filipin or depletion of membrane cholesterol with methyl- β -cyclodextrin results in the blurring of cluster boundaries and an apparent dispersion of clusters for all four proteins. Interestingly, the transferrin receptor (TrfR), which is thought to be located outside lipid rafts, exhibits clusters that are half the size and are less affected by modifying the membrane cholesterol content. Furthermore, TrfR clusters hardly co-localize with IL-2R α , HLA and CD48 molecules (cross-correlation coefficient is <0.12), while IL-2R α co-localizes with both HLA and CD48 (cross-correlation coefficient is >0.37). This co-clustering is confirmed by electron microscopy. The sub-micron clusters of IL-2R α chains and their co-clustering with HLA and CD48, presumably associated with lipid rafts, could underlie the efficiency of signaling in lymphoid cells.

7.2 Introduction

Cytokines regulating immune responses have their specific, private receptor, but may also share public receptors with other cytokines. Interleukin-2 (IL-2) secreted by T lymphocytes when stimulated with antigen or mitogens is essential for T cell growth [1,2]. The private receptor for IL-2 is the IL-2R α subunit, exhibiting relatively low affinity for IL-2 compared to the IL-2R $\alpha\beta\gamma$ heterotrimer, which is considered a fully functional receptor [3]. We have recently shown in a fluorescence resonance energy transfer study that the IL-2R α , β and γ subunits are preassembled even on the surface of unstimulated Kit 225 K6 T lymphoma cells, and cannot, therefore, be considered as a transient signaling assembly [4]. It is still unclear how IL-2R α is recruited to the less abundant β and γ chains to form the functionally active receptor.

Similar assemblies (non-random co-localization) of cell surface antigens and receptors have been reported previously for lymphoid cells, as reviewed e.g. in [5]. Such supramolecular formations on the nanometer level have primarily been explored using flow cytometric energy transfer [6], joined by other, mostly fluorescence based techniques that assess lateral or rotational mobility of membrane proteins or assemblies thereof [7-9]. Possibly functional protein association patterns were discovered, including the di/oligomerization of HLA I and II molecules on activated T cells and lymphoid cell lines [10-13], the heteroassociation between HLA I and HLA II glycoproteins [14], or HLA I and the IL-2R α subunit [15]. These observations argue against independent, freely moving membrane proteins postulated by the fluid mosaic membrane model; instead, a segregated, "corralled" structure may be the valid hypothesis, with specific molecules confined to specific regions [16].

Various studies directed at the plasma membrane have provided evidence for the existence of such distinct domains in the sub-micron range [12,17-19]; for a most recent

Cholesterol-dependent clustering of IL-2R α and its colocalization with HLA and CD48 on T lymphoma cells suggest their functional association with lipid rafts

overview see [20]. From the biochemical point of view, these domains appear as detergent insoluble / resistant, glycolipid enriched membrane domains (DRMs, DIGs or GEMs [21]) and are often termed lipid rafts [22]. Physically, they are expected to be represented by cell surface patches found for both lipid and protein molecules [23]. The physical and chemical forces giving rise to such domains are under intensive investigation [8,24]. One presumes that several intracellular, extracellular, and intramembrane constraints and forces influence the size and distribution of these clusters, one of them being the cholesterol content of the membrane area in question [22,25]. There is indeed evidence that changing the cholesterol composition of the cell membrane alters the association pattern and signaling properties of various molecules [25,26]. Such a change can be brought about by treating the cell membrane with filipin, a polyene antibiotic specifically complexing cholesterol [27], or by extracting cholesterol from the membrane by methyl- β -cyclodextrin [28].

The physiological significance of the lateral micro-domain organization of biological membranes is not clear yet. One can assume that a larger scale local accumulation of receptors and their signal transduction machinery [29,30] may enhance the efficiency of transmembrane signaling by providing a focusing effect. We have previously shown patchy aggregation of platelet derived growth factor receptors on glioblastoma cells [19] as well as assemblies of up to 1000 erbB2 molecules on various mammary tumor cell lines [31]. Also, in addition to the molecular association of MHC class I and class II glycoproteins on lymphoma cells, we have observed their sub-micron scale clusters and co-clusters [12,17]. Given this knowledge, as well as the evidence that MHC class I glycoproteins are in the molecular vicinity of IL-2R α on some cell lines [15], in the present study we have undertaken to investigate the higher order clustering of IL-2R α on Kit 225 K6 and MT-1 lymphoma cells, and the possible heteroassociation of IL-2R α with MHC glycoproteins on the sub-micron-micron scale. To shed light on the possible role

of lipid rafts [20,22] in organizing these receptor assemblies, we have examined the co-localization of IL-2R α and MHC molecules with CD48, a GPI-linked T cell membrane protein reported to associate with rafts [21] and with the transferrin receptor that is excluded from glycosphingolipid enriched membrane micro-domains [32,33]. Furthermore, we have tested the influence of membrane cholesterol composition on the sub-micron scale clustering of these molecules by extracting cholesterol with methyl- β -cyclodextrin or complexing cholesterol *in situ* with filipin.

7.3 Materials and Methods

Cell culture and treatment

Kit 225 K6 and MT-1 T cell lines were cultured in RPMI-1640 medium (5% CO₂) supplemented with 10 % fetal calf serum and antibiotics. To maintain the growth of Kit 225 K6 cells, 20 U/ml recombinant IL-2 was added every 48 hours. Resting cells were obtained by culturing for 72 hours in IL-2 free medium. Filipin III (Sigma, St. Louis, Missouri, 0.1 mg/ml) was used to complex cholesterol in the cell membrane. Incubation (10⁶ cells/ml) for 1 hr at 37°C was followed by washing twice in PBS. Cholesterol extraction was achieved by treating 10⁶ cells/ml with 7 mM methyl- β -cyclodextrin (MBCD, Sigma, St. Louis, Missouri) for 1 hr at 37°C and its efficiency was assessed from the decrease of fluorescence polarization of the TMA-DPH membrane probe [26].

Monoclonal antibodies

The IL-2R α subunit, MHC class I and II were labeled with α Tac, W6/32 and L-243, respectively [4,12]. Anti-CD48 (MEM102) and anti-transferrin receptor (MEM75) were a generous gift of V. Horejsi (Inst. Mol. Genetics, Acad. Sci., Czech Republic). Fab fragments were prepared from

227

Cholesterol-dependent clustering of IL-2R α and its colocalization with HLA and CD48 on T lymphoma cells suggest their functional association with lipid rafts

mAbs as previously described [34]. Whole mAbs or Fab fragments were conjugated with long-linker fluorescein or rhodamine succinimidyl esters, (XF or XR, Molecular Probes, Eugene, OR), or sulfoindocyanine-succinimidyl ester (Cy3, monofunctional, Amersham Life Sci. Inc., Cleveland, Ohio) as described earlier [14,15].

Labeling of cells with monoclonal antibodies

10^6 cells/ml suspended in ice cold PBS were labeled for 40 min at 4°C in the dark. Optimal antibody concentrations were determined from saturation curves. Antibodies were air-fuged (20,000 g, 30 min) before labeling. Labeled cells were washed in cold PBS and either fixed with 1 % formaldehyde, used unfixed immediately, or further processed for electron microscopy.

Labeling of cells with colloidal gold for electron microscopy

Labeling with the first Fab (see above) was followed by incubation with polyclonal secondary antibodies conjugated to gold beads of 10 or 30 nm diameter (Aurogamig G-10, against the heavy and light chains, or Aurogamig G-30 against the Fc fragment; from Amersham Life Sci. Inc., Cleveland, Ohio) for 40 min. After washing with PBS (10 min, 250 x g) the cells were fixed with 2 % paraformaldehyde for 1 hr and then with 2% glutaraldehyde in 0.1M sodium cacodylate buffer (pH 7.2) overnight on ice. For sequential double labeling, the first antibody was a Fab followed by Aurogamig G-10, and then the unused binding sites of the polyclonal antibodies were blocked for 5 min with the Fab fragments used for primary labeling. Monoclonal antibodies against the second target epitope were whole antibodies that were tagged with Aurogamig G-30 against the Fc fragment. These beads will only label that fraction of the second target epitope which is not hidden by the first cohort of beads tagging the first target epitope [17].

Electron microscopy

After immunogold labeling cells were spread on poly-L-lysine-coated Formvar grids, dehydrated

in ascending ethanol series and air-dried from ether. Gold beads were counted in a JEOL electron microscope (JEM 100 B microscope operated at 100 kV) on the periphery and thinner parts of cells, where transparency allowed a good contrast.

Calculation of actual and expected cell surface distribution of gold labeled antigens

For a random distribution of the gold particles, the statistics of the number of beads per unit area should be Poissonian [12,17]. The average density of gold particles was calculated from their number and the area over which they were distributed. The area assigned to one bead on average was taken as the unit and thus the parameter λ of the assumed Poisson distribution was taken as 1. The number of beads counted in each unit area on the cell surface was used to calculate the actual distribution.

Comparison of characteristic inter-particle distances of colloidal gold labels

Scanned images of electron micrographs were processed using a custom-written program developed in the LabView (National Instruments, Austin, TX) environment. The coordinates of recognized labeling particles were used to produce the distribution of all inter-particle distances in the sample.

Confocal microscopy

Cells were labeled with fluorescent Fab fragments, fixed in 1% formaldehyde or left unfixed in control experiments, and attached to poly-L-lysine coated slides. A Zeiss LSM 420 laser scanning confocal microscope (Oberkochen, Germany) was used for measurements. Cy3 and XR were excited at 543 nm, XF at 488 nm. For double labeled samples in cross correlation studies a 515-525 nm narrow bandpass emission filter was used to detect XF fluorescence instead of the usual 510 nm LP. 512x512 pixel, 0.6 μm thin confocal sections were obtained with a pinhole

229

Cholesterol-dependent clustering of IL-2R α and its colocalization with HLA and CD48 on T lymphoma cells suggest their functional association with lipid rafts

setting of 25, 5-8x zoom, through a 100x (N.A.=1.3) objective. The intensity distribution of surface labeling was generated from the 3D reconstruction of sections using a projection algorithm in NIH Image (NIH, Bethesda, MD). In addition to the reconstructed free surfaces of cells, single confocal sections of each cell, flattened against the glass slide, were also analyzed.

Determination of cluster size from confocal images

Average cluster size was determined from both projected surface distributions and flattened single confocal images using the two dimensional autocorrelation function

$$G(\rho, \varphi) = \langle f(r, \Theta) f(r+\rho, \Theta+\varphi) \rangle \tag{7.1}$$

where the angle brackets indicate summation over the whole domain of the ρ radius and φ angle. The autocorrelation image was calculated by taking the inverse Fourier-transform of the two-dimensional power spectrum matrix of the original images. Since in our case we do not expect the distribution to be anisotropic, $G(\rho, \varphi)$ is independent of φ . Consequently, an angle-invariant autocorrelation function $G(\rho)$ can be generated by averaging $G(\rho, \varphi)$ over the range $0 \leq \varphi < 2\pi$. $G(\rho)$ is fitted to the equation

$$G(\rho) = \sum_i A_i \exp(-(\rho/R_i)^2) \tag{7.2}$$

where the R_i characteristic radii serve as an adequate measure of the mean size (half-width at the 1/e height of a Gaussian distribution) of each class of clusters distinguishable on the basis of its size [23]. Calculation of $G(\rho)$ and fitting equation 3 using the Levenberg-Marquardt algorithm was performed with a custom-written program developed in the LabView environment. Using

two exponentials gave a good fit with small residuals. The smaller value of R_i , generally in the 100-500 nm range, was taken as the radius of sub-micron sized clusters, in coherence with individual cluster sizes measured directly on the images. The larger value of R_i , several microns in magnitude, was assumed to be characteristic for background fluctuation [31].

Determining co-localization from image cross correlation

Co-localization of pairs of cell surface antigens was determined from confocal images of double-labeled cells. For a pair of images x and y , the cross-correlation coefficient was calculated as

$$C = \frac{\sum_i \sum_j (x_{i,j} - \langle x \rangle)(y_{i,j} - \langle y \rangle)}{(\sum_i \sum_j (x_{i,j} - \langle x \rangle)^2 \sum_i \sum_j (y_{i,j} - \langle y \rangle)^2)^{1/2}} \quad (7.3)$$

where $x_{i,j}$ and $y_{i,j}$ are fluorescence pixel values at coordinates i,j in images x and y . Only those pixels were used for the summation that were above detection threshold in both images. The theoretical maximum is $C = 1$ for identical images, and a value close to 0 implies disparate localization of the label. A program in LabView was written to register and threshold image pairs and compute the cross-correlation coefficient.

7.4 Results

Immunogold labeling and electron microscopy reveals a sub-micron level clustering of IL-2R α subunits on K6 cells

Fig. 7.1 shows immunogold labeled IL-2R α on Kit225 K6 cells. Clusters of several gold beads can be observed in addition to singly placed labels, and larger areas with no label at all. Counting

231

Cholesterol-dependent clustering of IL-2R α and its colocalization with HLA and CD48 on T lymphoma cells suggest their functional association with lipid rafts

the labels, we constructed the actual probability distribution (Fig. 7.2a, diamonds) and compared it to the theoretical Poissonian (Fig. 7.2a, closed circles). It is clear that there are a larger number of unit areas without any label than that expected for a Poissonian, and that unit areas with 4 or more gold labels are more abundant as well. Due to this disproportion, unit areas close to the expected Poissonian parameter (i.e. those with 1,2 and 3 labels) are lesser in number than predicted for a random distribution. The observed and expected distributions are different beyond a confidence level of 99.99 using the Chi-squared test. Thus, the localization of labels follows a non-random distribution, manifesting as clustering on the sub-micron scale.

Quantitative assessment of inter-particle distances reveals no difference in the higher level clustering of IL-2R α on IL-2 fed and starved K6 cells and MT-1 cells

Since the receptor clusters are not expected to be anisotropic, the calculation of a relevant autocorrelation function that can be used to quantify cluster size simplifies to constructing the distribution histogram of all inter-particle distances, without regard to the direction of localization. Such a distribution histogram is presented on Fig. 7.2b (diamonds) for the sample shown in Fig. 7.1. It is compared against a simulated distribution of the same number of particles

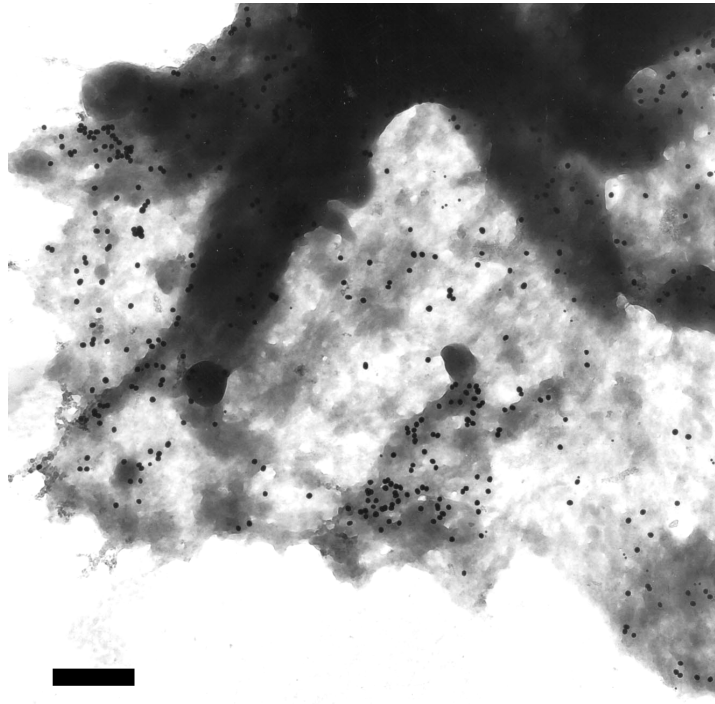


Fig. 7.1. Non-random distribution of IL-2R α on Kit 225 K6 cells revealed by colloidal gold labels. Kit 225 K6 cells were labeled with anti-Tac as primary antibody and then with 30 nm colloidal gold conjugated to the secondary antibodies. A representative electron micrograph of the periphery of a cell is shown. The distribution of gold labels appears to be non-random. Scale bar is 470 nm.

randomly scattered over the same area (closed circles). The actual distribution is comprised of two peaks, while the randomly generated particle pattern shows a single Poissonian peak. The first peak of the actual distribution likely corresponds to the average inter-particle distance within the small clusters of gold beads, while the second peak characterizes the average distance to labels outside the cluster. These average distances quantitatively describe the sub-micron level receptor patterns on various T cells. On Fig. 7.2c we see that in the case of Kit 225 K6 cells, the distance distribution is not influenced by IL-2 deprivation. Furthermore, the average distances within the clusters are the same in the case of MT-1 cells as for the K6 line.

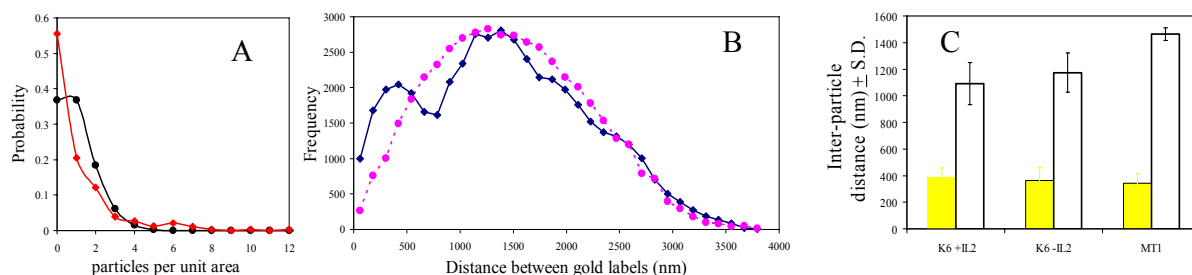


Fig. 7.2. Quantitative analysis of the distribution of gold labels on IL-2R α subunits. (A) Gold labels shown in Fig. 7.1. were counted ($n=406$) and the unit area was defined such that the expected value of gold labels per unit area was one. The image was divided into equal squares of one unit area each and the actual distribution of labels among the squares determined. The probability distribution of the particle density per unit area is plotted for the actual finding (\blacklozenge) and compared against a Poisson distribution with parameter $\lambda=1$ (\bullet). (B) The coordinates of all labels in Fig. 7.1. were determined and the distribution of all inter-particle distances was plotted (\blacklozenge). A model distribution was also generated assuming Poissonian statistics (dashed line, \bullet). In contrast to the single peak of the expected random distribution, the measured distribution has two peaks. The first peak around 400 nm represents the characteristic distance of gold labels within clusters. (C) Characteristic distances for gold labels determined as in (B) are plotted for Kit 225 K6 (K6+IL2), IL-2 - starved Kit 225 K6 (K6-IL2) and MT-1 cells. Characteristic distances within clusters are represented by filled columns, average distances within the whole sample area are shown with open columns. Data are mean \pm S.D. from 6 independent experiments.

Confocal laser scanning microscopy of hydrated samples confirms the presence of sub-micron IL-2R α clusters on MT-1 and Kit225 K6 cells

Confocal laser scanning microscopy was used to confirm the presence of sub-micron IL-2R α clusters on MT-1 and K6 cells. Cells were labeled on ice with Fab fragments to visualize receptors without inducing aggregation artifacts. Fig. 7.3 shows images of Kit 225 K6 cells labeled with Cy3-conjugated α Tac (panel a), or XR conjugated MEM-75 against the TrfR (panel b). A patchy receptor distribution is observed with clusters of 500-800 nm for the IL-2R α and

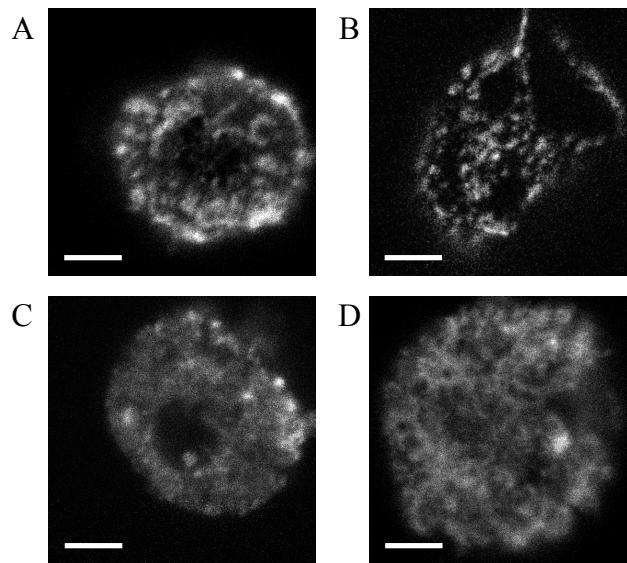


Fig. 7.3. Confocal laser scanning microscopy of Cy3 labeled IL-2R α and TrfR. Kit 225 K6 cells were labeled with Cy3-conjugated α Tac Fab against the IL-2R α subunit (A, C, D), or XR conjugated MEM-75 against the transferrin receptor (TrfR, panel B). Cells in panels c and d were treated with filipin and methyl- β -cyclodextrin, respectively. Confocal slices of 0.6 μ m thickness were obtained. Surface fluorescence distribution was reconstructed from z directional projection of image slices. Scale bar is 4 μ m. A patchy receptor distribution can be observed with clusters of 200-1200 nm diameter depending on the type of receptor and the treatment.

200-300 nm for the TrfR. Controls on pre-fixed and live cells indicate that this clustering is not caused by the labeling procedure. Cluster diameter for the IL-2R α determined from $G(\rho)$ (Eqs. 7.1-7.2) was \sim 600 nm (see also Fig. 7.4). This implies that the minimum and maximum distances between immunogold labels within a cluster would be 0 and 600 nm, averaging to \sim 300, which corresponds well to the \sim 380 nm average inter-particle distance within clusters determined in EM (Fig. 7. 2).

Cluster size of IL-2R α , HLA glycoproteins and CD48 is dependent on the integrity of cholesterol-rich lipid rafts

Interestingly, clusters of the transferrin receptor are significantly smaller in size (250 nm) than

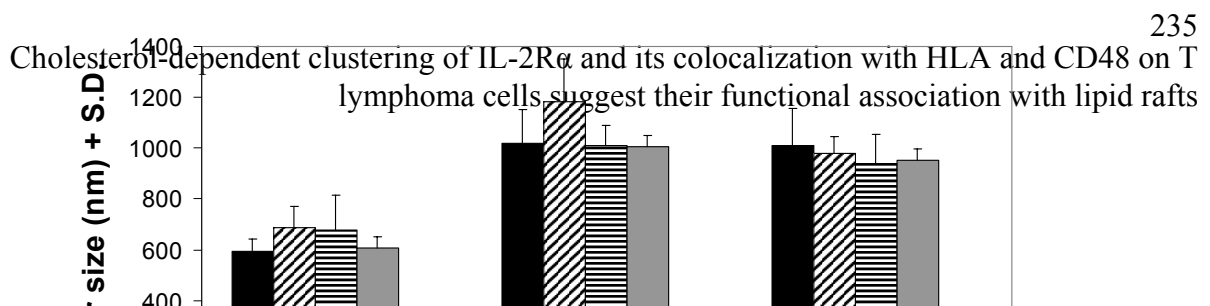


Fig. 7.4. Cluster sizes of IL-2R α , HLA class I and II, CD48 and TrfR and their modulation by membrane cholesterol content. Cluster sizes on Kit 225 K6 cells determined from the angle-averaged autocorrelation function are presented for IL-2R α (filled columns), HLA class I (cross-hatched columns) and class II (striped columns), CD48 (grey columns) and TrfR (open columns). The effect of modulating the cholesterol content of the membrane is also displayed: with the exception of TrfR, all receptor clusters exhibit a significant increase of cluster size upon both cholesterol depletion by cyclodextrin or in situ complexation of cholesterol by filipin. (n>9, from 3 independent experiments).

those of IL-2R α . TrfR is thought to be localized outside rafts [32], whereas several src-family kinases that play a role in T cell activation are detected in association with rafts [22,33]. To check if these cholesterol-rich regions could be held responsible for keeping together the islets of IL-2R α subunits, we have examined the change of cluster size after modifying the membrane cholesterol content with cyclodextrin or filipin. Fig. 7.3C and d show that cluster boundaries become blurred and their size increases upon both treatments. Thus, modulation of cholesterol content seems to break up the tightness of IL-2R α clusters. The increase in cluster size is significant in both cases (Fig. 7.4, filled columns), and is paralleled by a decrease of absolute fluorescence intensities, indicating dispersion of the labeled proteins. The same observations can be made for MT-1 cells (data not shown).

As Fig. 7.4 shows, both class I and II MHC glycoproteins and the raft marker CD48 behave similarly to IL-2R α : their cluster size is comparable to that of IL-2R α (control group,

cross-hatched, striped and grey columns), and is dispersed significantly upon cyclodextrin and filipin treatment. On the other hand, TrfR not only possesses smaller clusters in control cells, but its cluster size hardly changes upon either of the treatments modifying membrane cholesterol (open columns). The same molecules behave similarly on the surface of MT-1 cells (data not shown).

Cross-correlation analysis of confocal images reveals partial co-clustering of IL-2R with MHC and CD48 molecules, but not with TrfR

Since flow cytometric energy transfer measurements gave evidence of nm level proximity between IL-2R α and MHC antigens, we have used double labeling with fluorescent Fabs in confocal microscopy to investigate the co-localization of IL-2R α with MHC glycoproteins. Fig. 7.5A shows the co-localization of IL-2R α (green) and HLA class II (red). Owing to the high degree of co-localization (cross-correlation coefficient $C=0.37$, see Fig. 7.6), many pixels of the image appear orange when the red and green channels are overlaid. Fig. 7.5b demonstrates that IL-2R α (green) and TrfR (red) images from the same cell exhibit disparate localization of these two receptors. Accordingly, their cross-correlation coefficient is very low ($C=0.05$). In similar experiments, the cross correlation coefficient was measured for a set of receptor pairs (Fig. 7.6). While IL-2R α co-localizes with HLA class I, II and CD48, neither IL-2R α nor CD48 co-localizes with TrfR. A similar co-localization pattern was observed on MT-1 cells. This is coherent with a selective association of IL-2R α , MHC and the raft marker CD48 with cholesterol rich membrane rafts that are perturbed by filipin or cyclodextrin treatment, and the observation that TrfR clusters are virtually unaffected by the modification of membrane cholesterol.

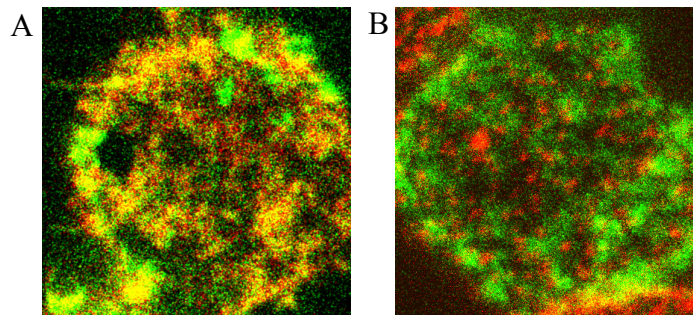


Fig. 7.5. IL-2R α exhibits sub-micron scale co-localization with MHC II but not with TrfR. A representative confocal fluorescence image of the co-localization of IL-2R α and HLA class II is shown in panel a. IL-2R α and HLA class II are labeled with XF (green) and XR (red), respectively. Because of the high degree of co-localization, many pixels appear orange when the two channels are fused. Panel b demonstrates that IL-2R α (green) and TrfR (red) co-detected in a similar experiment are mostly localized at different areas of the plasma membrane. Scale bar is 2 μ m.

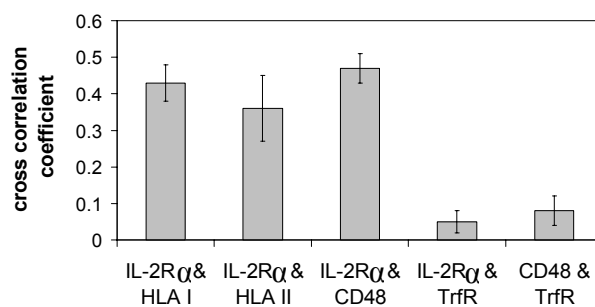


Fig. 7.6. IL-2R α staining cross-correlates with MHC glycoproteins and CD48, but not with TrfR. Kit 225 K6 cells were double labeled with pairs of antibodies against IL-2R α , HLA class I and II, CD48 and TrfR. The cross correlation coefficient is measured for the following receptor pairs: IL-2R α and HLA class I, IL-2R α and HLA class II, IL-2R α and CD48, IL-2R α and TrfR, CD48 and TrfR. While IL-2R α co-localizes with HLA class I and II, and CD48, a raft marker, neither IL-2R α nor CD48 co-localizes with TrfR (n=7).

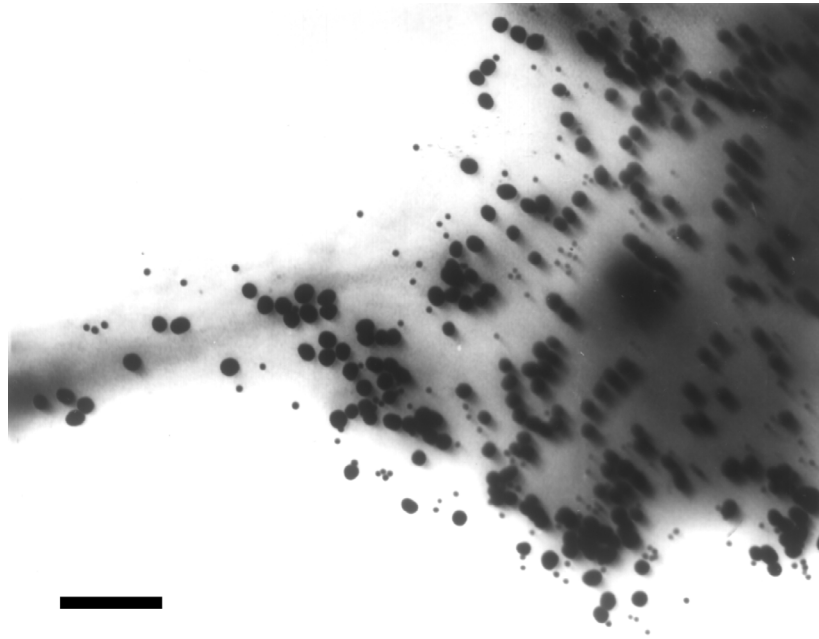


Fig. 7.7. Electron microscopy confirms the partial co-clustering of IL-2R α and MHC molecules. Immunogold labeling followed the sequence: α Tac Fab - 10 nm AuroGamig - blocking by α Tac Fab - W6/32 whole antibody - 30 nm AuroGamig (anti-Fc). Electron microscopy shows that the selective labels against the IL-2R α and the MHC are partially, though not completely co-localized, thus confirming the confocal microscopic data (scale bar is 200 nm).

Sequential immunogold labeling and electron microscopy confirms the higher level partial co-localization of IL-2R α and MHC

Earlier we have developed a strategy to examine co-clustering of class I and class II MHC antigens on lymphoid cells [17]. Fig. 7.7 shows an example of IL-2R α labeled with 10 nm gold followed by 30 nm gold tags on MHC-I molecules on the surface of Kit225 K6 cells. While there are also some labels that are not proximal to the other labeling species, many of the small and large beads are seen co-clustered. A similar partial co-localization of IL-2R α and MHC-II was observed on both Kit 225 K6 and MT-1 cells (data not shown). Thus, the co-clustering deduced from confocal images is supported by electron microscopic evidence.

When the surface density of 30 nm gold labels on IL-2R α is averaged for several cells, 25/ μm^2 are seen. If IL-2R α is labeled after covering MHC class II molecules with L243 Fab and

Cholesterol-dependent clustering of IL-2R α and its colocalization with HLA and CD48 on T lymphoma cells suggest their functional association with lipid rafts

10 nm gold beads, the detectable 30 nm labels on IL-2R α decrease to 13/ μm^2 . This is consistent with the idea that the interaction of MHC-II and IL-2R α at the molecular level allows detection of only about 50% of the IL-2R α after having shielded those α subunits that are in the vicinity of MHC-II antigens. A similar, \sim 50% co-clustering ratio could be determined for IL-2R α in relation to MHC class I molecules on these cells. This observation is in line with the 37-43% cross correlation coefficient seen between fluorescent labels on IL-2R α and MHC antigens.

7.5 Discussion

Recently we have presented fluorescence resonance energy transfer efficiency data indicating spontaneous assembly of the α , β and γ_c subunits of the multisubunit IL-2 receptor on Kit 225 K6 T lymphoma cells even in the absence of IL-2 [4]. Here we show using immunogold labeling in electron microscopy that this molecular-level assembly of the IL-2 receptor is extended to a higher hierarchical level, i.e., on the several hundred nanometer scale in the plasma membrane of human T lymphoma cells. The distribution of colloidal gold labels attached to IL-2R α was significantly different from a hypothetical random Poissonian pattern ($p < 0.01\%$). The distribution of inter-particle distances also showed two peaks, one close to that expected for the single peak of a Poissonian pattern, and another at smaller distances, likely corresponding to the average cluster radius of 350-380 nm.

Clusters of similar size were observed both on Kit 225 K6 cells, which have an absolute requirement of IL-2 for their growth, and on MT-1 cells, which do not express the β subunit of the IL-2 receptor and grow independently of IL-2. Also, IL-2 deprivation of Kit 225 K6 cells had no effect on cluster size. Thus the molecular interactions producing sub-micron scale clusters seem to be largely independent of the presence of the IL-2R β subunits or the specific ligand IL-2.

Confocal laser scanning microscopy of both fixed and live cells confirmed the sub-micron clusters observed with electron microscopy. Also, the cluster size deduced from electron microscopy corresponded well to that seen in confocal slices and surface reconstructions. The cluster sizes measured are on the same order of magnitude as the areas of confined diffusion determined from single particle tracking for ganglioside GM1 and the Thy-1 antigen [35], furthermore, they are comparable to those assessed for ErbB2 [31] and PDGF receptor molecules [19] by scanning near-field optical microscopy.

Such high degree of receptor aggregation has been found both as a ligand induced phenomenon [36] and as a stably maintained structure with yet undetermined lifetimes. The latter frequently occurs under polarizing conditions, especially in the nervous system [37], or in the neuromuscular junction [38]. However, similar receptor clustering can also be found on cells that are non-polarized, e.g. lymphoid cells. Earlier we have demonstrated higher hierarchical level distribution patterns of the MHC class I [12] and class II molecules [17]. These findings have recently been corroborated by data revealing anomalous diffusion of MHC I and II molecules [11,39].

The present experiments significantly support the view that such above-nanometer-level co-distribution patterns could be common among various receptor types even on non-polarized cells. The existence of lipid rafts in the plasma membrane can easily have a central role in maintaining such receptor superstructures [22]. Besides glycosphingolipids, cholesterol has been postulated as an important functional component of lipid rafts. Coherent with this, modifying membrane cholesterol content was shown to influence signaling by raft-associated molecular assemblies [25,40]. We found that specifically complexing cholesterol *in situ* with filipin, or extracting it from the membrane with cyclodextrin changes the higher level co-localization

patterns by dispersing and blurring the clusters of both IL-2R α , HLA I, II and the raft protein CD48. At the same time, flow cytometric energy transfer measurements have shown that IL-2R α is in the nm scale proximity of both MHC-I and MHC-II on Kit 225 K6 and MT-1 cells (fluorescence resonance energy transfer efficiency was in the range of 12-21%, unpublished data). These data together support the notion that IL-2R α and MHC proteins may be partially confined to lipid rafts. In accordance with this, a significant cross-correlation of different color fluorescent labels on pairs of CD48 and these molecules was found, while the sub-micron clusters of the transferrin receptor, which is not a constituent of rafts [32,33], were significantly smaller and did not co-localize with either IL-2R α or CD48.

The combined application of fluorescence resonance energy transfer, electron microscopy, confocal laser scanning microscopy and image processing suggest that both small receptor islands and larger rafts can accommodate the IL-2 receptor α subunit together with HLA class I and class II glycoproteins. The importance of the organizing role of lipid rafts is underlined by the finding that caveola-like domains serve as concentrators of various signal transduction machineries [29,41], and several small cytoplasmic kinases, a group vastly important in the signal transduction of T lymphocytes [21,42], are bound to lipid rafts [22,30,43]. Thus, the clusters on both the molecular and the sub-micron level could underlie the efficiency of signaling in lymphoid cells and might play a role in the directed secretion of lymphokines and in specific internalization pathways.

MHC class II, recently reported to co-aggregate with lipid rafts upon stimulation by crosslinking [44], and class I molecules seem to be partially recruited into the signaling platform of IL-2R subunits and CD48 formed by rafts. Although it is believed so far that posttranslational modification (fatty-acylation, GPI-linkage) is a specific predictor for targeting lipid rafts [21], for transmembrane proteins with (MHC molecules) or without (IL-2R α) intracellular tails it is hard

to predict their partitioning behavior based on their sequence. In these domains, MHC molecules may provide a stabilizing effect through their direct cytoskeletal connections [45]. In addition, MHC class I molecules may also contribute to this biochemical switchboard as potential regulators of IL-2 receptor signaling by an intracellular tyrosine phosphorylation cross-talk, as reported for the insulin receptor recently [46].

Co-immobilization of GPI-anchored raft proteins, including CD48, on T cells has been reported to inhibit recruitment of IL-2R α chains with the signaling β and γ subunits, but not the association of β and γ chains with the Janus kinases [47]. In light of our data showing a “focusing” effect of rafts for IL-2R α , this might be due to co-immobilization of IL-2R α as well and/or a steric blocking of its interaction with the β and γ . Thus, T cell rafts related to the cell surface clusters of the proteins investigated here may promote IL-2R mediated signaling by recruiting the α chains into a signaling platform regardless of their ligand binding, and, on the other hand, may also have a control on T cell growth [47] through the co-localized GPI-linked proteins (CD48 or Thy-1).

7.6 Acknowledgements

This research has been supported by grants OTKA F025210, T23873, T30411, T19372, T30399, T029947 and FKFP 0518/99. REZSO

References

1. Waldmann TA. (1986) The structure, function, and expression of interleukin-2 receptors

243

Cholesterol-dependent clustering of IL-2R α and its colocalization with HLA and CD48 on T lymphoma cells suggest their functional association with lipid rafts

- on normal and malignant lymphocytes. *Science*;232:727-732.
2. Waldmann TA. (1991) The interleukin-2 receptor. *J. Biol. Chem.*;266:2681-2684.
 3. Nakamura Y, Russell SM, Mess SA, Friedmann M, Erdos M, Francois C, Jacques Y, Adelstein S, Leonard WJ. (1994) Heterodimerization of the IL-2 receptor beta- and gamma- chain cytoplasmic domains is required for signaling. *Nature*;369:330-333.
 4. Damjanovich S, Bene L, Matkó J, Alileche A, Goldman CK, Sharrow S, Waldmann TA. (1997) Preassembly of interleukin 2 (IL-2) receptor subunits on resting Kit 225 K6 T cells and their modulation by IL-2, IL-7, and IL-15: a fluorescence resonance energy transfer study. *Proc. Natl. Acad. Sci. USA*;94:13134-13139.
 5. Damjanovich S, Gáspár R, Jr., Pieri C. (1997) Dynamic receptor superstructures at the plasma membrane. *Q. Rev. Biophys.*;30:67-106.
 6. Damjanovich S, Trón L, Szöllösi J, Zidovetzki R, Vaz WLC, Regateiro F, Arndt-Jovin DJ, Jovin TM. (1983) Distribution and mobility of murine histocompatibility H2K^k antigen in the cytoplasmic membrane. *Proc. Natl. Acad. Sci. USA*;80:5985-5989.
 7. Edidin M, Zuniga MC, Scheetz M. (1994) Truncation mutants define and locate cytoplasmic barriers to lateral mobility of membrane glycoproteins. *Proc. Natl. Acad. Sci. USA*; 91:3378-3382.
 8. Jacobson K, Sheets ED, Simson R. (1995) Revisiting the fluid mosaic model of membranes. *Science*; 268:1441-1442.
 9. Cherry RJ, Smith PR, Morrison IE, Fernandez N. (1998) Mobility of cell surface receptors: a re-evaluation. *FEBS Lett.*; 430:88-91.
 10. Bene L, Balázs M, Matkó J, Most J, Dierich MP, Szöllösi J, Damjanovich S. (1994) Lateral organization of the ICAM-1 molecule at the surface of human lymphoblasts: a possible model for its co-distribution with the IL-2 receptor, class I and class II HLA molecules. *Eur. J. Immunol.*; 24:2115-2123.
 11. Cherry RJ, Wilson KM, Triantafilou K, O'Toole P, Morrison IE, Smith PR, Fernandez M. (1998) Detection of dimers of human leukocyte antigen HLA-DR on the surface of living cells by single-particle fluorescence imaging. *J. Cell Biol.*;140:71-79.
 12. Damjanovich S, Vereb G, Schaper A, Jenei A, Matkó J, Starink JP, Fox GQ, Arndt-Jovin

- DJ, Jovin TM. (1995) Structural hierarchy in the clustering of HLA class I molecules in the plasma membrane of human lymphoblastoid cells. *Proc. Natl. Acad. Sci. USA*;92:1122-1126.
13. Matkó J, Bushkin Y, Wei T, Edidin M. (1994) Clustering of class I MHC molecules on the surfaces of activated and transformed human cells. *J. Immunol.*;152:3355-3360.
 14. Szöllösi J, Damjanovich S, Balázs M, Nagy P, Trón L, Fulwyler MJ, Brodsky FM. (1989) Physical association between MHC class I and class II molecules in cytoplasmic membranes. A flow cytometric energy transfer study. *J. Immunol.*;143:208-213.
 15. Szöllösi J, Damjanovich S, Goldman CK, Fulwyler MJ, Aszalós A, Goldstein G, Rao P, Waldmann TA. (1987) Flow cytometric resonance energy transfer measurements support the association of a 95 kDa termed T27 with the 55 kDa Tac peptide. *Proc. Natl. Acad. Sci. USA*;84:7246-7250.
 16. Damjanovich S, Szöllösi J, Trón L, Edidin M. *Mobility and proximity in Biological membranes*: CRC Press, Inc.; 1994.
 17. Jenei A, Varga S, Bene L, Mátyus L, Bodnár A, Bacsó Z, Pieri C, Gáspár R, Jr., Farkas T, Damjanovich S. (1997) HLA class I and II antigens are partially co-clustered in the plasma membrane of human lymphoblastoid cells. *Proc. Natl. Acad. Sci. USA*;94:7269-7274.
 18. Kenworthy AK, Edidin M. (1998) Distribution of Glycosylphosphatidylinositol-anchored Protein at the Apical Surface of MDCK Cells Examined at a Resolution of < 100 Å Using Imaging Fluorescence Resonance Energy Transfer. *J. Cell Biol.*;142:69-84.
 19. Vereb G, Meyer CK, Jovin TM. Novel microscope-based approaches for the investigation of protein - protein interactions in signal transduction. In: Heilmeyer Jr LMG, editor. *Interacting protein domains, their role in signal and energy transduction*. NATO ASI series. Volume H102. New York: Springer-Verlag; 1997. p 49-52.
 20. Jacobson K, Dietrich C. (1999) Looking at lipid rafts? *Trends Cell Biol.*; 9:87-91.
 21. Horejsi V, Cebecauer M, Cerny J, Brdicka T, Angelisova P, Drbal K. (1998) Signal transduction in leucocytes via GPI-anchored proteins: an experimental artefact or an

- aspect of immunoreceptor function? *Immunol. Lett.*;63:63-73.
22. Simons K, Ikonen E. (1997) Functional rafts in cell membranes. *Nature*;387:569-572.
 23. Hwang J, Gheber LA, Margolis L, Edidin M. (1998) Domains in cell plasma membranes investigated by near-field scanning optical microscopy. *Biophys. J.*;74:2184-2190.
 24. Edidin M. (1997) Lipid microdomains in cell surface membranes. *Curr. Opin. Struct. Biol.*;7:528-532.
 25. Rothberg KG, Ying YS, Kamen BA, Anderson RG. (1990) Cholesterol controls the clustering of the glycosphospholipid-anchored membrane receptor for 5-methyltetrahydrofolate. *J. Cell Biol.*;111:2931-2938.
 26. Bodnár A, Jenei A, Bene L, Damjanovich S, Matkó J. (1996) Modification of membrane cholesterol level affects expression and clustering of class I HLA molecules at the surface of JY human lymphoblasts. *Immunol. Lett.*;54:221-226.
 27. de Kruijff B, Demel RA. (1974) Polyeneantibiotic-sterol interactions in membranes of *Acholeplasma laidlawii* cells and lecithin liposomes. III. Molecular structure of the polyene antibiotic-cholesterol complexes. *Biochim. Biophys. Acta*;339:57-63.
 28. Christian AE, Haynes MC, Phillips MC, Rothblat GH. (1997) Use of cyclodextrins for manipulating cellular cholesterol content. *J. Lipid Res.*;38:2264-2272.
 29. Liu P, Ying Y, Anderson RG. (1997) Platelet-derived growth factor activates mitogen-activated protein kinase in isolated caveolae. *Proc. Natl. Acad. Sci. USA*;94:13666-13670.
 30. Harder T, Simons K. (1999) Clusters of glycolipid and glycosylphosphatidylinositol-anchored proteins in lymphoid cells: accumulation of actin regulated by local tyrosine phosphorylation. *Eur. J. Immunol.*;29:556-562.
 31. Nagy P, Jenei A, Kirsch AK, Szöllösi J, Damjanovich S, Jovin TM. (1999) Activation dependent clustering of the erbB2 receptor tyrosine kinase detected by scanning near-field optical microscopy. *J. Cell Sci.*; 112:1733-1741.
 32. Smart EJ, Ying YS, Mineo C, Anderson RG. (1995) A detergent-free method for purifying caveolae membrane from tissue culture cells. *Proc. Natl. Acad. Sci. USA*;92:10104-10108.

33. Xavier R, Brennan T, Li Q, McCormack C, Seed B. (1998) Membrane compartmentation is required for efficient T cell activation. *Immunity*; 8:723-732.
34. Matko J, Edidin M. (1997) Energy transfer methods for detecting molecular clusters on cell surfaces. *Meth. Enzymol.*;278:444-462.
35. Sheets ED, Lee GM, Simson R, Jacobson K. (1997) Transient confinement of a glycosylphosphatidylinositol-anchored protein in the plasma membrane. *Biochemistry*; 36:12449-12458.
36. Ciruela F, Saura C, Canela EI, Mallol J, Lluís C, Franco R. (1997) Ligand-induced phosphorylation, clustering, and desensitization of A1 adenosine receptors. *Mol. Pharmacol.*; 52:788-797.
37. Craig AM, Blackstone CD, Huganir RL, Banker G. (1994) Selective clustering of glutamate and gamma-aminobutyric acid receptors opposite terminals releasing the corresponding neurotransmitters. *Proc. Natl. Acad. Sci. USA*; 91:12373-12377.
38. Campanelli JT, Hoch W, Rupp F, Kreiner T, Scheller RH. (1991) Agrin mediates cell contact-induced acetylcholine receptor clustering. *Cell*;67:909-916.
39. Smith PR, Morrison IE, Wilson KM, Fernandez N, Cherry RJ. (1999) Anomalous diffusion of major histocompatibility complex class I molecules on HeLa cells determined by single particle tracking. *Biophys. J.*; 76:3331-3344.
40. Keller P, Simons K. (1998) Cholesterol is required for surface transport on influenza virus hemagglutinin. *J. Cell Biol.*; 140:1357-1367.
41. Wu C, Butz S, Ying Y, Anderson RG. (1997) Tyrosine kinase receptors concentrated in caveolae-like domains from neuronal plasma membrane. *J. Biol. Chem.*;272:3554-3559.
42. Ihle JN, Kerr IM. (1995) Jaks and Stats in signaling by the cytokine receptor superfamily. *Trends Genet.*;11:69-74.
43. Ko YG, Liu P, Pathak RK, Craig LC, Anderson RG. (1998) Early effects of pp60(v-src) kinase activation on caveolae. *J. Cell. Biochem.*;71:524-535.
44. Huby RD, Dearman RJ, Kimber I. (1999) Intracellular phosphotyrosine induction by

major histocompatibility complex class II requires co-aggregation with membrane rafts. *J. Biol. Chem.*; 274:22591-22596.

45. Geppert TD, Lipsky PE. (1991) Association of various T cell-surface molecules with the cytoskeleton. Effect of cross-linking and activation. *J. Immunol.*;146:3298-3305.
46. Ramalingam TS, Chakrabarti A, Edidin M. (1997) Interaction of Class I Human Leukocyte Antigen (HLA-I) Molecules with Insulin Receptors and Its Effect on the Insulin-Signaling Cascade. *Mol. Biol. Cell*; 8:2463-2474.
47. Marmor MD, Bachmann MF, Ohashi PS, Malek TR, Julius M. (1999) Immobilization of glycosylphosphatidylinositol-anchored proteins inhibits T cell growth but not function [In Process Citation]. *Int. Immunol.*; 11:1381-1393.

Summary

The advent of confocal microscopy, fast microcomputers with high storage capacity and, moreover, the availability of fluorescent proteins of various excitation and emission properties have made fluorescence microscopy the method of choice in the study of protein behaviour in living cells. In this thesis we investigated in detail two important quantitative methods, fluorescence correlation spectroscopy (FCS) and fluorescence recovery after photobleaching (FRAP). Model systems used in demonstrating the complementarity of the techniques and their merits included the nuclear excision repair (NER) system, transcription regulation by the androgen receptor (AR), and signal transduction by two membrane receptors, the EGF receptor and the IL2-receptor.

In Chapter 1 an introduction to microscopy is given. A brief history traces the development of microscopy from the modest lens arrangement of Zacharias Janssen to modern fluorescence microscopes allowing quantitative investigation of protein dynamics in living cells. A discussion of fluorescence properties of the GFP is presented and several quantitative fluorescence microscopy techniques used are discussed. Also the model systems studied are described.

In Chapter 2 the long-lived dark state of EGFP, the fluorescent tag used in most live cell studies, is investigated as observed in a set-up similar to a typical fluorescence recovery after photobleaching (FRAP) experiment. A method is presented to measure light induced fluorescence fluctuations due to transitions between the dark and excitable state of EGFP in bulk samples. We have found that the average lifetime of the long-lived dark state of the chromophore is about 2.3 s irrespective of the excitation intensity whereas the average on-time is dependent on the intensity used. The

consequence of this behaviour for quantitative FRAP assays, i.e. the non-diffusion related recovery of fluorescence due to these "blinking" molecules are discussed.

Chapter 3 compares two quantitative confocal fluorescence microscopy techniques, FCS and FRAP, in the study of protein mobility, first, when biologically inert systems are the subjects of investigation and, second, in the interpretation of measured data when biologically active proteins are investigated. Using GFP chains of different sizes it is shown that FCS provides a sensitive method for diffusion measurements although difficult to apply in live cells studies. Not only does finding the appropriate place to measure constitute a challenge to its application in live cell studies, the photobleaching of immobile or slow moving molecules complicates FCS autocorrelation curves and the mobility of the cells should be considered. On the other hand, mathematical analysis of FRAP data is complicated by the relatively large observation volume and multitude of parameters contributing to the recovery of fluorescence. We present an optimal approach in the study of protein mobility in living cells by combining the sensitivity of FCS to mobility with the ability of FRAP to extract binding parameters.

In Chapter 4, the complementarity of FRAP and FCS was used to study the behaviour of DNA repair molecules. In this study the focus was on the nuclear dynamics of nucleotide excision repair factors in the absence of DNA damage. Combined FCS and FRAP shows that in the absence of DNA damage NER proteins are freely mobile and move as separate entities through the nucleus. No evidence was found for temporary storage of the inactive factors for instance in nuclear subcompartments, nor for the formation of large precursor complexes ('repairosomes'). In this direct comparison of the mobility of NER proteins we found that when moving, NER proteins diffuse with diffusion coefficients consistent with their molecular weights and any discrepancy in

mobility can be explained by binding or transient interactions with other nuclear matter. Our data show that chromatin-transacting proteins that are not engaged in their function are freely mobile throughout the nucleus. Our results therefore provide further support for a general model of chromatin-transacting processes in which free diffusion and random collision allows for the efficient formation of functional and adaptable protein complexes directly at the site of need. In this way, individual factors can be easily exchanged or used for multiple actions within one or more processes, rendering a cell capable of adapting quickly and efficiently to environmental or internal challenges.

Chapter 5 presents a study of the mechanism of deployment of the NER endonuclease XPG to sites of UV-induced DNA damage using the ability of the photobleaching techniques to characterize transient long-term binding events. We found that XPG diffuses freely as a monomer in both living CHO cells and human fibroblasts, not showing any prominent interactions other than with the nascent NER complex that is formed in UV-damaged cells after binding of the damage sensor XPC and the transcription/repair factor TFIIH. The *in vivo* dynamics of the XPG protein are similar in human cells and Chinese hamster cells, showing that major differences in genetic background hardly affect XPG behaviour.

In Chapter 6, results are presented of the application of FRAP and FCS in a minimally invasive assessment of the effects of stimulation by EGF on the localization and mobility of the EGF receptor. FCS measurements on GFP-tagged EGFR revealed a microheterogeneity of local diffusion conditions in the cell membrane both in terms of mobility and the effect of obstacles hindering diffusion as reflected by the large SD of the values of the diffusion constants and the anomaly parameters. This indication of the microdomain structure of the cell membrane and its influence on the motion of cell

surface receptors is further supported by the anomalous nature of diffusion obtained from FRAP experiments. Similar to the work presented in the previous chapters, these analyses also show that FCS and FRAP provide complementary information on the local (sub-micron) and long-range (several microns) diffusion properties of plasma membrane receptors.

Chapter 7 presents our result on the investigation of the organization and localization of IL2-receptor in the cell membrane of lymphoid cells with respect to lipid rafts and MHC glycoproteins. Submicron colocalization was assessed with high-resolution confocal microscopy and digital image processing while dynamically averaged molecular proximities were studied with fluorescence resonance energy transfer (FRET). Our results show that IL-2 receptor α subunits exhibit non-random surface distribution on human T lymphoma cells. Analysis of inter-particle distances detected in immuno-electronmicroscopy revealed that this clustering on the submicron scale is independent of the presence of IL-2 and of the expression of the IL-2R β subunit. Clustering of IL-2R α is confirmed by confocal microscopy, yielding the same average cluster size, \sim 600-800 nm, as electron microscopy. HLA class I and II and CD48 molecules also form clusters of the same size and co-cluster with IL-2R α chains, indicating the association of these molecules with lipid rafts. The clusters of IL-2R α are dispersed by extraction of cholesterol and are proposed to underlie the efficiency of IL-2 signalling in lymphoid cells.

Samenvatting

De opkomst van confocale microscopie, snelle computers met grote opslagcapaciteit en, bovendien, de beschikbaarheid van fluorescerende eiwitten met verschillende excitatie- en emissie-eigenschappen hebben er voor gezorgd dat fluorescentiemicroscopie de belangrijkste methode is geworden voor het bestuderen van het gedrag van eiwitten in levende cellen. In dit proefschrift worden twee belangrijke kwantitatieve fluorescentiemicroscopische methoden, fluorescentie correlatie spectroscopie (FCS) en fluorescentie redistributie na photobleking (*fluorescence recovery after photobleaching*, FRAP) in detail onderzocht. Nucleotide excisie reparatie (NER), transcriptieregulatie door androgeen receptoren (AR), en signaaltransductie door twee membraanreceptoren, de EGF receptor en de IL2-receptor, dienden daarbij als modelsystemen.

In Hoofdstuk 1 wordt een inleiding gegeven in de fluorescentiemicroscopie. Een kort historisch overzicht laat de ontwikkeling van de microscoop zien, van de eerste eenvoudige microscoop van Zacharias Janssen tot en met de meest moderne digitaal bestuurbare confocale fluorescentiemicroscoop waarmee zelfs processen kunnen worden bestudeerd die zich afspelen in het binnenste van zeer kleine structuren zoals de celkern. Daarna wordt dieper ingegaan op diverse aspecten van moderne kwantitatieve fluorescentietechnieken zoals FCS en FRAP. Tevens wordt in detail de eigenschappen van het groen fluorescerend eiwit beschreven. Ten slotte wordt een korte beschrijving gegeven van de hierboven beschreven modelsystemen.

In Hoofdstuk 2 wordt een studie beschreven waarin de *dark state* van het groen fluorescerend proteïne (GFP) nauwkeurig wordt onderzocht onder omstandigheden vergelijkbaar met die waaronder FRAP experimenten worden uitgevoerd. Er wordt een methode beschreven waarmee het mogelijk is om de lichtgeïnduceerde fluctuaties door de

overgangen te bestuderen van *dark state* naar grondtoestand van het GFP en *vice versa*. We hebben gevonden dat de levensduur van de *dark state* ongeveer 2.3 seconde is, onafhankelijk van lichtintensiteit, terwijl de *on-time* afhangt van de lichtintensiteit waarmee het molecuul belicht wordt. De consequenties van dit gedrag voor het kwantificeren van FRAP experimenten wordt bediscussieerd.

In Hoofdstuk 3 worden twee kwantitatieve fluorescentiemethoden vergeleken, FCS en FRAP, voor het bestuderen van cellen, ten eerste wanneer biologisch niet actieve moleculen worden bestudeerd en ten tweede wanneer de onderzochte moleculen biologisch wel actief zijn. Met behulp van GFP-ketens van verschillende lengte wordt aangetoond dat FCS vooral geschikt is om de diffusiesnelheid van moleculen te meten, hoewel dat moeilijk is in levende cellen. Niet alleen is het moeilijk om de goede plaats in cellen te vinden, maar ook moet ernstige rekening gehouden worden met het bewegen van cellen tijdens de meting. Aan de andere kant wordt de mathematische analyse van FRAP metingen bemoeilijkt door het relatief grote volume dat bemeten wordt en door het grote aantal parameters dat moet worden gemodelleerd. Er wordt een door ons ontwikkelde methode beschreven die gebruik maakt van de gevoeligheid van FCS voor diffusieverschillen en de mogelijkheid die FRAP experimenten bieden om immobilisatieparameters te bepalen.

In Hoofdstuk 4 wordt de complementariteit van FCS en FRAP gebruikt om het gedrag van DNA-reparatie-eiwitten in levende cellen te bestuderen. In dit onderzoek was de aandacht gevestigd op het gedrag van reparatiefactoren in de afwezigheid van DNA schade. In de afwezigheid van schade bleken de meeste van deze eiwitten vrij door de celkernen te bewegen. Er werden geen aanwijzingen gevonden voor tijdelijke opslag in nucleaire substructuren, noch voor het vormen van grote *precursor*complexen ('reparosomen'). In een directe vergelijking tussen de verschillende eiwitten bleek bovendien dat de

diffusiesnelheid in afwezigheid van schade vooral bepaald werd door de grote van de onderzochte eiwitten, en dat iedere afwijking daarvan kon worden toegeschreven aan kortstondige binding aan immobiele structuren in de celkern. Deze gegevens geven verdere ondersteuning aan algemene modellen voor systemen die met chromatine interacteren, waarin DNA-eiwit complexen op de plaats waar ze nodig zijn worden gevormd uit hun losse onderdelen die door diffusie en toevallige botsingen op de goede plek terecht komen. Op die manier kunnen individuele factoren makkelijk en snel worden uitgewisseld tussen verschillende typen schadecomplexen en kan de cel snel reageren op bedreigingen uit het externe of interne milieu.

In Hoofdstuk 5 wordt een onderzoek beschreven naar de manier waarop de NER factor XPG betrokken is bij het repareren van UV-geïnduceerde DNA-schade. In dit onderzoek werd gebruik gemaakt van de mogelijkheid om met behulp van FRAP langdurige immobilisatie te kwantificeren. We laten zien dat de XPG factor vrij als monomeer door de celkern beweegt en geen andere interacties aangaat dan met DNA-schade waaraan reeds XPC en TFIIH zijn gebonden. De *in vivo* dynamiek van XPG was bovendien hetzelfde in hamster en mens, waaruit blijkt dat het gedrag van XPG niet afhankelijk is van genetische achtergrond.

In Hoofdstuk 6 worden de resultaten getoond van de toepassing van FCS en FRAP in minimaal invasieve experimenten om de localisatie en mobiliteit van door EGF gestimuleerde EGF receptoren te bepalen. FCS-experimenten op GFP-gelabelde EGF receptoren lieten een kleinschalige heterogeniteit zien van zowel diffusiesnelheid als van obstakels die de vrije diffusie van EGFR hinderden, zoals bleek uit grote variatie en anomalieparameters. Deze aanwijzingen die duiden op een microdomeinstructuur van de celmembraan werden verder ondersteund door FRAP-experimenten die anomale diffusie

lieten zien. Deze resultaten laten op vergelijkbare wijze met de eerder beschreven experimenten zien dat FCS en FRAP complementair zijn in de zin dat FCS bijzonder geschikt is voor snelle diffusiemetingen en FRAP voor het meten van lange termijn effecten.

In Hoofdstuk 7 worden de resultaten beschreven van onderzoek naar de organisatie en lokalisatie van de IL-2 receptor in de celmembranen van lymfopoïde cellen met betrekking tot *lipid rafts* en MHC-receptoren. Submicron lokalisatie werd bepaald met hoge resolutie microscopie en digitale beeldbewerking, terwijl dynamisch gemiddelde moleculaire afstanden werden bestudeerd met behulp van fluorescentie resonantie energie transfer (FRET). De resultaten laten zien dat *subunits* van de IL-2 receptor α op een niet toevallige manier verdeeld zijn in clusters over het oppervlak van menselijke T-lymphoma cellen. Analyse van de afstanden tussen de clusters m.b.v. immunogoud labeling en electronenmicroscopie liet zien dat deze clusters niet afhankelijk zijn van de aanwezigheid van IL-2 receptor β *subunits* en de aanwezigheid van IL-2. Clustering van IL-2 receptor α werd bevestigd door confocale microscopie, waar de zelfde dimensies werden gemeten als met electronenmicroscopie (~600-800 nm). HLA klasse I en II en CD48 moleculen vormen ook clusters van dezelfde grootte en clusteren samen met IL-2 receptor α ketens. De clusters gevormd door IL-2 receptor α zijn gevoelig voor cholesterol extractie, dit geeft een aanwijzing dat ze waarschijnlijk aanwezig zijn in *lipid rafts* en zou de basis kunnen vormen voor de efficiëntie waarmee signalen worden doorgegeven in lymfocytische cellen.

Acknowledgements

First, I would like to thank my Promoter, Prof. Jan Hoeijmakers for his believing and understanding. To my co-promoters Dr. Adriaan Houtsmuller and Dr. Gyorgy Vereb my indebtedness is immeasurable. Thank you for giving me the opportunity to work with you. Without your patience this work would not have been completed.

The life of a scientist is certainly a nomadic one, from the Centre for Energy Research and Training, ABU, Zaria, Nigeria to the Institute of Experimental Physics, Debrecen, Hungary. Thereon to the department of Biophysics and Cell Biology, Medical and Health Sciences Center, University of Debrecen, Hungary and finally to of Pathology Erasmus MC, Rotterdam, I have been fortunate to work with numerous colleagues who have helped in various ways culminating in the successful completion of this thesis. Dr. Sandor Szegedi, Prof. Sandor Nagy and my friend, Engr. Gabor Nagy thank you for your help in KISFIZ. Thanks to Profs. Sandor Damjanovich and Janos Matko for accepting me into the Dept. of Biophysics, Prof. Janos Szollosi, Dr. Gyorgy Panyi and my friend, Peter Salga for their encouragements and Dr. Gyorgy Vamosi for introducing me to FCS.

Special thanks to "my boss" Dr. Gert van Cappellen for giving me the opportunity to work with him and to Dr. Arthur van der Kamp and Dr. Wim Vermeulen for facilitating my employment in the department of Genetics during which a substantial portion of the work leading to this thesis was carried out. And my move to the Netherlands couldn't have happened without the kind advice of Dr. Ronald R. de Krijger.

Thanks to all members of Adriaan's group (former, old and new). Miranda and Eddy who prepared the NFPs and regularly supplied me with H2B cells, Alex for his patience and readiness to help with my numerous computer related requests. To Pascal, I say thank you for your friendship and support and accepting to be my paranimf. To my second paranimf, Martin, thank you for all your help. My sincere thanks to my friends and colleagues; Pierre-Olivier Mari, Angelika Zotter, Karin Mattern, Bart Geverts, Lady Cunha and Chris Dinant.

Special thanks to my friends Zoltan Nagy, Ekine, George, Abdul-Ganiyu, Natty, Shir, Christian and Mamela and her family. And to my “ore bi omo-iya” friends, Ayo Yusuf, Sahifullah, Taofeeq Ige, Boda Azeez, Boda Rauf, Alfa Nassam, I-sho pepper (Akinbitan), Habeeb thank you for believing in me.

To members of my household, this is for you. My darling girl, Kunmeme, Padimi Mukhtar, Bobo mi Yinkus, Ra-shidat, Kudirat, Haji Zub. Thank you for putting up with my long absence. To Miluc, thank you bringing joy to our lives. To my siblings, Tunde, Haja Bilkis, Bash and Ahmad, thank you for taking care of home in my absence.

To my Laduke, no words can express my thanks for your patience, love and unlimited support. I can only say Alhamdu Lillah that you are and Jazaka Allahu Khairan. To Cuki thank you for loving me.

Special thanks to my in-laws, Alhaji Moyosore, Alhaja Iya-Aduke, Mrs Katalin Isvanne Ori. Thank you for your support and taking care of my family.

To my mum Alhaja Hawau Alake Ibrahim and my dad Alhaji Ibrahim Ayinla Gidado, thank you for your unconditional love, support, patience and understanding.

May Allah continue to bless the souls of my departed uncles Alhaji Labaika Mustapha and Alhaji Abdu-Raheem Mustapha, my aunty Alhaja Munirat Abdul-Kareem, my grand parents Alhaji Zubair Bami-Ibadan, Alhaja Fatima Iya-Ibadan, Alhaji Mustapha Ilorin and my darling (grand)-mother Alhaja Raihanat Mustapha (Alhaja-Agba). Olorun dakun f'orun ke won.

And ALHAMDU LILLAH.

List of publications

1. A. Zotter, M.S. Luijsterburg, D.O. Warmerdam, **S.M. Ibrahim**, A. Nigg, W.A. van Cappellen, J.H.J. Hoeijmakers, R. van Driel, W. Vermeulen, A.B. Houtsmuller. (2006) Recruitment of the Nucleotide Excision Repair Endonuclease XPG to Sites of UV-induced DNA Damage Depends on Functional TFIIH. *Mol. Cell. Biol.*:MCB.00695-706.
2. G. Vereb G. Jr, J. Matkó, G. Vámosi, **S.M. Ibrahim**, E. Magyar, S. Varga, J. Szöllösi, A. Jenei, R. Gáspár, T.A. Waldmann, and S. Damjanovich. (2000): Cholesterol-dependent clustering of IL-2R α and its colocalization with HLA and CD48 on T lymphoma cells suggests their functional association with lipid rafts. *Proceedings of the National Academy of Sciences of the United States of America*, 97: 6013-6018.
3. **S.M.Ibrahim**; S.Szegedi. (1998): Hydrogen Determination in Coal Samples by the Recoil Proton Method. *J.Radioanal.Nucl.Chem.* 237(1-2) 167-170.
4. J.Csikai; S.Szegedi; L.Olah; **S.M.Ibrahim**; A.M.El-Megrab; N.I.Molla; M.M.Rahman; R.Y. Miah; F.Habbani and I.Shaddad. (1997): Production of Solid Deuterium targets by Ion Implantation. *Nucl. Instr. and Meth. A* 397 : 75-80.
5. S.Szegedi and **S.M.Ibrahim**. (1996): Possible Use of Low Voltage Accelerators in PIXE Analysis. *J.Radioanal. Nucl.Chem. Art.* 209(1): 201-210.
6. S.Szegedi; K.M.Tun; **S.M.Ibrahim**. (1996): Determination of Ash Content in Coals by Gamma Reflection Method. *J.Radioanal.Nucl.Chem.* 213(6) 403-409.

7. I.M.Umar; S.B.Elegba; B.B.Dewu; **S.M.Ibrahim**; P.O.Ogunleye. (1994): Soil Analysis using Instrumental Neutron Activation Analysis. Proceedings of the First National Conference on Nuclear Methods (A.B.U., Zaria, Nigeria)
8. J. Csikai; S.Nagy; S.B.Elegba; **S.M.Ibrahim**; K.Usman; T.Ige. (1992): Neutron Field Produced by a Kerman A-711 Sealed-Tube Generator. J. Radional Nucl. Chem., 166(4).
9. J.Adetunji and **S.M.Ibrahim** (1991): Measurement of Condensation Nucleus Concentration in the Harmattan Dust. Journal of Nigerian Institute of Physics, Vol.3.

Curriculum Vitae

The author, Shehu Mustapha Ibrahim was born on 27th February 1958 in Ilorin, the capital of Kwara state, Nigeria. He graduated as the best student in Physics from Ahmadu Bello University, Zaria in 1984. He joined the services of the same university as a graduate assistant in 1986 after his Nigerian National Youth service.

Shehu completed his M.Sc degree in nuclear physics in 1989 and proceeded on an International Atomic Energy Agency fellowship to Hungary the same year. While at the Institute of Experimental Physics, Debrecen University, he worked on the application of X-ray fluorescence spectroscopy. On his return to Nigeria in 1990 he was the research officer in charge of the X-ray fluorescence facility of the Centre for Energy research and Training, Ahmadu Bello University, Zaria where he rose to the position of research fellow I in 1997.

In 1998, he joined the Biophysics and Cell Biology Department of the University of Debrecen Medical School, Hungary to pursue a career in Biophysics. Under a co-operation with Dr. Adriaan Houtsmuller's group he came to Rotterdam in 2001 to work on the "Photo-induced fluorescence fluctuation of EGFP" under the supervision of Dr. Adriaan Houtsmuller before joining the services of the university as the laser facilities manager in charge of fluorescence correlation spectroscopy. He became a Ph.D candidate in 2003 under the supervision of Prof. Dr.J.H.J. Hoeijmakers.

Shehu is presently a laser facilities manager in the Institute for Molecular Biophysics, Department of Physics and Astronomy, Leeds University, United Kingdom.